Conference Proceedings of the Society for Experimental Mechanics Series

Brandon J. Dilworth
Michael Mains *Editors*

Topics in Modal Analysis & Testing, Volume 8

Proceedings of the 39th IMAC, A Conference and Exposition on Structural Dynamics 2021

SEM

Springer

Conference Proceedings of the Society for Experimental Mechanics Series

Series Editor

Kristin B. Zimmerman, Ph.D.
Society for Experimental Mechanics, Inc.,
Bethel, CT, USA

The Conference Proceedings of the Society for Experimental Mechanics Series presents early findings and case studies from a wide range of fundamental and applied work across the broad range of fields that comprise Experimental Mechanics. Series volumes follow the principle tracks or focus topics featured in each of the Society's two annual conferences: IMAC, A Conference and Exposition on Structural Dynamics, and the Society's Annual Conference & Exposition and will address critical areas of interest to researchers and design engineers working in all areas of Structural Dynamics, Solid Mechanics and Materials Research.

More information about this series at http://www.springer.com/series/8922

Brandon J. Dilworth • Michael Mains
Editors

Topics in Modal Analysis & Testing, Volume 8

Proceedings of the 39th IMAC, A Conference and Exposition on Structural Dynamics 2021

Springer

Editors
Brandon J. Dilworth
Lincoln Laboratory
Massachusetts Institute of Technology
Lexington, MA, USA

Michael Mains
University of Cincinnati
Cincinnati, OH, USA

ISSN 2191-5644 ISSN 2191-5652 (electronic)
Conference Proceedings of the Society for Experimental Mechanics Series
ISBN 978-3-030-75995-7 ISBN 978-3-030-75996-4 (eBook)
https://doi.org/10.1007/978-3-030-75996-4

This Springer imprint is published by the registered company Springer Nature Switzerland AG
The registered company address is: Gewerbestrasse 11, 6330 Cham, Switzerland

Preface

Topics in Modal Analysis, Testing & Parameter Identification represents one of the nine volumes of technical papers presented at the 39th IMAC, A Conference and Exposition on Structural Dynamics, organized by the Society for Experimental Mechanics and held on February 8–11, 2021. The full proceedings also include volumes on Nonlinear Structures & Systems; Dynamics of Civil Structures; Model Validation and Uncertainty Quantification; Dynamic Substructures; Special Topics in Structural Dynamics & Experimental Techniques; Rotating Machinery, Optical Methods & Scanning LDV Methods; Sensors and Instrumentation, Aircraft/Aerospace, Energy Harvesting & Dynamic Environments Testing; and Data Science in Engineering.

Each collection presents early findings from experimental and computational investigations on an important area within Structural Dynamics. Topics in Modal Analysis, Testing and Parameter Identification represents papers on enabling technologies for dynamic systems and applications of Modal Analysis in specific application areas.

The organizers would like to thank the authors, presenters, session organizers, and session chairs for their participation in this track.

Lexington, MA, USA — Brandon J. Dilworth
Cincinnati, OH, USA — Michael Mains

Contents

Chapter 1
A Structural Dynamics Approach to Modeling Human Performance

Michael C. Sevier and Michael D. Cook

Abstract Health and athletic performance models can be used to prescribe an individualized training regimen to maximize improvement over a given period (e.g., preparing for a peak event). The Banister impulse-response (IR) model is a popular approach to describe the cumulative dynamic effects of training on athletic performance. The model describes both positive and negative training effects (PTEs and NTEs, respectively) that occur from a single training impulse, each having magnitude and decay parameters determined via testing of individual athletes. This work proposes that PTE and NTE responses from a single training impulse can similarly be described by the response of a single degree of freedom (SDOF) viscoelastic system. Cumulative training effects can then be modeled using the discrete form of the convolution integral in a manner similar to the IR model. The pedagogical advantage of this approach is to offer students studying mechanical vibrations a physical sense for how cumulative impulses relate to the response of a system. The other advantage of this approach is to initiate the discussion on how concepts from structural dynamics can be used to solve problems in exercise physiology.

Keywords Banister impulse-response model · Exercise physiology · Viscoelastic model · Vibrations · Biomechanical model

1.1 Background: Banister IR Model

Human performance models are used to prescribe individualized exercise routines in order to optimize physiological capability at a target date. The Banister impulse-response (IR) model [1, 2] is a popular method of monitoring cumulative fitness and fatigue effects due to training over the course of a season. Banister [3] proposed defining the magnitude of training impulses (TRIMPs) by:

$$\text{TRIMP} = t \cdot k \cdot \text{FHRR} \tag{1.1}$$

$$\text{FHRR} = \frac{\text{HR}_{\text{average}} - \text{HR}_{\text{rest}}}{\text{HR}_{\text{max}} - \text{HR}_{\text{rest}}} \tag{1.2}$$

where t is the duration of the exercise bout in minutes, FHRR is the fraction of the heart rate (HR) reserve, and k is defined by Eqs. (1.3) and (1.4) for men and women, respectively.

$$k = 0.64e^{1.92 \cdot \text{FHRR}} \tag{1.3}$$

$$k = 0.86e^{1.67 \cdot \text{FHRR}} \tag{1.4}$$

M. C. Sevier (✉)
Department of Mechanical Engineering, Milwaukee School of Engineering, Milwaukee, WI, USA
e-mail: sevier@msoe.edu

M. D. Cook
Rockwell Automation, Milwaukee, WI, USA

B. J. Dilworth, M. Mains (eds.), *Topics in Modal Analysis & Testing, Volume 8*, Conference Proceedings of the Society for Experimental Mechanics Series, https://doi.org/10.1007/978-3-030-75996-4_1

Note that related approaches, such as the training stress score (TSS), have been adapted for cycling by utilizing power meter readings instead of heart rate [4]. The TSS approach has also been extended to running and swimming [5–10]. Calvert et al. [11] determined that a linear ordinary differential equation (ODE) can be used to represent the change in performance capacity $p(t)$ over time t:

$$\frac{\mathrm{d}p(t)}{\mathrm{d}t} = -\frac{1}{\tau}p(t) + w(t) \tag{1.5}$$

where $w(t)$ is training stress and τ is the decay time constant. Note that the performance value $p(t)$ can represent a variety of performance metrics such as speed or power. The solution of the ODE in Eq. (1.5) can be represented as the following convolution integral:

$$p(t) = \int_0^t e^{-(t-\Theta)/\tau} w\left(\Theta\right) \mathrm{d}\Theta, \tag{1.6}$$

or in discretized form:

$$p(t) = \sum_{i=1}^{t-1} e^{-(t-i)/\tau} w(i) \Delta t = \sum_{i=1}^{t-1} e^{-(t-i)/\tau} w(i), \tag{1.7}$$

where i is the ith day leading up to day t and Δt is set equal to a constant value of 1 day. During the initial stages of training, athletes often experience reduced performance capacity (i.e., negative $p(t)$) that Eq. (1.7) could not capture in its current form [11]. The equation was modified to account for positive training effects (PTEs) and negative training effects (NTEs) separately:

$$\mathrm{PTE}(t) = k_1 \sum_{i=1}^{t-1} e^{-(t-i)/\tau_1} w(i), \tag{1.8}$$

$$\mathrm{NTE}(t) = -k_2 \sum_{i=1}^{t-1} e^{-(t-i)/\tau_2} w(i), \tag{1.9}$$

where k_1 and k_2 are gain parameters for PTE and NTE, respectively. Similarly, τ_1 and τ_2 are the decay time constants for each of the training effects. The total performance is measured as the sum of both training effects combined with an initial performance parameter $p(0)$.

$$p(t) = p(0) + \mathrm{PTE}(t) + \mathrm{NTE}(t) \tag{1.10}$$

Note that the PTEs and NTEs are a qualitative representation of cumulative physiological parameters and are not representative of a single quantifiable result. Typically, NTEs are larger in magnitude than PTEs but also decay more rapidly. If training loads are too frequent and/or too intense, the NTEs accumulate and can lead to overtraining and/or fatigue. If training loads are spaced too far apart, then the PTEs decay to a point where negligible training benefit occurs. The five adjustable parameters (i.e., k_1, k_2, τ_1, τ_2, $p(0)$) in Eqs. (1.8)–(1.10) would be determined by fitting an individual's performance throughout normal in-season training with that predicted by an equation. This could subsequently be used to determine which type of training would best suit the individual for a season. For example, results reproduced from Clarke and Skiba [12] in Fig. 1.1 show how a triangular training schedule might be advantageous for one athlete ($\tau_1 = 25$, $\tau_2 = 10$) but not for another ($\tau_1 = 30$, $\tau_2 = 5$) when compared to a constant training schedule.

The purpose of this work is to see if the Banister IR model for human performance can be replicated using the response of simple single degree of freedom (SDOF) viscoelastic oscillators due to initial conditions. The motivation for this is twofold:

1. Introduce students of vibration mechanics to the convolution integral commonly used for a system's response to an arbitrary forcing function. This may be advantageous since the student will be able to kinesthetically relate their own experiences from hard exertion to what is being experienced by a vibrating specimen.

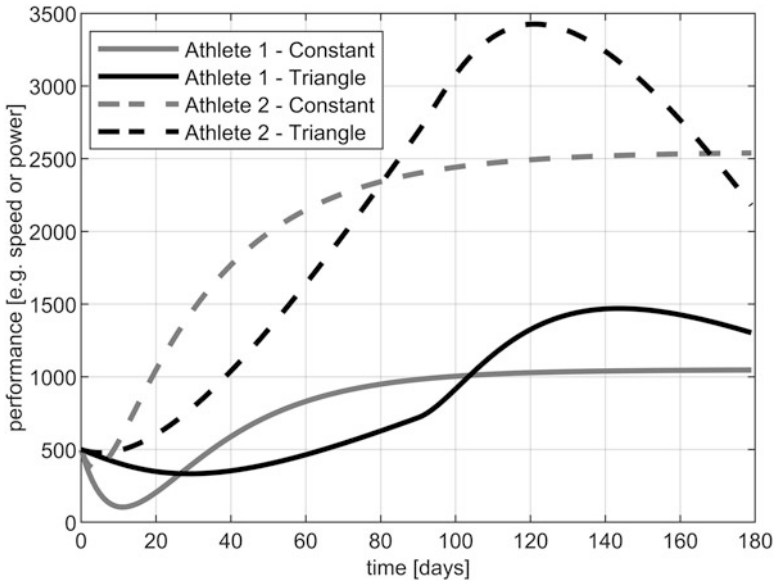

Fig. 1.1 Performance comparison between athlete 1 ($\tau_1 = 25$, $\tau_2 = 10$) and athlete 2 ($\tau_1 = 30$, $\tau_2 = 5$) when subject to constant training load (100 TRIMP) vs. triangular training load (10 TRIMP at the beginning and end, 180 TRIMP in the middle). Both athletes have gain parameters $k_1 = 1$ and $k_2 = 2$

2. Suggest that a potential relationship may exist between how the human body adapts to applied impulses and the principals of vibrations and modal analysis. There is a wealth of information in the field of structural dynamics that may lead to new insights in how the body responds to training loads.

1.2 Viscoelastic Model

The model presented here is based on the position response, $x(t)$, over time, t, of a critically damped single degree of freedom viscoelastic system having natural frequency, ω_n, due to initial displacement, x_0, and zero initial velocity:

$$x(t) = x_0 \left(1 + \omega_n t\right) e^{-\omega_n t}. \tag{1.11}$$

The form of this equation was chosen because it most closely represents the NTE and PTE form of response in the Banister IR model. Equation (1.11) could be reinterpreted in the form shown below for the PTE response due to an initial PTE displacement (i.e., product of training load ω_0 and gain parameter k_{PTE}):

$$\text{PTE}(t) = k_{\text{PTE}} \cdot w_0 \cdot \left(1 + \omega_{\text{PTE}} t\right) e^{-\omega_{\text{PTE}} t} \tag{1.12}$$

where ω_{PTE} would represent the natural frequency of the PTE response akin to the inverse of the time constant, $1/\tau$, in Eqs. (1.6) and (1.7). Equation (1.12) can be expanded to the discretized form of the convolution integral to evaluate the PTE and NTE response due to multiple training sessions as:

$$\text{PTE}(t) = k_{\text{PTE}} \sum_{i=1}^{t-1} w(i) \cdot \left(1 + \omega_{\text{PTE}} \left(t(i) - i\right)\right) e^{-\omega_{\text{PTE}} \left(t(i) - i\right)}, \tag{1.13}$$

$$\text{NTE}(t) = -k_{\text{NTE}} \sum_{i=1}^{t-1} w(i) \cdot \left(1 + \omega_{\text{NTE}} \left(t(i) - i\right)\right) e^{-\omega_{\text{NTE}} \left(t(i) - i\right)}, \tag{1.14}$$

where time t would be measured in days and each increment i corresponds to 1 day. The total performance response $p(t)$ could similarly be determined from Eq. (1.10) as the sum of both training effects combined with an initial performance parameter $p(0)$. Similar to the Banister IR model, there are five adjustable parameters (i.e., k_{PTE}, k_{NTE}, ω_1, ω_2, $p(0)$) that would be determined from an individual's in season training.

Note that a variation of Eq. (1.11) was considered where the initial velocity would represent the training impulse instead of the initial displacement. The advantage of this form would be that it would more closely represent the relationship between a mechanical impulse, $\hat{\boldsymbol{F}}$, and velocity, $\boldsymbol{v}$, provided by the impulse-momentum relationship $\hat{\boldsymbol{F}} = \boldsymbol{\Delta m v}$ (where $\boldsymbol{m}$ is an object's mass). This approach was disbanded to have a more similar relationship with the Banister IR model. However, it should be noted that the initial velocity form might be a better fit in cases where the physical response is determined within the timeframe of the training period. Additionally, the combination of positive initial training velocity and negative initial displacement could result in a single equation that would adequately represent the total performance response. This approach would represent supercompensation performance models that predate the Banister IR model [13].

1.3 Results and Discussion

1.3.1 Response to Single Impulse

Figure 1.2 compares the response due to a single 100 TRIMP impulse using both the Banister IR ($k_1 = 1$, $k_2 = 2$, $\tau_1 = 27$, $\tau_2 = 10$) and viscoelastic ($k_{\mathrm{PTE}} = 1$, $k_{\mathrm{NTE}} = 2$, $\omega_{\mathrm{PTE}} = 0.075$, $\omega_{\mathrm{NTE}} = 0.2$) models. The slope in the viscoelastic model is more horizontal near the training impulse due to the assumption of zero initial velocity in Eq. (1.11). Although differences between the two models can be observed, the authors believe these differences to be within the error already present in the Banister IR model. Additionally, if important differences are discovered, they could be ameliorated by an adjustment in parameters.

1.3.2 Cumulative Response over Season

A basic season training schedule might include constant training for most of the season with a taper period of reduced training leading to the final race. A well-timed taper period allows for NTEs to diminish before a substantial loss in PTEs.

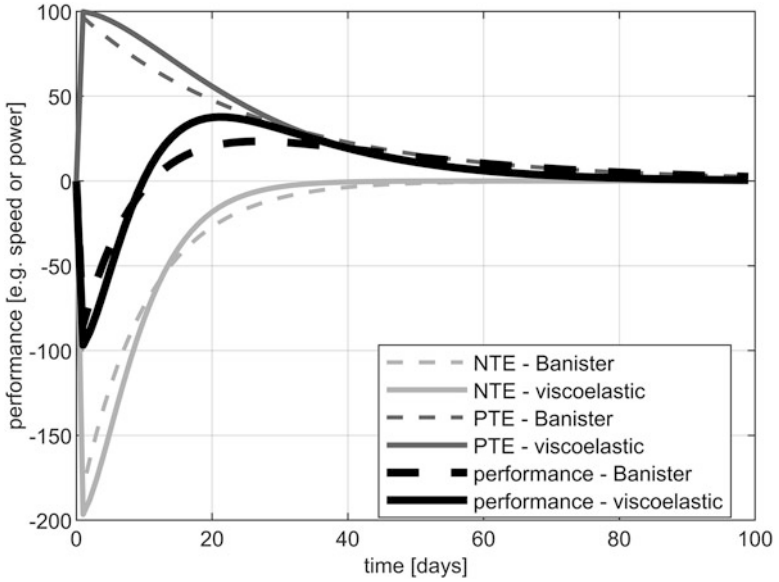

Fig. 1.2 Banister IR ($k_1 = 1$, $k_2 = 2$, $\tau_1 = 27$, $\tau_2 = 10$) and viscoelastic ($k_{\mathrm{PTE}} = 1$, $k_{\mathrm{NTE}} = 2$, $\omega_{\mathrm{PTE}} = 0.075$, $\omega_{\mathrm{NTE}} = 0.2$) response due to a single 100 TRIMP impulse

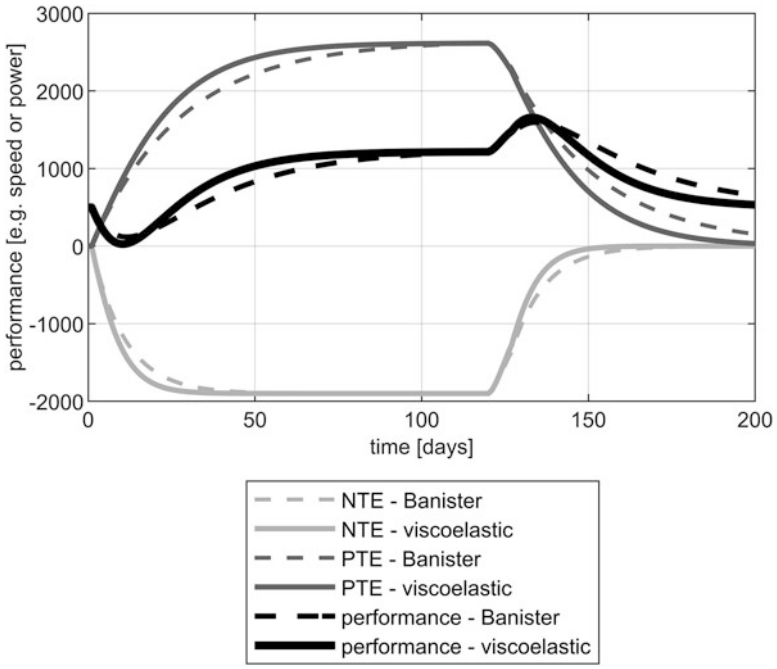

Fig. 1.3 Cumulative performance prediction for the Banister IR and viscoelastic models throughout season. Initial performance, $\boldsymbol{p}(\mathbf{0})$, set to 500 (arbitrary units)

This would lead to a supercompensation effect of peak performance near the target event. Figure 1.3 illustrates such an effect using both models (same parameters as Fig. 1.2) for a constant training load of 100 TRIMPs for 120 days, a seven-day period of reduced training (80, 60, 50, 40, 35, 30, 30 TRIMPs), followed by no training for 3 days until the target event at day 130.

1.3.3 Parameter Fitting

The results shown in Figs. 1.2 and 1.3 assume that the five adjustable parameters for the athlete are known for either model. These parameters include initial performance, $p(0)$, two gain parameters (k_1, k_2 for the Banister IR model and k_{PTE}, k_{NTE} for the viscoelastic model), and two decay parameters (τ_1, τ_2 for the Banister IR model and ω_{PTE}, ω_{NTE} for the viscoelastic model). The values can be determined via a minimization algorithm evaluating the difference between measured performance data and the performance predication model. For example, if there are N data points, a minimization function might take the form of:

$$f_{\min} = \sqrt{\sum_{i=1}^{N} \left(p_{\text{model}}(i) - p_{\text{data}}(i)\right)^2} \tag{1.15}$$

where $p_{\text{data}}(i)$ is the measured performance data and $p_{\text{model}}(i)$ is the performance prediction from either model at the same time. Suppose that nine average power readings were measured from a one-hour cycling time trial as shown in Table 1.1. A possible set of athletic parameters derived from a minimization algorithm performed on Eq. (1.15) would be given in Table 1.2. Figure 1.4 demonstrates how well each model compares to the measured data points given in Table 1.1 with the parameters indicated in Table 1.2.

Table 1.1 Sample time-trial cycling results

Test day number	Test power (W)
45	271
48	274
56	282
70	290
77	292
83	296
105	299
115	296
132	302

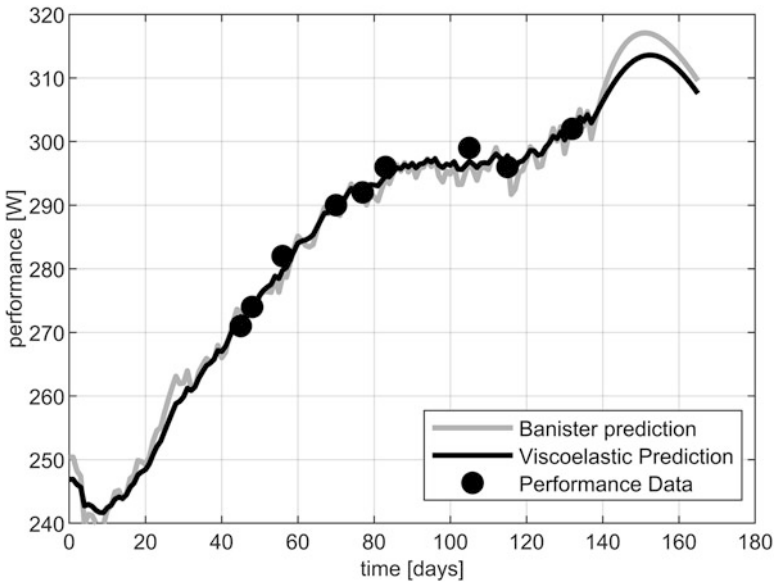

Fig. 1.4 Performance models with parameters fitted to performance data

Table 1.2 Model parameters based on sample time-trial cycling results shown in Table 1.1

Parameter	Banister IR model		Viscoelastic model	
Initial performance	$p(0)$	250	$p(0)$	247
PTE gain	k_1	0.31	k_{PTE}	0.141
NTE gain	k_2	0.36	k_{NTE}	0.159
PTE decay	τ_1	29.3	ω_{PTE}	0.0465
NTE decay	τ_2	20.2	ω_{NTE}	0.0754

1.3.4 Potential for Pedagogical Purposes

In the authors' experience teaching mechanical vibrations and dynamics of systems, students often seem to struggle with terms within the convolution integral equation. Equation (1.16) demonstrates one such form of the equation where the displacement response, x, at time t due to forcing function $F(t)$ is evaluated for an underdamped viscoelastic system having mass, m, natural frequency, ω_n, damping factor, ζ, and damped natural frequency, $\omega_{\text{d}} = \omega_{\text{n}}\sqrt{1-\zeta^2}$:

$$x(t) = \int_0^t \frac{F(\tau)}{m\omega_{\text{d}}} e^{-\zeta\omega_{\text{n}}(t-\tau)} \sin\omega_{\text{d}}(t-\tau)\, d\tau. \tag{1.16}$$

The main source of confusion seems to lie in a misunderstanding of what τ and t represent. It is the authors' hope that the viscoelastic model presented in Eqs. (1.10)–(1.14) would bolster a better understanding by offering a kinesthetic analogy. Most people recognize how soreness from a substantial workout can last for multiple days while eventually subsiding. This could be used to explain how the influence of a force at time τ diminishes as the difference between the current time, t, and

τ increases due to the exponential term shown in Eqs. (1.13), (1.14), and (1.16). Additionally, it is the authors' hope that students would recognize how the body feels is not due to simply one training session but the cumulation of multiple training sessions and thereby understand the necessity of the integral in Eq. (1.16) and the summation terms in Eqs. (1.13) and (1.14).

1.3.5 Potential Future Applications of Vibration Principals to Human Performance

It is not uncommon for structural dynamics principals traditionally applied to inanimate objects such as buildings, satellites, and aircraft to also be applied to the human body [14, 15]. However, as far as the authors are aware, the field of structural dynamics has not yet been applied to describe the adaptive capabilities of biological systems. One of the main advantages of structural vibrations is its ability to model the interaction of various structural modes which are excited depending on the amplitude and frequency content of the input load. This may prove useful for predicting specific types of training that the participant can perform that will excite systems that are sufficiently recovered (i.e., NTEs decay more rapidly) while not exacerbating already fatigued systems (i.e., NTEs that decay more slowly). While there are already efforts via machine learning [16] to obtain similar results from loosely correlated variables, the application of structural dynamic principals may offer a more deterministic approach to human performance prediction.

Initial work could involve modeling how individual systems (e.g., bones, muscles, tendons) respond to training impulses. The propagation of training loads from an activity (e.g., running) to loads experienced by individual systems has already been studied in substantial detail. Individual variations to these loads may be monitored by real-time feedback mechanisms [17]. The cumulative effect of training can be determined and compared with human tissue limits. An overall optimization approach may involve the optimization of critical performance systems (e.g., certain muscle groups, VO_2 max) while staying within constraints such as avoiding illness and injury for all systems.

1.4 Conclusions

A critically damped single degree of freedom viscoelastic model is proposed as a viable tool for predicting human performance. The authors believe reasonable agreement with Banister impulse-response (IR) human performance model has been shown for response to a single training impulse, response due to cumulative training loads over the course of a season, and in parameter prediction based on performance data. The authors believe this viscoelastic model offers students of mechanical vibrations a kinesthetic sense for how cumulative impulses relate to the response of a system. Additionally, the authors believe that there may be potential for applying vibration principals to describe adaptive capabilities of the human body in the hopes of gaining further insights for human performance.

References

1. Banister, E., Calvert, T., Savage, M., Bach, T.: A systems model of training for athletic performance. Autr. J. Sports Med. **7**, 57–61 (1975)
2. Taha, T., Thomas, S.: Systems modelling of the relationship between training and performance. Sports Med. **33**, 1061–1073 (2003)
3. Banister, E.W.: Modeling elite athletic performance. In: MacDougall, J.D., Wenger, H.A., Green, H.J., Canadian Association of Sports Sciences (eds.) Physiological Testing of the High-Performance Athlete, pp. 403–424. Human Kinetics, Champaign, IL (1991)
4. Allen, H., Coggan, A.: Training and Racing with a Power Meter. VeloPress, Boulder, CO (2010)
5. McGregor, S., Weese, R., Ratz, I.: Performance modeling in an Olympic 1500-m finalist: a practical approach. J. Strength Cond. Res. **23**, 2515–2535 (2009)
6. Skiba, P.: Analysis of power output and training stress in cyclists: the development of the bikescore algorithm [Online]. http://www.physfarm.com/bikescore.pdf. Accessed 28 Feb 2013
7. Skiba, P.: Calculating power output and training stress in swimmers: the development of the swimscore algorithm [Online]. http://www.physfarm.com/swimscore.pdf. Accessed 28 Feb 2013
8. Skiba, P.: Calculation of power output and quantification of training stress in distance runners: the development of the GOVSS algorithm [Online]. http://www.physfarm.com/govss.pdf. Accessed 28 Feb 2013
9. Skiba, P.: Quantification of training stress in distance runners. Arch. Phys. Med. Rehabil. **87**, 29 (2006)
10. Skiba, P.: The Triathlete's Guide to Training with Power. PhysFarm, Chicago, IL (2008)
11. Calvert, T., Banister, E., Savage, M., Bach, T.: A systems model of the effects of training on physical performance. IEEE Trans. Syst. Man. Cybern. SMC. **6**, 94–102 (1976)

12. Clarke, D., Skiba, P.: Rationale and resources for teaching the mathematical modeling of athletic training and performance. Adv. Physiol. Educ. **37**, 134–152 (2013)
13. Selye, H.: The Stress of Life. McGraw-Hill, New York, NY (1956)
14. von Gierke, H., Oestreicher, H., Franke, E., Parrack, H., von Wittern, W.: Physics of vibrations in living tissues. J. Appl. Physiol. **4**(12), 886–900 (1952)
15. McElhaney, J.: Dynamic response of bone and muscle tissue. J. Appl. Physiol. **21**(4), 1231–1236 (2010)
16. Ellis, D.: How artificial intelligence could transform coaching of endurance cyclists. Training With Data [Online]. https://www.trainingwithdata.com/how-artificial-intelligence-could-transform-coaching-of-endurance-cyclists/. Accessed 17 June 2019
17. Van Hooren, B.: Real-time feedback by wearables in running: current approaches, challenges and suggestions for improvements. J. Sports Sci. **28**(2), 214–230 (2019)

Chapter 2
Feature Based Monitoring Application for Automatic Crack Detection Using WaveImage

Maik Gollnick, Patrick Giese, and Daniel Herfert

Abstract Monitoring systems for machines, plants, materials, and equipment are increasingly used in production processes. These online condition monitoring systems can detect damage or excessive loads at an early stage and can drastically reduce or prevent long downtimes of plants and machines as well as high repair and maintenance costs. This paper depicts a method for online crack detection with pattern recognition and computer vision methods for specimens joined by self-pierce riveting under cyclic load in fatigue tests (laboratory application) (Giese et al. *Early stage crack detection in mechanically joined steel/aluminium joints by condition monitoring*; 2020).

In this context a parameter-free detection of significant frequencies during the test procedure was developed. To achieve this goal, the vibration data is recorded by a triaxial structure-borne sound sensor during the test. The evaluation is used for online crack detection, so that an early shutdown of the testing machine and thus a meaningful result over the life cycle of a mechanically joined joint is guaranteed.

For this purpose, time series are described in the frequency domain at each function value by a novel feature vector. The characteristics used are independent of external test parameters, such as the test frequency or force level. This makes it possible to change test parameters without additional algorithmic effort and without expert knowledge.

Keywords Crack detection · Computer vision · Mechanical joining · Self-pierce riveting · Fatigue

2.1 Introduction

The precise description of the durability of machines and production facilities can help to prevent long downtimes and reduce repair and maintenance costs in industrial environments. A contribution to this characterization is the investigation of mechanically joined joints, which are used in almost every component. Thereby, fatigue strength tests are performed to describe the lifetime of the investigated samples. The application of nondestructive testing methods for condition monitoring using structure-borne sound sensors is becoming more and more important [1].

The aim of this thesis is the development of a condition monitoring system with structure-borne sound sensors for early detection of cracks in mechanically joined components and structures. In a research project [2] the algorithm was developed and evaluated on several samples. Uniform failure criteria are necessary for a comparability of mechanically joined joints and their design. Such criteria are not yet defined. In addition, two conditions are frequently tested based on the testing machine used. The first criterion refers to the stiffness curve. A drop of the associated function of approx. 40% indicates a failure of the component. The second condition refers to the course of the excitation frequency during the test procedure. A change that is too high also indicates crack initiation and is therefore used to investigate the fatigue strength. Both criteria are not sufficient for a uniform description of crack formation, because either only the complete failure of the component can be predicted or the criterion is not transferable between different specimens. Furthermore, due to the complexity of crack development, it cannot be guaranteed that one of the two criteria will show a significant change when a crack develops. Therefore, crack type and crack degree can differ for the same failure criterion.

M. Gollnick · D. Herfert (✉)
Society for the Advancement of Applied Computer Science, Berlin, Germany
e-mail: gollnick@gfai.de; herfert@gfai.de

P. Giese
Laboratory for Material and Joining Technology, University of Paderborn, Paderborn, Germany
e-mail: patrick.giese@lwf.uni-paderborn.de

B. J. Dilworth, M. Mains (eds.), *Topics in Modal Analysis & Testing, Volume 8*, Conference Proceedings of the Society for Experimental Mechanics Series, https://doi.org/10.1007/978-3-030-75996-4_2

In the preceding project [2] the basic algorithm and the control of the testing machines servo- and resonance pulsers were already implemented. Thereby the interfaces to the data recorder and to switch off the test were implemented in the software WaveImage (gfai tech GmbH). To describe the vibration behavior during the test process, the magnitude curve in the frequency domain was considered. The focus in the frequency domain was to put on the excitation frequency, since a significant change of this frequency signals leads to a disturbance in the oscillation pattern and to a readjustment of the testing machine. The tests carried out showed that this assumption is correct for crack formation and can therefore also ensure early crack detection. Furthermore, a feature vector [2] was developed so that a reliable classification between intact and damaged specimen can be made.

To find the excitation frequency, the maximum magnitude value in the considered frequency range was used. This simple method is extremely influenced by sensor noise and/or other signal interferences and in the worst case it can lead to a wrong classification result. For this reason, a classification-based approach for the detection of peaks [3] has been used in this paper and adapted to the problem of crack detection for mechanically joined connections. With this method it is possible to describe misclassifications in advance and to teach them in a model. This reduces the number of wrong decisions in the later classification process and increases the stability of the whole system.

The method used and the adjustments made for crack detection of mechanically joined samples are presented in this thesis.

2.2 Background

The aim of fatigue tests is to determine the fatigue strength of a material or component. The samples used are permanently loaded by a sinusoidal excitation. In the study [2] tests were carried out on a servo-hydraulic testing machine with an excitation frequency of 20 Hz, see Fig. 2.1 (right). Shear tensile specimens with the material combinations steel HC340LA ($t = 1.5$ mm)–aluminum EN AW-6016 ($t = 2.0$ mm) were used and mechanically joined by means of semi-tubular rivets.

To record the time series during the test procedure, a triaxial structure-borne sound sensor from “Metra Mess- und Frequenztechnik Radebul e.K.” (MMF) was applied to the sample below the joining element, see Fig. 2.1 (left). A mechanical clamp was used to attach the accelerometer. The data acquisition was done with a data recorder of the company Goldammer GmbH of the USB Basis Series (G0V-1034-0). The sampling rate was set to 192 kHz to increase the resolution. The time series were recorded for the measurement directions X, Y, and Z.

For the evaluation regarding crack initiation during the test, the time series were divided into smaller and nonoverlapping sections. The length of the sections was determined experimentally and fixed at 10 s. For the classification of a crack, the oscillation behavior during a test can be divided into three sections. The first phase describes the oscillation of the sample. Here the oscillation behavior is irregular and changes to an almost constant state as the test time progresses. This state is

Fig. 2.1 Shear tensile specimen with applied accelerometer (left) and servo-hydraulic test system (right)

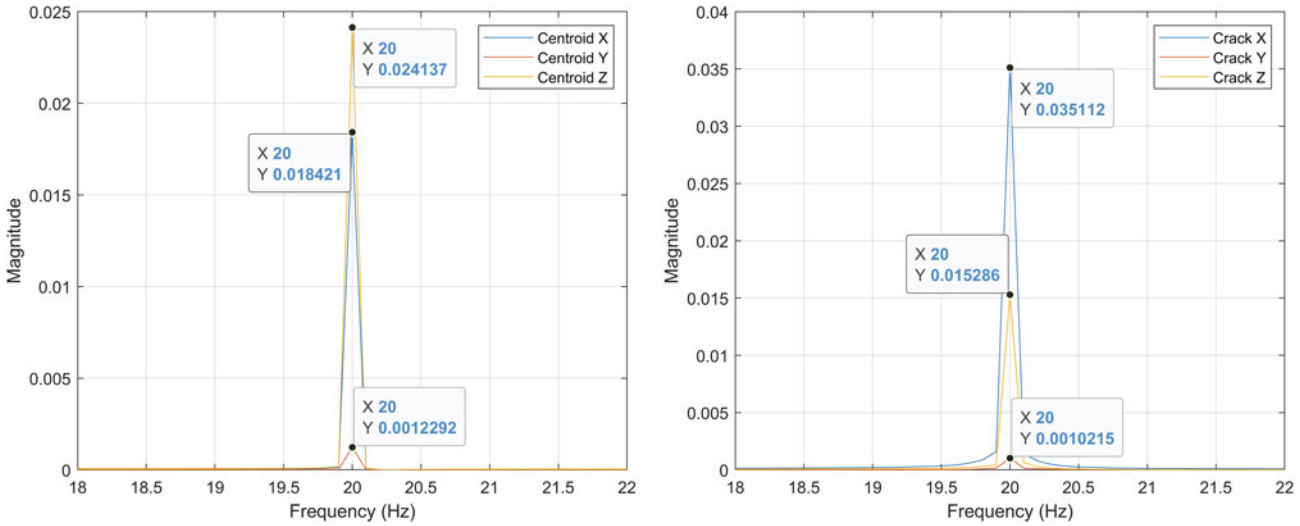

Fig. 2.2 Representation at the location of the excitation frequency of an intact sample (left) and at the time of cracking (right)

described by the second phase. The oscillation response is nearly constant and changes with increasing deformation. If the load limit of the sample is exceeded, the failure phase is reached.

For the acquisition of the crack timing the focus was put on the deformation phase. The time series were transformed into the frequency domain and described. Therefore the magnitude curve below 100 Hz was considered. For the description of the magnitude curves the excitation frequency plays a decisive role. Since the frequency can also change during the experiment [2], it is determined automatically. The determination is based on a maximum value method, where a peak differs from other function values only by its maximum amplitude. The following Fig. 2.2 illustrates the behavior of the magnitude curve at the position of the excitation frequency.

In Fig. 2.2 you can see a significant deviate of the peak at the position of the excitation frequency of about 94% for channel *X*, channel *Y* by about 16%, and channel *Z* about 36%. The curve for each measuring channel is shown. As representative of an intact sample, the centroid of the training quantity is shown in the left graph. In contrast, the right figure shows the magnitude progression at the time of a crack. This shows the clear difference between intact and damaged sample.

Based on this observation the feature vector was created. It is used for the classification of cracks and consists of two components. The first component results from the description of the peak at the excitation frequency. For this purpose, the peak width and the peak height are used as values. The width is normalized by the number of frequency lines. For the independent representation of the height in relation to the existing force level, the amplitude is normalized by a reference standard deviation. This value results from the amplitudes of all training examples at the position of the excitation frequency [2].

The second component is represented by the correlation of the currently observed magnitude progression with the training data and describes the change of the entire progression. For training data, this value is formed by the negative correlation to each other. This three-dimensional vector is created for each measuring direction and chained to a total feature vector.

For the final crack classification a local four-step model was created. In the first step, the transient phase is detected and skipped. In the second step, a local training set is built up. The amount of data used results from the excitation frequency and an experimentally determined value. After the training set has been created the actual classification follows. The time series are transformed into feature vectors and checked against the training set by means of negative correlation. The result value is represented as an indicator function. The function values are assigned to the classes “intact sample” and “damaged sample” by a threshold value procedure.

2.3 Automatic Peak Search

In the work [3] a parameterless method for the recognition of peaks in indicator functions was already presented. Due to the simple calculation and the frequent application in the field of modal analysis the “Complex Mode Indicator Function” [4, 5] was used as reference. Each single function value was described by a feature vector and integrated into a synthetically

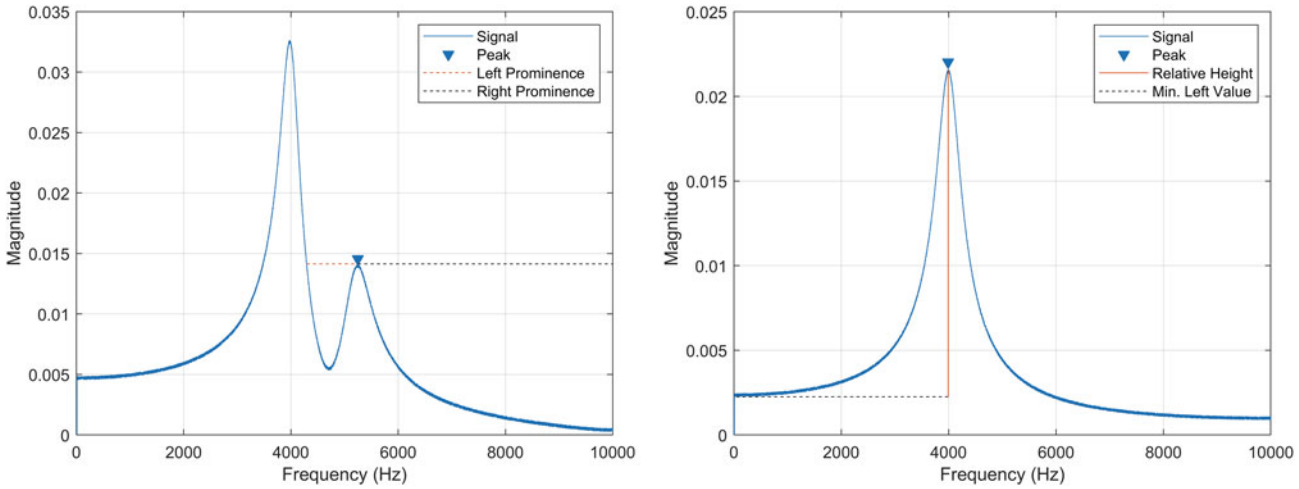

Fig. 2.3 Visualization of the feature calculation for automatic peak search. The calculation of the left and right peak prominence for two sample peaks (left). The calculation of the relative height (right)

learned classification model. Three features were used to create the vectors. The first two characteristics describe the function values to the left and right of the currently considered location, which are smaller than the current function value. Sine a shift in the feature space occurs due to the varying peak position, the description was supplemented by the relative peak height. Thus, the third feature compensates for the weaknesses of the first two features and guarantees a clear representation in the feature space. For the calculation of the features all amplitudes are scaled to the range between zero and one. The following Fig. 2.3 illustrates the calculation of these characteristics.

Figure 2.3 (left) shows the determination of the left and right peak prominence. For this purpose the values smaller than the currently considered function value are counted and normalized by the number of frequency lines to the range [0,1]. This normalization is important, because otherwise a binding to the signal size would be present. Figure 2.3 (right) illustrates the calculation of the relative peak height. Here the value is defined as the difference between the maximum of the left and right minimum and the currently considered amplitude. The left and right minimum is determined when calculating the left and right peak prominence. The normalization results from the previous scaling of all amplitudes to the range [0,1].

2.4 Adjustment of the Automatic Peak Search

Since the selection of the test frequency plays a decisive role for the stability of the crack detection, the existing procedure for the selection of the peaks was replaced by the automated peak detection [3]. For this purpose the generally applicable method was adapted to the conditions of crack detection for fatigue tests.

For the description of the function values the basic feature vector of the classification-based method was used. This vector was taught with synthetic data and with data from previous experiments. As classification model a “Support Vector Machine” [6] optimized with the “Iterative Single Data Algorithm” [7] was used. To generate the data sets, tests were carried out with the material combinations HC340LA ($t = 1.5$ mm)–EN AW-6016 ($t = 2.0$ mm) and EN AW-6016 ($t = 2.0$ mm)–HC340LA ($t = 1.5$ mm). The samples were mechanically joined by means of semi-tubular rivets. The combination of synthetic and real test series should lead to a better adaptation of the method. Furthermore, the data were modified with a noise function to better represent the influence of external disturbances.

A post-processing step has been added to adjust the automatic peak search. Since the excitation frequency always occurs in connection with its harmonic frequencies, an additional check of the detected frequencies for their multiples was added. If a frequency occurs as a multiple, the smallest multiple was returned as detected excitation frequency. The following Fig. 2.4 shows the mode of operation of the applied method.

Figure 2.4 shows all detected peaks. It quickly becomes clear that some peaks are only caused by interference in the signal and are not related to an excitation frequency. In addition to these interference peaks, the harmonics of the excitation frequency must also be excluded. With this simple strategy the detected peaks could be reduced and noise or interference peaks could be excluded.

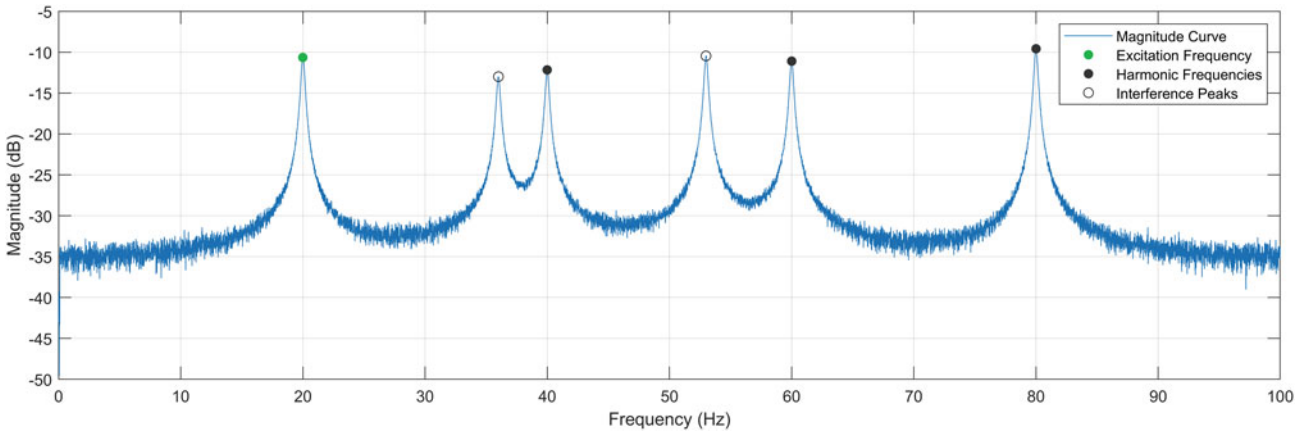

Fig. 2.4 Illustration for the calculation of the excitation frequency using automatically detected peaks

In summary, it can be said that the classification method used for automated peak detection has significantly improved the stability of crack detection. By the additional testing for harmonic frequencies and peaks that do not represent any excitation frequency could be excluded.

2.5 Conclusion

In this thesis a classification-based method for the automatic detection of peaks was presented. This method was extended for the context of crack detection in fatigue tests with mechanically joined specimens. Thus, the previously used method, which only used the maximum function value as an indicator, could be replaced. The associated weaknesses such as sensor noise or other disturbing signals could be successfully solved. In the one-time learning phase of the classifier all known influences could be mapped and a later misinterpretation during the assignment process could be avoided. A more precise adaptation could be achieved by the additional extension of the training process with real measurement data. Since the method works without parameters, no additional expert knowledge is required. This facilitates the practical application. Thus, the applied model improves the quality and robustness of crack classification.

In further investigations disturbing signals from, e.g., nearby test machines will be recorded and integrated into the training process.

Acknowledgments The research results presented and used originate from the IGF research project 19700N of the Society for the Advancement of Applied Computer Science (GFaI) and the "Forschungsvereinigung Stahlanwendung" (FOSTA), which was funded by the "Arbeitsgemeinschaft industrieller Forschungsvereinigungen" (AiF) within the framework of the program for the promotion of industrial research (IGF) by the Federal Ministry of Economics, Mittelstand and Energy (BMWi) based on a resolution of the German Bundestag.

References

1. Kolerus, J., Wassermann, J.: Condition Monitoring of Machines—The Textbook and Workbook for the Practitioner, 7th edn. Expert Verlag, Renningen (2017) (in German)
2. Giese P., Hein D., Meschut G., Gollnick M., Herfert D.: Early stage crack detection in mechanically joined steel/aluminium joints by condition monitoring. Materials Testing 62/9 (2020)
3. Gollnick, M., Herfert, D., Heimann, J.: Automatic modal parameter identification with methods of artificial intelligence. Proc. IMAC. **38**, (2020)
4. Leurs W., Deblauwe F., Lembregts F.: Modal parameter estimation based on complex mode indicator functions, LMS Intl. Leuven, Belgium. In: Proceedings of 11th International Modal Analysis Conference, pp. 1035–1041 (1993)
5. Allemang R.J., Brown D.L.: A complete review of the complex mode indicator function (CMIF) with Applications. In: Proceedings of ISMA2006 Int. conference on noise and vibration engineering, Sep 2006, pp. 3209–3246 (2006)
6. Schölkopf, B., Smola, A.: Learning with Kernels: Support Vector Machines, Regularization, Optimization, and Beyond (Adaptive Computation and Machine Learning). MIT Press, Cambridge, MA (2002)
7. Kecman, V., Huang, T.-M., Vogt, M.: Iterative single data algorithm for training kernel machines from huge data sets: theory and performance. In: Wang, L. (ed.) Support Vector Machines: Theory and Applications, pp. 255–274. Springer-Verlag, Berlin (2005)

Chapter 3
High Spatial Resolution Modal Parameter Estimation via Low-Cost Fiber Optic Strain Sensors

Benjamin L. Martins

Abstract An experimental demonstration is presented highlighting the ability of low-cost, mass-produced, Bragg-grated fiber optic strain sensors to be used in response-only modal analysis. For the demonstration, a lightweight carbon fiber testbed instrumented with a single optical fiber containing 59 fiber optic strain sensors was mounted in a cantilever configuration. The dynamic strain response of the beam to impact excitation of an unknown magnitude and direction were recorded for five impacts. The resulting strain response time-history data was processed into sensor-to-sensor power spectral density information to allow for modal parameter estimation using ATA's IMAT™ software. The information for each of the derived power spectral density functions was combined into a power spectral mode indicator function to identify the poles of the system and extract the modal frequencies and damping ratios for the first seven flexible modes of the testbed. A scanning laser vibrometer was used to validate the modal parameters obtained by the fiber optic strain sensing system using conventional frequency-response-function-based experimental modal analysis techniques.

Keywords Modal testing · Modal parameter estimation · Fiber optic sensing · Dynamic strain · Operational modal analysis

Nomenclature

ATA	ATA Engineering, Inc.
DOF	Degree of freedom
EMA	Experimental modal analysis
IMAT	Interface between MATLAB, Analysis, Test
OFDR	Optical frequency domain reflectometry
PSD	Power spectral density
PSMIF	Power spectral mode indicator function
SLV	Scanning laser vibrometer
UUT	Unit under test

3.1 Introduction

Modal parameter estimation is a fundamental part of research and development programs spanning a broad range of industries. Understanding the vibration response of the unit under test (UUT) provides important information typically used in model correlation and validation efforts. The common practice in modal parameter estimation is to instrument the UUT with an array of accelerometers and measure the response while a known (and measured) force is applied [1]. While this approach has unquestioned utility that has led to it being the industry standard, there are instances where increased spatial resolution with negligible mass loading may be desirable.

Fiber optic strain sensors provide an opportunity for high spatial resolution modal data to be obtained on lightweight, flexible structures without influencing the modal response of the host structure in a meaningful manner [2]. Historically,

B. L. Martins (✉)
ATA Engineering, Inc., 13290 Evening Creek Drive South, San Diego, CA, USA
e-mail: Benjamin.Martins@ata-e.com

B. J. Dilworth, M. Mains (eds.), *Topics in Modal Analysis & Testing, Volume 8*, Conference Proceedings of the Society for Experimental Mechanics Series, https://doi.org/10.1007/978-3-030-75996-4_3

the monitoring of structural dynamics with fiber optic strain sensors has been done using customized fibers and wavelength division multiplexing [3]. The use of optical frequency domain reflectometry (OFDR) demodulation, on the other hand, allows standardized sensing fibers to be mass-produced at a fraction of the cost. These standardized sensing fibers are produced at differing spatial resolutions providing point measurements down to 1/8 inch of separation on a single fiber [4]. Recent advancements in OFDR processing technologies have enabled accurate monitoring of high spatial resolution dynamic strain response [5]. Leveraging this technology, this paper explores modal parameter estimation using response-only strain data and compares such a technique to scanning laser vibrometer (SLV)-based experimental modal analysis (EMA)-derived parameters.

3.2 Experimental Setup

To demonstrate the utility of OFDR fiber optic strain sensors in modal parameter estimation, an experimental testbed was identified [5]. The testbed used in this study was composed of a thin-wall carbon/epoxy composite tube, a network of distributed OFDR fiber optic strain sensors, and three airfoil-shaped steel masses. The root-most 6 inches of the 98-inch beam were clamped, simulating an aircraft wing with cantilever boundary condition. The experimental testbed is shown in Fig. 3.1.

The cross section of the composite tube was near rectangular, having nominal dimensions of 2 inches by 1 inch and a wall thickness 0.04 inches. Each of the three airfoil masses was waterjet from A36 steel to have a NACA-0016 profile with a 17-inch chord that is 1-inch thick. The airfoil masses were mounted to the composite beam at 36, 65.75, and 97.5 inches from the beam's root to the center of the mass. The inclusion of airfoil masses reduced the modes of the structure such that the first six bending vibration modes were less than 25 Hz. This includes the first three bending modes in the soft-plane (bending about the y-axis, out-of-plane, or flapping) and first three bending modes in the stiff-plane (bending about the z-axis, in-plane, or lead-lag).

A single optical fiber was attached to one of the long faces of the carbon tube at the maximum distance from each neutral axis of the beam (without the fiber lying on the corner) to maximize the sensitivity of the fiber to the dynamic strain in both of the beam's bending planes. A representative diagram of the fiber's location relative to the tube's cross section is provided in Fig. 3.2. The fiber itself was a Bragg-grated fiber developed specifically for OFDR sensing systems that have the same central wavelength for each grating set, leading to a low-cost (mass-production), high-sensor-count fiber. The optical fiber (including cladding) had a nominal diameter of 0.005 inches and a linear weight of 0.00102 pound per foot. The chosen grating spacing was 0.157 inches (4 mm) on center with a grating length of 0.0787 inches (2 mm). This combination led to 59 point strain measurements in total along the span of the cantilever tube. A proprietary OFDR fiber optic strain sensing system developed by NASA Armstrong Flight Research Center was used to measure the dynamic strain data.

In addition to the response-only modal parameters estimated from the dynamic strain data, an SLV was used to conduct non-contact EMA. A Polytec PSV-400 SLV provided a full-field assessment of the UTT's vibration response for use as a baseline comparison for the fiber optic system estimates. The vibrometer used in the current study was a one-dimensional system, i.e., vibration data in only one plane at a time was acquired. As a result, two scans were required to capture the data in both the soft-bending and stiff-bending planes. In total, 52 vibrometer targets were affixed to the beam on the short face and 64 targets on the tall face, including targets on the airfoil masses and fixturing. The targets were made of 3M reflective tape, measured to be 1/8 inch squares. The three images in Fig. 3.3 show the setup of the vibrometer for the tall face (left), short face (right), and a zoomed view of some of the targets associated with the center section of the beam (center).

3.3 Results

Response-only data was collected from the fiber optic strain sensors, allowing for computation of the power spectral density (PSD) matrix (auto- and cross-spectra) between sensor pairs. The testbed was excited via impact on the upper airfoil mass (closest to the clamped end) to provide the requisite broad-spectrum excitation for calculation of the PSD. The airfoil mass was impacted using an industrial hammer at an angle relative to the leading edge such that modes in both planes of the beam were excited. Five excitation cycles were repeated to allow for complex averaging of the PSD. The response of the testbed was monitored using the 59 fiber optic strain sensors along the single optical fiber. The strain time history of each of the sensors along the beam's length is plotted in three-dimensional space in Fig. 3.4, with the plot oriented to look down the sensor location axis.

Fig. 3.1 Experimental testbed as tested (the red line showing the fiber location is computer generated for clarity)

Note the coordinates of the beam range from 92 inches (the free end) to 0 inches (the fixed end), where the first 6 inches of the beam contain the mounting fixture and are assumed to be fixed (and hence not shown). The remaining plots are done in a consistent manner where the effective length of the beam is 92 inches and the clamped 6-inch root is neglected. At the locations surrounding 30, 60, and 92 inches, the localized strain effects of the airfoil masses on the strain time histories are visible in Fig. 3.4. Another important conclusion from Fig. 3.4 is there was a good distribution of strain energy throughout the majority of the beam's length. This is important to ensure quality data was available from most, if not all, of the available sensors. To better visualize the strain time histories, the response of sensor 5 was extracted from the three-dimensional plot and is given in Fig. 3.5. An artifact of the developmental fiber optic system used in the data acquisition is the spurious negative spikes shown in the strain time history in Fig. 3.5. These spikes are not fundamental to the technology and are inconsequential to the current study.

Once the strain time histories were obtained, the PSD of each sensor was calculated relative to a chosen reference degree of freedom (DOF). Using sensor 5 as the reference DOF, the magnitude of the PSD for each of the 59 sensors was calculated, using five spectral averages in the complex domain, and plotted in Fig. 3.6.

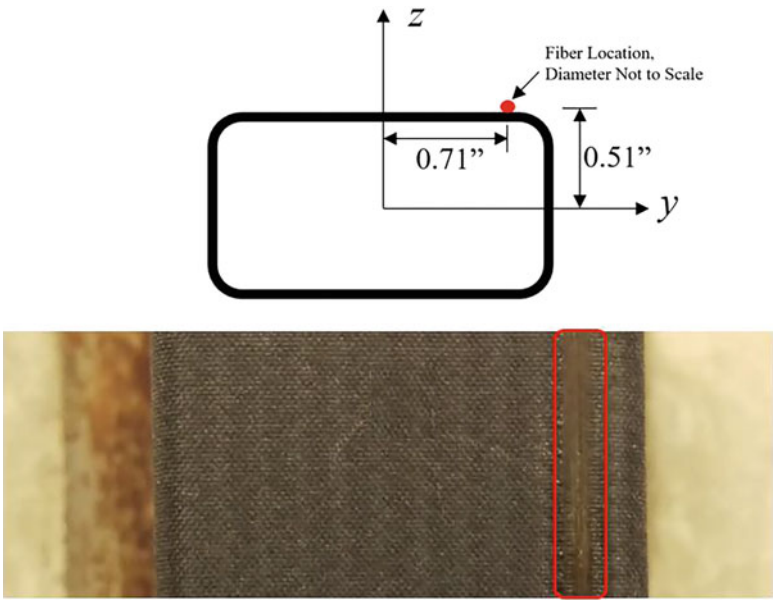

Fig. 3.2 Section of the experimental testbed as tested (the red line showing the fiber location is computer generated for clarity)

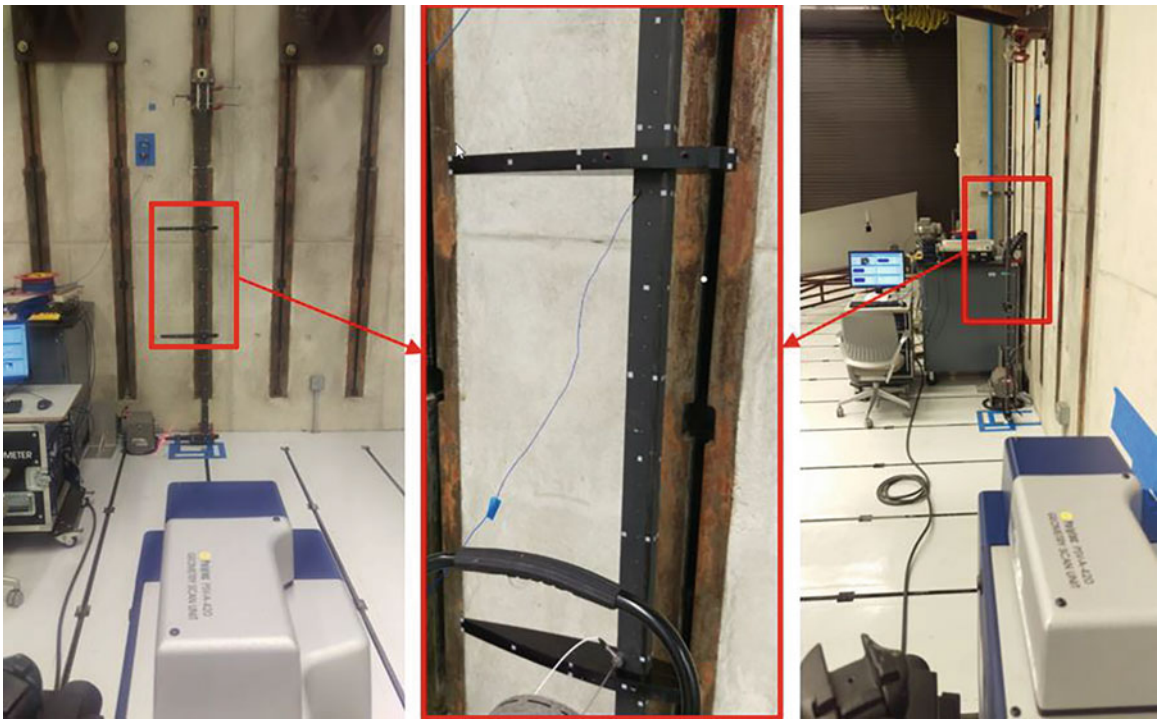

Fig. 3.3 Section of the experimental testbed as tested (the red line showing the fiber location is computer generated for clarity)

As shown in Fig. 3.6, the PSD of the two tip-most sensors have higher responses than the neighboring sensors. This increased response is believed to be a combination of two effects, the first being the localized strain associated with the tip airfoil mass. Second, at the end of the fiber is a crude termination inflicted to end the transmission of light. This termination tends to produce localized reflections in the data, impacting the sensors nearest the end of the optical fiber. As a result, the two sensors nearest the tip were removed prior to the selection of the poles during the modal parameter estimation procedure. To provide a more clear representation of a quality measurement, the PSD of sensor 2 relative to sensor 5 was isolated from the three-dimensional plot and is shown in Fig. 3.7. In addition to the magnitude of the PSD, the coherence between the signals and the real and imaginary components of the PSD are also plotted.

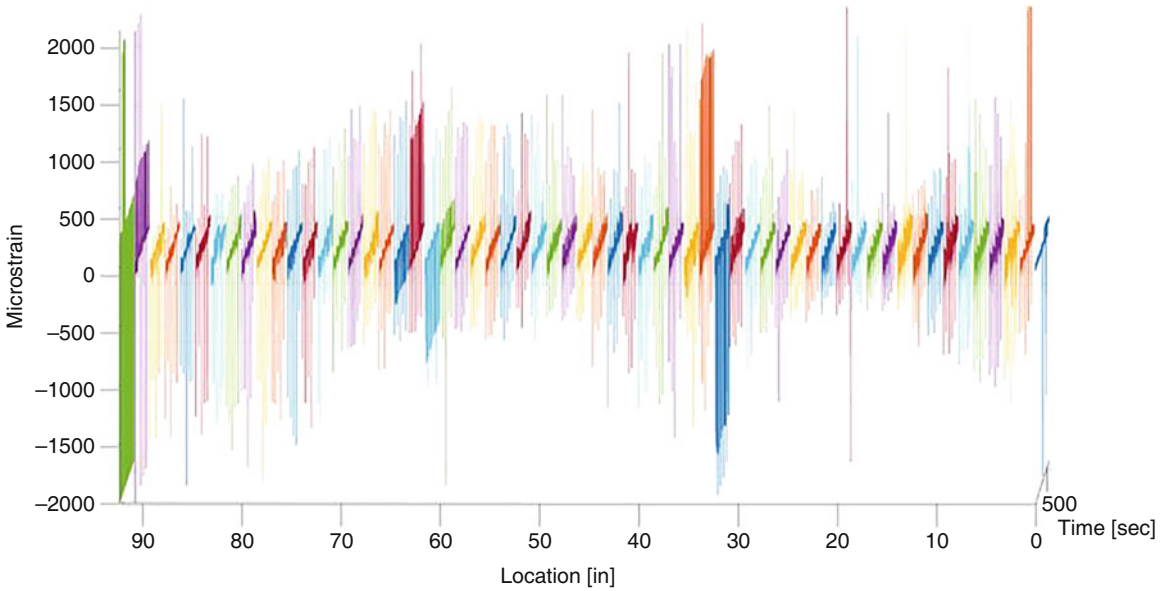

Fig. 3.4 Strain time histories of each of the strain sensors for the five impact excitations

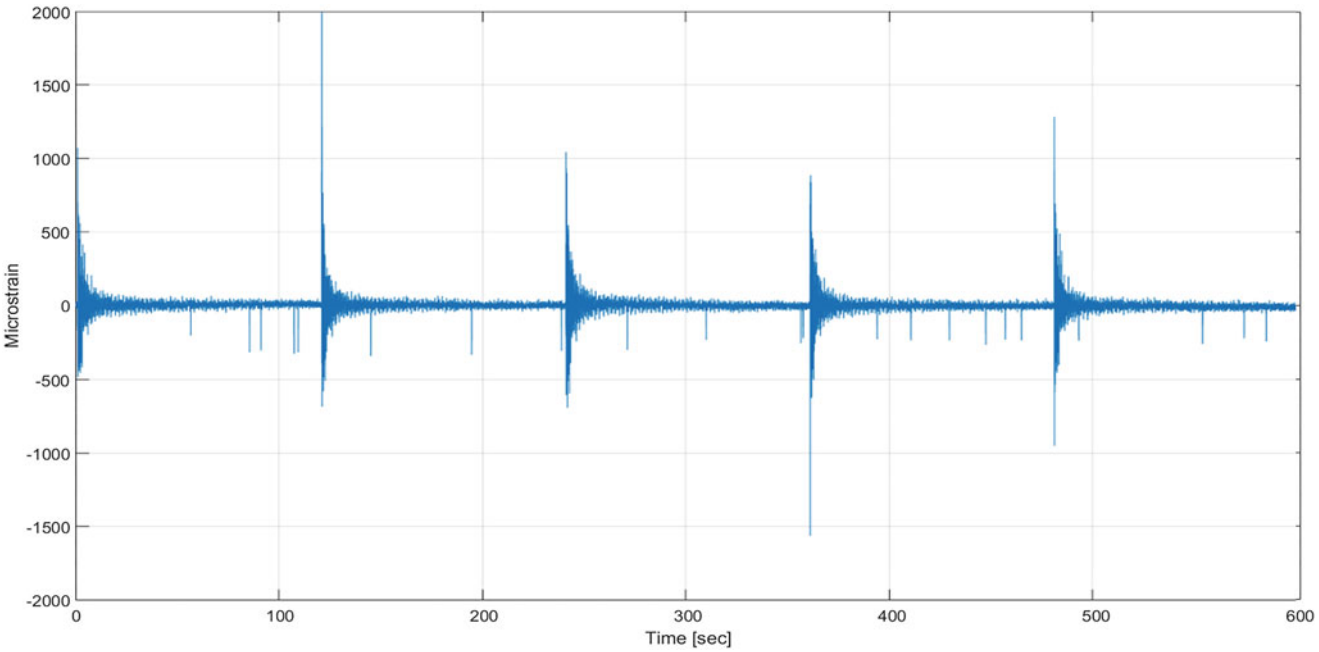

Fig. 3.5 Strain time history of strain sensor 5 over each of the five impact excitations

Modal parameters were estimated from the PSDs given in Fig. 3.6 using ATA's Interface between MATALAB, Analysis, Test (IMAT™) software in conjunction with ME'Scope. Using IMAT's OPoly toolkit, the power spectrum mode indicator function (PSMIF) was computed and plotted in Fig. 3.8 using the 57 root-most PSDs provided in Fig. 3.6. From the PSMIF, poles of the system were identified and modal parameters extracted in accordance with standard EMA techniques.

The estimated frequency and damping information for the global testbed modes under 25 Hz are provided in Table 3.1. Also provided in Table 3.1 are the values obtained via EMA on the same UUT using the SLV for comparison. The estimated modal parameters from both the fiber optic and SLV are in excellent agreement, validating the ability of the OFDR-based fiber optic sensors to obtain accurate modal information. Although only a single axial fiber was used in the current study, it is important to note the fiber was able to capture the bending behavior of the UUT in both planes as well as the torsional response. This is a distinct advantage when compared to conventional EMA measurement technologies such as accelerometers and vibrometers.

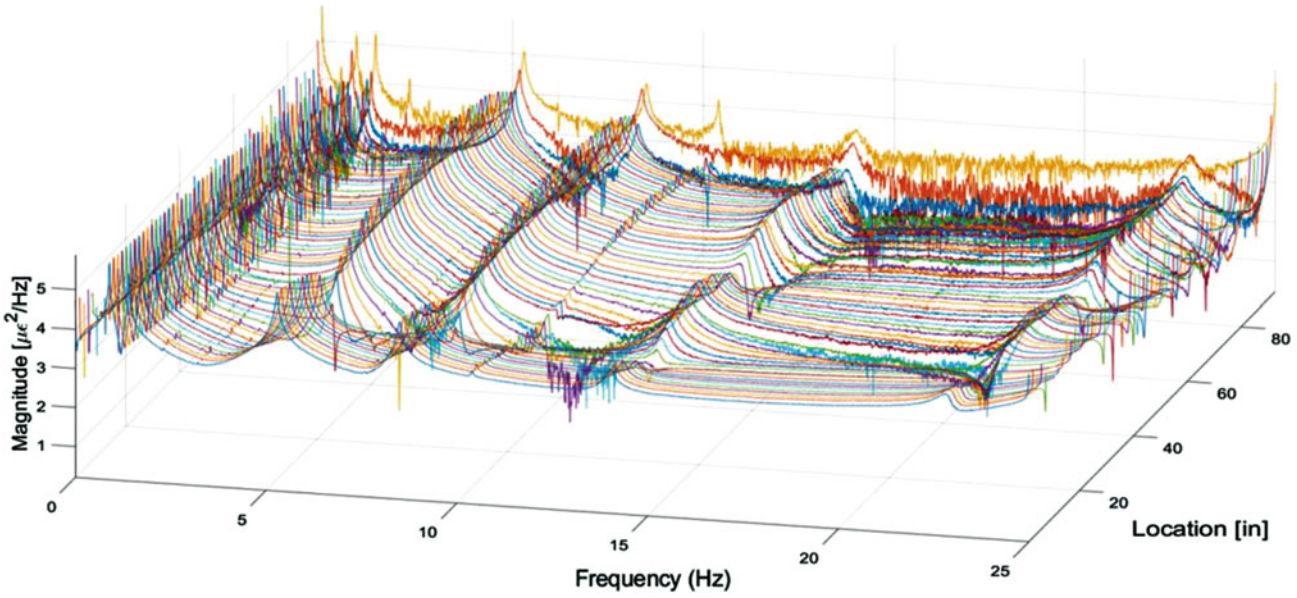

Fig. 3.6 PSD of each of the 59 strain sensors as a function of frequency and location. In the current plot, sensor 5 is the reference sensor

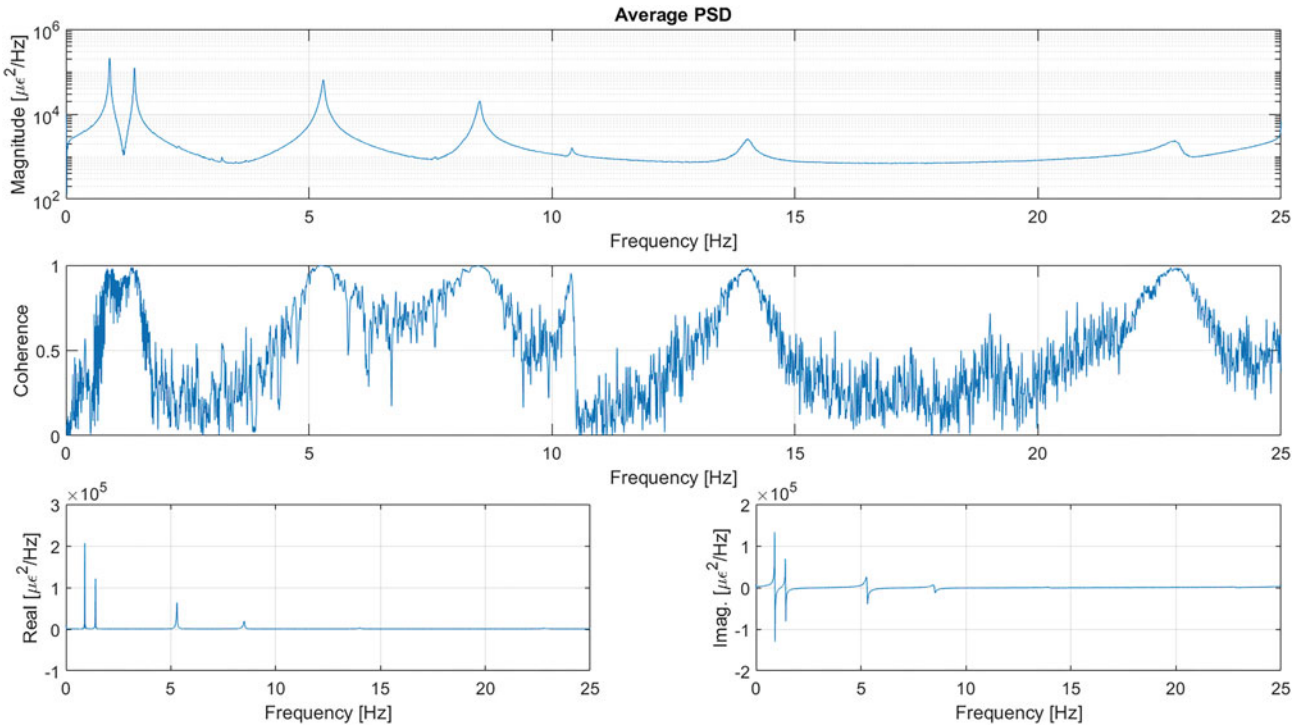

Fig. 3.7 PSD of sensor 2 relative to sensor 5, averaged over the five impacts in the complex domain. The upper plot shows the magnitude of the PSD, the middle plot gives the coherence between the two signals, and the lower plot shows the real and imaginary portions of the PSD

3.4 Conclusion

An experimental study was performed which validated the use of OFDR-based fiber optic strain sensors for response-only modal parameter estimation. A carbon/epoxy composite testbed was instrumented with a single Bragg-grated optic fiber providing 59-point strain measurements evenly distributed along the fiber's length. Impact excitation was used to excite the UUT and record response-only strain time histories. These time histories were used in the computation of the sensor-to-

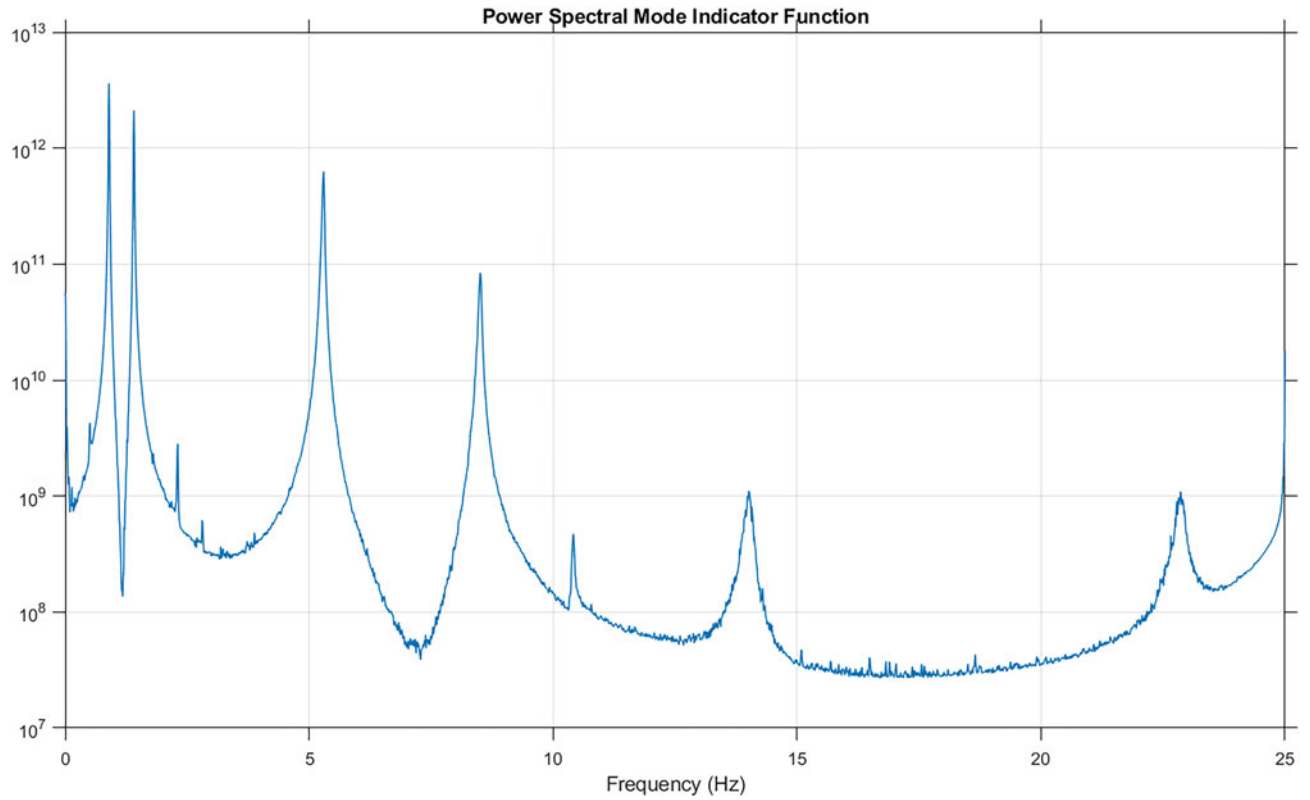

Fig. 3.8 PSMIF of the 57 root-most sensors

Table 3.1 Estimated frequency and damping for the first seven flexible modes of the testbed

		Fiber optic system		Vibrometer	
Mode	Description	Frequency (Hz)	Damping (%)	Frequency (Hz)	Damping (%)
1	First bending—soft-plane	0.90	0.50	1.01	0.72
2	First bending—stiff-plane	1.41	0.93	1.41	1.01
3	Second bending—soft-plane	5.31	0.58	5.33	0.47
4	Second bending—stiff-plane	8.55	0.08	8.57	0.14
5	First torsion	10.43	1.18	10.50	1.16
6	Third bending—soft-plane	14.05	0.78	14.10	0.77
7	Third bending—stiff-plane	22.95	0.91	23.00	0.83
Frequency resolution		0.033 Hz		0.078 Hz	

sensor cross PSDs of the strain response. By implementing conventional modal parameter estimation techniques, the study estimated a set of modal frequencies and damping values from the set of cross PSDs. These estimated parameters compared favorably to a set of modal parameters estimated using EMA on a SLV data set for the same UTT.

Acknowledgments Experimental testing was conducted in the Aerospace Structures Laboratory at the University of California San Diego in collaboration with Professor John B. Kosmatka. The author also wishes to thank NASA Armstrong Flight Research Center for providing the optical strain sensing system used to interrogate the UUT.

References

1. Ewins, D.: Modal testing: theory, practice and application (mechanical engineering research studies: engineering dynamics series), Research studies Pre, 2nd edn. (2000). ISBN-13, 978-0863802188
2. Richards, W.L., Parker Jr, A.R., Ko, W.L., Piazza, A., Chan, P. Application of fiber optic instrumentation, Advisory Group for Aerospace Research and Development Flight Test Instrumentation Series – Volume 22, ISBN 978-92-837-0164-4 (2012)

3. Materials, A.: Application of interferometer technology to achieve accurate optical wavelength measurements. https://www.azom.com/article.aspx?ArticleID=9502 (2013)
4. Martins, B.L., Kosmatka, J.B.: Evaluation of fiber optic strain sensors for applications in structural health monitoring, In 57th AIAA/ASCE/AHS/ASC structures, structural dynamics, and materials conference, p. 0708 (2016)
5. Martins, B.L.: Ambient Excitation Based Model Updating for Structural Health Monitoring Via Dynamic Strain Measurements. University of California San Diego, San Diego (2019)

Chapter 4
Machine Learning Vibration-Based Damage Detection and Early-Developed Damage Indicators

R. Rocha Ribeiro, L. A. C. M. Veloso, and R. M. Lameiras

Abstract The vibration-based damage detection of structures has been an active topic among many research fields for, at least, the past four decades. In its early years, great effort has been devoted towards developing damage indicators computed from experimental data. Recently, as this problem is increasingly studied with a data science perspective, efforts are shifting towards finding highly meaningful features in experimental vibrational data, which is key to Machine Learning success. The present work had the objective of analysing how the performance of a Machine Learning approach compares to and may benefit from early-developed damage indicators. A performance comparison is presented between some early-developed damage indicators, based on both frequency and mode shapes, and an Artificial Neural Network (ANN) supplied with vibrational data. Also, the use of the early-developed damage indicators as inputs in the ANN was investigated. A two-span simply supported beam was used as the numerical experiment for the tests. The performance of each approach in different damage scenarios was discussed, as well as insights were drawn by putting the Machine Learning vibration-based damage detection approach into perspective with some of the simplest early-developed damage indicators.

Keywords Damage detection · Vibration · Modal analysis · Machine learning · SHM

4.1 Introduction

The vibration-based damaged detection, as part of the Structural Health Monitoring (SHM) discipline, has been an active topic on many fields, such as Mechanical, Aerospace, Manufacturing and Civil Engineering, for at least the past four decades [1]. While the first vibration-based damage detection techniques were formulated in the form of damage indicators derived in a physics framework, the damage detection problem, as many other SHM subjects, is now increasingly being treated as a Machine learning problem, using techniques such as artificial neural networks (ANNs), convolutional neural networks and k-means clustering [2–5]. However, the accumulated knowledge contained in the early damage indicators may be extremely valuable tools when used in conjunction with Machine Learning techniques, since they can fulfil the role of feature extraction methods, deriving meaningful information from experimental data. Also, a performance comparison that puts some early damage indicators in perspective to recently trending Machine Learning techniques, such as ANNs, may be useful to enlighten how the damage detection problem has evolved throughout the years.

In this sense, the present work had the objective of analysing how the performance of a Machine Learning approach compares to and may benefit from early-developed damage indicators. A dense backpropagation Artificial Neural Network (ANN) was selected as the Machine Learning tool, and the Cawley-Adams [6] and Kim-Stubbs [7] indices were selected to represent early-damage indicators. A two-span simply supported beam was used as the numerical experiment for the tests. Different features were used in the ANN, including the damage indicators themselves, and the performances in different damage scenarios were compared to withdraw insights about each method.

R. Rocha Ribeiro (✉) · R. M. Lameiras
Department of Civil and Environmental Engineering, College of Technology, University of Brasília, Campus Universitário Darcy Ribeiro, Brasília-DF, Brazil

L. A. C. M. Veloso
Department of Mechanical Engineering, College of Technology, University of Brasília, Campus Universitário Darcy Ribeiro, Brasília-DF, Brazil

B. J. Dilworth, M. Mains (eds.), *Topics in Modal Analysis & Testing, Volume 8*, Conference Proceedings of the Society for Experimental Mechanics Series, https://doi.org/10.1007/978-3-030-75996-4_4

4.2 Methodology

The experimental outline of this work is summarized on Fig. 4.1.

The Finite Element (FE) model used as the test structure comprised a two-span simply supported beam (Fig. 4.2), with the properties presented on Table 4.1, modelled in the software SAP2000 [8], in which it was discretized in 30 frame elements of equal length. The test structure was inspired in [7], with the span lengths changed to avoid a symmetric structure, which reportedly affects unevenly the Cawley-Adams index [6]. Only the vertical displacements on the y-axis and the rotations around the z-axis were allowed in the model. The SAP2000 API for Python was used to generate the data used in this work.

Damage was modelled as a percentage reduction on the E-modulus of a frame element. Damage cases, which refer to a model into each damage is present, consisted in applying a given damage level in a single frame element. So, for each damage level tested, 30 damaged cases could be generated, considering the model was discretized in 30 frame elements. Figure 4.3 illustrates this logic.

The Cawley-Adams, Kim-Stubbs index B and Kim-Stubbs index C were tested with all the damaged cases generated from the damage levels of 1, 10, 50 and 90%, which cover a wide range of damage levels. In order to allow the comparison between the damage indicators and the ANNs, which require separate training and test datasets, the ANNs trainings were performed with the damage cases as indicated in Fig. 4.1, which did not contain any damage case related to the damage levels of 1, 10, 50 and 90%. This work did not address cases of multiple damage locations.

To standardize the performance comparison, this work treated the damage location identification problem as a classification problem both while using the damage indicators and the ANNs. The possible damage locations are denominated as "classes" throughout the work, and each class refers to a portion of the length of the structure. A positive value in a class meant that location is the damaged location.

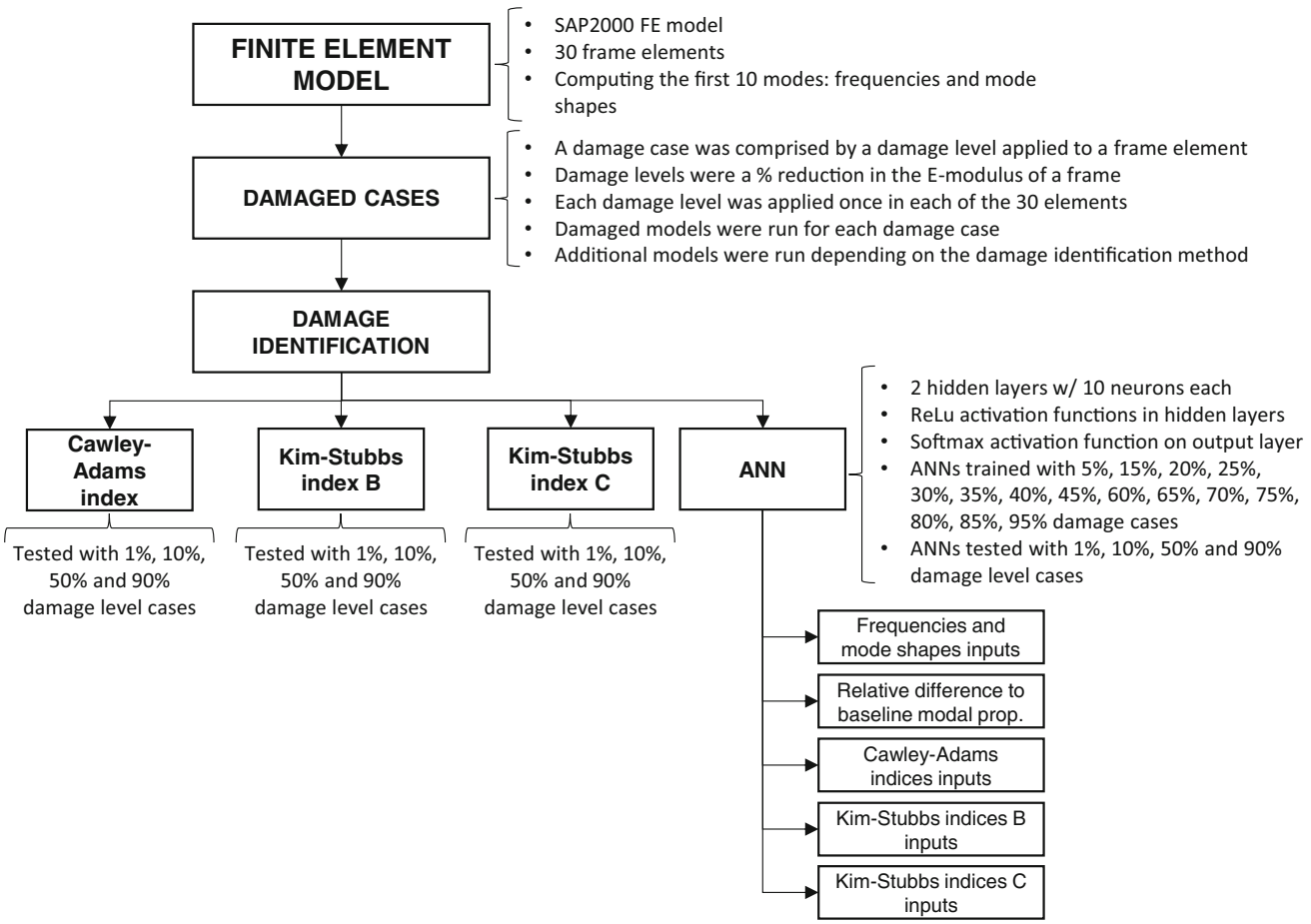

Fig. 4.1 Experimental outline

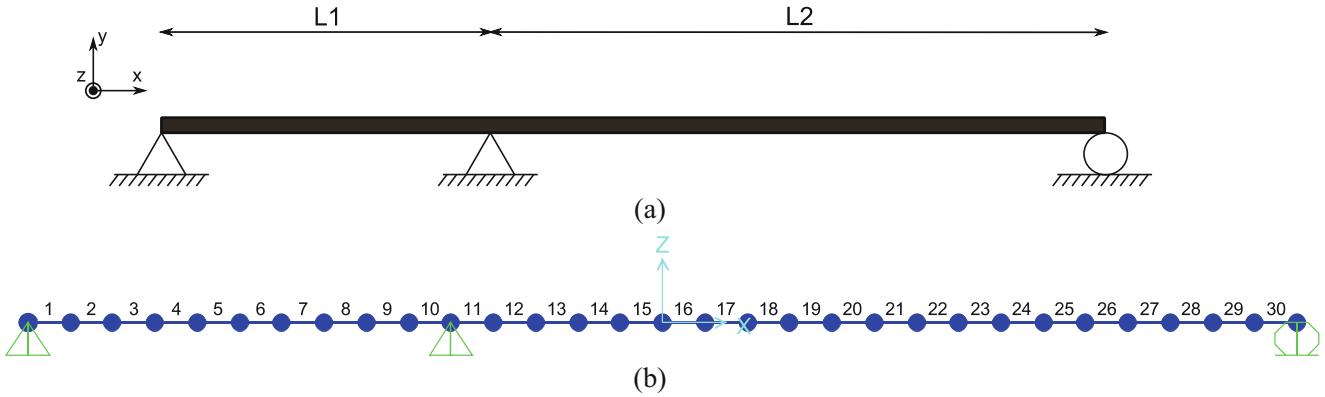

Fig. 4.2 Models: (**a**) physical model; (**b**) FE model

Table 4.1 Model properties

Property	Value	Property	Value	Property	Value
L1 span	2.67 m	Cross-section inertia	5.40E−03 m^4	Mass per volume	2500 kg/m^3
L2 span	5.33 m	Cross-section area	0.18 m^2	E-modulus	3.30E+10 N/m^2

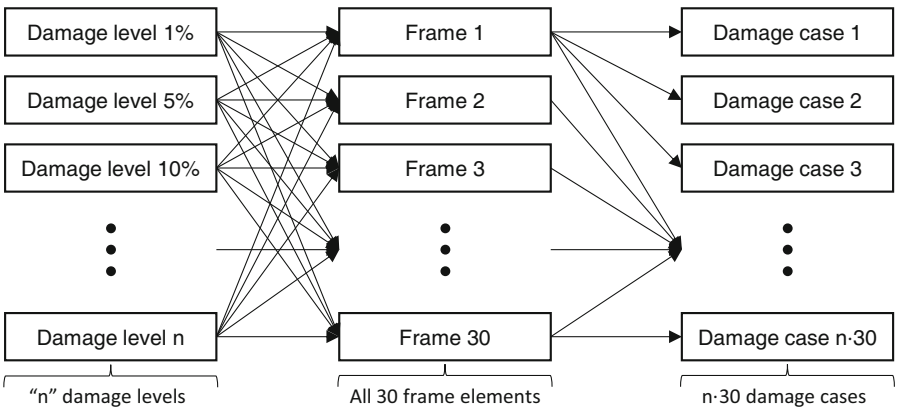

Fig. 4.3 Logic behind the damage cases production

Initially, each frame of the FE model consisted in a class and potential location for damage, leading to a 30 class classification problem. However, a strategy of reduction of available classes was implemented, based on two reasons: ANNs typically require large datasets in the training stage and the number of frames could be insufficient to produce a large enough dataset; the damage indicators analysed usually predict damage occurring in two or more adjacent frames, which is physically reasonable but could interfere with the performance metrics adopted in this work. This strategy consisted in mapping, during the data processing stage prior to the classification itself, the original 30 classes, associated to the 30 frame elements in the FE model, to a coarser mesh of 15 classes, with each new class corresponding to a portion of the structure of twice the length of the original classes. All the numerical analysis and data extraction of the model were still performed with the 30-element FE mesh. This strategy had the effect of both multiplying the size of the dataset in relation to the available classes in the classification problem, which is positive for the ANN, and also relaxing the requirements on location precision while still maintaining a reasonable location resolution.

The method's performance was assessed comparing ground truth class vectors, which contained the correct location of the damage, to the results provided by each method analysed. To provide quantitative results, for each method a Confusion Matrix was built, which is a common tool for classification performance evaluation that separates the method results in four categories: True Negatives, False Negatives, False Positives and True Positives [9]. Since the damage indicators analysed are formulated such that indication of damage location in more than one place is possible even for single damage location scenarios, the comparisons for the Confusion Matrix were performed class-wise, i.e. each entry of the result class vector was compared to its equivalent in the ground truth class vector, contributing as one unit in one of the four Confusion Matrix categories.

From the Confusion Matrix, the Accuracy, Precision, Recall and F_1 scores were computed to aid in the performance comparison. These scores are defined as [10]:

$$\text{Accuracy} = \frac{\text{True positives} + \text{True Negatives}}{\text{True positives} + \text{True Negatives} + \text{False Positives} + \text{False Negatives}} \tag{4.1}$$

$$\text{Precision} = \frac{\text{True positives}}{\text{True positives} + \text{False Positives}} \tag{4.2}$$

$$\text{Recall} = \frac{\text{True negatives}}{\text{True negatives} + \text{False Positives}} \tag{4.3}$$

$$F_1 = 2 \times \frac{\text{Precision} \times \text{Recall}}{\text{Precision} + \text{Recall}} \tag{4.4}$$

The precision and recall parameter are better suited for performance evaluation, as they indicate how well the damage indicators can find the damaged frames in the dataset while also presenting a trade-off behaviour between themselves if the classification is being poorly done. The F_1 allows to consider both these parameters simultaneously with equal weights. Ideally, the higher the F_1 parameter, the better the damage indicator is in identifying the damaged classes in the dataset.

The damage indicators analysed in this study are briefly presented in the sequence, and the reader is referred to the original works for detailed explanations about their formulation. The Cawley-Adams index is a frequency-based damaged indicator that requires baseline frequencies from an undamaged state of the structure and a numerical model of the tested structure to compute a sensitivity index defined as:

$$\delta\boldsymbol{\lambda}_{\boldsymbol{ij},\boldsymbol{r}} = \frac{\boldsymbol{x_i}^T \delta\mathbf{K}_{\boldsymbol{r}}\, \boldsymbol{x_j}}{\boldsymbol{x_i}^T \mathbf{M}\, \boldsymbol{x_j}} \tag{4.5}$$

in which: $\delta\boldsymbol{\lambda}_{\boldsymbol{ij},\boldsymbol{r}}$ is the sensitivity of mode j to mode i due to a damage in the position r, which is, in other words, the ratio between the eigenvalue variation of mode i and the eigenvalue variation of mode j, caused by a damage in the location r; $\boldsymbol{x_i}$ is the mode shape vector of mode i; $\delta\mathbf{K}_{\boldsymbol{r}}$ is a matrix containing the variation on the global stiffness matrix caused by damage in location r; and $\mathbf{M}$ is the global mass matrix. To identify a damage location in a tested structure, this method uses the frequencies identified in the tested structure and those from the baseline model to compute the sensitivities $\delta\boldsymbol{\lambda}_{\boldsymbol{ij}}$, which are then compared to each of the $\delta\boldsymbol{\lambda}_{\boldsymbol{ij},\boldsymbol{r}}$ computed from the numerical model, in order to identify the r that leads to the best fitting between $\delta\boldsymbol{\lambda}_{\boldsymbol{ij},\boldsymbol{r}}$ and $\delta\boldsymbol{\lambda}_{\boldsymbol{ij}}$. The best fit is usually measured with a score ranging from 0 to 100, with 0 indicating very unlikely damage locations and 100 indicating highly likely. Since this method is posed in a way that multiple locations may receive high scores, an arbitrary rule of requiring scores greater than 99 to classify a location as a damage location was adopted. Further details about the Cawley-Adams index can be found on the method's seminal paper [6].

The Kim-Stubbs method used in this work can be separated in two indices: B and C, both discussed in details by Kim and Stubbs [7]. The Kim-Stubbs index B is a mode-shape based method that also requires a numerical model of the tested structure and baseline mode shapes from an undamaged state of the structure to compute a damage index defined as:

$$\beta_r = \frac{\sum_{i=1}^{nm} \left(\gamma_{ir}^* + \sum_{k=1}^{ne} \gamma_{ik}^*\right) K_i}{\sum_{i=1}^{nm} \left(\gamma_{ir} + \sum_{k=1}^{ne} \gamma_{ik}\right) K_i^*} \tag{4.6}$$

in which: β_r is the damage index at location r; $\gamma_{ir} = \boldsymbol{x}_i^T \boldsymbol{C}_{r0} \boldsymbol{x}_i$ can be called a unit modal stiffness of mode i for element r, since $\boldsymbol{x}_i$ is the mode shape vector of mode i and $\boldsymbol{C}_{r0}$ is a global stiffness matrix containing only the geometric contributions of frame r, i.e. $\boldsymbol{K}_r = E_r \boldsymbol{C}_{r0}$, in which E_r is elastic modulus of the frame r, and $\boldsymbol{K}_r$ is the global stiffness matrix containing only the contribution of element r; γ_{ir}^* being the equivalent of γ_{ir}, but computed with damaged mode shapes $\boldsymbol{x}_i^*$ measured at the tested structure; K_i is the modal stiffness of mode i at the undamaged state, computed as $K_i = \boldsymbol{x}_i^T \boldsymbol{K} \boldsymbol{x}_i$, with $\boldsymbol{K}$ being the global stiffness matrix of the (undamaged) numerical model; K_i^* is the damaged modal stiffness of mode i at the damaged state, approximated by $K_i^* = \boldsymbol{x}_i^{*T} \boldsymbol{K} \boldsymbol{x}_i^*$; nm refers to the number of modes being considered; ne refers to the number of

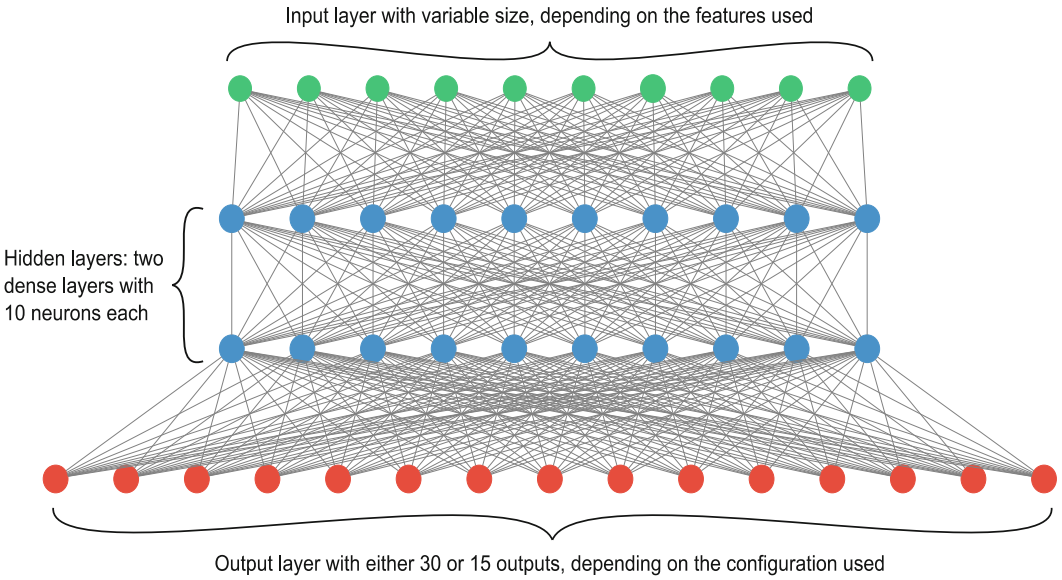

Fig. 4.4 ANN layout

elements in the numerical model. With the mode shapes measured at the test structure, the damage index β_r at location r can be computed and, accordingly to its original formulation, values $\beta_r > 1$ indicate presence of damage. In the present work, the criteria to classify a location as damaged was slightly modified, being inspired by Kim and Stubbs [7]: all the β_r were normalized and a Grubbs' outlier test, with significance level of 10%, was used to detect damage among the maximum values.

The Kim-Stubbs index C is a further development of the previous index, with allegedly advantages in situations with very few available modal data. The mechanics of the method remain the same, but now information about the frequency is also introduced in the damage index, defined as:

$$\beta_r = \frac{\sum_{i=1}^{nm} \gamma_{ir}^*}{\sum_{i=1}^{nm} \left(\gamma_i \left(\frac{\delta\lambda_i}{\lambda_i} + \frac{\delta M_i}{M_i} \left(1 + \frac{\delta\lambda_i}{\lambda_i} \right) \right) + \gamma_r \right)} \tag{4.7}$$

in which:γ_{ir}^* and nm have the same meaning as the previous index;$\gamma_i = \sum_{k=1}^{ne} \gamma_{ik}$, with each component having the same meaning as in the previous index; $\delta\lambda_i$ is the variation in the eigenvalue i due to the damage, i.e. the difference between the square of the measured frequency, in rad/s, and the square of the baseline frequency; λ_i is the baseline eigenvalue; δM_i is the variation of the modal mass of mode i due to the damage in the structure, computed approximately as $\delta M_i = \boldsymbol{x}_i^{*T} \boldsymbol{M} \boldsymbol{x}_i^* - \boldsymbol{x}_i^T \boldsymbol{M} \boldsymbol{x}_i$; M_i is the modal mass of mode i at the baseline model. Like the previous index, to perform the damage classification all β_r were normalized and a Grubbs' outlier test, with significance level of 5%, was used to detect damage among the maximum values. The significance level was further restricted in this index since no significant changes in performance were verified when adopting the standard significance level of 5% instead of the previously adopted value of 10%.

The ANNs used on this work were developed with the aid of the Keras API, TensorFlow 2.0 and Scikit Learn packages [11–13]. The Keras sequential model was used to build neural networks with two dense hidden layer, each with 10 neurons, and an output layer whose size was defined by the number of classes in the problem, i.e. number of potential positions for the damage. The hidden layers contained a rectified linear activation function (ReLu) and the output layer contained a Softmax activation function, which is a common configuration for multiclass classification neural networks. The size of the input layer was also adjusted accordingly to the features used in each analysis. Figure 4.4 illustrates the ANNs' general structure.

As indicated in Fig. 4.1, five different features were tested on the ANN: raw frequencies and mode shapes; frequencies and mode shapes divided by their respective values from baseline model, considering that all damage indicators analysed require the use of baseline modal information and, thus, this information was considered as available in the framework of this paper; Cawley-Adams damage indices for each class (damage position); Kim-Stubbs index B for each class; Kim-Stubbs index C for each class. For each feature, a new ANN was trained and tested. The training was performed, as previously mentioned, with samples containing damage levels that were not present in the test set, which, by its turn, comprised damage cases produced with damage levels of 1, 10, 50 and 90%. The training was performed with a backpropagation algorithm, a minibatch of

10 samples, the Adam optimizer [14], 300 epochs, and a cross entropy loss function. Cross validation of each ANN was performed with a stratified k-fold strategy, using fivefolds on the training dataset. Lastly, it is worth noting that the ANNs in this work were not modelled to detect undamaged states, i.e. there was no output to classify the structure as undamaged.

4.3 Results

The results obtained with the Cawley-Adams and Kim-Stubbs damage indices are presented on Table 4.2.

From the accuracies reported, which had high values, it can be observed that the implemented damage indicators seem to behave as expected, with no erratic behaviours. The close values reported for the accuracies reinforce the need to be cautious when analysing the performance of each damage indicator with such a global performance parameter, as the occurrence of each class label (i.e. damaged or not damaged) is skewed. In fact, when considering the case with 30 available classes (i.e. case with the possibility of identifying damage in 30 different and non-overlapping portions of the structure), the whole dataset, which was composed of four damage levels applied to each of the 30 frame elements individually, contained a total of 3600 labels of which only 120 were damaged labels, composing 3.33% of the dataset. The 15-classes case lead to a proportion of 6.66%, which is still a relatively low occurrence of damaged (positive) labels compared to not damaged (negative) labels. The accuracy parameter as computed in this work will always have a high value for this type of problem, as the probability of a class being truly not damaged is considerably higher than being damaged, contributing to bias the rate of total successful classifications. In an extreme example, a non-damage indicator that labels every class as not damaged would lead to an accuracy of 96.67% for the 30-classes case, and 93.34% for the 15-classes case. Therefore, while useful to highlight erratic performances, further performance comparisons need to consider the other metrics.

When analysing the Precision and Recall by comparing the F_1 scores, it can be considered that the Kim-Stubbs-B damage indicator presented the best performance. The at first unexpected observation that Kim-Stubbs-B outperformed Kim-Stubbs-C, as the latter is considered by its authors as a further development of the first, may be explained by the fact that the present work used the first 10 modes for damage identification, while the Kim-Stubbs-C was developed in the context of limited available modal data [7].

When considering the particularities of the damage identification problem, it can be argued that the Recall parameter, i.e. the ability to maximize the identification of damaged classes and minimize the misclassification of actual damaged class as not damaged, may be prioritized in detriment of the Precision parameter. With this perspective, the Kim-Stubbs-B damage indicator also presents the best performance. Lastly, as expected the relaxation caused by reducing the number of available classes from 30 to 15 also contributed to increase the damage indicators performances in all cases. This may be useful when such damage identification is being done in large structures as part of preliminary global assessments, whose goal would be identifying potential areas for further focused investigation.

The results obtained with the ANN are presented on Table 4.3. It is important to highlight that the stratified k-fold accuracy is a better ANN accuracy performance estimator than the Accuracy itself. The k-fold accuracy reported is computed as the subset accuracy, in which a correct classification is only computed when all the classes in the multiclass classification problem are properly labelled [15]. This is a more restricted measure when compared to the Accuracy parameter adopted in this work, in which classes are individually considered and, thus, the bias caused by the high occurrence of negative labels is present.

The stratified k-fold accuracies indicate that the ANNs with raw vibrational data (#1 and #2) presented the lowest performances. This illustrates the importance of using highly meaningful input data in the ANN to achieve reasonable performances. Even though the mode shapes and frequencies do contain information regarding the position of the damage, such information needs to be extracted and properly presented as inputs to the ANN. An illustration of this importance can be seen on the ANNs with the relative difference between the damaged models and a baseline (undamaged) model mode shapes and frequencies, in which this simply normalization increased the accuracy performance to reasonable values. The effect of even higher meaningful parameters on the accuracy can be observed in the performance of the ANN with Kim-Stubbs-B indices (#7 and #8), which was already the damage indicator with the best performance previously, indicating that its indices retain considerable correlation to damage location.

The analysis of the Precision, Recall and F_1 scores, however, suggests that the ANN with Cawley-Adams indices (#5 and #6) achieved the best classification performance, with simultaneously high values for both Precision and Recall. Although these ANNs did not present k-fold accuracies as high as Kim-Stubbs-B ANNs, these scores to the training set, which contained theoretically unseen data by the ANNs. This may indicate that the Kim-Stubbs-B ANN presented lower generalization capability when compared to the Cawley-Adams ANN. In fact, the high k-fold accuracy of both #7 and #8 ANNs, with the latter achieving 100%, may indicate occurrence of overfitting that leads to poor generalization. Further analysis involving hyperparameters optimizations of the ANNs are required to fully address this matter.

Table 4.2 Damage indicators results

Method	Type[a]	Number of available classes	True negatives	False positives	False negatives	True positives	Accuracy	Precision	Recall	F_1
Cawley-Adams	F	30	3400	80	74	46	95.72%	36.51%	38.33%	37.40%
Cawley-Adams	F	15	1621	59	55	65	93.67%	52.42%	54.17%	53.28%
Kim-Stubbs-B	MS	30	3283	197	4	116	94.42%	37.06%	96.67%	53.58%
Kim-Stubbs-B	MS	15	1576	104	3	117	94.06%	52.94%	97.50%	68.62%
Kim-Stubbs-C	F-MS	30	3380	100	57	63	95.64%	38.65%	52.50%	44.52%
Kim-Stubbs-C	F-MS	15	1622	58	55	65	93.72%	52.85%	54.17%	53.50%

Notes: [a]Type of damage indicator: *F* Frequency based, *MS* Mode-shape based. *F-MS* Frequency and mode-shape based

Table 4.3 ANN testing results

#	Feature	Number of classes	Stratified k-fold accuracy[a]	True negatives	False positives	False negatives	True positives	Accuracy	Precision	Recall	F_1
1	Mode shapes and frequencies	30	9.37% (1.74%)	3434	46	116	4	95.50%	8.00%	3.33%	4.71%
2		15	28.12% (5.59%)	1629	51	91	29	92.11%	36.25%	24.17%	29.00%
3	Relative difference to baseline modal properties	30	27.71% (5.38%)	3443	37	73	47	96.94%	55.95%	39.17%	46.08%
4		15	68.75% (6.00%)	1647	33	58	62	94.94%	65.26%	51.67%	57.67%
5	Cawley-Adams indices	30	95.63% (3.05%)	3477	3	3	117	99.83%	97.50%	97.50%	97.50%
6		15	96.88% (1.74%)	1679	1	1	119	99.89%	99.17%	99.17%	99.17%
7	Kim-Stubbs-B indices	30	99.58% (0.51%)	3461	19	19	101	98.94%	84.17%	84.17%	84.17%
8		15	100% (0.00%)	1670	10	13	107	98.72%	91.45%	89.17%	90.30%
9	Kim-Stubbs-C indices	30	88.75% (0.78%)	3448	32	44	76	97.89%	70.37%	63.33%	66.67%
10		15	92.92% (2.67%)	1648	32	37	83	96.17%	72.17%	69.17%	70.64%

Notes: [a]The reported accuracy is the so-called subset accuracy, computed accordingly to [15]. In parenthesis, it is reported the standard value of the k-fold subset accuracy results

The reduction of the number of available classes also contributed to increase the ANN performances, as observed with the damage indicators. For ANNs, such reduction not only relaxes the requirements on the precision of damage position identification, but also increases the dataset size relatively to the number of classes in the problem, which may benefit the ANN learning process by providing more examples of each class. The positive effect of the class reduction was more evident in the ANNs with poorer performance, such as #1 to #4, indicating that larger datasets may play a positive role when using less meaningful features in the damage identification problem.

4.4 Conclusion

This work presented a performance comparison of early-developed damage indicators and a Machine Learning approach based on Artificial Neural Network (ANN) for the damage identification of structures using vibrational data. A two-span simply supported beam, modelled with frame elements in a Finite Element Modelling (FEM) software, was used to provide the modal data (frequencies and mode shapes) of the first 10 modes. The damage identification addressed only the localization of the damage in the structure. The use of the early-developed damage indicators as inputs into ANNs was also studied.

The results illustrated the importance of providing Machine Learning based approaches to the damage identification problem with meaningful and information-rich inputs, which may be perfectly obtained from early developed damage indicators, which were shown to contain meaningful information about the damage location. When comparing the damage indicators performance to ANNs with raw modal data, the first generally presented better, or at least comparable, performance. It was also illustrated that Machine Learning tools, such as ANNs, may enhance the performance of the damage indicators when they are used together. Some specific observations can be highlighted:

- The damage indicators analysed presented a F_1 score, when considering each class separately, ranging from 37.40% to 68.62%. The poorest result was obtained with the Cawley-Adams indicator, and the best with Kim-Stubbs-B damage indicator.
- The ANNs analysed presented a F_1 score ranging from 4.71% to 99.17%. The poorest results were obtained with ANNs with raw vibrational data (mode shapes and frequencies) as inputs, and the best results were obtained when using the damage indicators themselves as inputs. The best performance was achieved using the Cawley-Adams damage indicator as input.

Acknowledgements The authors thank the Brazilian National Council for Scientific and Technological Development (CNPq) for the financial aid provided to conduct this work, in the form of a PhD scholarship for the first author.

References

1. Doebling, S.W., Farrar, C.R., Prime, M.B., Shevitz, D.W.: Damage Identification and Health Monitoring of Structural and Mechanical Systems from Changes in Their Vibration Characteristics—A Literature Review. Los Alamos National Laboratory, Los Alamos (1996)
2. Zhong, K., Teng, S., Liu, G., Chen, G., Cui, F.: Structural damage features extracted by convolutional neural networks from mode shapes. Appl. Sci. **10**(12), 4247 (2020)
3. Haugdal, H., Uhlen, K.: Mode shape estimation using complex principal component analysis and K-means clustering, In: 2019 Int. Conf. Smart Grid Synchronized Meas. Anal. SGSMA 2019 (2019)
4. Neves, A.C., González, I., Leander, J., Karoumi, R.: Structural health monitoring of bridges: a model-free ANN-based approach to damage detection. J. Civ. Struct. Heal. Monit. **7**(5), 689–702 (2017)
5. Cremona, C., Santos, J.: Structural health monitoring as a big-data problem. Struct. Eng. Int. **28**(3), 243–254 (2018)
6. Cawley, P., Adams, R.D.R.D.: The location of defects in structures from measurements of natural frequencies. J. Strain Anal. Eng. Des. **14**(2), 49–57 (1979)
7. Kim, J.T., Stubbs, N.: Improved damage identification method based on modal information. J. Sound Vib. **252**(2), 223–238 (2002)
8. CSI. SAP2000—integrated software for structural analysis and design [Online]. https://www.csiamerica.com/products/sap2000 (2020). Accessed 3 Dec 2020
9. Tharwat A.: Classification assessment methods. Appl. Comput. Informatics.**17**(1), 168–192. https://doi.org/10.1016/j.aci.2018.08.003
10. Ting, K.M.: Confusion matrix. In: Sammut, C., Webb, G.I. (eds.) Encyclopedia of Machine Learning, p. 209. Springer US, Boston, MA (2010)
11. Chollet, F.: About Keras [Online]. https://keras.io/about/. Accessed 24 Nov 2020
12. Pedregosa, F., Varoquaux, G., Gramfort, A., Michel, V., Thirion, B., Grisel, O., Blondel, M., Prettenhofer, P., Weiss, R., Dubourg, V., Vanderplas, J., Passos, A., Cournapeau, D., Brucher, M., Perrot, M., Duchesnay, E.: Scikit-learn: machine learning in python. J. Mach. Learn. Res. **12**, 2825–2830 (2011)

13. Abadi, M., Barham, P., Chen, J., Chen, Z., Davis, A., Dean, J., Devin, M., Ghemawat, S., Irving, G., Isard, M., et al.: Tensorflow: a system for large-scale machine learning. In: 12th ${$USENIX$}$ Symposium on operating systems design and implementation (${$OSDI$}$ 16), pp. 265–283 (2016)
14. Kingma, D.P., Ba, J.: Adam: a method for stochastic optimization. arXiv preprint arXiv:1412.6980 (2014)
15. Scikit-learn. Metrics and scoring: quantifying the quality of predictions, Scikit-learn Doc. [Online]. https://scikit-learn.org/stable/modules/model_evaluation.html#accuracy-score (2020). Accessed 22 Nov 2020

Chapter 5
Semi-Analytical Analysis for Dynamic Behaviors of Wind Turbine Blades Using Transfer Function Methods

Ali Hashemi, Jinwoo Jang, and Shahrokh Hosseini-Hashemi

Abstract One of the most challenging research areas in the field of structural dynamic and vibration is development of analytical solution for vibration and elasticity analyses of various structures. This paper focuses on developing a new semi-analytical solution to obtain lateral deflection of a wind turbine blade under external loadings. The proposed method maps a wind turbine blade to an Euler–Bernoulli beam with same conditions, in order to find vibration and dynamic responses of the blade by solving analytical vibration solutions of the Euler–Bernoulli beam. Piezoelectric patches are used in this research as actuator-sensor to excite the structures and sense the responses. The governing equations of the beam with piezoelectric patches are derived based on integration of the piezoelectric transducer vibration equations into the vibration equations of the Euler–Bernoulli beam structure. Finite Element model of the wind turbine blade with piezoelectric patches is developed. A unique transfer function matrix is derived by exciting the structures and achieving responses. The beam structure is projected to the blade by using the transfer function matrix under external forces. The results obtained from the mapping method are compared with the results achieved from the FE model of the blade. A satisfying agreement has been observed between the results. The results show that by increasing the distance from the base of the wind turbine blade structure, the accuracy of the method experiences a descending trend.

Keywords Structural dynamic · Analytical vibration analysis · Transfer function matrix · Piezoelectric actuator and sensor · Energy method

5.1 Introduction

Derivation of analytical solutions for vibration and elasticity analysis of structures have always been noticed as an important field of research in structures analysis and design. Analytical solutions of dynamic responses in various structures have attracted considerable attention for saving computational cost especially for large-scale structures. However, it could be very challenging to derive analytical solution for many structures due to their intricate geometry. Furthermore, these days, renewable energy such as wind energy has been widely considered as one of the alternative energy resources due to a dramatic increase of global warming. According to this fact, different types of wind turbine such as off-shore and on-shore wind turbines with various size and power generation have been studied in recent years. In general, bigger, complex wind turbines have gained more popularity due to their effectiveness in power generation capacity. A deep understanding of dynamic behaviors of wind turbine blades is critically significant in the development of designing wind turbines because of obtaining most efficient design. However, it is difficult to analyze dynamical and vibrational behaviors of wind turbine blades due to their complex shapes and continuous interaction between wind flows and their blades. Large-scale wind turbine can experience severe unwanted vibrational deflection especially on the edges of their blades. We can consider interaction between blades and wind flows and interaction between rotors and towers as the key causes for these vibrations. These undesirable vibrations, especially at the tip of blades, can cause extreme structural damages and failure of the power systems. In addition, a comprehensive perception of vibration and dynamic behaviors of wind turbine blades and deriving

A. Hashemi · J. Jang (✉)
Department of Civil, Environmental and Geomatics, Florida Atlantic University, Boca Raton, FL, USA
e-mail: ahashemi2020@fau.edu; jangj@fau.edu

S. Hosseini-Hashemi
School of Mechanical Engineering, Iran University of Science and Technology, Tehran, Iran
e-mail: shh@iust.ac.ir

B. J. Dilworth, M. Mains (eds.), *Topics in Modal Analysis & Testing, Volume 8*, Conference Proceedings of the Society for Experimental Mechanics Series, https://doi.org/10.1007/978-3-030-75996-4_5

analytical solution for vibration and dynamic responses to external loadings can be tremendously helpful in active unwanted vibration control and applying control rules to wind turbine blades which cause increase in the life of structures and also the performance of the turbines.

The development of analytical approaches to understand dynamic behaviors of wind turbine blades or other rotary structures poses significant challenges due to the complexity of the underlying physics and dynamic conditions. A new understanding of analytical approaches to analyze dynamic behaviors of these complex blade shapes can contribute to investigating various mechanical and structural systems such as helicopter rotor blades, various arms of robots, twisters, and heavy solid components. In general, analytical solutions, numerical simulations, and system definition can be integrated with an experimental testing to model various twister beams, such as twister turbines, helicopters, robot arms, and micro-electrical devices. The vibration of these twister structures has been mostly studied with finite element (FM) simulation and other numeric methods such as finite difference (FD) and differential quadrate (DQ) in comparison with analytical methods.

This research aims to define a semi-analytical solution for a wind turbine blade, which can describe lateral blade deflections under specific external forces. In general, a semi-analytical solution technique is presented for solving linear partial differential equations. The semi-analytical technique relies on analytically solving the equations obtained from discretizing the spatial coordinates of a partial differential equation. The most significant advantage of semi-analytical methods over numerical methods is tremendously shorter solving time. This work demonstrates an innovative approach to project an actual shape of a wind turbine blade to the same scale of an Euler–Bernoulli beam in order to derive an analytical solution for the wind turbine blade's dynamic and vibration response. The blade of the GE 1.5-megawatt model, which has 45 m blades on a 9 m tower, is considered in this work. To simplify deriving equations, we assume this blade is a steel blade. Plumbum-Titania-Zirconia is considered as piezoelectric sensor-actuator patches in order to sense and actuate structures.

5.2 Background

The vibrations of twister beams have been widely studied with different types of beam models, e.g., Euler–Bernoulli and Timoshenko, using analytical or semi-analytical solutions and numerical or finite element methods (FEMs). The majority of previous research considered Euler–Bernoulli and Timoshenko models to describe twister and under-loading beams without considering shear deformations. Several research has been conducted in order to understand dynamic behaviors of rotary beams, including the normal frequencies, mode shapes, and maximum vertical displacements. However, obtaining dynamic responses of rotary beams under different loadings, including wind flow and gravity loads, has been challenging. Huang et al. [1] obtained the natural frequencies of an Euler–Bernoulli beam during high-speed rotation using an exponential series solution. Arvin [2] studied the nonlinear free vibrations of a rotating beam. He performed the von Kamran-strain displacement relations and derived nonlinear motion equations by Hamilton's principal. Da Silva [3] presented a systematic and versatile research of a helicopter rotor blade's responses. First, he presented complete nonlinear partial differential equations governing the blade's motion which consider the geometric nonlinearities that occur due to deformation, and then the system's equilibrium solution was specified by the system. Yigit et al. [4] studied the flexural movement of a radially rotating beam connected to a rigid body. By using the extended Hamilton Principle, fully coupled nonlinear motion equations were obtained. Hanagud [5], Baruh [6], and Choura et al. [7] studied dynamical models of rotating Euler–Bernoulli beams without considering centripetal forces on beams. Most of the previous studies did not investigate the interaction between fluids and structures [8]. Song et al. [8] established an elaborate model in understanding the fluid-structure interaction between a structure and airflow. Through using the open source OpenFOAM tools coupled with the arbitrary mesh interface (AMI) framework, Wang et al. [9] provided numerical simulations of wind turbine blade-tower interaction. Vibration analysis of wind turbine blades or other rotary beam shape structures can be divided into two main parts. The first part includes edgewise vibration that happens out of the beam's rotation circle, and the second part consists on the flap-wise vibration that occurs in the rotation plate. Lee et al. [10] studied flap-wise vibration of a composite rotational Euler–Bernoulli beam and the relationship between rotational speed and natural frequencies. Asr et al. [11] suggested prestressing in the blade structure of the H-Darrieus wind turbine in the context of axial compression stress. Their research presented a structural comparison in terms of their dynamic vibrational response among reference and prestressed turbine rotor configurations. Jokar et al. [12] obtained the dynamic modeling and free vibration analysis of horizontal axis wind turbine blades in the flap-wise direction by evaluating blade kinetic and potential energies and using Hamilton's principle. Farsadi et al. [13] performed a semi-analytical solution for the free vibration analysis of uniform and symmetric pre-twisted rotating TW. They adopted the Green-Lagrange strain tensor to derive the strain field of the system and Hamilton's principle to derive the governing equations of the dynamic system. Afzali et al. [14] derived a vibration model for a H-rotor/Giromill blade. They assumed that the blade under transverse bending and twisting deformation was treated as a uniform straight elastic Euler–Bernoulli beam. Derivation of the energy

equations and simplified aerodynamic models for bending and twisting blades have been distributed and the equations of Lagrange have been extended to assumed modal coordinates to derive nonlinear motion equations for bending and twisting blades [15–19]. Meksi et al. [20] derived the equations of motion of functionally graded sandwich plates from Hamilton's principle based on a new shear deformation plate theory. Alsabagh et al. [21] implemented the Rayleigh-Ritz method for a typical 5-MW wind turbine blade and developed MATLAB codes and then obtained natural frequencies for both flap-wise and edgewise vibrational behavior. Chen et al. [22] derived a dynamic model of curved beams by using the Absolute Nodal Coordination Formulation based on the radial point interpolation method (RPIM). Chen et al. [23] examined the free vibration of rotating tapered Timoshenko beams by using the technique of variational iteration. Mokhtar et al. [24] investigated the rotor-stator interaction phenomenon in the finite element (FE) framework by using Lagrange multiplier based on contact mechanics. Tang et al. [25] presented a developed approach that is used to identify the operational blade vibration modes by measuring the vibrational displacements with a non-contact single point laser sensor during the wear process. Liu et al. [26] studied structural vibration by establishing a dynamic equilibrium equation of a coupled system consisting of a five-leaf blade. A blade excitation force model consists of transverse and vertical excitation forces generated by using a quasi-steady method. The Hamilton principle and the finite element (FE) method with a rotating pre-twisted and leaned cantilever beam model (RPICBM) with the flap-wise-chordwise-axial-torsional coupling was set up by Zheng et al. [27]. They validated the efficacy of the model through comparisons with the literature and the FE models in ANSYS. Warminski et al. [28] studied dynamics of a rotor composed of a flexible beam linked to a slewing rigid hub based on extended Bernoulli–Euler theory for a slender beam model, which considers a nonlinear curvature, synchronized transverse and longitudinal oscillations and the hub's non-constant angular velocity. In different engineering structures, rotating composite beams and blades have a wide variety of applications [29]. Rafiee et al. [29] presented a comprehensive analysis of scientific papers on rotating composite beams as presented in the past decades. For the flexural study of a sandwich beam combined with a piezoelectric layer, Wang [30] proposed a fundamental mechanics model. The Maxwell equation was used in the formulation in order to extract the distribution of the piezoelectric potential. Chen et al. [31] developed a semi-analytical solution of the dynamic features of the AG-WEC by the frequency and time domain analysis based on the potential flow principle.

5.3 Theory and Modeling

Unlike complex structures such as wind turbine blades, the Euler–Bernoulli beam has been widely investigated in order to obtain analytical solutions for dynamic and vibration responses to any external forces and excitations since the Euler–Bernoulli beam theory relies on a couple major assumptions, and also the beam has a simple geometry shape that makes analytical analysis possible for the Euler–Bernoulli beam. The two primary assumptions made by the Bernoulli–Euler beam theory are that "plane sections remain plane" and that deformed beam angles (slopes) are small, then shear deformations can be neglected. The novelty of this research work includes the projection of a wind turbine blade's deformations and lateral deflections to the same scale of Euler–Bernoulli beam. We proposed a unique transfer function matrix to undertake the projection of a wind turbine blade to an Euler–Bernoulli beam. The proposed transfer function matrix is used to transfer latera deflections of the Euler–Bernoulli beam to the wind turbine blade. This projection will permit us to simply obtain the dynamic and vibration responses of a wind turbine using the Euler–Bernoulli beam.

To develop the transfer function matrix, we need to excite both the wind turbine blade and the Euler–Bernoulli beam with same external excitations and then derive the lateral deflections of selective specific nodes on their surfaces. The Euler–Bernoulli beam should be in the same length with the wind turbine blade which is 45 meters. The lateral movements of the Euler–Bernoulli beam are obtained analytically in this research. FE models are used to calculate the counterpart of the wind turbine blade. To apply external forces and obtain the dynamic responses of both the wind turbine blade and the Euler–Bernoulli beam, the piezoelectric patches are considered. The electromechanical properties of piezoelectric materials make them powerful material as sensors and actuators. These piezoelectric sensors/actuators are patched on the surfaces of both structures. These piezoelectric patches provide the measurements of the external excitation and the dynamic responses. Two initial function matrices are derived for the Euler–Bernoulli beam with PZT patches and the wind turbine blade with PZT patched by applying same external loading and obtaining corresponding responses. Then, a total transfer function is achieved by using two initial function matrices.

5.3.1 The Euler–Bernoulli Beam Includes Piezoelectric Patches

An estimated form of the beam considered with patches is shown in Fig. 5.1. The beam under consideration here is assumed as an Euler–Bernoulli beam in its length (L), width (b), and height (h) and divided into n equal sections. To achieve the best results, the boundary conditions of the beam are assumed as those of a cantilever beam, just like a blade in a wind turbine, anchored at one end to a support. Therefore, edgewise vibrations are discarded. Moreover, the piezoelectric patches were assumed to be continuous along the transversal direction. Thus, the length of each piezoelectric patch L_p became the following:

$$L_p = x_{2bj} - x_{1bj}, \tag{5.1}$$

where j indicates that the number of sensors, b represents the beam, 2 and 1 are the beginning and the end of the patch, respectively. x_{2bj} and x_{1bj} are the distance of the end tip and the beginning of the nth sensor-actuator from the base, respectively. In this research L_p was assumed as 10 cm for each sensor. The width of every piezoelectric patch is the same as the width of beam b and is located at the end of each section on the beam.

5.3.2 Analytical Modeling of the Euler–Bernoulli Beam Includes PZT Patches

The Euler–Bernoulli theory neglects shearing deformations; hence, the shearing tension and strain are not included. In this theory, the shear force is only derived by this equation:

$$V = \frac{dM}{dx} \tag{5.2}$$

The governing equation of the Euler–Bernoulli beam with PZT patches is achieved by the energy method and Lagrange equations. Then acquired obtained equation is solved by the assumed mode method. The total strain energy of the Euler–Bernoulli beam is expressed as the following:

$$U = \frac{1}{2}\int_0^L \int_A (\sigma_{xx}\varepsilon_x)\, dA dx \tag{5.3}$$

By substituting the correlated equations for stress and strain of the Euler–Bernoulli beam, Eq. (5.3) can be represented as:

$$U = \frac{1}{2}\int_0^L D_{xx}\left(\frac{\partial u_z(x,t)}{\partial x}\right)^2 dx \tag{5.4}$$

D_{xx} is defined as the following:

$$D_{xx} = EI(x) \tag{5.5}$$

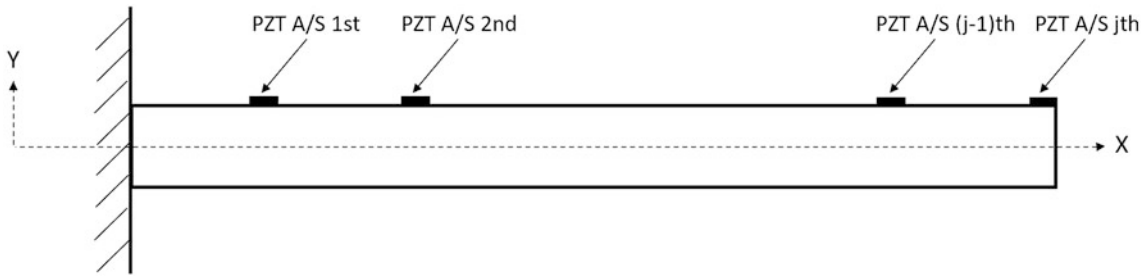

Fig. 5.1 Estimated figure of the beam includes piezoelectric patches

σ_{xx} and ε_x are the normal stress and normal strain in x-direction, respectively. E is the Young module, and $I(x)$ is the second moment of area in x direction. The related strain energy equation for the beam is derived by substituting Eq. (5.5) into Eq. (5.4), the following:

$$U = \frac{1}{2}\int_0^L \left(EI(x)\left(\frac{\partial u_z(x,t)}{\partial x}\right)^2 \right) dx, \tag{5.6}$$

where $u_z(x)$ describes transverse deflection of the beam at some position x. A total kinetic energy of the Euler–Bernoulli beam is formulated as

$$T = \frac{1}{2}\int_0^L \int_A \left(\rho v_z^2\right) dA dx, \tag{5.7}$$

where v_z is velocity and it can be shown as

$$v_z = \frac{\partial u_z(x,t)}{\partial t} \tag{5.8}$$

The Euler–Bernoulli beam's cumulative kinetic energy can be formulated and simplified by replacing Eq. (5.8) into Eq. (5.7) as

$$T = \frac{1}{2}\int_0^L \left(\rho A(x)\left(\frac{\partial u_z(x,t)}{\partial t}\right)^2 \right) dx \tag{5.9}$$

Upon deriving the governing equation of the vibration of the PZT patches, by considering the linear PZT constitutive relations, the stress and strain of these patches can be developed as:

$$\sigma_{xx}^p = c_{11}^E S_1 - e_{31} E_3 \tag{5.10}$$

$$\varepsilon_{xx}^p = S_1 = -y\frac{\partial^2 u_z(x,t)}{\partial x^2}, \tag{5.11}$$

where 1, 2, and 3 indicate the X, Y, and Z directions, respectively. c_{11}^E, e_{31}, and E_3 are modules of elasticity of the PZT in constant electric field, piezoelectric stress constant, and the electric field across the electrodes of the PZT, respectively. The relations between the electrical field and voltage applied to the piezoelectric patch electrodes is presented as the following:

$$E_3 = \frac{V(t)}{h_a} \tag{5.12}$$

$V(t)$ is applied harmonic voltage. The correlation between the piezoelectric stress constant and the associated strain constant, d_{31}, is provided as:

$$e_{31} = c_{11}^E d_{31} \tag{5.13}$$

Thus, the equations of the strain energy and kinetic energy of a piezoelectric patch are formulated as:

$$U_j^p = \frac{1}{2}\int_{x_{1a}}^{x_{2a}} \left(c_{11}^E I_p \left(\frac{\partial^2 u_z(x,t)}{\partial x^2}\right)^2 + J_p V(t)\left(\frac{\partial^2 u_z(x,t)}{\partial x^2}\right)^2 \right) dx \tag{5.14}$$

$$T_j^p = \frac{1}{2}\int_{x_{1a}}^{x_{2a}} \rho_a h_a b \left(\frac{1}{2}\frac{\partial u_z(x,t)}{\partial x}\right)^2 dx \tag{5.15}$$

The strain energy of the piezoelectric patches must be added to the strain energy of the Euler–Bernoulli beam in order to achieve the overall strain of the Euler–Bernoulli beam along with the piezoelectric sensor and actuator. The mentioned process must be applied for the kinetic energy of the piezoelectric patches and the Euler–Bernoulli beam, respectively. The cumulative strain energy and kinetic energy of the beam with PZT patches can therefore be obtained as follows:

$$U = \frac{1}{2}\int_0^L \left(EI(x)\left(\frac{\partial u_z(x,t)}{\partial x}\right)^2 \right) dx + \frac{1}{2}\int_{x_{1a.j}}^{x_{2a.j}} \left(c_{11}^E I_p \left(\frac{\partial^2 u_z(x,t)}{\partial x^2}\right)^2 + J_p V(t)\left(\frac{\partial^2 u_z(x,t)}{\partial x^2}\right)^2 \right) dx_{j=1:n}, \tag{5.16}$$

$$T = \frac{1}{2}\int_0^L \left(\rho A(x)\left(\frac{\partial u_z(x,t)}{\partial t}\right)^2 \right) dx + \int_{x_{1a.j}}^{x_{2a.j}} \rho_a h_a b\left(\frac{1}{2}\frac{\partial u_z(x,t)}{\partial x}\right)^2 dx_{j=1:n}, \tag{5.17}$$

where j indicates the number of piezoelectric patches.

5.4 Assume Mode Method

The assumed mode approximation is called to solve the governing equations of the beam and the piezoelectric patch. Under the actuation of a surface-bonded PZT patch, the transverse deflection can be expressed as:

$$u_z(x.t) = \sum_{k=1}^{b} \Pi_k(x) q_k(x), \tag{5.18}$$

where n_k is the admissible function which satisfies geometrical boundaries and q_k describes the corresponding unknown. By replacing Eq. (5.18) into Eqs. (5.16) and (5.17), these equations can be expressed as:

$$U = \frac{1}{2}\int_0^L EI \sum_{k=1}^{b}\sum_{l=1}^{b} (q_k \Pi_k')(q_l \Pi_l') dx + \left(\frac{1}{2}\int_{x_{1a.j}}^{x_{2a.j}} c_{11}^E I_p \sum_{k=1}^{b}\sum_{l=1}^{b} q_k q_l \Pi_k'' \Pi_l'' dx + \frac{1}{2}\int_{x_{1a.j}}^{x_{2a.j}} J_p V(t) \sum_{k=1}^{b} q_k \Pi_k'' dx \right)_{j=1:n} \tag{5.19}$$

$$T = \frac{1}{2}\int_0^L \rho A \sum_{k=1}^{b}\sum_{l=1}^{b} \dot{q}_k \dot{q}_l \Pi_k \Pi_l dx + \left(\frac{1}{2}\int_{x_{1a.j}}^{x_{2a.j}} \rho_a h_a b \sum_{k=1}^{b}\sum_{l=1}^{b} \dot{q}_k \dot{q}_l \Pi_k \Pi_l dx \right)_{j=1:n} \tag{5.20}$$

The Lagrange equation is presented as:

$$\frac{\mathrm{d}}{\mathrm{d}t}\left(\frac{\partial T}{\partial \dot{q}_j}\right) - \frac{\partial T}{\partial q_j} + \frac{\partial U}{\partial q_j} = 0 \tag{5.21}$$

By substituting Eqs. (5.19) and (5.20) into the Lagrange Eq. (5.21), the simple matrix form of governing equation of the Euler–Bernoulli beam along with the PZT patch becomes

$$M\{\ddot{q}\} + K\{q\} = -V(t)\eta, \tag{5.22}$$

where M, K, and η are presented as

$$M = \left[\frac{1}{2}\int_0^L \rho A \pi_k \pi_l \, dx + \left(\frac{1}{2}\int_{x_{1a.j}}^{x_{2a.j}} \rho_a h_a b \pi_k \pi_l \, dx\right)_{j=1:n}\right] \tag{5.23}$$

$$K = \left[\frac{1}{2}\int_{-\frac{L}{2}}^{\frac{L}{2}} \rho A \pi_k' \pi_l' \, dx + \left(\frac{1}{2}\int_{x_{1a.j}}^{x_{2a.j}} c_{11}^E I_p \pi_k'' \pi_l'' \, dx\right)_{j=1:n}\right] \tag{5.24}$$

$$\eta = \left(\frac{1}{2}\int_{x_{1a}.j}^{x_{2a.j}} J_p \pi_i'' dx\right)_{j=1:n} \tag{5.25}$$

5.4.1 Finite Element Modeling

The blade's FE modeling of GE 1.5 MW wind turbine is constructed in ANSYS code. The length of the blade is 45 m which includes PZT patches. The piezoelectric patches are set on the blade similarly to the Euler–Bernoulli beam and the scheme is represented in Fig. 5.2. It is assumed that the connection between the PZT patches and the beam is perfect. The blade with the same geometry of the beam which was used in the analytical modeling is modeled and the simulation is performed three-dimensionally. In the combined field of transient structural dynamics and the electric field, the simulation of the model is performed. Defining the structural damping of the blade in FEM has a high impact on obtaining an appropriate approximation of the real blade's behavior. The Rayleigh damping is considered as the structural damping model of the blade. The coefficients are obtained as $\alpha = 0.0027$ and $\beta = 0.0000017$ which are the mass corresponding coefficient and stiffness corresponding coefficient, respectively.

5.4.2 The Wind Turbine Blade Projection on the Euler–Bernoulli Beam

Due to the fact that the velocity of wave propagation in solid media is only related to the frequency variants of actuation, not the time when forces are applied to a structure, we can consider both systems (the wind turbine blade and the Euler–Bernoulli beam) as time invariant. Because both the systems are linear time-invariant (LTI), the linear properties can be used to identify vibrational characteristics subjected to any external force. The linear time-invariant feature of the system is used to represent an efficient, feasible, and accurate model as a result of finding a semi-analytical solution for the wind turbine blade

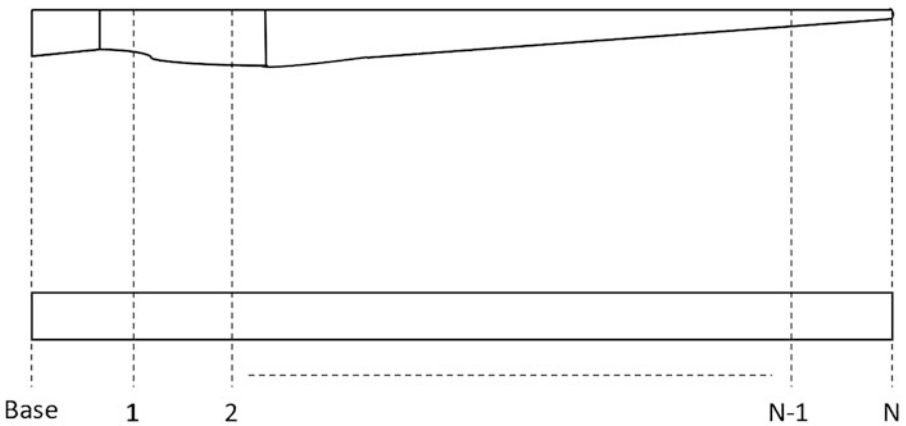

Fig. 5.2 Section's estimated diagram from the blade to the beam

for deriving lateral blade deflections under external various forces. The proposed method leverages the linear time-invariant characteristics. Therefore, the use of transfer projection function is limited to LTI systems. To obtain the frequency responses of both the FE model of the blade and the Euler–Bernoulli beam, the transmitted pulse signal is considered as an impulse function. For the Euler–Bernoulli beam with piezoelectric patches, a pulse signal is applied to every actuator's location. Then, the n outcomes of pulse signals are reached using the analytical equations by each applying the pulse signal to an actuator. In LTI systems, the unit step function can be used instead of sending the transmitted pulse signal to determine structure frequency responses. Herein, the unit step function is used to solve the equations in the time domain. Then, the achieved amplitude responses from n points are differentiated to obtain the system's responses to the transmitted pulse signal. To extract exact responses, the frequency domain is considered, since many noises were present among the reached responses. In the frequency domain, noises exhibit small frequencies and are recognizable. Additionally, high frequencies caused by the resonance phenomenon can be eliminated in the frequency domain. To increase the ratio of signals to noises, overvoltage is required. A step function output is defined as $y_u(t)$. To derive the responses to the impulse function, the outcomes needed to be differentiated with respect to time. The response of the impact function $y_\delta(t)$ equaled as the following:

$$y_\delta(t) = \frac{dy_u(t)}{dt} \tag{5.26}$$

Then, the frequency response is as the following:

$$Y_\delta(\omega) = \mathrm{FFT}\left(y_\delta(t)\right) \tag{5.27}$$

By applying the unit step function to each PZT actuator, n outputs from each n sensors are obtained in every actuation (n is 45 in this research). Each element of the function matrix of the beam and the blade is achieved as the following:

$$g_{ij} = \mathrm{FFT}\left(j\text{th output}\right) / \mathrm{FFT}\left(i\text{th input}\right), \tag{5.28}$$

where j indicates the number of sensor (output) and i presents the number of actuator (input). Repeating this procedure for every section, the $[N \times N]$ matrix of function G is derived as the following:

$$G(i, j) = g_{ij} \quad i, j = 1, 2, \ldots, n \tag{5.29}$$

Therefore, the $n \times n$ initial function matrix is derived for the Euler–Bernoulli beam with piezoelectric patches through the use of these external excitations and related responses. A $n \times n$ initial function matrix is derived for the wind turbine blade with patches by applying the same external excitations and deriving lateral movements in the same way. In order to obtain amplitude responses of the blade, the FE model of the wind turbine blade with patches is constructed in ANSYS code.

Two initial function matrices are achieved, G_b and G_w for the beam with PZT patches and the blade with PZT patches, respectively, by applying the mentioned method on the beam and the blade. At this step, by applying any same external dynamic load (U_s) to both systems and concerning the linear feature of the whole system, the total transfer function matrix is derived as:

$$Y_b = G_b.U_s \tag{5.30}$$

$$Y_w = G_w.U_s \tag{5.31}$$

By using linear feature of the whole system

$$Y_w = \left(G_w \Big/ G_b\right).Y_b \tag{5.32}$$

Next, the total transfer function matrix is obtained by using two initial metrices that are achieved in previous step as

$$G_T = \left(G_w \Big/ G_b\right) \tag{5.33}$$

The total transfer function G_T can project vibrational and tensional outcomes of the analytical solution of the Euler–Bernoulli beam with PZT patches to the wind turbine blade with PZT patches under the same external loading (Eqs. (5.31), (5.32), and (5.33)). Obtaining lateral movements of the wind turbine blade with the semi-analytical approach consists of the following steps:

- Step 1. Deriving governing equations of the Euler–Bernoulli beam with the attached piezoelectric actuator and sensor using energy method.
- Step 2. The derived governing equations are solved by assumed mode method.
- Step 3. Finite Element model of the wind turbine blade with PZT patched is developed.
- Step 4. Obtaining frequency responses of both systems, the FE model of the blade and the Euler–Bernoulli beam, by applying the transmitted pulse signal.
- Step 5. Deriving initial function matrices for the beam and the blade.
- Step 6. Obtaining total transfer function by using two achieved initial function matrices with respect to linear properties of the systems.

5.5 Results and Discussion

To verify the proposed semi-analytical solution includes the transfer function matrix method for the wind turbine blade, the Euler–Bernoulli beam and the FEM model of the wind turbine blade are loaded separately with three external different loadings. A sine distributed load with an amplitude of 20 kg/m^3 and attack angles of 15, 30, and 45 degrees are applied, respectively. The loadings cause a continuous force on the Euler–Bernoulli beam that should be discretized to the number of divided pieces (number of actuators-sensors) which is performed by using the Reilly–Ritz method. Figure 5.3 represents the comparison between analytical results and FEM results at the location of the twentieth sensor.

As shown in Fig. 5.3, acceptable compliance is found between analytical results and FEM results. Furthermore, Fig. 5.4 displays the error between the outcomes of the analytical solution and FEM for each sensor by applying the mentioned loadings. As it can be seen from Fig. 5.4, there are no clear and exact patterns in the error rates based on the sensor locations. The results show that the accuracy of the method decreases as the sensors' distance from the base of the wind turbine increases; however, there are some exceptions in the trends. One reason for obtaining ascending rate of errors by increasing the sensors' distance from the base is that the vibration domain of the structure naturally grows with augmentation of the

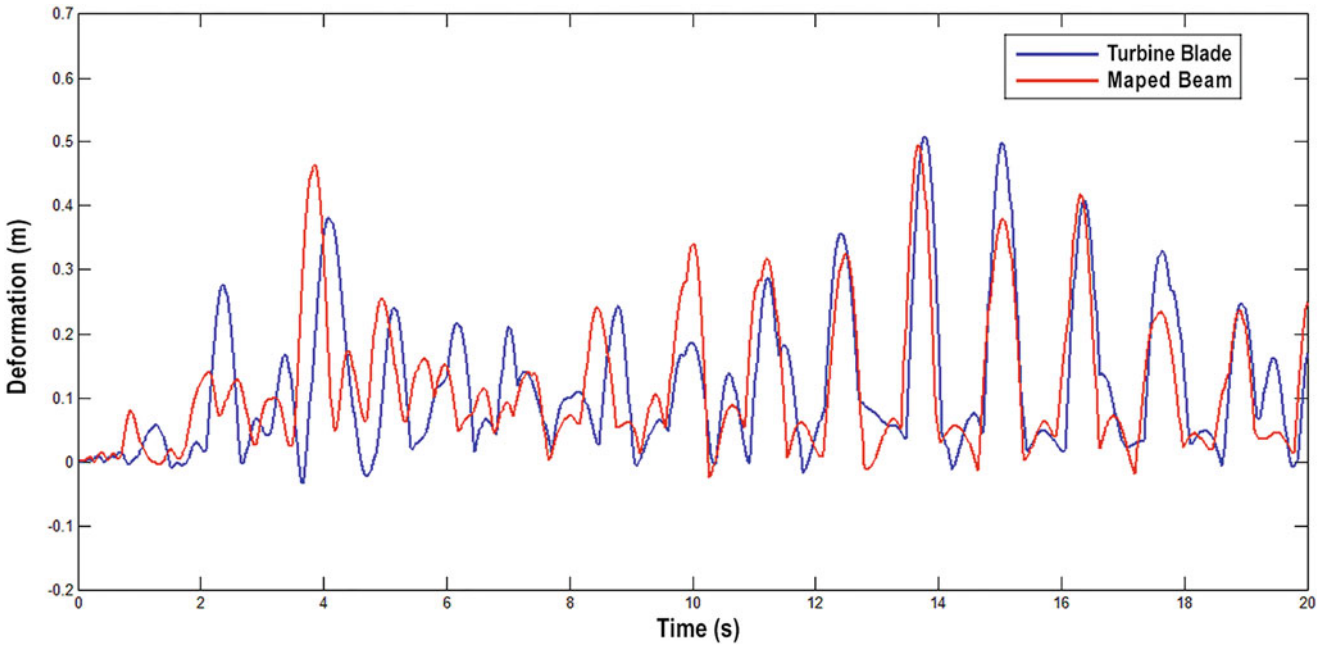

Fig. 5.3 The outcomes of the analytical results and FEM results for the twentieth sensor under loading number 1 (15 degrees attack angle)

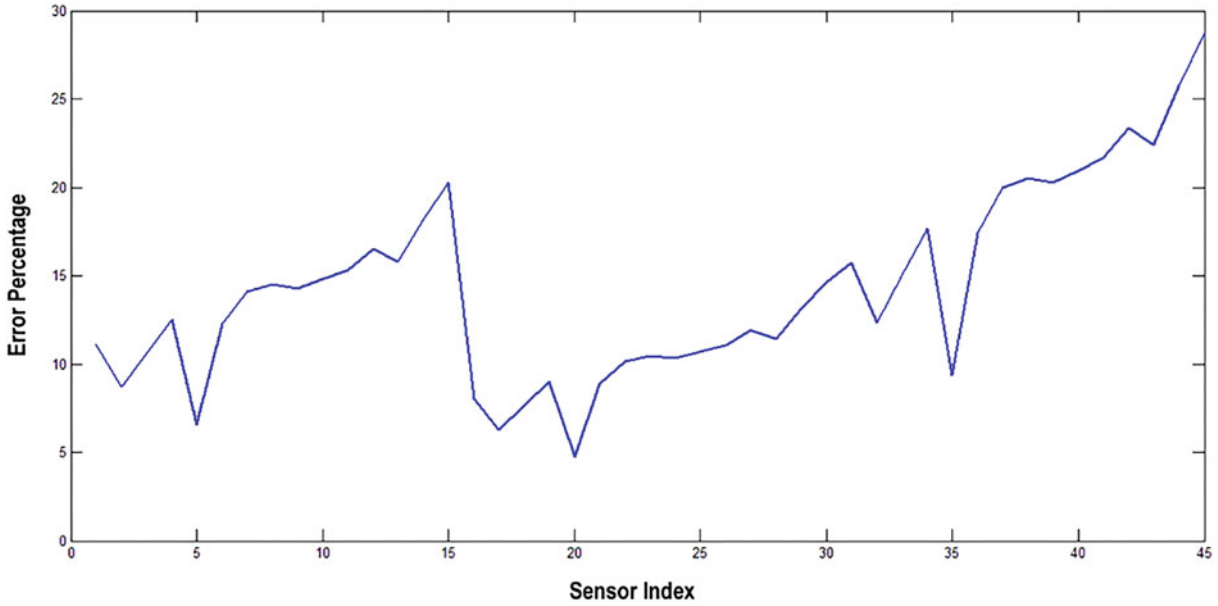

Fig. 5.4 Error percentage for each sensor under loading number 1 (15-degree attack angle)

interval from support. As it can be observed, the span from the base can be known as a determining factor for the method's accuracy.

5.6 Conclusion

An effective semi-analytical solution based on a unique transfer function matrix for a wind turbine blade is presented in the paper. First, the governing equations of the Euler–Bernoulli beam with the attached piezoelectric actuator and sensor were driven using energy method. By integrating the characteristic vibration equations of the piezoelectric patches into the characteristic equations of the Euler–Bernoulli beam, the impact of changing mass, stiffness, and electromechanical coupling between the beam and the piezoelectric actuator and sensor is taken into account. Then with the assumed mode method, the obtained governing equations are solved. The FE model of the wind turbine blade and piezoelectric patches is then developed by Rayleigh damping factors. In order to derive initial transfer function matrices for the Euler–Bernoulli beam with PZT patches and the wind turbine blade with PZT patches, a pulse signal is applied to every actuator's location in both systems and then responses are reached. Concerning the linear feature of the whole system, the final transfer function matrix is derived by applying same external dynamic force to both systems. To validate the mapping performance of the final transfer function matrix, the Euler–Bernoulli beam and the FE model of a wind turbine blade are loaded separately with three different loads. Findings show satisfactory correlations between the deflections that are derived directly from the FE model of the wind turbine blade and the movements that are achieved from the proposed method. Moreover, the accuracy of the method declined by increasing the distance of the sensors from the base of the wind turbine blade due to natural growth of the structure's vibration domain in longer distance from the support. The potential outcomes of this presented method are derivation of vibration equations of various complex shapes and also equations of deformations, strains, and tensions that are related to them. Future investigations could enhance the accuracy of the results by changing the number of sensors/actuators and their efficient installment and applying the method on other solid structures.

References

1. Huang, C.-L., Lin, W., Hsiao, K.M.: Free vibration analysis of rotating Euler beams at high angular velocity. Comput. Struct. **88**, 991–1001 (2010). https://doi.org/10.1016/j.compstruc.2010.06.001

2. Arvin, H., Bakhtiari-Nejad, F.: Non-linear modal analysis of a rotating beam. Int. J. Non-Linear Mechanics. **46**, 877–897 (2011). https://doi.org/10.1016/j.ijnonlinmec.2011.03.017
3. Crespo Da Silva, M.R.M.: A comprehensive analysis of the dynamics of a helicopter rotor blade. Int. J. Solids Struct. **35**, 619–635 (1998). https://doi.org/10.1016/S0020-7683(97)00065-6
4. Yigit, A., Scott, R.A., Galip Ulsoy, A.: Flexural motion of a radially rotating beam attached to a rigid body. J. Sound Vib. **121**, 201–210 (1988). https://doi.org/10.1016/S0022-460X(88)80024-5
5. Hanagud, S., Sarkar, S.: Problem of the dynamics of a cantilevered beam attached to a moving base. J. Guid. Control Dyn. **12**, 438–441 (1989). https://doi.org/10.2514/3.20429
6. Baruh, H., Tadikonda, S.S.K.: Issues in the dynamics and control of flexible robot manipulators. J. Guid. Control Dyn. **12**, 659–671 (1989). https://doi.org/10.2514/3.20460
7. Choura, S., Jayasuriya, S., Medick, M.A.: On the modeling, and open-loop control of a rotating thin flexible beam. J. Dyn. Sys. Meas. Control. **113**, 26–33 (1991). https://doi.org/10.1115/1.2896354
8. Song, B., Jiang, Y., Huang, S., He, W.-S.: Study on the Wind-induced Dynamic Response of Wind Power Tower in Consideration of Fluid-structure Interaction. Atlantis Press (2014). doi: https://doi.org/10.2991/icmce-14.2014.57.
9. Wang, Q., Zhou, H., Wan, D.: Numerical simulation of wind turbine blade-tower interaction. J. Marine Sci. Appl. **11**, 321–327 (2012). https://doi.org/10.1007/s11804-012-1139-9
10. Lee, S.H., Shin, S.H., Yoo, H.H.: Flapwise bending vibration analysis of rotating composite cantilever beams. KSME Int. J. **18**, 240–245 (2004). https://doi.org/10.1007/BF03184733
11. Asr, M.T., Masoumi, M.M., Mustapha, F.: Modal behaviour of vertical axis wind turbine comprising prestressed rotor blades: a finite element analysis. Pertanika J. Sci. Technol. **25**, 977–982 (2017). http://www.pertanika.upm.edu.my/Pertanika%20PAPERS/JST%20Vol.%2025%20(3)%20Jul.%202017/27%20JST%20Vol%2025%20(3)%20July%202017_JST(S)-0275-2017_pg977-982.pdf. Accessed 21 Mar 2020
12. Jokar, H., Mahzoon, M., Vatankhah, R.: Dynamic modeling and free vibration analysis of horizontal axis wind turbine blades in the flap-wise direction. Renew. Energy. **146**, 1818–1832 (2020). https://doi.org/10.1016/j.renene.2019.07.131
13. Farsadi, T., Şener, Ö., Kayran, A.: Free Vibration Analysis of Uniform and Asymmetric Composite Pretwisted Rotating Thin Walled Beam. American Society of Mechanical Engineers Digital Collection (2018). doi: https://doi.org/10.1115/IMECE2017-70531.
14. Afzali, F., Kapucu, O., Feeny, B.F.: Vibration Analysis of Vertical-Axis Wind-Turbine Blades, American Society of Mechanical Engineers Digital Collection (2016). doi: https://doi.org/10.1115/DETC2016-60374.
15. Acar, G.D., Feeny, B.F.: Bend-bend-twist vibrations of a wind turbine blade. Wind Energy. **21**, 15–28 (2018). https://doi.org/10.1002/we.2141
16. Wait, I., Yang, Z.J., Chen, G., Still, B.: Wind-induced instabilities and monitoring of wind turbine. Earthq. Eng. Eng. Vib. **18**, 475–485 (2019). https://doi.org/10.1007/s11803-019-0515-8
17. Lagrangian formulation for the rapid estimation of helicopter rotor blade vibration characteristics. The Aeronautical Journal | Cambridge Core. https://www.cambridge.org/core/journals/aeronautical-journal/article/abs/lagrangian-formulation-for-the-rapid-estimation-of-helicopter-rotor-blade-vibration-characteristics/B10B369138A33EB3D2D46B9DB16605B8 (n.d.). Accessed 4 Dec 2020
18. Pardo, A.C., Goulos, I., Pachidis, V.: Modelling and analysis of coupled flap-lag-torsion vibration characteristics helicopter rotor blades. Proc. Inst. Mech. Eng. Part G J. Aerospace Eng. (2016). https://doi.org/10.1177/0954410016675891
19. Navabi, M., Ghaffari, H.: Modeling and simulation of nonlinear dynamics of helicopter rotor flapping considering offset, blade weight moment and frequency of flapping. Modares Mech. Eng. **19**, 2523–2534 (2019). http://mme.modares.ac.ir/article-15-19245-en.html. Accessed 4 Dec 2020
20. Meksi, R., Benyoucef, S., Mahmoudi, A., Tounsi, A., Adda Bedia, E.A., Mahmoud, S.: An analytical solution for bending, buckling and vibration responses of FGM sandwich plates. J. Sandwich Struct. Mater. **21**, 727–757 (2019). https://doi.org/10.1177/1099636217698443
21. Alsabagh, A.S.Y., Fayyad, S.M., Darweesh, N., Alfaqs, F.: Fundamental natural frequencies investigation for a typical 5-MW wind turbine blade. Noise Vib. Worldwide. **51**, 77–84 (2020). https://doi.org/10.1177/0957456520901355
22. Chen, Y., Zhang, D., Li, L.: Dynamic analysis of rotating curved beams by using Absolute Nodal Coordinate Formulation based on radial point interpolation method. J. Sound Vib. **441**, 63–83 (2019). https://doi.org/10.1016/j.jsv.2018.10.011
23. Chen, Y., Zhang, J., Zhang, H.: Free vibration analysis of rotating tapered Timoshenko beams via variational iteration method. J. Vib. Control. **23**, 220–234 (2017). https://doi.org/10.1177/1077546315576431
24. Mokhtar, M.A., Kamalakar Darpe, A., Gupta, K.: Investigations on bending-torsional vibrations of rotor during rotor-stator rub using Lagrange multiplier method. J. Sound Vib. **401**, 94–113 (2017). https://doi.org/10.1016/j.jsv.2017.03.026
25. Tang, N., Zhang, B., Lord, C., Marshall, M.: Identification of blade operational mode shapes during wear of abradable coating. J. Sound Vib. **472**, 115204 (2020). https://doi.org/10.1016/j.jsv.2020.115204
26. Liu, Y., Han, J., Xue, Z., Zhang, Y., Yang, Q.: Structural vibrations and acoustic radiation of blade–shafting–shell coupled system. J. Sound Vib. **463**, 114961 (2019). https://doi.org/10.1016/j.jsv.2019.114961
27. Zeng, J., Ma, H., Yu, K., Xu, Z., Wen, B.: Coupled flapwise-chordwise-axial-torsional dynamic responses of rotating pre-twisted and inclined cantilever beams subject to the base excitation. Appl. Math. Mech. **40**, 1053–1082 (2019). https://doi.org/10.1007/s10483-019-2506-6
28. Warminski, J., Kloda, L., Lenci, S.: Nonlinear vibrations of an extensional beam with tip mass in slewing motion. Meccanica. **55**, 2311–2335 (2020). https://doi.org/10.1007/s11012-020-01236-9
29. Rafiee, M., Nitzsche, F., Labrosse, M.: Dynamics, vibration and control of rotating composite beams and blades: a critical review. Thin-Walled Struct. **119**, 795–819 (2017). https://doi.org/10.1016/j.tws.2017.06.018
30. Wang, Q., Quek, S.T.: Flexural vibration analysis of sandwich beam coupled with piezoelectric actuator. Smart Mater. Struct. **9**, 103–109 (2000). https://doi.org/10.1088/0964-1726/9/1/311
31. Investigation on semi-analytical solution of dynamic characteristics of an anti-pitching generating WEC (AG-WEC) | SpringerLink. https://link.springer.com/article/10.1007/s00773-020-00705-w (n.d.). Accessed 26 Nov 2020

Chapter 6
Evaluating the Mechanical Redesign of a Biped Walking Robot Using Experimental Modal Analysis

Tobias F. C. Berninger, Philipp Seiwald, Felix Sygulla, and Daniel J. Rixen

Abstract Structural dynamics can have a significant influence on the performance of robots. This has already been extensively shown for robot manipulators. In a previous work, we have also shown this for our biped walking robot LOLA. Vibration issues caused by the mechanical structure of LOLA are visible in the joint controllers and are limiting the performance of her walking and balancing controllers. We showed this by measuring the open-loop transfer functions of these controllers and linking the dynamics of the control plant to the structural dynamics of LOLA by comparing the results to an Experimental Modal Analysis. The knowledge gained from this analysis influenced the redesign of LOLA's upper-body structure. In this work, we will show the benefits gained from the new mechanical design by performing and comparing the same tests as done in our previous work.

Keywords Robotics · Humanoid robot · Mechanical design · Structural dynamics · Experimental modal analysis

6.1 Introduction

Over the past decade, tremendous progress has been made in the field of biped walking robots. Companies like *Boston Dynamics* [1], *Honda* [2], and *Agility Robotics* [3] have demonstrated versatile and robust biped walking machines in various scenarios. However, while pushing the performance of these machines to their limits, increasingly complex effects have to be taken into account. In case of our own biped walking robot LOLA (Fig. 6.1), we noticed various structural vibration problems that prevent us from further increasing the bandwidth of both our walking [5] and joint position controllers [6]. We investigated these issues in [7] and found strong indications that the main reason for this is the influence of LOLA's own structural dynamics on the control plants, which are not yet considered in the control design.

To our knowledge, the dynamics of the mechanical structure of biped walking robots have not been investigated yet by the biped walking robotics community. This is probably because until very recently biped walking robots have been moving quite slowly for various reasons and only required relatively low control bandwidth compared to high-performance mechatronic systems like parallel kinematics pick-and-place robots [8–10]. The rigid body assumption for stiffly designed position-controlled robots like LOLA was therefore still somewhat valid. There have been various efforts to design biped walking robots with compliant joints, e.g., [11], which inherently have to consider the dynamics introduced by their flexible elements. However, based on our experience, we assume that most other types of walking robots, position or torque controlled, will also have to deal with the structural dynamics of their previously assumed to be stiff links, when trying to further push the bandwidth of their controllers to achieve better performance.

The influence of the structural dynamics of robot manipulators on their performance has already been acknowledged and studied quite extensively. Most publications concentrate on the dynamics introduced by flexible joints or gears [12–15], while others look into the dynamics of the flexible links [16–19]. Works that consider both, flexibilities of the joints and links, are done a bit more rarely [20–22], and however, it seems to become increasingly apparent that this has to be done in order to acquire high-fidelity models [23].

Experimental Modal Analysis (EMA) is one of the main tools in structural dynamics to experimentally acquire models that can be used to verify simulation results and generally analyze the dynamics of a mechanical system. For this reason,

T. F. C. Berninger (✉) · P. Seiwald · F. Sygulla · D. J. Rixen
Department of Mechanical Engineering, Technical University of Munich, Garching, Germany
e-mail: t.berninger@tum.de; philipp.seiwald@tum.de; felix.sygulla@tum.de; rixen@tum.de

B. J. Dilworth, M. Mains (eds.), *Topics in Modal Analysis & Testing, Volume 8*, Conference Proceedings of the Society for Experimental Mechanics Series, https://doi.org/10.1007/978-3-030-75996-4_6

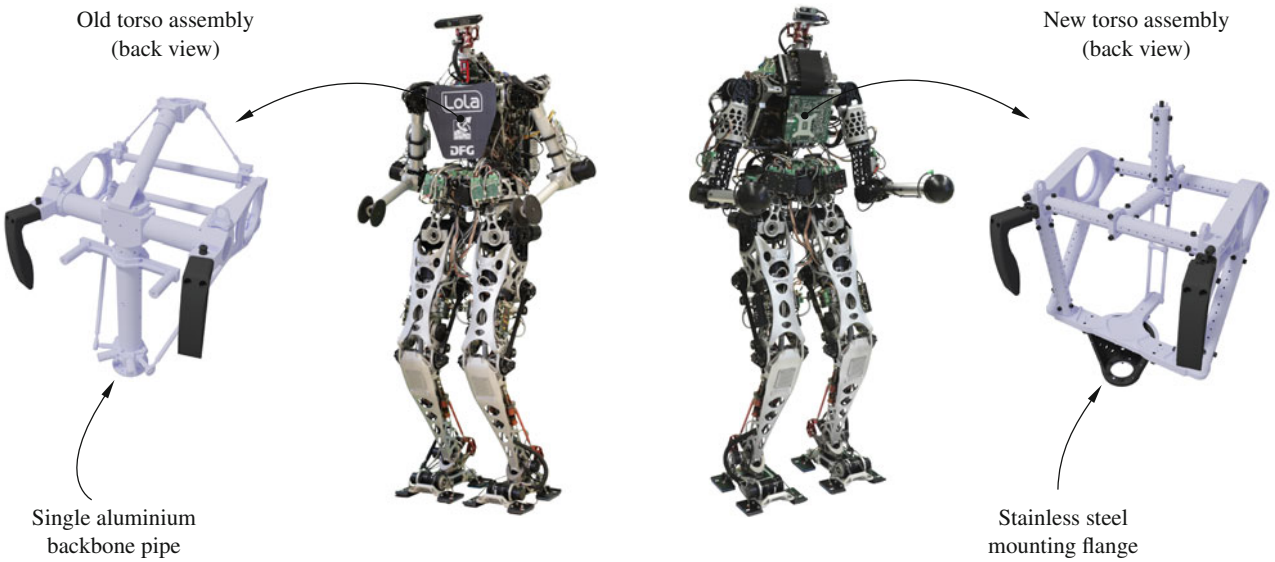

Fig. 6.1 Old (left) and new (right) mechanical design of LOLA with the old and new torso assembly (adapted from [4])

EMA has already been in use in the robot manipulator community for quite some time [24–26]. However, the only case where an EMA has been applied to a biped walking robot seems to be our own previous work [7].

The purpose of this work is to reevaluate the structural dynamics of our robot LOLA after we had to redesign her upper-body structure to make her more suitable for multi-contact locomotion [4].

6.2 Mechanical Redesign and System Overview

For the new design, LOLA received a new set of arms with one additional degree of freedom (DOF) each, Fig. 6.2. In the results of our previous EMA, we noticed that the weakest component of LOLA's structure was her single backbone pipe (Fig. 6.1), which had a large contribution to basically all mode shapes, Fig. 6.4a. This was particularly problematic, since the inertial measurement unit (IMU), which provides the balancing controller with inclination measurements of the upper body, was mounted on this backbone pipe. For this reason, we also redesigned the torso of LOLA by replacing the single backbone pipe with a box-like assembly that now houses the IMU and is attached to the hip of the robot via a particularly stiff stainless steel mounting flange. The hip and legs of the robot were left unchanged. Overall, the robot's DOF increased to 26 (+2), height to 1.763 m (+1.21 %), and mass to 68.2 Kg (+7.74 %). A more detailed description of LOLA's redesign can be found in [4]. We also published a video that showcases the new hardware upgrades [27].

The robot is actuated by 26 drives, most of which are custom-designed BLDC motors featuring harmonic drive gears, motor-side incremental encoders, and link-side absolute encoders, see [28] for details. In each foot and hand, a 6-axis force/torque sensor measures the interaction forces with the robot's environment. The IMU in the torso measures the upper-body pitch and roll inclinations. The control structure can be separated into two main control loops:

1. A balancing control loop receives the desired ideal contact wrenches at the feet from a walking pattern generator [29]. The balancing controller then modifies these desired contact wrenches based on the inclination feedback from the IMU to compensate external disturbances and modeling errors. The modified desired contact wrenches are then sent to the hybrid position/force controller.
2. The hybrid position/force controller uses the measurements of the 6-axis force/torque sensors to implement the modified desired contact wrenches by changing the pose of the robot. The desired joint angles for the pose change are then sent to the decentralized joint position controllers [6].

A more detailed description of LOLA's control architecture can be found in [5]. The first balancing controller is therefore a non-collocated control loop with the upper-body inclinations measured by the IMU as the input and the modified desired contact wrenches at the feet as the output. The entire mechanical structure from the mounting point of the IMU at LOLA's torso down to the force/torque sensors at the feet is therefore included in the control plant. The influence of LOLA's structural

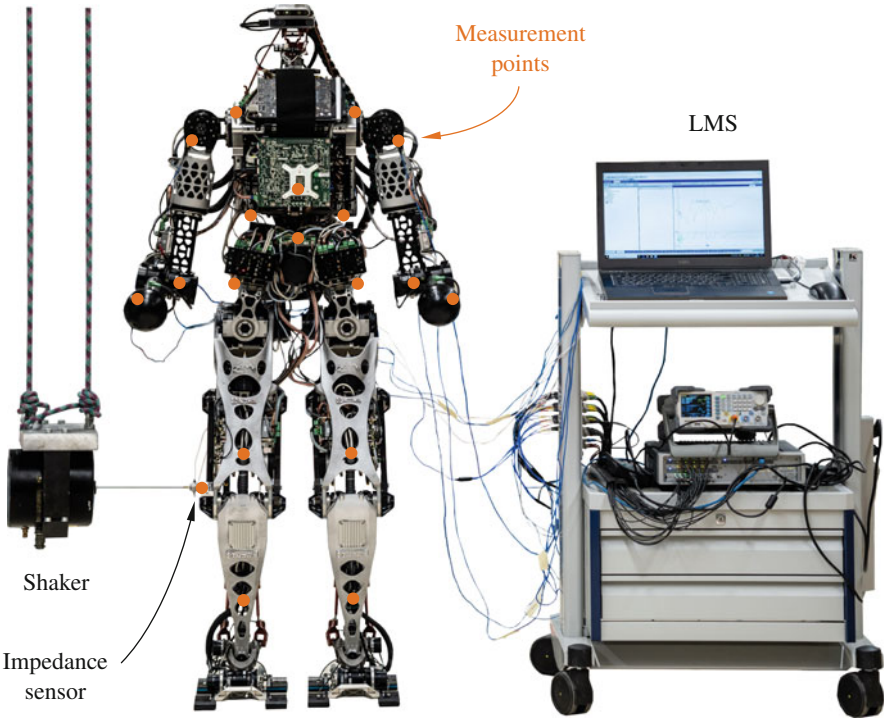

Fig. 6.2 New mechanical design of LOLA with measurement setup

dynamics is very clearly visible in the controller's open-loop transfer function, which we have shown in [7]. The hybrid position/force controller and joint position controllers experience similar effects.

6.3 Experimental Setup

In order to evaluate the effect of the mechanical redesign on LOLA's structural dynamics, we repeated the EMA in a similar way as we have already done in [7]. Six tri-ax acceleration sensors with a dimension of $12.5 \times 12.5 \times 12.5$ mm, a weight of 6.7 g, and a sensitivity of 100 mV/g are used to measure the response of the system. The sensors are a good compromise between delivering an acceptable accuracy in the low frequency range needed in this test, while also being small and lightweight enough to be easily attachable to LOLA's structure via wax. Since we already know from our previous measurements that the hip motors stay quite rigid relative to each other, even for higher frequency modes (Fig. 6.4a), we concentrated the sensors more around the torso region. Three sensors are placed near the hand, elbow, and shoulder of each arm. Four sensors are placed in each corner of the new box-shaped torso assembly. One sensor is placed directly on the IMU and three sensors near the shin, knee, and hip of each leg. Additionally, the driving point is measured using an impedance sensor next to the right knee with a sensitivity of 22 mV/N for force and 100 mV/g for acceleration. In summary, there were 18 measurement locations with 3 DOFs each, plus one point where force and acceleration were measured. The output accelerations at the 18 locations were measured in three separate measurement runs.

The system is excited by a modal shaker, which is hung from the ceiling and attached to the impedance sensor at the knee using a stinger. The excitation signal is a logarithmic sweep from 2–50 Hz over 20 s. The amplitude is chosen such that the arms show visible vibration amplitudes of up to 1 cm. It is important to use a quite strong excitation signal to overcome nonlinear effects like stick–slip or static friction in the gears and various other components of LOLA, which have a much more pronounced effect during low-vibration amplitudes.

The EMA is performed using an LMS system from Siemens, which utilizes the PolyMax algorithm [30] to identify a modal model.

During the experiments, LOLA is standing in her typical starting position for walking tests. The joint angles are actively held in place by the joint position controllers; however, the balancing and force controllers are turned off for these tests.

6.4 Results

Figure 6.3 shows two exemplary frequency response functions (FRFs) measured during the EMA. Figure 6.3a shows the FRF from the input at the shaker to the output acceleration measured at the left elbow in vertical direction. The measured FRF shows a very good coherence in the frequency range of interest up to 30 Hz, which covers all the modes that are of interest to us. The synthesized FRF derived from the modal model identified by the PolyMax algorithm also shows excellent agreement with the measurements in amplitude and phase.

Figure 6.3b shows the FRF from the input at the shaker to the output acceleration measured at the lower right corner of the torso in vertical direction. This FRF is much more challenging to measure with good quality, since the vibration amplitudes at the torso are quite a bit lower than at the arms. However, we still managed to achieve an acceptable coherence at the resonance peaks of the measured FRF. The anti-resonances are expectedly much more noisy, which also causes the PolyMax algorithm to misidentify an anti-resonance around 15 Hz. However, all following poles are still identified correctly, which can be seen by the acceptable fit of the model for the amplitude and the correct shape of the phase following the misidentified anti-resonance after 15 Hz. Since we are only interested in the mode shapes and eigenfrequencies of the system for this evaluation, the results are still of good quality here.

This indicates an overall very good result of the EMA, since we are still getting good synthesized FRFs at all resonance peaks, even for the more challenging measurement points. Applying the Modal Assurance Criterion (MAC) to the identified mode shapes also shows a good independence between mode shapes, Table 6.1. The resulting mode shapes are plotted in Fig. 6.4b and can be compared to the old shapes Fig. 6.4a, which were identified in [7]. Since these mode shapes are quite difficult to depict on paper, we highly recommend to watch the comparison of the mode shapes in motion in a video that we will publish on [31].

The first mode shape is basically the same as before and only slightly increased its eigenfrequency from 6.5 Hz to 6.9 Hz (+6.1%). This is unsurprising, since the mode is a rigid rotation of the upper body around the yaw axis that is caused by twisting of the legs. We suspect that for the old design, the torsion of the backbone pipe also had a slight contribution to this mode, which is now improved a bit by the stiffer torso. The only marginal improvement for this mode is expected, since we did not change the hip and leg design of the robot. Fortunately, this mode causes no problem for our walking control system, since the rotation around the yaw axis is not measured for the feedback of the balancing controller. This mode is therefore unobservable for the controller and thus not relevant.

The second mode of the old design at 9.7 Hz, however, caused us a lot of trouble for the control design, since this mode involved a large amount of bending of the backbone pipe, which very clearly showed up in the measurements of the IMU around the roll axis. The eigenfrequency of the new second mode is now 19.6% higher at 11.6 Hz and only involves very little motion of LOLA's upper body. Even for the small upper-body motion, the measurement points of the torso itself all stay rigid relative to each other. The main contribution to this mode shape is mainly the deformation of the arms and a bit of twisting of the legs. While the eigenfrequency of this mode only increased by about 20%, it is very good that the torso and

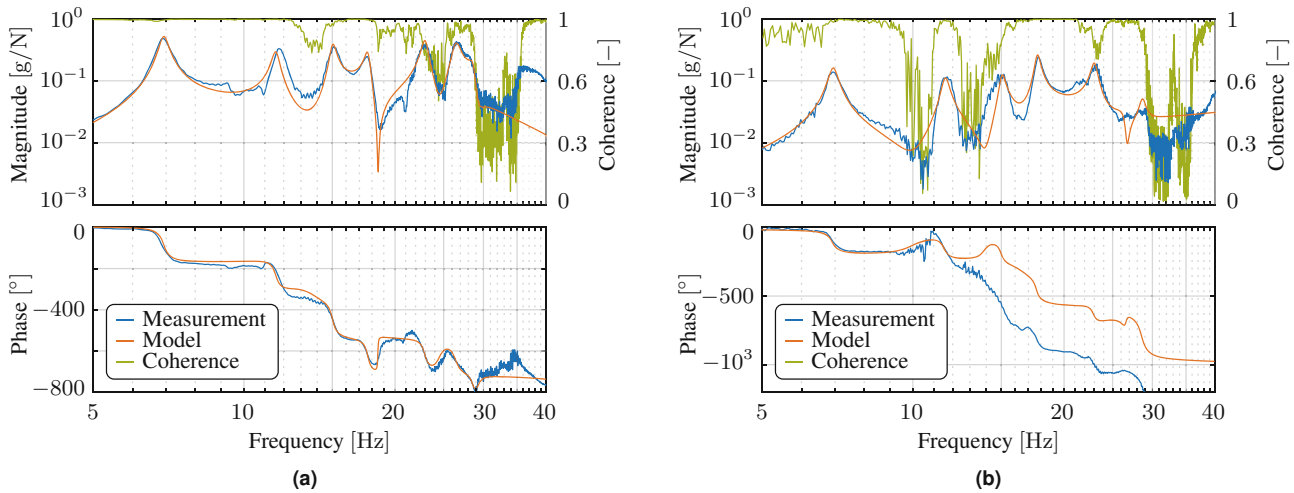

Fig. 6.3 Exemplary measured FRFs with the synthesized model and coherence. (**a**) FRF from the input at the shaker to the output acceleration at the left elbow in vertical direction. (**b**) FRF from the input at the shaker to the output acceleration at the lower right corner of the torso in vertical direction

Table 6.1 MAC of the first five modes in %

Mode	1	2	3	4	5
1	100	0.03	0.63	0.32	2.08
2	0.03	100	3.71	0.12	0.03
3	0.63	3.71	100	0.40	1.96
4	0.32	0.12	0.40	100	0.71
5	2.08	0.03	1.96	0.71	100

hip now stay rigid relative to each other. We suspect that this will have a positive effect on the open-loop transfer function of the balancing controller, which goes from the IMU measurements at the torso to the forces/torques at the feet.

The same is also true for the third and fourth modes, which are basically just different combinations of arm and leg motions, while the torso and hip stay relatively rigid. The first deformation of the upper body can be seen at the fifth mode shape at 23 Hz. While the torso itself including the IMU still stays rigid, there is now a relative rotation around the roll axis between the torso and the hip.

While we are highly satisfied with these results regarding the new mode shapes and higher eigenfrequencies, since the control path between IMU and the feet now behaves much more rigidly, we also lost a quite significant amount of damping, Fig. 6.4. For example, the second mode decreased its damping ratio from 3.5% to 1.6%, which is less than half the amount of modal damping than in the old design. This was probably caused by the old design using a lot of old rivet connections, which also started to deteriorate over the years. This likely introduced a significant amount of damping at the interfaces of the connections between the torso components. The new torso is assembled much more tightly and probably lost a bit of its damping properties compared to the old design.

6.5 Discussion

These results show that we definitely achieved the secondary goal of this redesign, which was to make LOLA's upper-body structure more rigid. Whether or not this has a positive effect on the performance of the robot still remains to be seen. As of the time of writing, we are still in the process of evaluating the influence of the LOLA's new structural dynamics on the control system. We can report the preliminary results that the changes are definitely visible in the open-loop transfer function of the balancing controller. We also needed to retune the joint position controllers of LOLA, because of the lower amount of damping in the mechanical system. We plan to publish a more thorough investigation of these effects in the future.

We still wanted to publish the results of the new EMA in this separate work to emphasize our opinion on the importance of having a good understanding of the structural dynamics of a biped walking robot. We could show here again that an EMA is a very useful tool to reliably evaluate the structural dynamics of biped walking robots, despite these machines being highly complex mechatronic systems. With sufficient expert knowledge, an EMA as shown here can be setup in 1–2 days and provide very useful information about the global structural dynamics of the system that can potentially be of great help to trouble shoot specific problems caused by the dynamics of the mechanical structure as already discussed in [7].

In our opinion, the structural dynamics of biped walking robots play an important role in their design to maximize their potential performance. It seems that, in the current state of the art for walking robots that are not inherently compliant like [11], the structural dynamics are either completely ignored or only investigated after they started to cause problems. We can also see in Fig. 6.4 that, while the mode shapes are more favorable now, the eigenfrequencies did not increase by much. The reason for this is that the dynamics of mechanical structures often do not scale very well and stay roughly the same for structures of similar topology and size. This is because stiffer materials or designs are often also heavier, which keeps the overall eigenfrequencies of the structure in the same ball park. For example, the first eigenfrequency of robot manipulators are often in the region of 7–10 Hz [25], because of all robots being a similar tree-like structure regardless of size. This means that there is probably no way around considering the structural dynamics of even stiffly designed humanoid robots in their control system to further improve their performance, since there are only quite limited possibilities to further increase the rigidity of the system just by improving the mechanical design.

Robot manipulator companies like *ABB* are already trying to incorporate high-fidelity flexible multibody simulation models in their development process to investigate dynamic effects caused by the mechanical structure of the robot as early as possible in the development cycle [23]. Sooner or later, there will also be no way around this for groups in the humanoid robots community. This also opens up a still quite unexplored and challenging field of developing efficient flexible multibody simulations of biped walking robots that can be coupled with their control systems in order to predict unfavorable interactions between their control design and structural dynamics as early as possible.

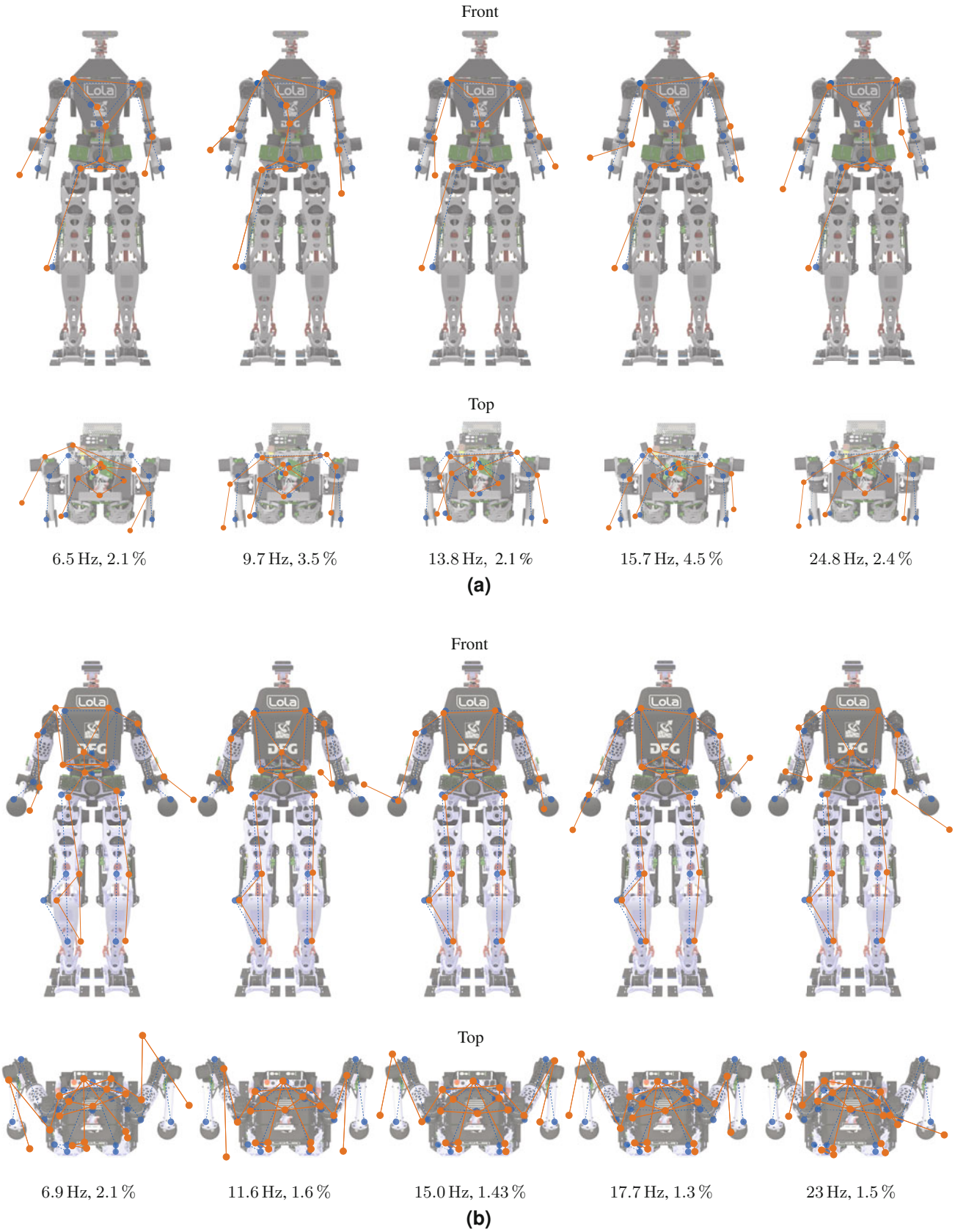

Fig. 6.4 Front and top views of the first five mode shapes before and after the redesign with their respective eigenfrequency and damping ratio. (**a**) Mode shapes before the redesign [7]. (**b**) Mode shapes after the redesign

6.6 Conclusions and Future Works

In this work, we performed an EMA of our redesigned biped walking robot LOLA. The results showed that we were able to design the torso in a much more rigid way, which we suspect will give us a beneficial effect for the possible bandwidth of the balancing controller of LOLA. This again showed the potential of utilizing an EMA to evaluate the structural dynamics of a biped walking robot and to use its results to investigate structural vibration problems.

For the future, we plan to thoroughly investigate the effects of the changed dynamics of the new upper-body structure on LOLA's control system. In the long term, we will also try to extend our current **B**eautiful **Ro**bot **C++ Co**de **Li**brary (Broccoli [32]) with a flexible multibody simulation to be able to better predict dynamic effects caused by the mechanical structure of our robot.

References

1. Nelson, G., Saunders, A., Playter, R.: The PETMAN and Atlas Robots at Boston dynamics. In: Humanoid Robotics: A Reference, pp. 169–186. Springer Netherlands, Heidelberg (2018)
2. Sakagami, Y., Watanabe, R., Aoyama, C., Matsunaga, S., Higaki, N., Fujimura, K.: The intelligent ASIMO: system overview and integration. In: IEEE/RSJ International Conference on Intelligent Robots and System. IEEE, New York (1990)
3. Agility Robotics. https://www.agilityrobotics.com/ (visited on 09/12/2020)
4. Seiwald, P., Wu, S.-C., Sygulla, F., Berninger T., Staufenberg, N.-S., Sattler M., Rixen, D., Tombari, F.: LOLA v1.1 – an upgrade in hard- and software-design for dynamic multi-contact locomotion. In: IEEE-RAS International Conference on Humanoid Robots (2021, submitted)
5. Sygulla, F., Rixen, D.: A force-control scheme for biped robots to walk over uneven terrain including partial footholds. Int. J. Adv. Robot. Syst. **17**(1), 172988141989747
6. Sygulla, F., Wittmann, R., Seiwald, P., Berninger T., Hildebrandt, A.-C., Wahrmann, D., Rixen, D.: An EtherCAT-based real-time control system architecture for humanoid robots. In: 2018 IEEE 14th International Conference on Automation Science and Engineering (CASE), August 2018. IEEE, New York (2018)
7. Berninger, T.F.C., Sygulla, F., Fuderer, S., Rixen, D.J.: Experimental analysis of structural vibration problems of a biped walking robot. In: 2020 IEEE International Conference on Robotics and Automation (ICRA). IEEE, New York (2020)
8. Rognant, M., Courteille, E., Maurine, P.: A systematic procedure for the elastodynamic modeling and identification of robot manipulators. IEEE Trans. Robot. **26**(6), 1085–1093
9. Wiens, G.J., Hardage, D.S.: Structural dynamics and system identification of parallel kinematic machines. In: 30th Annual Mechanisms and Robotics Conference Parts A and B, vol. 2. ASME, New York (2006)
10. Zhou, Z., Mechefske, C.K., Xi, F.: Modeling of configuration-dependent flexible joints for a parallel robot. Adv. Mech. Eng. **2**, 143961 (2010)
11. Tsagarakis, N.G., Morfey, S., Cerda, G.M., Zhibin, L., Caldwell, D.G.: COMpliant huMANoid COMAN: optimal joint stiffness tuning for modal frequency control. In: 2013 IEEE International Conference on Robotics and Automation, IEEE, May 2013
12. Sweet, L., Good, M.: Redefinition of the robot motion-control problem. IEEE Control Syst. Mag. **5**(3), 18–25 (1985)
13. Kuntze, H.-B., Jacubasch, A.: Control algorithms for stiffening an elastic industrial robot. IEEE J. Robot. Autom. **1**(2), 71–78 (1985)
14. Luca, A.D., Flacco, F.: A PD-type regulator with exact gravity cancellation for robots with flexible joints. In: 2011 IEEE International Conference on Robotics and Automation, IEEE, May 2011
15. Albu-Schäffer, A., Hirzinger, G.: A globally stable state feedback controller for flexible joint robots. Adv. Robot. **15**(8), 799–814 (2001)
16. Book, W.J.: Controlled motion in an elastic world. J. Dyn. Syst. Measure. Control **115**(2B), 252 (1993)
17. Luca, A.D., Giovanni, G.D.: Rest-to-rest motion of a one-link flexible arm. In: 2001 IEEE/ASME International Conference on Advanced Intelligent Mechatronics. Proceedings (Cat. No.01TH8556). IEEE, New York (2001)
18. Cannon, R.H., Schmitz, E.: Initial experiments on the end-point control of a flexible one-link robot. Int. J. Robot. Res. **3**(3), 62–75 (1984)
19. Post, B.K.: Robust State Estimation for the Control of Flexible Robotic Manipulators. PhD thesis. Georgia Institute of Technology, 2013
20. Ohr, J., Moberg, S., Wernholt, E., Hanssen, S., Pettersson, J., Persson, S., Sander-tavallaey, S.: Identification of flexibility parameters of 6-axis industrial manipulator models. In: ISMA 2006 (2006)
21. Behi, F., Tesar, D.: Parametric identification for industrial manipulators using experimental modal analysis. IEEE Trans. Robot. Autom. **7**(5), 642–652 (1991)
22. Berninger, T.F.C., Ochsenius, M.A., Rixen, D.J.: Evaluation of an external vibration damping approach for robot manipulators using a flexible multi body simulation. In: 2019 IEEE/ASME International Conference on Advanced Intelligent Mechatronics (AIM), IEEE, July 2019
23. Zimmermann, S.A., Berninger, T.F.C., Derkx, J., Rixen, D.J.: Dynamic modeling of robotic manipulators for accuracy evaluation. In: 2020 IEEE International Conference on Robotics and Automation (ICRA), pp. 8144–8150 (2020)
24. Jacobus, R., Serna, M.: Modal analysis of a three dimensional flexible robot. In: Proceedings of the 1994 IEEE International Conference on Robotics and Automation, pp. 2962–2967 (1994)
25. Berninger, T.F.C., Fuderer, S., Rixen, D.J.: Modal analysis of a 7 DoF sweet pepper harvesting robot. In: Topics in Modal Analysis & Testing, May 2019, vol. 8, pp. 163–170. Springer International Publishing, Cham (2019)
26. Fuentes, A.T., Kipfmueller, M., Prieto, M.A.: 6 DOF articulated-arm robot and mobile platform: dynamic modelling as multibody system and its validation via experimental modal analysis. In: IOP Conference Series: Materials Science and Engineering , vol. 257, p. 1 (2017)
27. Youtube video about Lola's hardware upgrade. https://www.youtube.com/watch?v$=$mpDqMFppT68&t (visited on 09/12/2020)
28. Lohmeier, S.: Design and Realization of a Humanoid Robot for Fast and Autonomous Bipedal Locomotion. Dissertation. TU Munich, 2010

29. Seiwald, P., Sygulla, F., Staufenberg, N.-S., Rixen, D.: Quintic spline collocation for real-time biped walking-pattern generation with variable Torso height. In: IEEE-RAS International Conference on Humanoid Robots. Preprint (2019, accepted for publication)
30. Peeters, B., Van Der Auweraer, H.: PolyMAX: a revolution in operational modal analysis. In: International Operational Modal Analysis Conference (IOMAC), 2005
31. Youtube channel of the Chair of Applied Mechanics. https://www.youtube.com/channel/UCrZeG0XNWj-kyn2qC8jOLJg (visited on 09/12/2020)
32. Seiwald, P., Sygulla, F.: broccoli: Beautiful Robot C++ Code Library 2020

Chapter 7
Novel Wirelessly Synchronised Modal Testing of Operational Buildings Using Distributed OCXO High-Precision Data Loggers

Wai Kei Ao and Aleksandar Pavic

Abstract This chapter describes a novel and oven-controlled crystal oscillator (OCXO) high-precision synchronised wireless data acquisition system for modal testing of large structures. The system was used for the first time for a rare FRF-based modal testing of a full-scale multi-storey building in operation. National Instruments' CompactRIO and LabVIEW were utilised to develop wireless multi-channel data loggers to resolve typical, and sometimes insurmountable, problems related to the logistics of long cables connecting sensors with data acquisition in ambient vibration testing (AVT) exercises on operational structures. Several OCXO-based data loggers were used to distribute sensors wirelessly across the structure, using a sub-microsecond sensor synchronisation procedure to measure simultaneously not only the structural vibration response but also the forcing function needed in FRF measurements. As part of the setup, a spectrum analyser (SA) was used to provide the shakers' excitation signal and perform a point accelerance FRF measurement at a location close to the data acquisition centre and with minimum wired infrastructure. Two different data acquisition systems (OCXO- and SA-based) used independent time clocks.

To validate the OCXO-based FRF measurement in buildings, modal testing was carried out on a 15-tonne laboratory-based test floor and a full-scale seven-storey condominium building made of cross-laminated timber. The combination of distributed OXCO-based wireless and synchronised data loggers coupled with an SA-based force generation and FRF point mobility quality assurance measurement was successfully used to identify the sway modes' dynamic properties of the structure.

Keywords Distributed OCXO-based data logger · Spectrum analyser-based system · Time synchronisation · Modal analysis

7.1 Introduction

The number of multi-storey, mid- to high-rise buildings in urban areas has been increasing rapidly for some time now as the world decided to go up rather than out of its growing cities. For such structures, the wind-induced lateral sway motion and the related the vibration serviceability performance nowadays govern the design, replacing the strength considerations in determining the size and shape of the structure.

The damping and natural frequencies of high-rise buildings are the key but traditionally unreliable design parameters as it is quite difficult to predict them in advance. The way forward is to learn about the as-built modal properties of operational structures subjected to wind dynamic load in service. For this, output-only ambient vibration testing (AVT) has commonly been used for many years. However, it is well known that the experimentally estimated modal properties based on the output-only AVT are much less reliable than their FRF-based counterparts based on the input–output relationship.

The FRF-based modal testing could deal much more effectively than the AVT with the non-linear dynamic behaviour of the structure and provide a more robust, informed and reliable estimation of the as-built modal properties. For example, amplitude-dependent behaviour and properties of higher modes of vibration are much easier to investigate and measure using the FRF-based methodology, compared with its AVT-based counterpart.

To carry out the FRF-based modal testing in an operational building, a novel distributed OCXO-based high-precision data acquisition system featuring robust time synchronisation was developed. The OCXO-based data loggers can provide time synchronisation wirelessly, without the need for Wi-Fi, radio or GPS signals. This means that the data loggers could

W. K. Ao (✉) · A. Pavic
University of Exeter, Vibration Engineering Section, College of Engineering, Mathematics and Physical Sciences, Exeter, UK
e-mail: wka203@exeter.ac.uk; a.pavic@exeter.ac.uk

B. J. Dilworth, M. Mains (eds.), *Topics in Modal Analysis & Testing, Volume 8*, Conference Proceedings of the Society for Experimental Mechanics Series, https://doi.org/10.1007/978-3-030-75996-4_7

be easily distributed through the building at different levels and locations, without any wires to connect sensors to the main data acquisition system. This solves the key logistical obstacle in modal testing of operational high-rise buildings: running long wires up and down the building across multiple floor levels. This is the key advantage of the wireless OCXO-based data loggers over the traditional wired method. The wired method typically features a multi-channel spectrum analyser (SA) capable of 'live' monitoring of the force and response data, as well as of the formation of FRFs through averaging. This is an important quality assurance feature in FRF-based modal testing of any structure, including operational buildings, and—as will be seen—the OCXO-based system makes use of this 'live' feature as much as possible without compromising its essentially wireless capability.

The novel OCXO-based data loggers are combined with a wired multi-channel spectrum analyser (SA) to perform FRF measurements. The SA-based sub-system is used to provide an input signal to drive the modal testing exciter(s) simultaneously and provide real-time measured force and response data monitoring, but only at a single test point rather than throughout the whole building. That point is at the same level and close to where the FRF data acquisition centre is (typically at the top of the building next to the exciters), thus minimising the number and length of wires. This hybrid system, comprising the wired SA- and wireless OCXO-based data loggers, is considered an optimum solution. It combines the need for the predominantly wireless data acquisition across different floor levels with the need to have quality-assured 'live' measurements of the point accelerance FRF, arguably the most important type of FRF measured.

It is very important to quality assure the FRF measurements in situ, in particular, for civil engineering applications where return to the test site is difficult or impossible in case of errors. It also makes use of an existing standard and wired modal testing infrastructure.

To illustrate the process of time synchronisation and operation of the new OCXO-based modal testing systems for a single-input multi-output (SIMO) FRF measurement, firstly a laboratory-based 15-tonne full-scale and reconfigurable single-floor panel structure was used. The aim was to experimentally estimate horizontal sway modes of vibration, mimicking what is typically required for real high-rise structures. In addition, in addition to the hybrid system, a standard wired multi-channel SA-based system measurement was also used to repeat the test and obtain FRF data for the validation of the hybrid modal testing system.

After this, the hybrid system was developed successfully for the first time on a full-scale seven-storey condominium building made of cross-laminated timber (CLT) during its normal operation resulting in a unique FRF-based modal testing data from such a structure.

This chapter has five sections. Following the introduction, the second section introduces the oven-controlled crystal oscillator (OCXO) high-precision synchronised data acquisition system. The third section describes the laboratory test structure on which the above-mentioned two FRF-based modal tests were carried out, using (1) the hybrid OCXO- and SA-based wireless/wired method and (2) the wired SA-based method. The fourth section describes the deployment of the hybrid system in FRF-based modal testing of a full-scale CLT building. Conclusions are presented in the last section.

7.2 Oven-Controlled Crystal Oscillator (OCXO) High-Precision Synchronised Data Acquisition System

Figure 7.1a shows an OCXO-based data logger [1] and a CompactRIO-9064 embedded into a Peli storm case. Furthermore, it shows a 14.5V LiPloy battery housed within the case, along with DC–DC and AC–DC voltage converters. The data logger can work with both DC (battery) or AC supply.

To record force and vibration data, National Instruments (NI) 9234 (Fig. 7.1b) was coupled (in CompactRIO-9064) with other NI modules. CompactRIO-9064 chassis has four slots. The first slot is occupied by the mentioned NI-9234 C Series Sound and Vibration Input Module. This module gives a wide dynamic range of signal conditioning and configures a software-selectable 24-bit AC/DC coupling converter that ensures measured signal accuracy. The NI-9234 can also measure integrated electronic piezoelectric (IEPE) and non-IEPE sensors. Each channel of this module (4-channel, 51.2 kS/s/channel, ± 5 V) has built-in anti-aliasing filters that enable automatic adjustment of the sample rate.

Then, the NI-9402 module (Fig. 7.1b) was attached to the second slot of the CompactRIO-9064 chassis, which is a low-voltage transistor-to-transistor logic (LVTTL), 4 bidirectional channels, 55 ns C Series Digital Module and configures a high-speed digital I/O counter/timer. Each of the CompactRIOs in the OCXO-based data loggers is also used to monitor the 'local' OCXO clock/tick, which reaches 120 MHz. As such, the field programmable gate array (FPGA) module of the CompactRIO, which is compatible with graphical programming LabVIEW, could implement the corresponding vibration data acquisition by overriding the native CompactRIO clock with the acquired OCXO clock/ticks, as shown in Fig. 7.2a.

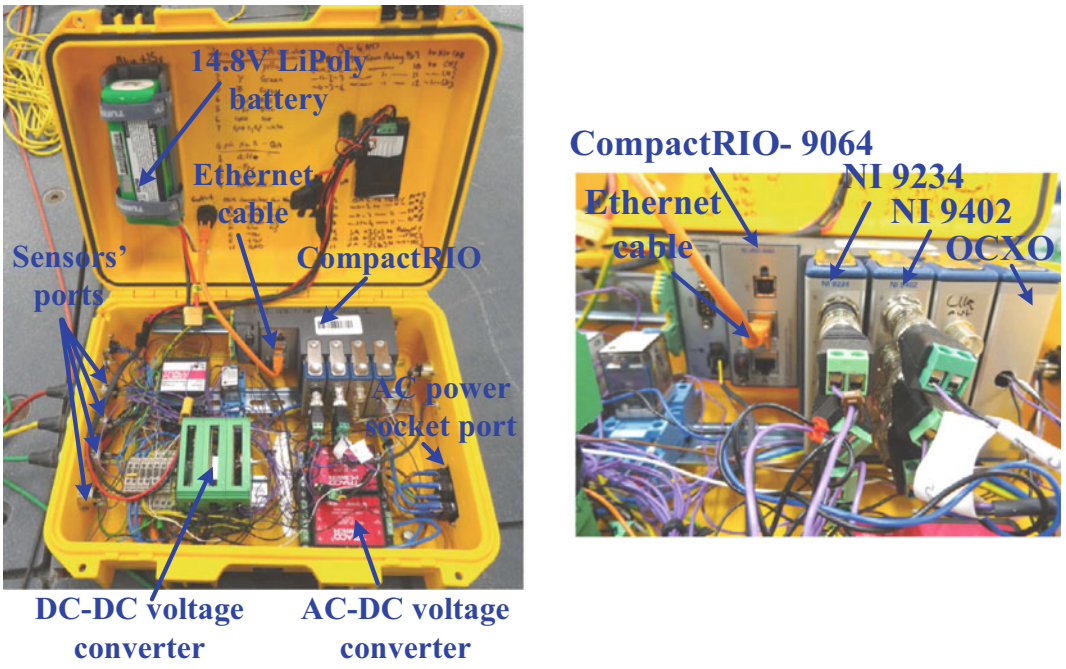

Fig. 7.1 OCXO-based high-precision synchronised data acquisition system. (**a**) OCXO-based data logger. (**b**) CompactRIO-9064 embedded a waterproof Peli

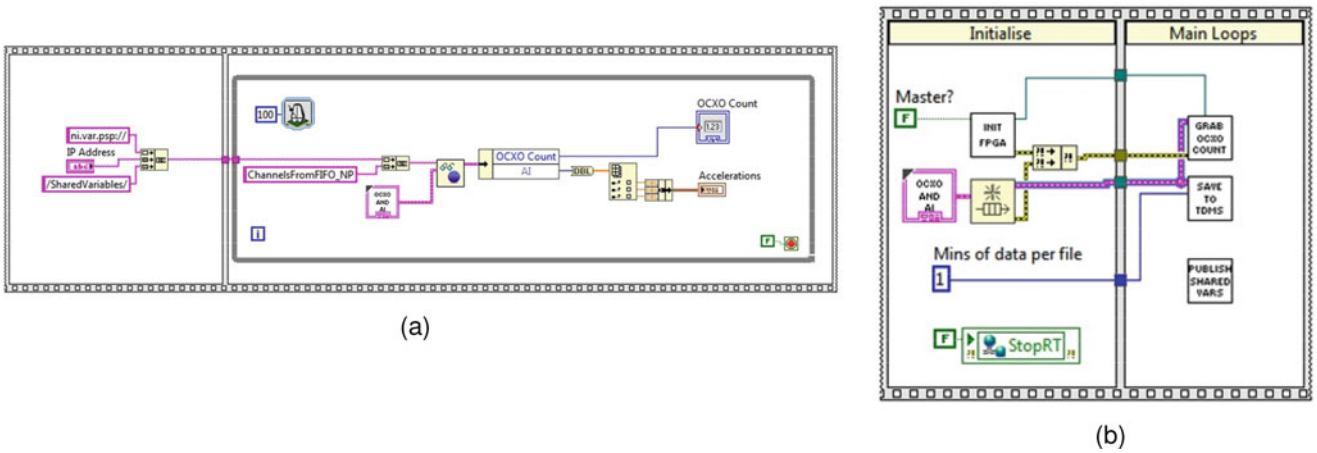

Fig. 7.2 LabVIEW graphical programming of the CompactRIO-9064. (**a**) LabVIEW field programmable gate array (FPGA) module block diagram. (**b**) LabVIEW real-time block diagram

Oven-controlled crystal oscillators (OCXOs) are used in control circuitry to provide accurate binary-numbered clock ticks. The crystal oscillators have a steady and very much constant temperature, which guarantees stability of the high-frequency measurements. It should be noted that the OCXO is typically applied in radio transmitters, cellular base stations and military communications equipment to control the frequency measurement very precisely. For convenience, the OCXO was packaged inside a blank C Series module and inserted into the fourth slot of the CompactRIO chassis.

A Honeywell QA750 accelerometer is connected (via a relatively short 10–20 long cables) to the sensors' port of the OCXO-based data logger, as shown in Fig. 7.3a. The accelerometer, or any other suitable sensor, can be placed at a test point on the structure, typically at the same level in the case of building structures, which amplifiers logistics considerable.

As part of the process for data synchronisation between different OCXO-based data loggers, one of the distributed data loggers is first selected to act as a 'master' clock. The selected 'master' data logger needs to connect to the DC/AC power to activate the embedded CompactRIO. A successful setting of the master clock is announced by a 'beep' sound and an

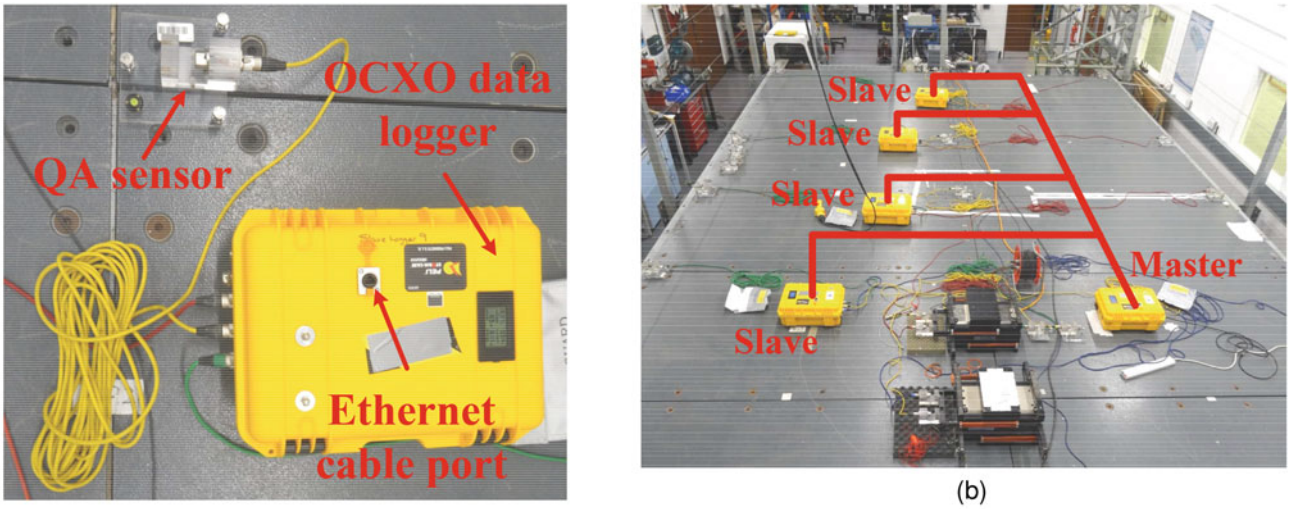

Fig. 7.3 Master and slave OCXO units time synchronisation. (**a**) Connecting QA sensor to OCXO-based data logger. (**b**) Time synchonisation: connecting a 'master' OCXO to 'local' OCXO units

illumination of an indicator (green) on its CompactRIO. Then, the other 'slave' data loggers are powered up and individually activated using the same method resulting in a setup of 'local' clock/ticks. The next step is to synchronise the 'local' units by briefly connecting them to the 'master' OCXO clock. This is done using a BNC cable to connect the 'master' data logger output port with each of the 'slave' units' input port, for all slave units in turn, as demonstrated in Fig. 7.3b. This syncing process only takes a few seconds for each 'slave' unit and is done only once at the start of the test. The synchronisation achieved is within a fraction of a microsecond, practically ideal for the purpose of modal testing of large civil engineering structures and with negligible drift.

The CompactRIO-9064 has high-speed direct memory access. The acquired data, for example, acceleration, is recorded using a Technical Data Management Streaming (TDMS) format file. In our application, the recorded acceleration TDMS files were stored one per minute, as shown in Fig. 7.2b, which could very much guarantee no acquired data loss and control of each file size. The CompactRIO-9064 housing contains a USB port that could extend the file storage through plugging an external flash memory stick. Once the testing is complete, the stored data could then be accessed through Ethernet, FTP, or retrieved from a USB flash drive.

7.3 Forced Vibration Modal Testing in the Use of OCXO-Based Distributed Data Loggers

This section describes a laboratory scale floor structure and its modal testing.

7.3.1 Description of the Test Structure

A reconfigurable laboratory-based test floor structure (Fig. 7.4a) was tested to validate the novel hybrid wireless/wired measurement method of FRF-based modal testing. The weight of the rectangular floor panel structure was approximately 15 tonnes with of dimensions 7.5×5 m^2. This floor panel was located in the laboratory of the Vibration Engineering Section at the University of Exeter, UK. The structure was constructed of sandwich plate system (SPS) panels, I section (UB and UC) steel beams, steel plates and bolts. This is a reconfigurable structure, and in this study, Type C floor structure [2] was used.

As it can be seen in Fig. 7.5, two main girders were UB $457 \times 191 \times 82$ mm section, while the two secondary beams were UB $305 \times 165 \times 40$ mm, whereas a beam (UC $203 \times 203 \times 60$ mm) was set in the middle of the panel connected to the midpoints of the main girders. M22 bolts were used to connect all elements of this core structural frame. M22 countersunk

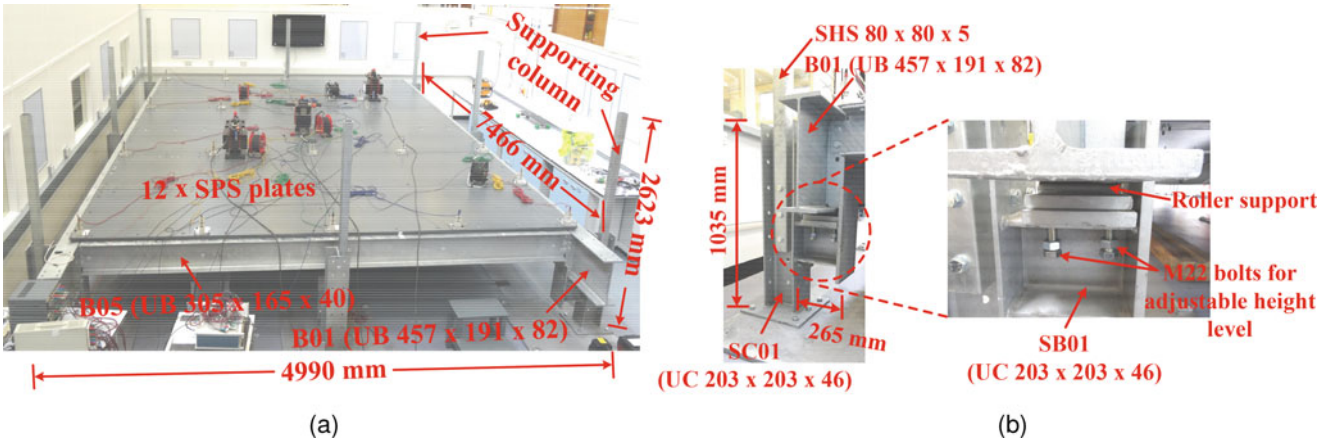

Fig. 7.4 Reconfigurable test-bed floor panel structure. (**a**) Test floor panel. (**b**) Zoom in view of the support boundary condition

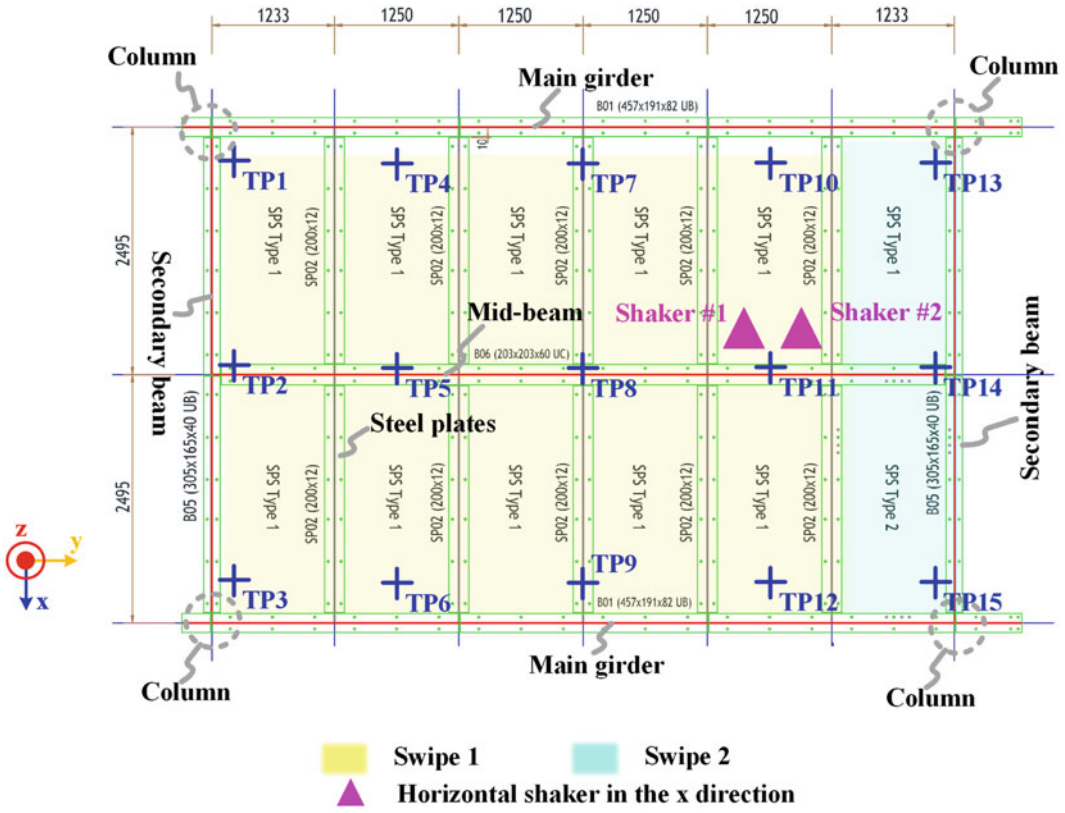

Fig. 7.5 Modal testing test grid

bolts were used to interconnect 12 SPS panel via steel strips (SP02 200 × 2279 × 12 mm). The four corners of the constructed floor were laid on roller supports, as shown in Fig. 7.4b, which were placed on short transfer beams (SB01 UC 203 × 203 × 46) and then bolted to columns (SC01 UC 203 × 203 × 46 mm). The constructed floor test structure was used for the FRF-based modal testing to identify the horizontal sway modes of vibration of the whole structure in the x-direction only (Fig. 7.5).

7.3.2 *Modal Testing Setup Featuring Wired SA- and Wireless OCXO-Based Distributed Data Loggers*

For convenience, a total of 15 test points (TPs) were defined, as shown in Fig. 7.5. This study used two horizontal APS400 electrodynamic shakers, represented by a triangle symbol, to excite the tested floor structure nominally at TP11 in the x-direction only. Two movements (termed here 'swipes') of 12 available accelerometers were used to cover the 15 test points by moving the horizontal accelerometers over the 15-point test grid. The first swipe covered TP1 to TP12, while the second swipe required accelerometers only at the three remaining locations: TP13, TP14 and TP15. To check the robustness of the FRF measurement, which used the hybrid (OCXO- and SA-based) system, the traditional wired method (only SA-based) was also used separately to repeat nominally identical modal testing to obtain benchmark modal testing results for comparison with hybrid system. Figures 7.6 and 7.7 show the equipment and its connections for the traditional SA-based method featuring plenty of wires. There are, as previously mentioned, a considerable logistical challenge in operational buildings and one of the key reasons why FRF-based modal testing of operational buildings is so rare, practically non-existent.

The OCXO-based data logger can be utilised to overcome these problems, and Fig. 7.8 shows the relevant equipment connections for the hybrid OCXO- and SA- based systems. The key advantage is that there are no long cables from connection reels (accommodating 4 accelerometers per reel, the same number an OCXO data logger handles) to signal conditioner (which exist as pink lines in the standard wired setup shown in Fig. 7.6).

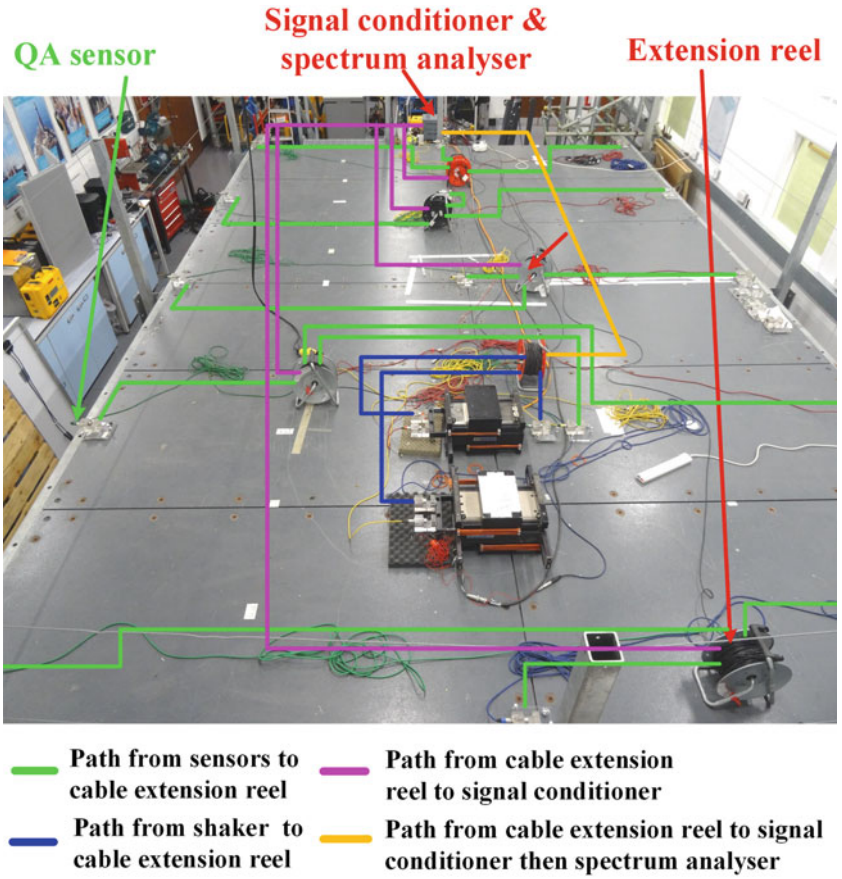

Fig. 7.6 Standard SA-based wired measurement system featuring connections between accelerometers and cable extension reel, long cables from cable extension reels to the signal conditioner and spectrum analyser

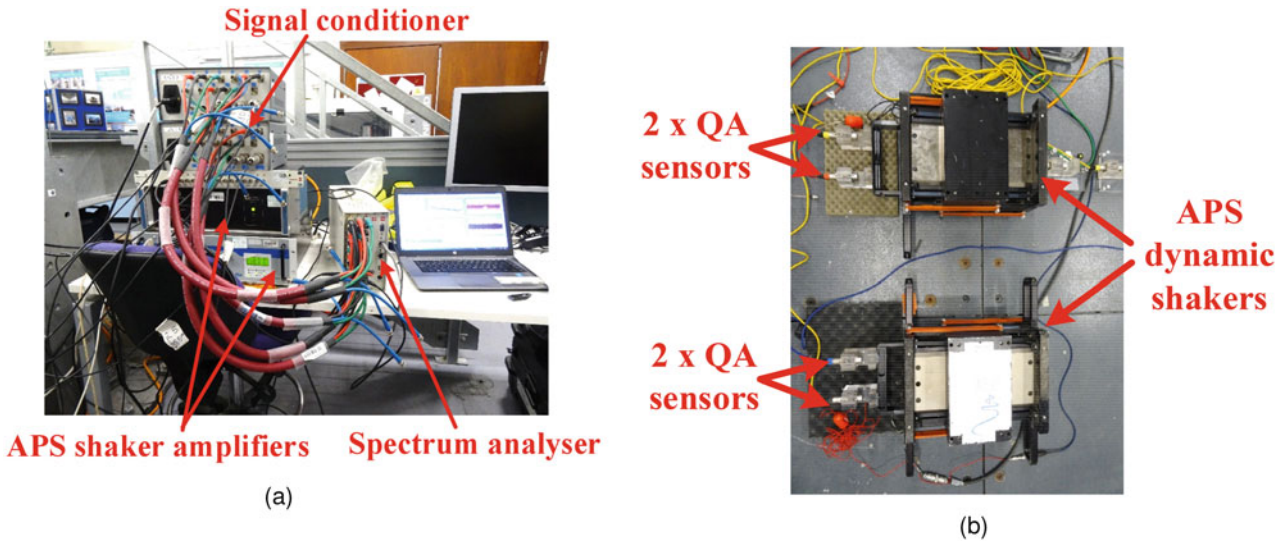

Fig. 7.7 Experimental equipment setup. (**a**) Signal conditioners, spectrum analyser and APS amplifiers. (**b**) Two horizontal APS Dynamic Inc. shakers setup

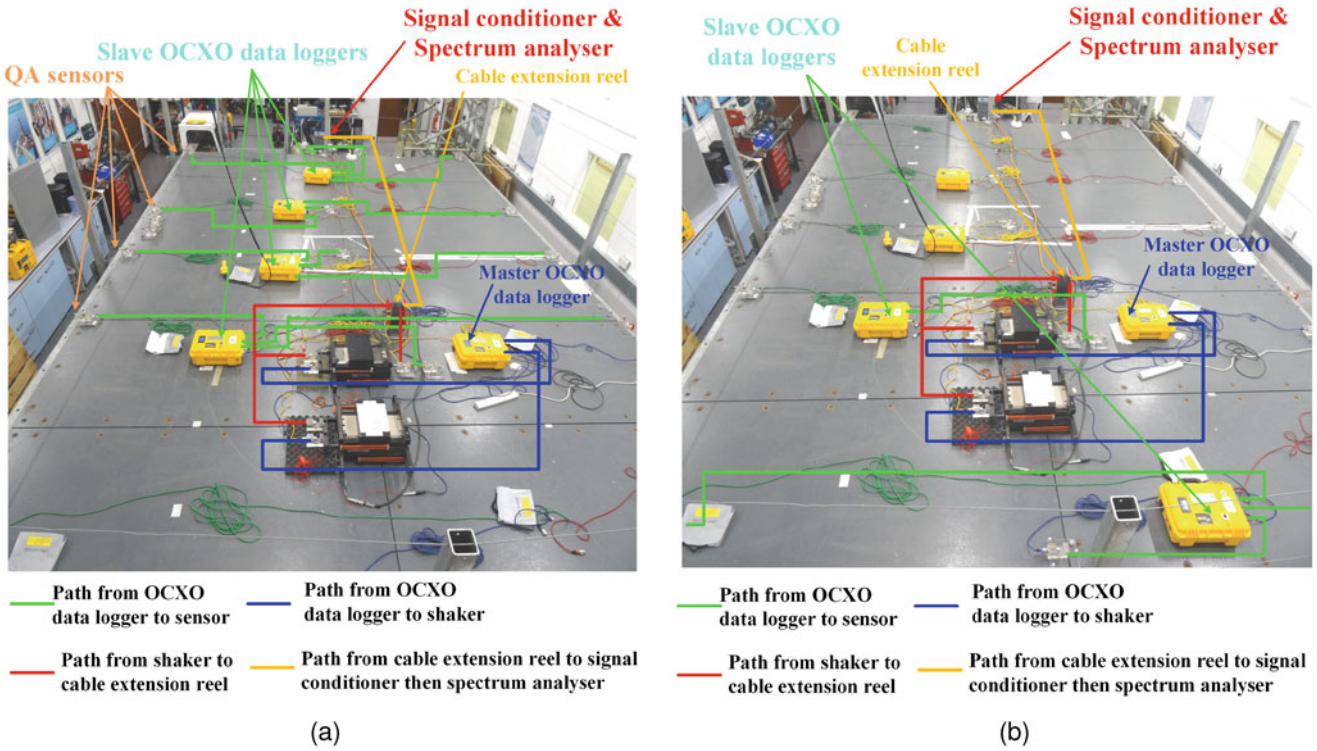

Fig. 7.8 Connections in the OCXO-based system featuring only connections between accelerometers and OCXO-based data loggers (yellow box). (**a**) Swipe 1. (**b**) Swipe 2

7.3.3 Modal Analysis

The electrodynamic excitation for both shakers was identical and random in nature, being a pick noise in the frequency range of 0–30 Hz. This was provided by a Data Physics Spectrum Analyser with digital data acquisition enabling 0.01 Hz resolution of the force and response signals. Typical time histories acquired simultaneously by the SA and OCXO system are shown in Fig. 7.9.

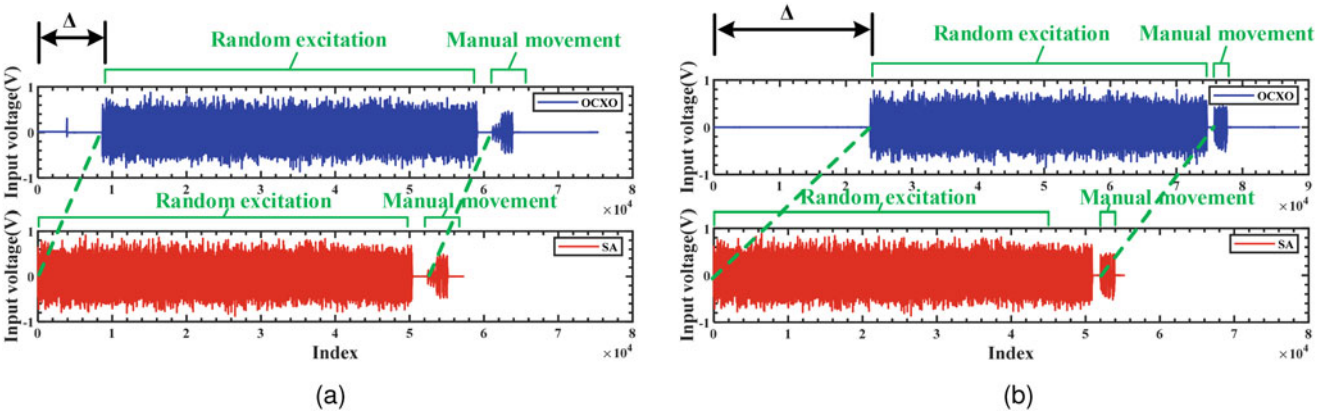

Fig. 7.9 Different staring time of OCXO-based data loggers and spectrum analyser. (**a**) Swipe 1. (**b**) Swipe 2

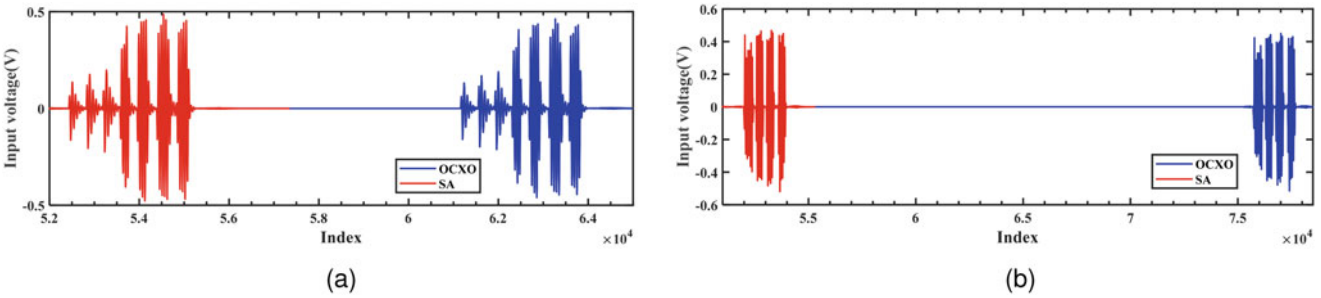

Fig. 7.10 OCXO- and SA-based measured signal before alignment. (**a**) Swipe 1. (**b**) Swipe 2

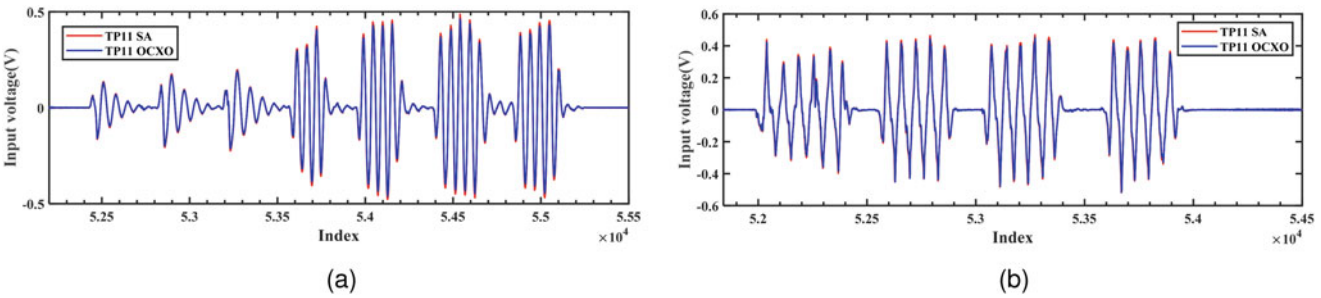

Fig. 7.11 OCXO-based (blue line) and SA-based (red line) measured signal after time shifting indicating perfect alignment of the two signals, indicating practically identical signal after the time alignment. (**a**) Swipe 1. (**b**) Swipe 2

The force on both shakers was measured directly by recording their moving mass acceleration. Therefore, all force and response data were measured as acceleration using the same type of accelerometers and OCXO-based data loggers. The wired part of the hybrid system used the SA to generate the excitation signal for the shakers and to provide in situ single point accelerance FRF data monitoring. This is not possible using the OCXO data that are suitable only for offline post-processing after the test [3]. Since the OCXO- and SA-based data acquisition systems are separate and used in parallel, they have their independent time clocks and different triggers acquiring the same data, as shown in Fig. 7.9.

To enable informed offline time synchronisation between the SA- and OCXO-acquired structural excitation and response data, the delay between the two measured raw voltage signals of the shakers was calculated by observing difference between two easily identifiable 'events' caused by a manual movement of the shaker masses, which was recorded by both SA- and OCXO-based systems (see Fig. 7.9). After that, the time shift between the two signals was easy to calculate. Figures 7.10 and 7.11 show the initial signal misalignment and subsequent perfect alignment indicating that the resulting SA- and OCXO-based measurements were practically identical.

Figure 7.12 shows the total input force for the two 'swipes' after the signal scaling to appropriate physical units. The peak of the total random force (combined synchronous action of both shakers) was approximately 200 N. The SA- and

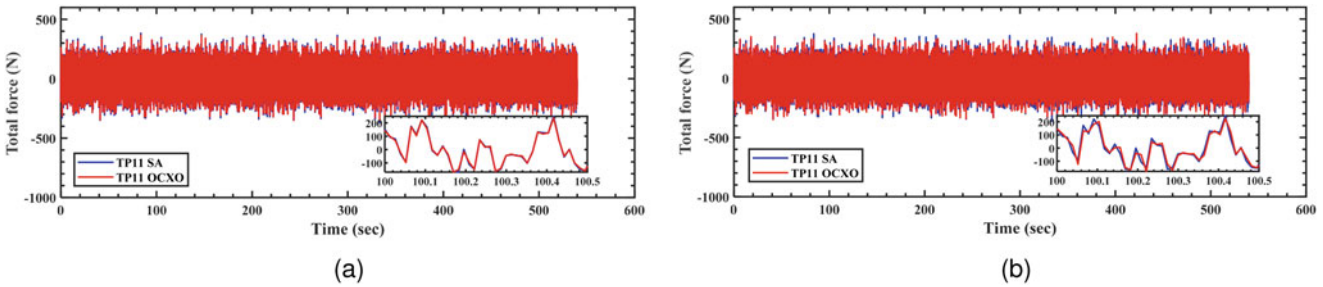

Fig. 7.12 Total force time history with respect to time after unit calibration. (**a**) Swipe 1. (**b**) Swipe 2

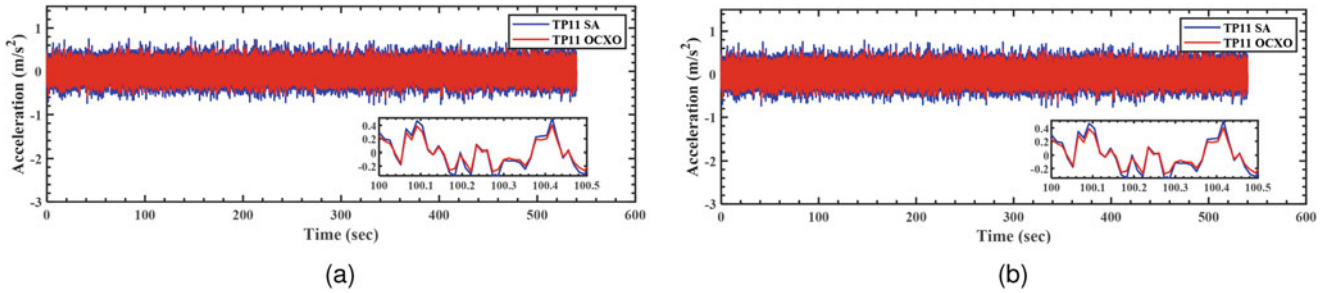

Fig. 7.13 TP11 acceleration time history with respect to time after unit calibration. (**a**) Swipe 1. (**b**) Swipe 2

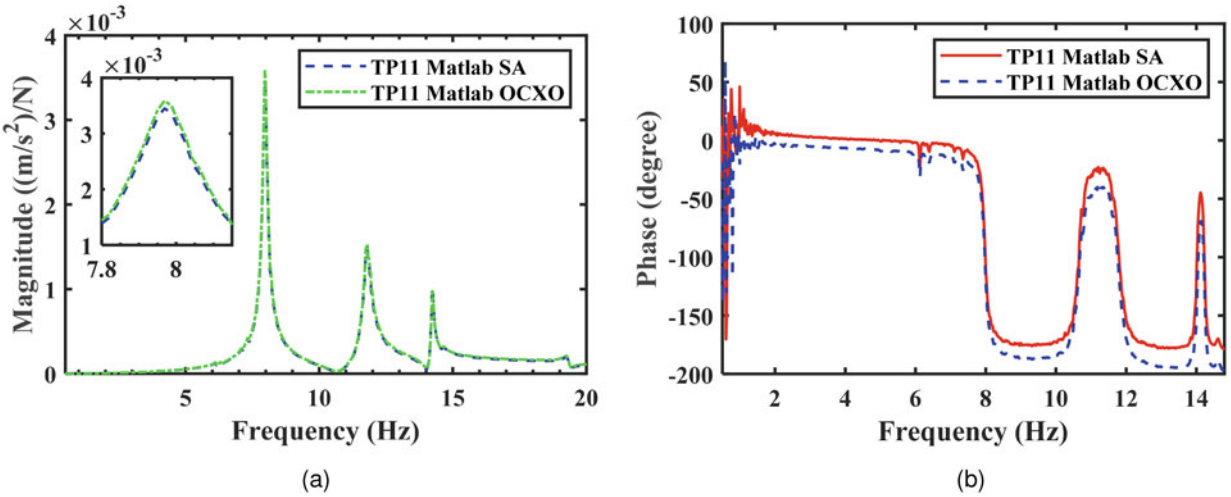

Fig. 7.14 TP11 FRF curve of swipe 1. (**a**) FRF magnitude. (**b**) FRF phase

OCXO-based systems produced practically identical measurements from both shakers forking together. Figure 7.13 shows the corresponding horizontal acceleration response at TP11 measured in the x-direction. The scaled results also gave indicate practically identical measurements of the corresponding accelerations reaching a magnitude of 0.5 m/s^2 in swipes 1 and 2.

By using the input–output force–acceleration data, the relevant FRFs for of each of the two swipes could be estimated, as shown in Figs. 7.14 and 7.15 for point accelerance FRF at TP11. The FRF calculation was based on 75% overlap and 100 averages with the Hanning window applied on each 53.33 s long data block. It can be seen that the FRFs are almost identical for the wired (SA) and wireless (OCXO) systems and that the FRF data is quite repeatable between the two swipes.

After the experimental FRF estimation, curve fitting was used to estimate the modal properties [4]. The results are shown in Fig. 7.16 and Table 7.1.

The first mode was the lateral swaying mode at 7.9 Hz. The second mode was horizontal ‘twisting’ (torsion) 11.7 Hz. The third mode was a highly complex mode at 14.2 Hz. However, this mode appears in both wireless OCXO- and wired SA-based measurements and is very consistent giving again confidence that the two systems produce practically identical results. Furthermore, Table 7.1 provides a numerical comparison between the estimated modal properties including the Modal

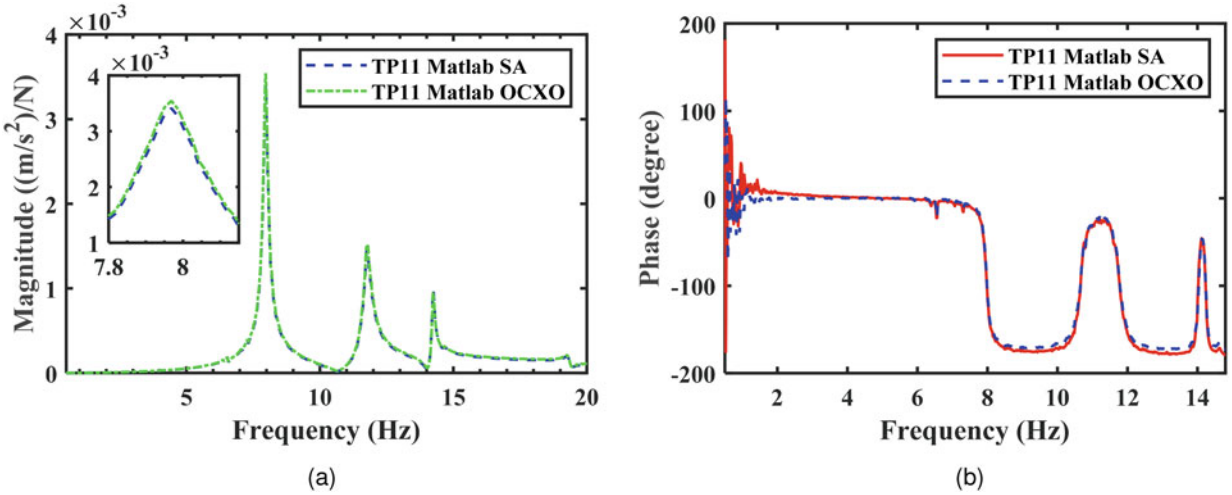

Fig. 7.15 TP11 FRF curve of swipe 2. (**a**) FRF magnitude. (**b**) FRF phase

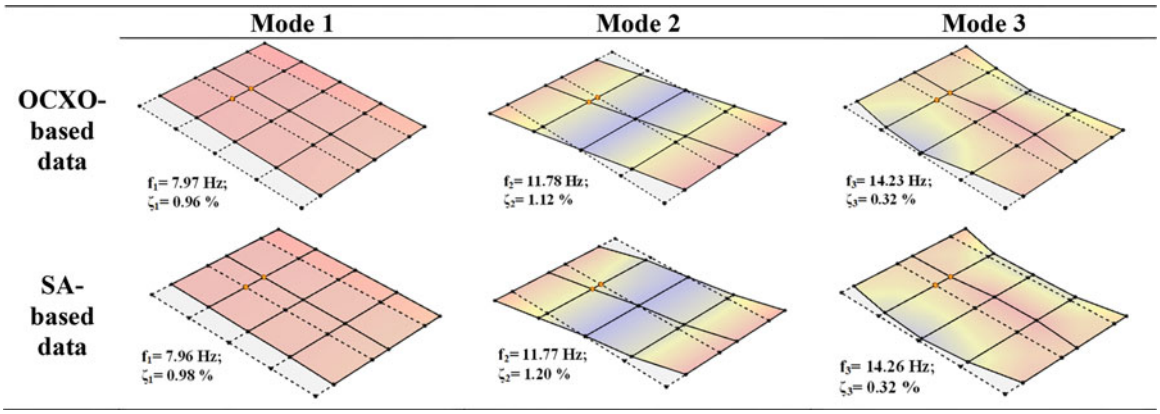

Fig. 7.16 Comparison of mode shapes using OCXO- and SA-based systems

Table 7.1 Comparison of modal properties of OCXO- and SA-based measurements

Mode number	OCXO		Spectrum analyser		Relative error		MAC value
	Modal frequency (Hz)	Modal damping (%)	Modal frequency (Hz)	Modal damping (%)	Frequency (%)	Damping (%)	
1	7.97	0.96	7.96	0.98	0.17	2.25	0.994
2	11.78	1.12	11.77	1.20	0.08	6.29	0.976
3	14.23	0.32	14.26	0.32	0.19	2.91	0.957

Assurance Criterion (MAC) values for comparing the mode shapes estimated using data from both data acquisition systems. The MAC values very close to 1.0 provided additional evidence that both systems provide almost identical mode shapes that are of good and consistent.

7.4 Modal Testing of Fully Operational CLT Building

This section describes the deployment of the hybrid data acquisition in FRF-based modal testing of a full-scale timber building. The test structure is the Yoker building at Clyde Riverfront in Glasgow, UK (Fig. 7.17). The £5.5 m, seven-storey residential building has a T-shape (Fig. 7.17b) with clearly separated (but structurally still connected) northern and southern wings. The residential building is constructed of CLT panels entirely [5] accommodating 42 flats. The building received the Structural Timber Award in 2018. The building is the tallest timber building in Scotland with a total height of 22 m.

Fig. 7.17 Yoker building, Glasgow, UK. (**a**) Photo of Yoker building. (**b**) 3D drawing and tested area

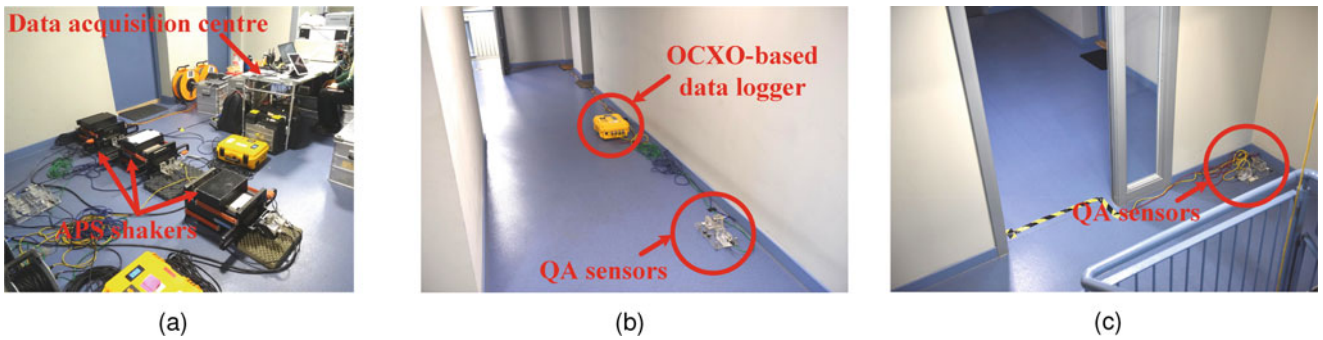

Fig. 7.18 Equipment setup for Yoker building FRF-based modal testing. (**a**) Shakers and data acquisition centre. (**b**) OCXO-based data logger connected with QA sensor. (**c**) QA sensor

The building was completed in 2017 and was fully occupied during the modal testing. To reduce disruption to the occupants, only the communal corridor zone was possible to be used (red coloured in Fig. 7.17b). At the top, a test area was set up housing the shakers and data acquisition centre with majority of cables (Fig. 7.18a). All accelerometers were distributed along the six levels of the test zone. In Fig. 7.17b, the test area is highlighted in red. The test zone was part of the north wing of the building.

Figure 7.18a shows three shakers used to excite the structure on the top floor. Two QA750 accelerometers were attached to each shaker armature using the same setup described in Sect. 7.3.2. The data acquisition centre including the SA, shaker power amplifiers, signal conditioners and control PC was also set up on the top floor and close to the exciters. This was done to minimise the length of the cables/wires from the data acquisition centre (signal conditions, SA and power amplifiers) to the shakers. Figures 7.18b and 7.18c shows an OCXO-based data logger connected to 4 QA750 accelerometers which location and orientation enabled identification of both bending and torsional modes of vibration.

Applying the previously described hybrid modal testing methodology (Sect. 7.3.3), the estimated modal properties are shown in Fig. 7.19. Notably, the first and second modes were close to each other, at 2.85 Hz and 2.93 Hz, respectively, but the FRF-based method had very little difficulty in identifying them. Identifying so clearly such close modes in AVT could be quite problematic. Also, it transpired that, due to the T-shape of the building, the first mode is a combination of torsion and bending. The second mode was bending in the x-direction. The other higher modes are presented in Fig. 7.19. Most interestingly, the methodology had little difficulty in identifying two modes at 8.74 Hz and 9.68 Hz, which are heavily bending in a manner difficult to excite using AVT due to lack of energy at such high frequencies. However, this kind of information can provide a good insight into the stiffness of connections engaged in those bending modes, seldom seen in the standard AVT literature.

The whole 26-channel instrumentation commissioning, modal testing and decommissioning were carried out within a single day by a test crew of only 3 people.

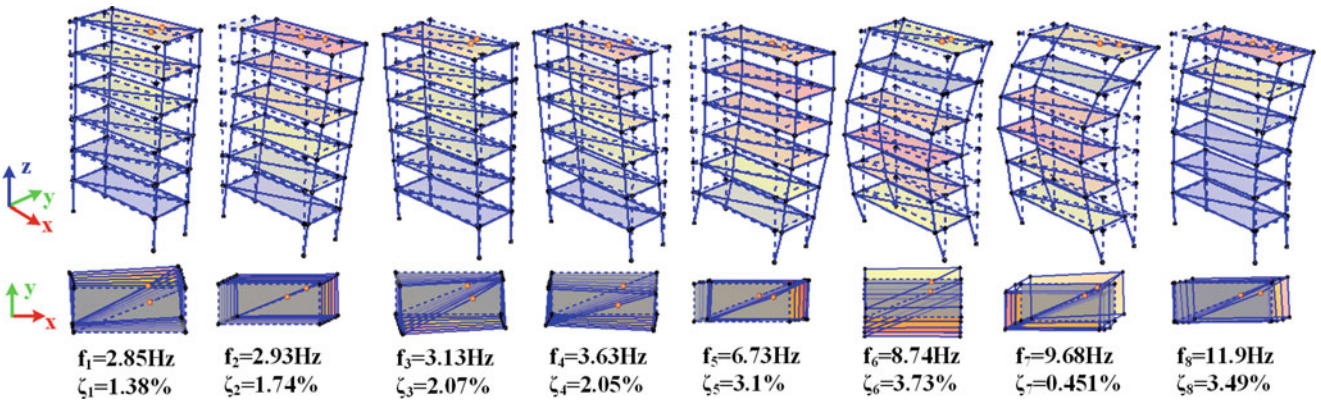

Fig. 7.19 Modal properties of Yoker building

7.5 Discussion and Conclusions

This chapter described a novel OCXO-based data acquisition system that provides a wireless time synchronisation for FRF-based modal testing of sway modes of full-scale buildings in operation, thus decimating the cabling required and enabling high-quality FRF-based modal testing of operational multi-storey buildings, such as residential or office buildings. The methodology was validated successfully using a 15-tonne laboratory-based floor panel structure. The modal testing of this structure using both the OCXO-based 'wireless' and standard multi-channel 'wired' method produced practically identical results.

After the successful laboratory trial, a full-scale timber building was instrumented using the wireless OCXO-based data loggers. These demonstrably facilitated a successfully modal testing of a seven-storey residential building in operation resulting in high-quality FRFs acquired and demonstrably good quality of modal estimates of the fundamental and higher modes of vibration, seldom seen in AVT-based modal testing. Equally important is the fact that the whole 26-channel instrumentation commissioning, modal testing and decommissioning were carried out within a single day by a test crew of only three people.

Acknowledgments The authors would like to acknowledge the financial support of the EU and UK Forestry Commission funded project The Dynamic Response of Tall Timber Buildings under Service Load (Dyna-TTB) supported under the umbrella of ERA-NET Cofund ForestValue.

References

1. Brownjohn, J.M.W., Au, S.-K., Zhu, Y., Sun, Z., Li, B., Bassitt, J., Hudson, E., Sun, H.: Bayesian operational modal analysis of Jiangyin Yangtze River Bridge. Mech. Syst. Signal Process. **110**, 210–230 (2018)
2. Hudson, E.J., Reynolds, P.: Design and construction of a reconfigurable pedestrian structure. Experimental Techniques: A Publication for the Practicing Engineer, 2006
3. Ao, W.K., Pavic, A.: FRF-based modal testing of horizontally swaying structures using OCXO synchronised wireless accelerometers for simultaneous force and vibration responses measurements. In: EURODYN 2020 XI International Conference on Structural Dynamics, Athens, 23–25 November, 2020
4. Ewins, D.: Modal Testing Theory and Practice. Research Studies Press LTD, Taunton (1984)
5. Brandner, R., Flatscher, G., Ringhofer, A., Schickhofer, G., Thiel, A.: Cross laminated timber (CLT): overview and development. Eur. J. Wood Wood Prod. **3**, 331–351 (2016)

Chapter 8
Empirical Fourier Decomposition for Time-Domain Signal Decomposition

Wei Zhou, Zhongren Feng, Y. F. Xu, Xiongjiang Wang, and Hao Lv

Abstract Signal decomposition is an effective tool to assist the identification of modal information in time-domain signals. Two signal decomposition methods, including the empirical wavelet transform (EWT) and Fourier decomposition method (FDM), have been developed based on Fourier theory. However, the EWT can suffer from a mode mixing problem for signals with closely spaced modes, and decomposition results by FDM can suffer from an inconsistency problem. An accurate adaptive signal decomposition method, called the empirical Fourier decomposition (EFD), is proposed to solve the problems in this work. The proposed EFD combines the uses of an improved Fourier spectrum segmentation technique and an ideal filter bank. The segmentation technique can solve the inconsistency problem by predefining the number of modes in a signal to be decomposed, and filter functions in the ideal filter bank have no transition phases, which can solve the mode mixing problem. A numerical investigation is conducted to study the accuracy of the EFD. It is shown that the EFD can yield an accurate and consistent decomposition result for a signal with closely spaced modes, compared with decomposition results by the EWT, FDM, variational mode decomposition, and empirical mode decomposition.

Keywords Signal decomposition · Empirical Fourier decomposition · Empirical wavelet transform · Fourier decomposition method · Ideal filter bank

8.1 Introduction

Signal decomposition is a widely used numerical tool in different fields, such as biomedical signal analysis [1], seismic signal analysis [2], mechanical vibration signal analysis [3, 4], and speech enhancement [5]. Time-domain signals that derive from a physical system usually comprise several superposed components, which are referred to as modes [6], and the modes can encompass meaningful frequency-domain information of the signals, i.e., modal information. Hence, it is crucial to obtain signal decomposition results with high accuracy and efficiency.

In the past few decades, several signal decomposition methods have been developed, and the empirical mode decomposition (EMD)[7] is one of the most significant methods, even though its mathematical understanding is limited and it has some known shortcomings, such as robustness of mode mixing [8] and end effects [9]. Improved versions of the EMD have been developed to overcome the shortcomings. The ensemble EMD [10] has been developed by adding white noise with finite

W. Zhou
School of Civil Engineering and Architecture, Wuhan University of Technology, Wuhan, P.R. China

Department of Mechanical and Materials Engineering, University of Cincinnati, Cincinnati, OH, USA
e-mail: weizhou@mail.uc.edu

Z. Feng
School of Civil Engineering and Architecture, Wuhan University of Technology, Wuhan, P.R. China

School of Urban Construction, Wuchang Shouyi University, Wuhan, P.R. China
e-mail: fengz515@163.com

Y. F. Xu (✉)
Department of Mechanical and Materials Engineering, University of Cincinnati, Cincinnati, OH, USA
e-mail: xu2yf@uc.edu

X. Wang · H. Lv
School of Civil Engineering and Architecture, Wuhan University of Technology, Wuhan, P.R. China
e-mail: wangxiongjiang@whut.edu.cn; liberty.hunter@whut.edu.cn

B. J. Dilworth, M. Mains (eds.), *Topics in Modal Analysis & Testing, Volume 8*, Conference Proceedings of the Society for Experimental Mechanics Series, https://doi.org/10.1007/978-3-030-75996-4_8

amplitudes to alleviate the problems of mode mixing and end effects. The complete ensemble EMD [11] was developed to further improve the EMD by adding completeness and a full data-driven number of modes, which are missing in the ensemble EMD. Li et al. presented a time-varying filter technique to solve the mode mixing problem [12]. However, these EMD methods cannot fundamentally solve the problems of mode mixing and end effects. The variational mode decomposition (VMD) [13] is a non-recursive signal decomposition method, which was developed based on a generalization of Wiener filters. However, the VMD can fail for non-stationary time-domain signals with chirp modes that have overlapping frequency ranges. To avoid this potential failure, McNeill [14] proposed the use of an optimized objective function with constraints on short-time narrowband modes, and Chen et al. [15] exploited a complete variational framework to generalize the VMD. The empirical wavelet transform (EWT) employs an adaptive wavelet filter bank based on segments of Fourier spectra [16]. The workability of the EWT has been improved in Refs. [17–19] to eliminate its requirement for a high signal-to-noise ratio in a signal to be decomposed. However, transition phases between filter functions in a wavelet filter bank in the EWT can lead to the model mixing problem for signals with closely spaced modes. Besides, the first decomposed mode by the EWT can correspond to a trivial residual, with which the number of segments is not equal to that of decomposed modes. Fourier decomposition method (FDM) [20] is an adaptive non-stationary, nonlinear signal decomposition method that can decompose a zero-mean signal into a set of Fourier intrinsic band functions (FIBFs) based on Fourier theory and Hilbert transform. Several limitations of the FDM have been identified. To obtain a FIBF, two frequency scan techniques were developed. One is called the low-to-high (LTH) technique and the other is high-to-low (HTL) technique. The LTH and HTL techniques recursively estimate upper and lower bounds of FIBFs, respectively. However, decomposition results by the FDM with the two frequency scan techniques, i.e., FDM-HTL and FDM-LTH, can be inconsistent, and one cannot determine which decomposition results are correct. Furthermore, the two frequency scan techniques are both iterative and can require long computation times for FDM.

In this work, the EWT and the FDM are briefly reviewed: the segmentation technique and the construction of a wavelet filter bank in the EWT are described, and the construction of FIBFs and the two frequency scan techniques of the FDM are described. A new adaptive signal decomposition method, called the empirical Fourier decomposition (EFD), is proposed to solve the aforementioned problems of the EWT and FDM. The EFD combines an improved segmentation technique and an ideal filter bank [21]. The improved segmentation technique has an adaptive sorting process to yield segmentation results that are less adversely affected by noise and contains meaningful modal information, and the ideal filter bank, whose filter functions have no transition phases, facilitates accurate decomposition for signals with closely spaced modes. A numerical investigation is conducted to study the accuracy of decomposition result by the EFD for a signal with closely spaced modes by comparing with decomposition results by the EMD, VMD, EWT, and FDM.

The remnant of this chapter is arranged as follows. In Sect. 8.2, the EWT and FDM are briefly reviewed. In Sect. 8.3, the proposed EFD is described. In Sect. 8.4, the numerical investigation is presented. Conclusions and some discussions on future works are presented in Sect. 8.5.

8.2 Reviews of EWT and FDM

8.2.1 EWT

The EWT employs an adaptive wavelet transform algorithm based on segments of Fourier spectra [16]. The two most important steps of the EWT are (1) the use of an adaptive segmentation technique to divide Fourier spectrum of a signal to be decomposed and (2) the construction of a wavelet filter bank [22]. Assume that the spectrum is defined on a normalized frequency range $[-\pi, \pi]$. The segmentation technique and wavelet filter bank for the spectrum in the frequency range $[0, \pi]$ are described below, and those for the spectrum in the frequency range $[-\pi, 0]$ can be deduced based on Hermitian symmetry of Fourier spectrum in the normalized frequency range $[-\pi, \pi]$.

One segmentation technique for the EWT is the local maxima technique [16], in which the spectrum in $[0, \pi]$ is divided into N contiguous frequency segments. Each segment is denoted by $S_n = [\omega_{n-1}, \omega_n]$ with $n \in [1, N]$, $\omega_0 = 0$ and $\omega_N = \pi$. To determine the values of ω_n, the first $N-1$ largest local maxima of the spectrum magnitude are identified. The frequencies that uniquely correspond to the identified maxima are reindexed in descending order and denoted by $[\Omega_1, \Omega_2, \ldots \Omega_{N-1}]$ such that $\Omega_1 < \Omega_2 < \cdots < \Omega_{N-1}$; in addition, $\Omega_0 = 0$ is defined. The value of ω_n is expressed by

$$\omega_n = \frac{\Omega_{n-1} + \Omega_n}{2}, n \in [1, N-1] \tag{8.1}$$

which concludes the local maxima technique. As an alternative to the local maxima technique, the lowest minima technique [23] was developed for the EWT: the spectrum division and frequency reindexing procedures, which are the same as those in the local maxima technique, are first carried out. Then, the minimum of the spectrum magnitude in the frequency range $[\Omega_{n-1}, \Omega_n]$ is identified, and the value of ω_n is determined by

$$\omega_n = \arg\min_{\omega} X_n(\omega), \tag{8.2}$$

where $X_n(\omega)$ denotes spectrum magnitudes in $[\Omega_{n-1}, \Omega_n]$ and $\arg\min(\cdot)$ denotes argument of the minimum, respectively, which concludes the lowest minima technique.

The wavelet filter bank is then constructed, and it consists of an empirical scaling function $\hat{\phi}_1(\omega)$ and a series of empirical wavelet functions $\hat{\psi}_n(\omega)$, which are expressed by

$$\hat{\phi}_1(\omega) = \begin{cases} 1 & \text{if} |\omega| \leq \omega_1 - \tau_1 \\ \cos\left[\frac{\pi}{2}\beta\left(\frac{1}{2\tau_1}\left(\tau_1 + |\omega| - \omega_1\right)\right)\right] & \text{if} \omega_1 - \tau_1 \leq |\omega| \leq \omega_1 + \tau_1 \\ 0 & \text{otherwise} \end{cases} \tag{8.3}$$

and

$$\psi_n(\omega) = \begin{cases} 1 & \text{if} \omega_n + \tau_n \leq |\omega| \leq \omega_{n+1} - \tau_{n+1} \\ \cos\left[\frac{\pi}{2}\beta\left(\frac{1}{2\tau_{n+1}}\left(\tau_{n+1} + |\omega| - \omega_{n+1}\right)\right)\right] & \text{if} \omega_{n+1} - \tau_{n+1} \leq |\omega| \leq \omega_{n+1} + \tau_{n+1} \\ \sin\left[\frac{\pi}{2}\beta\left(\frac{1}{2\tau_n}\left(\tau_n + |\omega| - \omega_n\right)\right)\right] & \text{if} \omega_n - \tau_n \leq |\omega| \leq \omega_n + \tau_n \\ 0 & \text{otherwise} \end{cases} \tag{8.4}$$

in which, respectively, $\hat{\cdot}$ denotes Fourier transform of a function, ω the circular frequency, β an arbitrary function, and τ_n a parameter that determines the size of the transition phase [16] associated with the nth and $(n+1)$th segments; the transition phase ranges in $[\omega_n - \tau_n, \omega_n + \tau_n]$. One of the most used forms of β in Eqs. (8.3) and (8.4) with a variable x is [22]

$$\beta(x) = \begin{cases} 0 & \text{if} x \leq 0 \\ x^4(35 - 84x + 70x^2 - 20x^3) & \text{if} 0 < x < 1 \\ 1 & \text{if} x \geq 1 \end{cases} \tag{8.5}$$

The parameter τ_n is calculated by

$$\tau_n = \gamma \omega_n \tag{8.6}$$

where γ is a sufficiently small parameter, so that it can prevent overlapping between boundaries of nonzero $\hat{\phi}_1(\omega)$ and $\hat{\psi}_n(\omega)$. A criterion for an acceptable value of γ is

$$\gamma < \min_n \left(\frac{\omega_{n+1} - \omega_n}{\omega_{n+1} + \omega_n}\right) \tag{8.7}$$

for all n values, and its value can be determined by

$$\gamma = \left(\frac{R-1}{R}\right) \min_n \left(\frac{\omega_{n+1} - \omega_n}{\omega_{n+1} + \omega_n}\right) \tag{8.8}$$

where R is the number of discrete data in the signal to be decomposed. The determination of $\hat{\phi}_1(\omega)$ and $\hat{\psi}_n(\omega)$ concludes the construction of the wavelet filter bank. Graphical illustrations of $\hat{\phi}_1(\omega)$ and $\hat{\psi}_n(\omega)$ are shown in Fig. 8.1a and b, respectively.

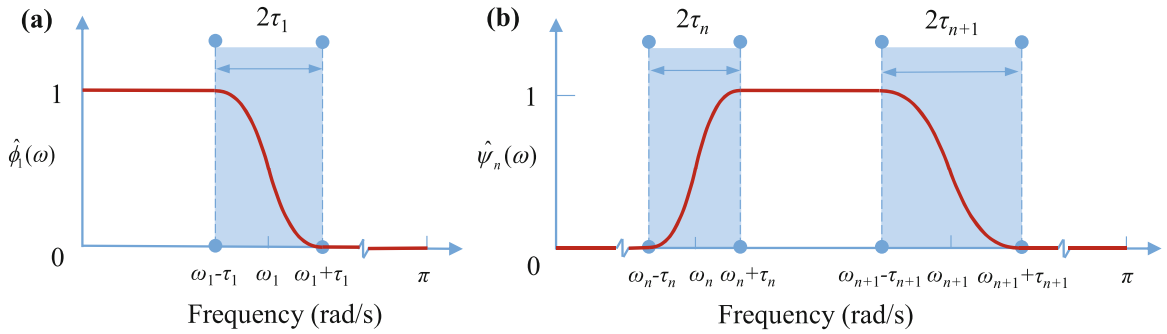

Fig. 8.1 Graphical illustrations of (**a**) $\hat{\phi}_1(\omega)$ and (**b**) $\hat{\psi}_n(\omega)$. Shaded parts are transition phases

After applying a segmentation technique and constructing a filter bank, a decomposed signal can be reconstructed as

$$\tilde{f}(t) = W_f^{\varepsilon}(0,t) * \phi_1(t) + \sum_{n=1}^{N-1} W_f^{\varepsilon}(n,t) * \psi_n(t) \tag{8.9}$$

where the asterisk $*$ denotes the convolution of two functions, and $W_f^{\varepsilon}(0,t)$ and $W_f^{\varepsilon}(n,t)$ are called the approximation coefficient function and detail coefficient function, respectively. The function $W_f^{\varepsilon}(0,t)$ is expressed by

$$\begin{aligned} W_f^{\varepsilon}(0,t) &= F^{-1}(\hat{f}(\omega)\hat{\phi}_1(\omega)) \\ &= \int_{-\omega_1-\tau_1}^{\omega_1+\tau_1} f(\tau)\bar{\phi}_1(\tau - t)\mathrm{d}\tau \end{aligned} \tag{8.10}$$

where the overbar denotes complex conjugation and F^{-1} denotes the inverse Fourier transform of a function. Note that $F^{-1}(\hat{\phi}_1(\omega)) = \phi_1(t)$ and $F^{-1}(\hat{\psi}_n(\omega)) = \psi_n(t)$. The function $W_f^{\varepsilon}(n,t)$ is expressed by

$$\begin{aligned} W_f^{\varepsilon}(n,t) &= F^{-1}(\hat{f}(\omega)\hat{\psi}_n(\omega)) \\ &= \int_{-\omega_{n+1}-\tau_{n+1}}^{\tau_n-\omega_n} f(\tau)\bar{\psi}_n(\tau - t)\mathrm{d}\tau + \int_{\omega_n-\tau_n}^{\omega_{n+1}+\tau_{n+1}} f(\tau)\bar{\psi}_n(\tau - t)\mathrm{d}\tau \end{aligned} \tag{8.11}$$

Resulting decomposed components of the signal can be expressed by

$$f_0(t) = W_f^{\varepsilon}(0,t) * \phi_1(t) \tag{8.12}$$

and

$$f_n(t) = W_f^{\varepsilon}(n,t) * \psi_n(t) \tag{8.13}$$

A step-by-step description of the EWT for a signal $f(t)$ is provided as follows:

Step 1. Obtain a Fourier spectrum of $f(t)$ using Fourier transform.
Step 2. Segment the spectrum in Step 1 using a segmentation technique, such as the local maxima technique and the lowest minimum technique.
Step 3. Construct a wavelet filter bank based on the frequency segments in Step 2.
Step 4. Express approximation and detail coefficient functions based on the wavelet filter bank in Step 3.
Step 5. Decompose $f(t)$ and reconstruct it using Eq. (8.9).

The EWT can yield accurate decomposition results when $f(t)$ does not have closely spaced modes. However, when $f(t)$ has closely spaced modes, a mode mixing problem can occur due to the transition phase, and the problem can become more serious when the closely spaced modes exist in high frequencies as τ_n in Eq. (8.6) becomes larger for higher frequencies.

8.2.2 FDM

Assume that $f(u)$ is a zero-mean, discrete, and length-limited signal within one period U, which is an even integer; the fundamental frequency of $f(u)$ can be expressed by

$$\varphi_0 = \frac{2\pi}{U} \tag{8.14}$$

In the FDM, $f(u)$ is approximated by a summation of K orthogonal FIBFs $g_k(u)$ [20]:

$$f(u) = \sum_{k=1}^{K} g_k(u) \tag{8.15}$$

Based on Eq. (8.15), the analytical signal of $f(u)$ can be expressed by [24]

$$\begin{aligned} z(u) &= f(u) + \mathrm{j}H(f(u)) \\ &= \sum_{k=1}^{K} \left[g_k(u) + \mathrm{j}H(g_k(u)) \right] \\ &= \sum_{k=1}^{K} z_k(u) \end{aligned} \tag{8.16}$$

where $H(\cdot)$ denotes Hilbert transform of a function, $\mathrm{j} = \sqrt{-1}$, and $z_k(u) = g_k(u) + \mathrm{j}H(g_k(u))$. The term $z_k(u)$ can be considered as the analytical signal corresponding to $g_k(u)$. Note that $z(u)$ can be expressed as Fourier series:

$$z(u) = \sum_{m=1}^{U/2-1} a_m \mathrm{e}^{\mathrm{j}m\varphi_0 u} \tag{8.17}$$

where

$$a_m = \frac{2}{U} \sum_{u=0}^{U-1} f(u) \mathrm{e}^{-\mathrm{j}m\varphi_0 u} \tag{8.18}$$

and values of a_m can be estimated using discrete Fourier transform.

The analytical signal $z_k(u)$ can be considered as a filtered signal by Hilbert transform filter [25], which is the counterpart of a filter in the wavelet filter bank in the EWT, and $z_k(u)$ can be further expressed by

$$z_k(u) = \sum_{m=M_{k-1}+1}^{M_k} a_m \mathrm{e}^{\mathrm{j}m\varphi_0 u} \tag{8.19}$$

where M_k ranges from 1 to $(U/2 - 1)$ with $M_0 = 0$. Determination of values of M_k is similar to the segmentation in the EWT. In the FDM, two frequency scan techniques have been proposed to determine the values of M_k in Eq. (8.19), including the LTH technique and the HTL technique [20]. Flowcharts of the LTH and HTL techniques are shown in Figs. 8.2 and 8.3, respectively. In the LTH technique, K values of M_k are searched in a forward manner so that $M_1 < M_2 < \ldots < M_k \ldots < M_K$, with which

$$z_1(u) = \sum_{m=M_0+1}^{M_1} a_m \mathrm{e}^{\mathrm{j}m\varphi_0 u}$$

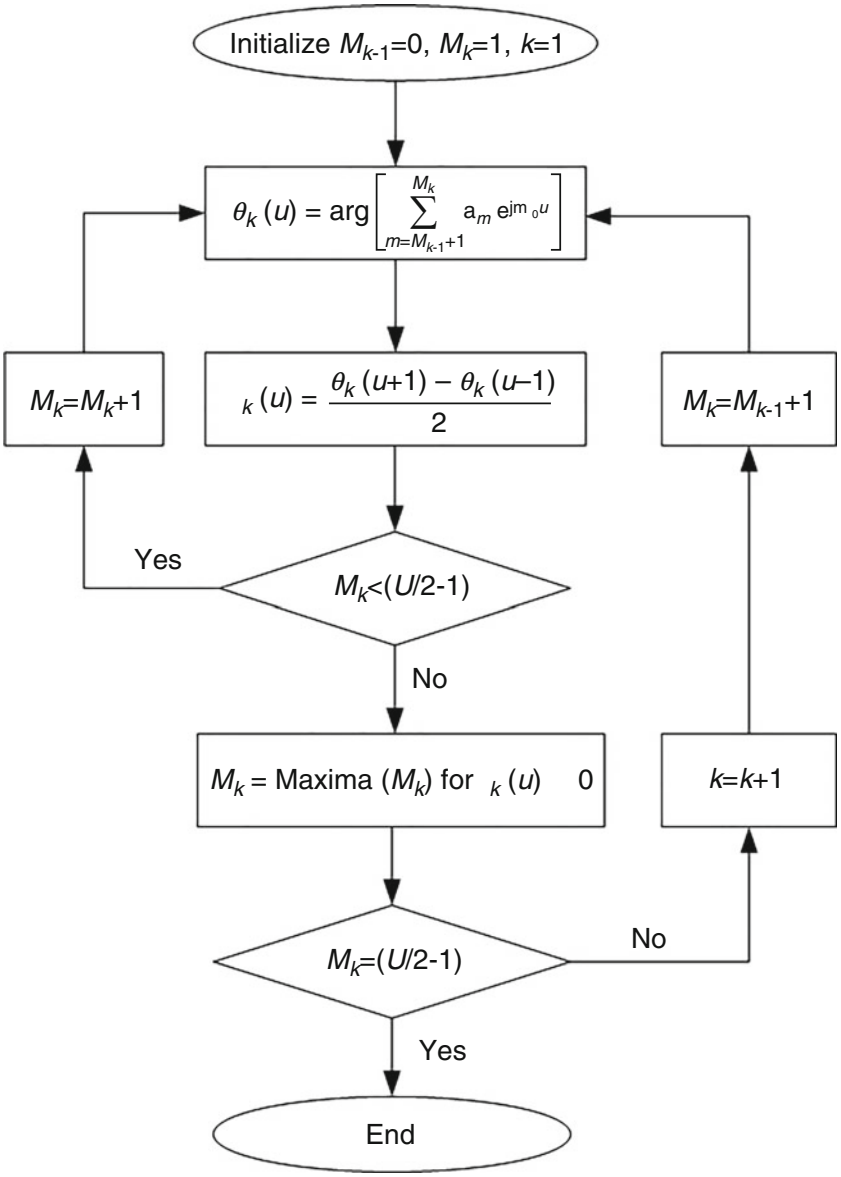

Fig. 8.2 Flowchart of the LTH technique

$$z_2(u) = \sum_{m=M_1+1}^{M_2} a_m e^{jm\varphi_0 u} \tag{8.20}$$

$$\vdots$$

$$z_K(u) = \sum_{m=M_{K-1}+1}^{M_K} a_m e^{jm\varphi_0 u}$$

where $M_0 = 0$ and $M_K = U/2 - 1$. The signal $z_k(u)$ can further be expressed by

$$z_k(u) = A_k(u) e^{j\theta_k(u)} \tag{8.21}$$

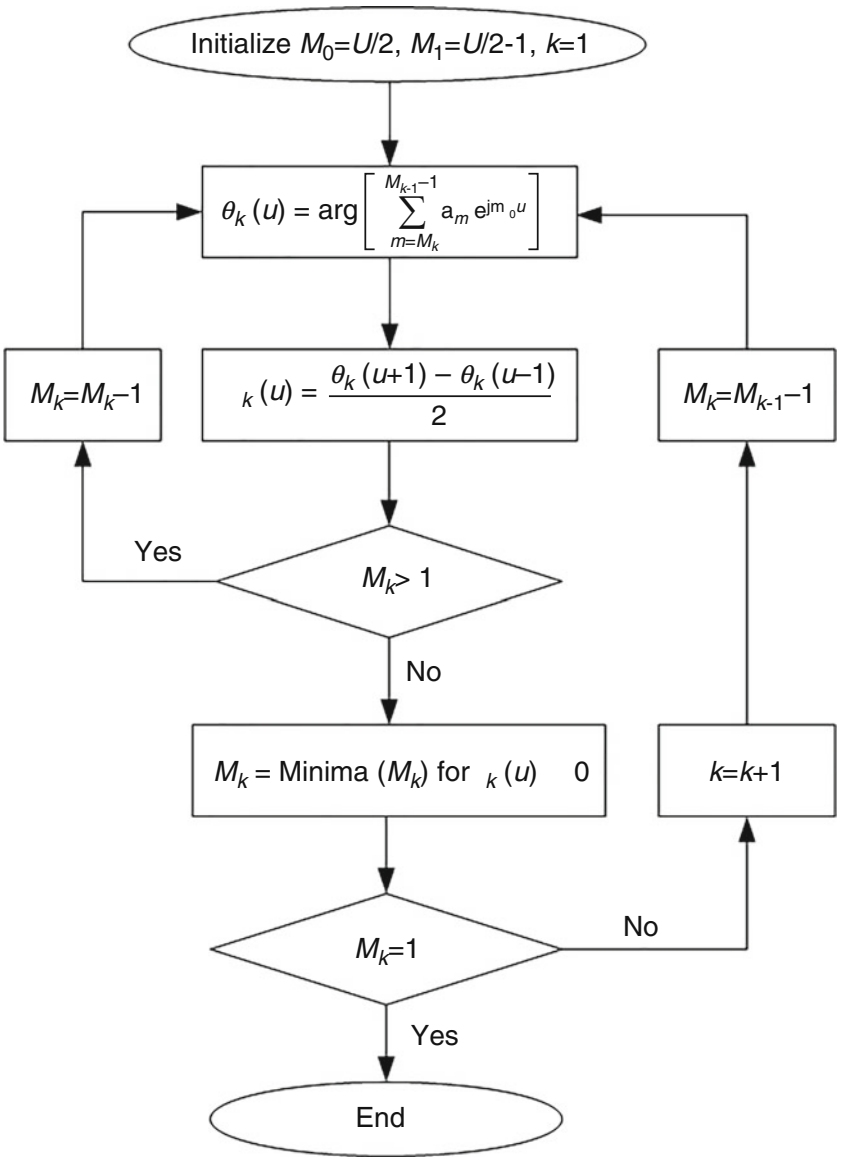

Fig. 8.3 Flowchart of the HTL technique

where

$$A_k(u) = \left\| \sum_{m=M_{k-1}+1}^{M_k} a_m e^{jm\varphi_0 u} \right\|_2 \tag{8.22}$$

and

$$\theta_k(u) = \arg\left[\sum_{m=M_{k-1}+1}^{M_k} a_m e^{jm\varphi_0 u} \right] \tag{8.23}$$

denote instantaneous amplitude and phase of $z_k(u)$, respectively, in which $\|\cdot\|_2$ and $\arg(\cdot)$ calculate Euclidean norm and argument of a complex quantity, respectively. The FIBFs $g_k(u)$ can be obtained by

$$g_k(u) = \mathrm{Re}\left[A_k(u) e^{j\theta_k(u)} \right] \tag{8.24}$$

where Re(·) is the real part of a function. In the HTL technique, K values of M_k are searched in a backward manner so that $M_K < \ldots M_k < M_{k-1} < \ldots < M_1$, with which

$$\begin{aligned} z_1(u) &= \sum_{m=M_1}^{M_0-1} a_m e^{jm\varphi_0 u} \\ z_2(u) &= \sum_{m=M_2}^{M_1-1} a_m e^{jm\varphi_0 u} \\ &\vdots \\ z_K(u) &= \sum_{m=M_K}^{M_{K-1}-1} a_m e^{jm\varphi_0 u} \end{aligned} \tag{8.25}$$

where $M_0 = U/2$ and $M_K = 1$.

A step-by-step description of the FDM for $f(u)$ is as follows:

Step 1. Obtain a Fourier spectrum of $f(u)$ using Fourier transform.
Step 2. Express $z(u)$ using the spectrum of $f(u)$ obtained in Step 1.
Step 3. Obtain K $z_k(u)$ using the LTH or HTL technique.
Step 4. Obtain FIBFs $g_k(u)$ from the real part of $z_k(u)$ obtained in Step 3.
Step 5. Reconstruct $f(u)$ as a summation of FIBFs $g_k(u)$ obtained in Step 4.

An issue of the FDM is that its decomposition results using the LTH technique can be inconsistent with those using the HTL technique, and the issue will be verified in the numerical investigation in Sect. 8.4.

8.3 EFD

Similar to the EWT and FDM, the EFD consists of two critical steps: an improved segmentation technique and a construction of an ideal filter bank. In the EFD, Fourier spectrum of a signal to be decomposed is defined on a normalized frequency range $[-\pi, \pi]$, and the improved segmentation technique and the construction of an ideal filter bank for the spectrum in the frequency range $[0, \pi]$ are described below.

8.3.1 Improved Segmentation Technique

The improved segmentation technique is proposed based on the lowest minima technique [23] described in Sect. 8.2.1. In the improved segmentation technique, $[0, \pi]$ is divided into N contiguous frequency segments. Unlike the local maxima and lowest minima techniques, ω_0 and ω_N are not necessarily equal to 0 and π, respectively, and their values are determined in an adaptive sorting process. In the sorting process, Fourier spectrum magnitudes at $\omega = 0$ and $\omega = \pi$ and their local maxima are identified and extracted to a series. All magnitudes in the series are sorted in descending order. Frequencies corresponding to the first N largest values in the sorted series are denoted by $[\Omega_1, \Omega_2, \ldots \Omega_N]$. In addition, $\Omega_0 = 0$ and $\Omega_{N+1} = \pi$ are defined. Boundaries of each segment are determined by

$$\omega_n = \begin{cases} \arg\min_{\omega} \check{X}_n(\omega) & \text{if} 0 \le n \le N \text{and} \Omega_n \ne \Omega_{n+1} \\ \Omega_n & \text{if} 0 \le n \le N \text{and} \Omega_n = \Omega_{n+1} \end{cases} \tag{8.26}$$

where $\check{X}_n(\omega)$ denotes the Fourier spectrum magnitudes between Ω_n and Ω_{n+1}, which concludes the improved segmentation technique.

8.3.2 Construction of an Ideal Filter Bank

Both the EWT and FDM consist of a step of constructing a filter bank. In the EWT, a wavelet filter bank is formed by the empirical scaling function and wavelet functions. In the FDM, Hilbert transform filter bank is constructed based on Fourier spectrum of the analytical signal associated with a signal to be decomposed. In the EFD, an ideal filter bank is constructed based on frequency segments obtained by the improved segmentation technique. In each frequency segment, the ideal filter is a band-pass filter with ω_{n-1} and ω_n serving as its cut-off frequencies and it has not transition phases. Hence, the ideal filter can retain the major Fourier spectrum component in the segment, and all other Fourier spectrum components beyond the segment are excluded.

Fourier transform of a signal to be decomposed $f(t)$ is expressed as

$$\hat{f}(\omega) = \int_{-\infty}^{\infty} f(t) \mathrm{e}^{-\mathrm{j}\omega t} \mathrm{d}t \tag{8.27}$$

An ideal filter bank can be constructed by $\hat{\mu}_n(\omega)$:

$$\hat{\mu}_n(\omega) = \begin{cases} 1 & \text{if} \omega_{\mathrm{n}-1} \leq \mid \omega \mid \leq \omega_{\mathrm{n}} \\ 0 & \text{otherwise} \end{cases} \tag{8.28}$$

where $1 \leq n \leq N$ and the values of ω_n are determined by Eq. (8.26). A graphical illustration of the ideal filter bank is shown in Fig. 8.4.

Filtered signals that correspond to $\hat{\mu}_n(\omega)$ are calculated by

$$\hat{f}_n(\omega) = \hat{\mu}_n(\omega)\hat{f}(\omega) = \begin{cases} \hat{f}(\omega) & \text{if} \omega_{\mathrm{n}-1} \leq \mid \omega \mid \leq \omega_{\mathrm{n}} \\ 0 & \text{otherwise} \end{cases} \tag{8.29}$$

Decomposed components in the time domain can be obtained using the inverse Fourier transform:

$$\begin{aligned} f_n(t) &= F^{-1}\left[\hat{f}_n(\omega)\right] = \int_{-\infty}^{\infty} \hat{f}_n(\omega) \mathrm{e}^{\mathrm{j}\omega t} \mathrm{d}\omega \\ &= \int_{-\omega_n}^{-\omega_{n-1}} \hat{f}(\omega) \mathrm{e}^{\mathrm{j}\omega t} \mathrm{d}\omega + \int_{\omega_{n-1}}^{\omega_n} \hat{f}(\omega) \mathrm{e}^{\mathrm{j}\omega t} \mathrm{d}\omega \end{aligned} \tag{8.30}$$

The reconstructed signal is calculated as a summation of all decomposed components:

$$\tilde{f}(t) = \sum_{n=1}^{N} f_n(t) \tag{8.31}$$

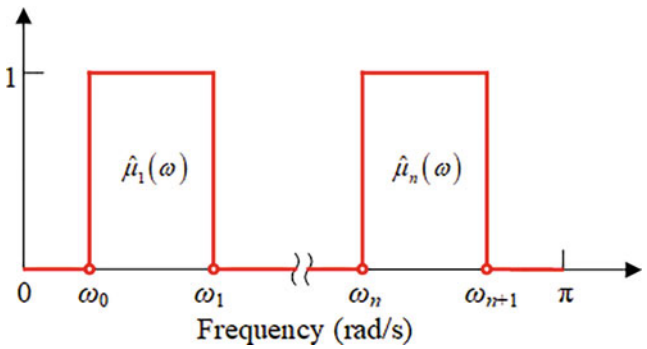

Fig. 8.4 Graphical illustration of an ideal filter bank of the EFD

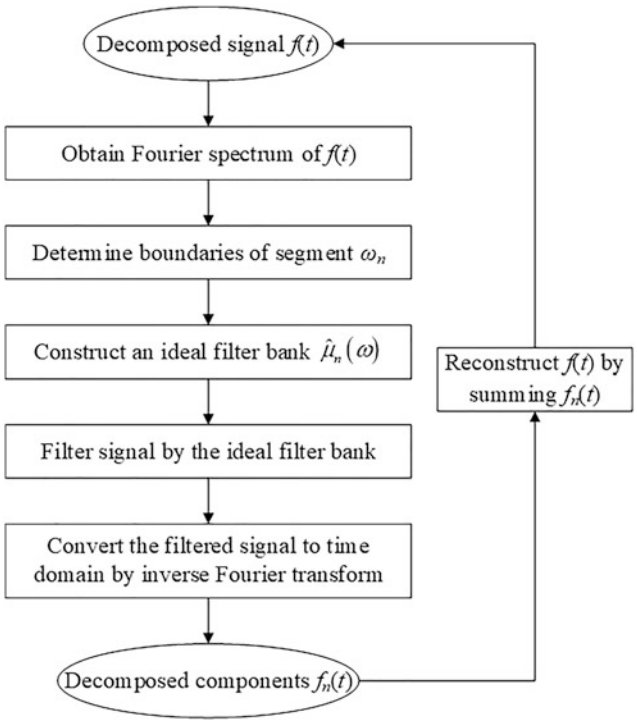

Fig. 8.5 Flowchart of the EFD

A flowchart of the EFD is shown in Fig. 8.5 and a step-by-step description of the EFD is provided as follows:

Step 1. Obtain Fourier spectrum of a signal to be decomposed $f(t)$ using Fourier transform.
Step 2. Determine boundaries of segment ω_n using the improved segmentation technique based on Fourier spectrum obtained in Step 1.
Step 3. Construct an ideal filter bank $\hat{\mu}_n(\omega)$ based on ω_n obtained in Step 2.
Step 4. Obtain filtered signals $\hat{f}_n(\omega)$ in the frequency domain using $\hat{\mu}_n(\omega)$ obtained in Step 3.
Step 5. Obtain decomposed components $f_n(t)$ in the time domain using inverse Fourier transforms of $\hat{f}_n(\omega)$ obtained in Step 4

8.4 Numerical Investigation

In this section, the effectiveness of the proposed EFD method for decomposing signals with closely spaced modes is studied. Decomposition accuracy of the EFD method is compared with that of the EWT [16], FDM [20], VMD [13], and EMD [7] methods.

A stationary signal with two modes [26] denoted by $f_{\mathrm{Sig}}(t)$ is constructed to compare performances of the different decomposition methods for signals with closely spaced modes, which is expressed by

$$\begin{cases} f_{\mathrm{SigC1}}(t) & = \cos(2\pi \mathrm{t}) \\ f_{\mathrm{SigC2}}(t) & = a\cos(2\pi\lambda_{\mathrm{r}}\mathrm{t}) \\ f_{\mathrm{Sig}}(t) & = f_{\mathrm{SigC1}}(t) + f_{\mathrm{SigC2}}(t) \end{cases} \tag{8.32}$$

where a and λ_r denote a ratio between the amplitudes of $f_{\mathrm{SigC2}}(t)$ and $f_{\mathrm{SigC1}}(t)$ and that between the frequencies of $f_{\mathrm{SigC2}}(t)$ and $f_{\mathrm{SigC1}}(t)$, respectively; $0.01 \leq a \leq 100$ and $0.01 \leq \lambda_r \leq 1$. When λ_r approaches to 1, $f_{\mathrm{SigC2}}(t)$ and $f_{\mathrm{SigC1}}(t)$ become closely spaced modes. The signal $f_{\mathrm{Sig}}(t)$ is sampled at a frequency of 10 Hz for 300 s. The EFD, EWT, FDM-LTH, FDM-

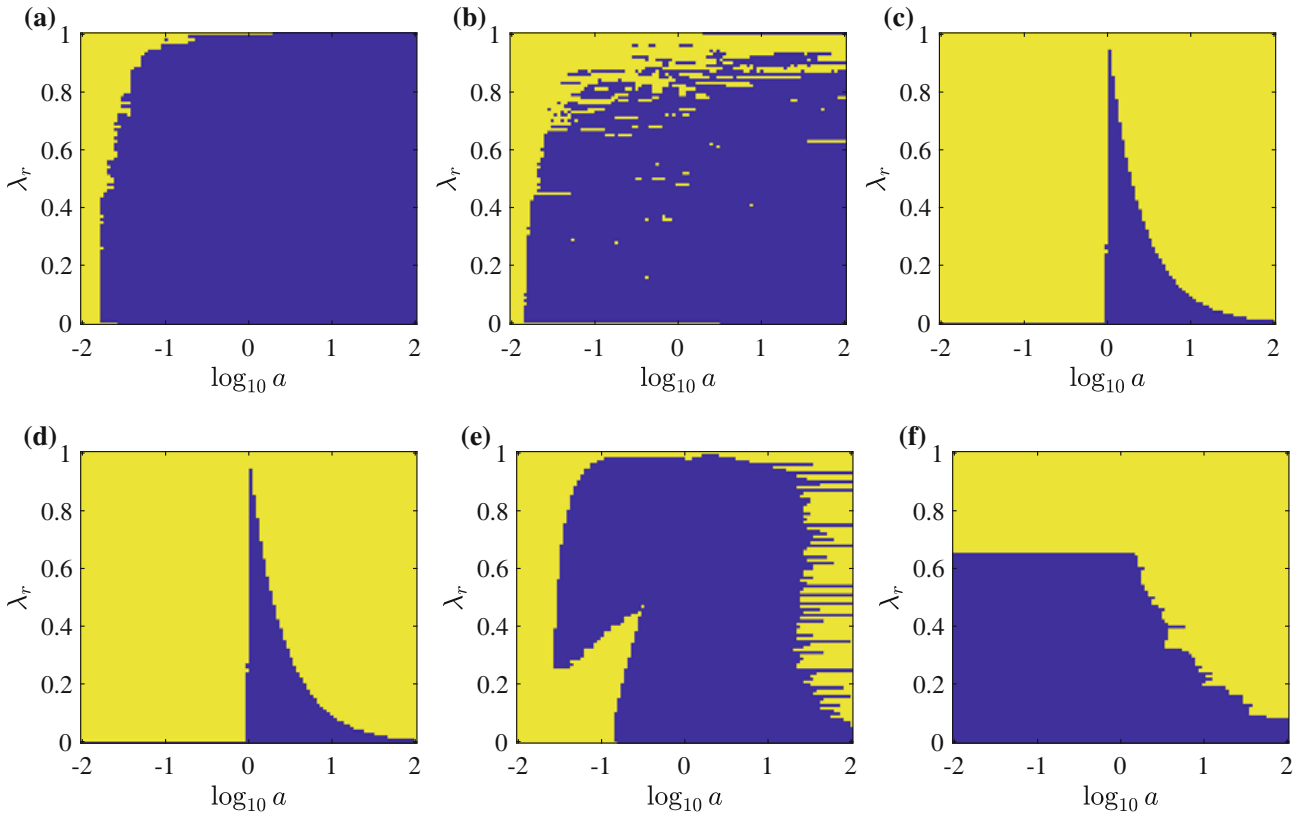

Fig. 8.6 Decomposition performance with respect to (a, λ_r) by the (**a**) EFD, (**b**) EWT, (**c**) FDM-LTH, (**d**) FDM-HTL, (**e**) VMD and (**f**) EMD

HLT, VMD, and EMD are deployed to decompose $f_{\text{Sig}}(t)$. A two-dimensional binary quantity $Q(a, \lambda_r)$ is used to measure the decomposition performance [26] of the different methods for $f_{\text{Sig}}(t)$ with different values of a and λ_r, and it is expressed by

$$Q(a, \lambda_r) = \begin{cases} 0 & \text{if} \frac{\|\text{C1} - f_{\text{SigC1}}\|_2}{\|f_{\text{SigC2}}\|_2} \leq \varepsilon \\ 1 & \text{if} \frac{\|\text{C1} - f_{\text{SigC1}}\|_2}{\|f_{\text{SigC2}}\|_2} > \varepsilon \end{cases} \tag{8.33}$$

where C1 is the decomposed component by a decomposition method corresponding to $f_{\text{SigC1}}(t)$ and ε is the threshold of Q. A zero value and a unit value of Q indicate an acceptable decomposition result and an unacceptable decomposition one, respectively, and the value of ε is chosen to be 0.5 in this study, which was also the cases in Refs. [4, 12, 26]. Resulting $Q(a, \lambda_r)$ corresponding to the six methods are shown in Fig. 8.6, where the colors of blue and yellow correspond to Q values of 0 and 1, respectively. It can be seen that the yellow area corresponding to the EFD is the smallest among the six Q results. Even as λ_r approaches to 1, $f_{\text{Sig}}(t)$ can still be well decomposed. However, the decomposition by the EFD is affected when a approaches to 0.01. Furthermore, the yellow area corresponding to the EWT is the second smallest, but its decomposition performance is affected when a approaches to 0.01 and λ_r is larger than 0.8. The yellow area corresponding to the VMD is the third smallest. Similar to Q corresponding to the EFD, as λ_r approaches to 1, $f_{\text{Sig}}(t)$ can still be well decomposed. However, the decomposition performance associated with the VMD is affected when a is close to 0.01 and 100. The yellow area corresponding to the EMD is the fourth smallest. The EMD cannot decompose $f_{\text{Sig}}(t)$, when λ_r is larger than 0.65 for all a. In addition, worse decomposition results are obtained when a approaches to 100. For the FDM-LTH and FDM-HTL, decomposition performances are almost the same but the worst among the six methods. Their decomposition results are greatly affected by the value of a. They can hardly decompose $f_{\text{Sig}}(t)$, when a is smaller than 1 for $\lambda_r \geq 0.01$. Based on the observations, it is indicated that the EFD can robustly and accurately decompose $f_{\text{Sig}}(t)$ as its decomposition results are the most accurate even when $f_{\text{Sig}}(t)$ becomes a signal with closely spaced modes, and both the FDM-LTH and FDM-HTL can yield inaccurate decomposition results for $f_{\text{Sig}}(t)$.

8.5 Concluding Remarks

In this paper, an accurate and efficient EFD method is proposed to decompose time-domain signals. The EFD consists of two critical steps: the improved segmentation technique and the construction of a filter bank. In the improved segmentation technique, only meaningful Fourier spectrum components are included, and the last segment that can contain noise is narrowed, which can decrease the size of the segment and alleviate adverse effects of noise. In a constructed filter bank, transition phases of filter functions are eliminated, which can improve the decomposition performance for closely spaced modes. A numerical investigation is conducted on a signal with closely spaced modes, it is shown that the EFD can yield a high accuracy and consistency decomposition result for the signal with closely spaced modes, and its decomposition result is more accurate than that by the other decomposition methods. A future work can be an investigation of the applicability of the EFD to signals/data of higher dimensions, such as digital images.

Conflicts of Interest
The authors declare no conflict of interest.

Acknowledgments The author Y.F. Xu is grateful for the financial support from the National Science Foundation through Grant No. CMMI-1762917. The authors gratefully acknowledge valuable discussions with and input from Dr. Gang Yu, Dr. Pushpendra Singh, Dr. Shiqian Chen, and Dr. Heng Li. They also thank people who share their contributions to the signal processing community.

References

1. Bhattacharyya, A., Pachori, R.B.: A multivariate approach for patient-specific EEG seizure detection using empirical wavelet transform. IEEE Trans. Biomed. Eng. **64**(9), 2003–2015 (2017)
2. Li, F., Zhang, B., Verma, S., Marfurt, K.J.: Seismic signal denoising using thresholded variational mode decomposition. Expl. Geophys. **49**(4), 450–461 (2018)
3. Pan, J., Chen, J., Zi, Y., Li, Y., He, Z.: Mono-component feature extraction for mechanical fault diagnosis using modified empirical wavelet transform via data-driven adaptive Fourier spectrum segment. Mech. Syst. Signal Process. **72**, 160–183 (2016)
4. Chen, S., Yang, Y., Peng, Z., Dong, X., Zhang, W., Meng, G.: Adaptive chirp mode pursuit: algorithm and applications. Mech. Syst. Signal Process. **116**, 566–584 (2019)
5. Upadhyay, A., Pachori, R.: Speech enhancement based on mEMD-VMD method. Electron. Lett. **53**(7), 502–504 (2017)
6. Iatsenko, D., McClintock, P.V., Stefanovska, A.: Nonlinear mode decomposition: a noise-robust, adaptive decomposition method. Phys. Rev. E **92**(3), 032916 (2015)
7. Huang, N.E., Shen, Z., Long, S.R., Wu, M.C., Shih, H.H., Zheng, Q., Yen, N.-C., Tung, C.C., Liu, H.H.: The empirical mode decomposition and the Hilbert spectrum for nonlinear and non-stationary time series analysis. Proc. R. Soc. Lond. Ser. A: Math. Phys. Eng. Sci. **454**(1971), 903–995 (1998)
8. Rilling, G., Flandrin, P., Goncalves, P., et al.: On empirical mode decomposition and its algorithms. In: IEEE-EURASIP Workshop on Nonlinear Signal and Image Processing, vol. 3, NSIP-03, Grado (I), pp. 8–11 (2003)
9. Rato, R., Ortigueira, M.D., Batista, A.: On the HHT, its problems, and some solutions. Mech. Syst. Signal Process. **22**(6), 1374–1394 (2008)
10. Wu, Z., Huang, N.E.: Ensemble empirical mode decomposition: a noise-assisted data analysis method. Adv. Adapt. Data Anal. **1**(01), 1–41 (2009)
11. Torres, M.E., Colominas, M.A., Schlotthauer, G., Flandrin, P.: A complete ensemble empirical mode decomposition with adaptive noise. In: 2011 IEEE International Conference on Acoustics, Speech and Signal Processing (ICASSP), pp. 4144–4147. IEEE, New York (2011)
12. Li, H., Li, Z., Mo, W.: A time varying filter approach for empirical mode decomposition. Signal Process. **138**, 146–158 (2017)
13. Dragomiretskiy, K., Zosso, D.: Variational mode decomposition. IEEE Trans. Signal Process. **62**(3), 531–544 (2013)
14. McNeill, S.: Decomposing a signal into short-time narrow-banded modes. J. Sound Vib. **373**, 325–339 (2016)
15. Chen, S., Dong, X., Peng, Z., Zhang, W., Meng, G.: Nonlinear chirp mode decomposition: a variational method. IEEE Trans. Signal Process. **65**(22), 6024–6037 (2017)
16. Gilles, J.: Empirical wavelet transform. IEEE Trans. Signal Process. **61**(16), 3999–4010 (2013)
17. Luo, Z., Liu, T., Yan, S., Qian, M.: Revised empirical wavelet transform based on auto-regressive power spectrum and its application to the mode decomposition of deployable structure. J. Sound Vib. **431**, 70–87 (2018)
18. Xin, Y., Hao, H., Li, J.: Operational modal identification of structures based on improved empirical wavelet transform. Struct. Control Health Monit. **26**(3), e2323 (2019)
19. Amezquita-Sanchez, J.P., Adeli, H.: A new music-empirical wavelet transform methodology for time–frequency analysis of noisy nonlinear and non-stationary signals. Digit. Signal Process. **45**, 55–68 (2015)
20. Singh, P., Joshi, S.D., Patney, R.K., Saha, K.: The Fourier decomposition method for nonlinear and non-stationary time series analysis. Proc. R. Soc. A: Math. Phys. Eng. Sci. **473**(2199), 20160871 (2017)
21. Alan, R.W.S., Oppenheim, V.,: Discrete Time Signal Processing, 3rd edn. Prentice Hall, Hoboken (2009)

22. Daubechies, I.: Ten Lectures on Wavelets. SIAM, Philadelphia (1992)
23. Gilles, J., Tran, G., Osher, S.: 2D empirical transforms. Wavelets, ridgelets, and curvelets revisited. SIAM J. Imag. Sci. **7**(1), 157–186 (2014)
24. Picinbono, B.: On instantaneous amplitude and phase of signals. IEEE Trans. Signal Process. **45**(3), 552–560 (1997)
25. Harris, F.J.: Multirate Signal Processing for Communication Systems. Prentice Hall PTR, Upper Saddle River, NJ (2004)
26. Rilling, G., Flandrin, P.: One or two frequencies? The empirical mode decomposition answers. IEEE Trans. Signal Process. **56**(1), 85–95 (2007)

Chapter 9
Vibration Isolation in 3D Printer Using Meta-Structures

Shantanu H. Chavan and Vijaya V. N. Sriram Malladi

Abstract Reducing vibrations in a 3D printer is crucial in improving the quality of printed prototypes. Ideally, the noise from the actuators in 3D printers should not hinder the print quality. However, isolating the printer surface from vibrations is challenging. Therefore, in this paper, a novel vibration-isolating frame is designed for building a novel 3D printer. Such a structure would absorb external vibrations and isolate the print-plate, thereby improving the print quality.

The proposed frame is a meta-structure that absorbs vibrations over a frequency bandwidth. The structure is built with assembling multiple identical unit cells. Each unit cell is an assembly of 1D beams of varying cross-sections. The current paper's objective is to design a fame that produces in-plane and out-of-plane bandgaps. Finite element models iterate over multiple designs, which are validated in the lab through robust experimentation. The paper discusses the design methodology and the corresponding results.

Keywords Meta-structure frame · Vibration isolation · 3D printer · Bandgaps

9.1 Introduction

3D printers have emerged as one of the most dominating technologies which are used extensively. The poor quality of the 3D prints is a significant problem and vibrations are one of the most prominent reasons for quality degradation. The quality of a 3D print could further be improved if the printer surface is isolated from all the external vibrations.

This paper evaluates if meta-structures are a feasible option in isolating the print bed from ambient vibrations. The ambient vibrations experienced by a Prusa 3D printer were first measured while printing a part. The power spectral densities have shown that there are significant vibrations in the frequency band of 50–108 Hz. Therefore, the aim is to design a meta-structure frame capable of isolating vibrations over this frequency bandwidth.

The frame is a 2D assembly of unit cells in series and parallel. The design of the meta-structural frame is iteratively tuned till the desired bandgap is achieved. For design flexibility, combination of (Poly-lactic acid) PLA 3D prints and aluminum beams of rectangular cross-section ($0.5'' \times 0.25''$) is used. Figure 9.1 shows the design of a single unit cell and the meta-structure made of multiple unit cells. These unit cells are assembled longitudinally such that the total length was equal to the length of the 3D printer base. This structure is tested to validate the finite element modelling. Furthermore, the longitudinal structure is extended laterally to match the width of the 3D printer base to produce the ultimate vibration isolating frame.

9.2 Bandgap Using the 1D Meta-Structure

Given the requirement of the band gap range, we conducted experiments on the proposed meta-structure to assess the position of the band gap. The smart shaker K2007E01 shown in Fig. 9.2 actuates the 1D meta-structure over the frequency range of interest. While the smart shaker is mounted on one end on the meta-structure, the other end is suspended with pre-tensed

S. H. Chavan (✉) · V. V. N. Sriram Malladi
Vibrations, Intelligent Testing and Active Learning of Structures (VITALS), Department of Mechanical Engineering—Engineering Mechanics, Michigan Technological University, Houghton, MI, USA
e-mail: shchavan@mtu.edu; smalladi@mtu.edu

B. J. Dilworth, M. Mains (eds.), *Topics in Modal Analysis & Testing, Volume 8*, Conference Proceedings of the Society for Experimental Mechanics Series, https://doi.org/10.1007/978-3-030-75996-4_9

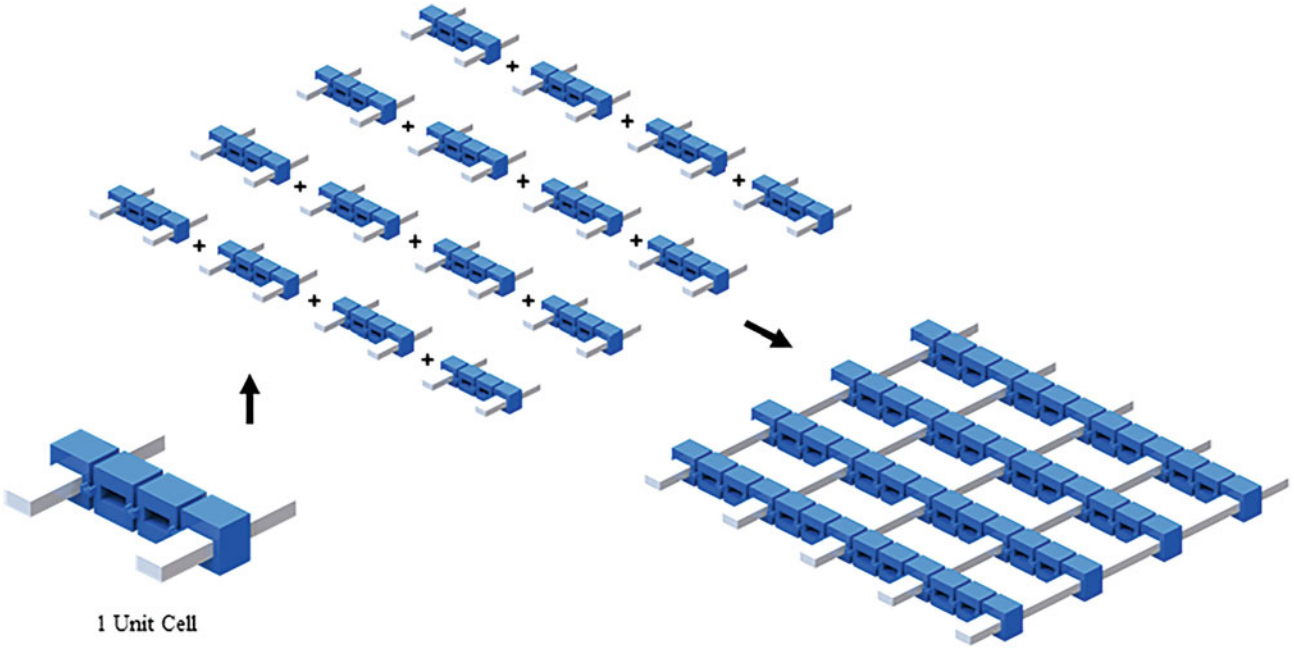

Fig. 9.1 Unit cell and meta-structure assembly

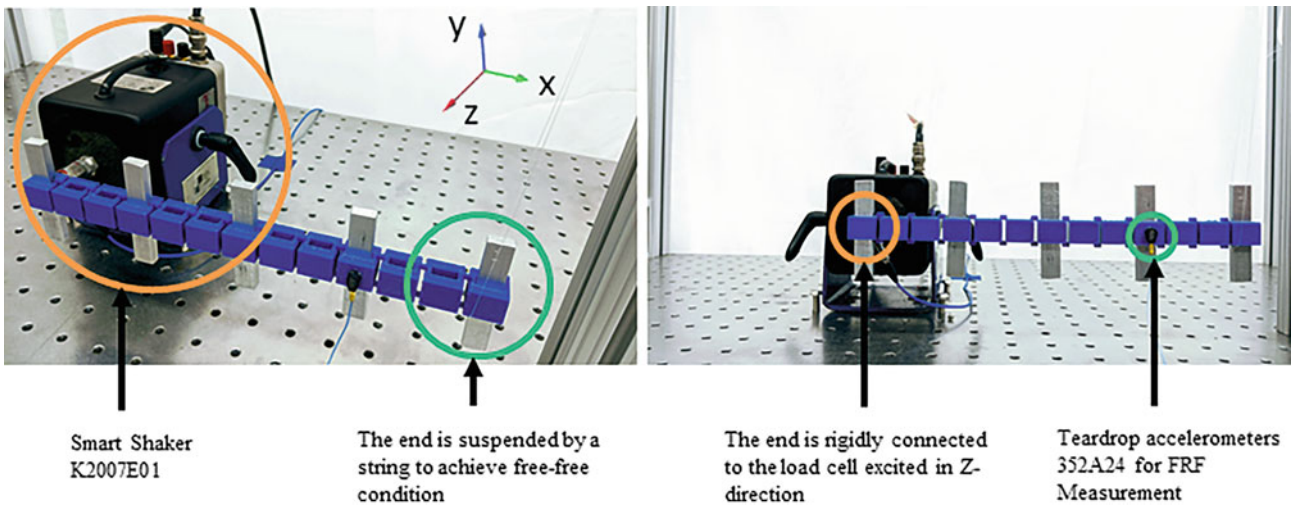

Fig. 9.2 Experimental setup

fishing lines to replicate free-free boundary conditions. PCB teardrop accelerometers 352A24 measured the response at multiple locations.

In finite element modelling, the experimental environment is replicated with all the appropriate boundary conditions, excitation points, and response measurement points. Figure 9.3 compares the simulated and the experimental frequency response functions of the 1D structure. The location of the bandgap in the experimental frequency response function agrees with the simulated FRFs. Also, the highlighted frequency band gap region aligns well with the peaks in the experimental PSD of the printer surface.

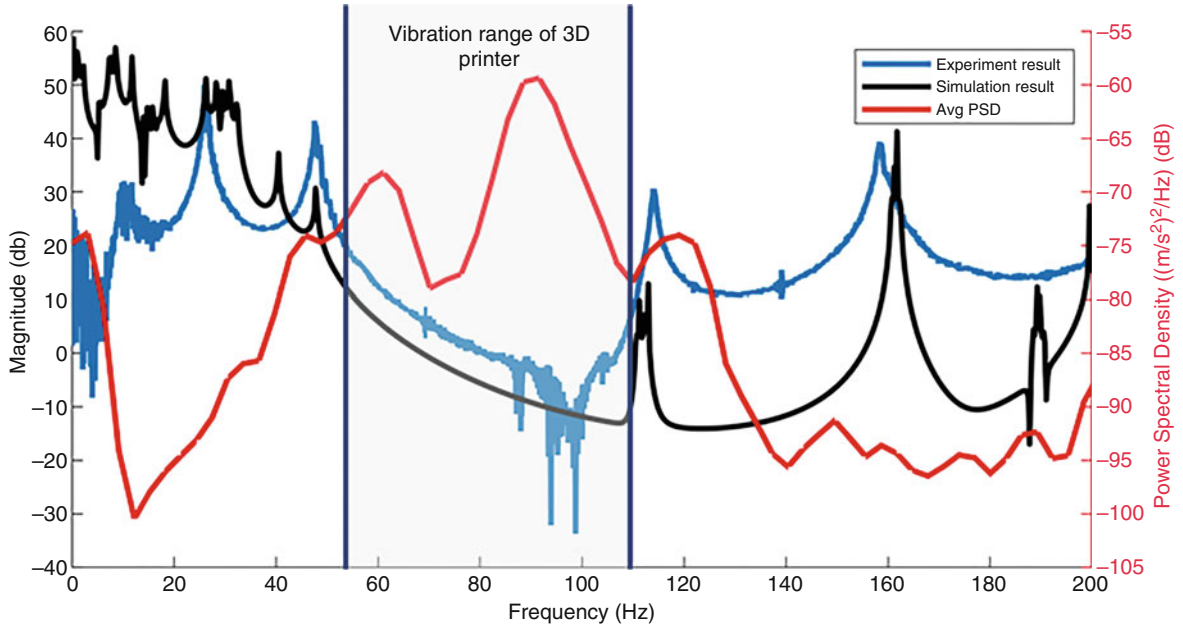

Fig. 9.3 Comparison of experimental and simulated FRFs of the meta-structure with PSD of the vibrations generated

9.3 Conclusion

The showcased work represents the use of meta-structures for isolation of vibrations in 3D printers. With the experiments conducted on Prusa i3 MK3S 3D printer and the meta-structure, the feasibility of the usage of proposed meta-structure is assessed. The structure can absorb all the vibrations from the 3D printer frame without transmitting it further to the printer bed. Band gap of 50–108 Hz is achieved successfully which hinders the transfer of vibrations in this vibration range. In future, the assemble of the meta-structure with the print bed will be studied.

Chapter 10
Experimental Modal Analysis Using Nontraditional Response Variables

Robert N. Coppolino

Abstract Recent introduction of enhancements for the Simultaneous Frequency Domain (SFD) method of experimental modal analysis, specifically the exploitation of left-hand eigenvector data to validate modal orthogonality and estimate kinetic energy distributions, opens the opportunity for incorporation of nontraditional measured response variables. These variables include (1) strains and/or stresses for structures, and (2) dynamic pressures for fluids and gases (e.g., for launch vehicle system dynamics and vibroacoustics). Justification for the exploitation of the above-cited, measured variables stems from the following facts: (a) stresses and fluid pressures are theoretically proportional to accelerations, and (b) SFD estimates an effective dynamic system and permits identification of complex eigenvectors that occur in multiphysics applications. Validity of these expanded opportunities is demonstrated with two simple analytically simulated examples.

Keywords Experimental modal analysis · Acceleration · Strain · Pressure

10.1 Introduction

The majority of modern modal test campaigns, especially in the aerospace community, employ acceleration responses and applied force or foundation acceleration excitations to estimate frequency response functions and modal characteristics of a structural test article. Modal test verification and validation goals are typically accomplished through (theoretical mass-weighted) orthogonality checks of (real) experimental mode shapes, which satisfy NASA and/or U.S. Air Force standards. In addition, correlation and updating of finite element mathematical models, ultimately intended for prediction of system performance during operations, are guided by mass-weighted cross-orthogonality and modal frequency correlation criteria specified in the same NASA and/or U.S. Air Force standards.

Over the past 50 years, technical organizations have augmented accelerometer sensors with strain and load gauges (which are basically scaled strain gauges) to gain additional insights into structural behavior, especially when critical load paths are redundant. While strain gauge data provides valuable detailed information, it has typically played a "surrogate" role in experimental modal analysis.

Satisfaction of U.S. government modal test orthogonality and test-analysis cross-orthogonality criteria are at times challenged by inaccessible key regions on a test article. Two such regions are (a) interior (flexible) structural components and (b) liquid propellant tank fluid free surfaces. It is contended in this paper that augmentation of measured dynamic response with strain gauge and pressure sensor data (playing a primary role in experimental modal analysis) may remedy these challenges. Finally, it is noted that the important category of vibroacoustics may be properly and rigorously addressed through employment of structural acceleration and interacting fluid (gas) dynamic pressure sensors. Specifically, fully coupled vibroacoustic system modes may be estimated by an expanded approach to experimental modal analysis.

This paper provides a systematic basis for the incorporation of strain gauge and pressure sensor data in experimental modal analysis. Theoretical foundations for the employment of strain and pressure degrees of freedom are discussed, and simulated structural and hydroelastic (vibroacoustic) data for simplified example systems are employed to demonstrate feasibility of incorporation of nontraditional response variables in experimental modal analysis.

R. N. Coppolino (✉)
Measurement Analysis Corporation, Torrance, CA, USA
e-mail: rcoppolino@macorp.net

B. J. Dilworth, M. Mains (eds.), *Topics in Modal Analysis & Testing, Volume 8*, Conference Proceedings of the Society for Experimental Mechanics Series, https://doi.org/10.1007/978-3-030-75996-4_10

10.2 Nomenclature

Symbol	Definition
$[A]$	Fluid-structure interface area matrix
$[A_\eta]$	Generalized state-space matrix
$[B]$	Viscous damping matrix
$[C]$	Fluid compliance matrix
[COH]	SFD modal coherence matrix
$\{F_e\}$	Applied force array
$[H]$	FRF matrix
$[K]$	Stiffness matrix
$[K_\varepsilon]$	Strain-displacement matrix
KE	Kinetic energy (distribution)
[LTM]	Load transformation matrix
$[M]$	Mass matrix
$\{P\}$	Fluid pressure array
$[R]$	Fluid "radiation" loss matrix
$[S]$	Fluid susceptance matrix
$[V]$	SFD generalized trial vector matrix
f	Circular frequency (Hz)
$[h]$	Modal FRF matrix
i	Imaginary unit
$\{q\}$	Modal displacement array
t	Time
$\{u\}$	displacement array
$\{v\}$	Fluid volumetric strain array
$[\Phi]$	Modal matrix
$[\Gamma_F]$	Applied force distribution matrix
$[I]$	Identity matrix
$\{\varepsilon\}$	Strain array
$[\gamma]$	State-space modal gain matrix
$\{\eta\}$	State-space modal displacement array
λ	Complex eigenvalue
$\{\sigma\}$	Stress array
ω	Angular frequency (rad/sec)
$\{\xi\}$	Generalized displacement array
ζ	Critical damping ratio

10.3 Theoretical and Experimental Considerations

10.3.1 In Vacuo Linear Structural Dynamics

The generally accepted matrix equations for an in vacuo, linear structural dynamic system are,

$$[M]\{\ddot{u}\} + [B]\{\dot{u}\} + [K]\{u\} = [\Gamma_F]\{F_e(t)\} \tag{10.1}$$

In addition, elastic strains (for axial deformations, $\varepsilon = \mathrm{d}u/\mathrm{d}x$) are described by a real, linear transformation with respect to the discrete displacement array,

$$\{\varepsilon\} = [K_\varepsilon]\{u\} \tag{10.2}$$

Moreover, it should be noted that "accelerated" strains,

$$\{\ddot{\varepsilon}\} = [K_\varepsilon]\{\ddot{u}\} \tag{10.3}$$

define an explicit transformation of accelerations, which (analytically) justifies an expanded role for strain measurements in experimental modal analysis.

Explicit substitution of displacements from Eq. (10.1) (a slightly more involved path must be taken for a singular stiffness matrix) results in a "load" transformation relationship (for strains),

$$\{\varepsilon\} = \left[K_\varepsilon K^{-1}\Gamma_F\right]\{F_\mathrm{e}\} - \left[K_\varepsilon K^{-1}M\right]\{\ddot{u}\} - \left[K_\varepsilon K^{-1}B\right]\{\dot{u}\} \tag{10.4}$$

The most commonly employed approximation of the above relationship ignores the small contribution of damping, resulting in,

$$\{\varepsilon\} \approx \left[K_\varepsilon K^{-1}\Gamma_F\right]\{F_\mathrm{e}\} - \left[K_\varepsilon K^{-1}M\right]\{\ddot{u}\} = \left[\mathrm{LTM}_{\varepsilon,\mathrm{F}}\right]\{F_\mathrm{e}\} + \left[\mathrm{LTM}_{\varepsilon,\ddot{u}}\right]\{\ddot{u}\} \tag{10.5}$$

Further substitutions of elastic stress-strain transformations yields internal stress and member loads in the form,

$$\{\sigma\} \approx \left[\mathrm{LTM}_{\sigma,\mathrm{F}}\right]\{F_\mathrm{e}\} + \left[\mathrm{LTM}_{\sigma,\ddot{u}}\right]\{\ddot{u}\} \tag{10.6}$$

When low-frequency (undamped normal) modes are substituted in Eqs. (10.5) and (10.6), the well-known mode acceleration relationships due to Williams [1] are defined as,

$$\{\varepsilon\} \approx \left[\mathrm{LTM}_{\varepsilon,F}\right]\{F_\mathrm{e}\} + \left[\mathrm{LTM}_{\varepsilon,\ddot{q}}\right]\{\ddot{q}_\ell\} \text{ and } \{\sigma\} \approx \left[\mathrm{LTM}_{s,F}\right]\{F_\mathrm{e}\} + \left[\mathrm{LTM}_{\sigma,\ddot{q}}\right]\{\ddot{q}_\ell\} \tag{10.7}$$

It should be noted that the mode acceleration relationships automatically account for the quasi-static response of all higher frequency modes.

10.3.2 Hydroelasticity and Vibroacoustics

Interaction of an inviscid, compressible fluid with a structure has been described by Zienkeiwicz [2] (and related to Toupin's variational principle [3, 4]) employing pressure perturbation degrees of freedom. In particular, dynamics of the fluid are described by,

$$[C]\left\{\ddot{P}\right\} + [R]\left\{\dot{P}\right\} + [S]\{P\} = -\left[A^T\right]\{\ddot{u}\} \tag{10.8}$$

The interacting structural system is described by,

$$[M]\{\ddot{u}\} + [B]\{\dot{u}\} + [K]\{u\} = [A]\{P\} + [\Gamma_F]\{F_\mathrm{e}\} \tag{10.9}$$

The resulting unsymmetric, coupled "hydroelastic" system equations are,

$$\begin{bmatrix} M & 0 \\ A^T & C \end{bmatrix}\begin{Bmatrix} \ddot{u} \\ \ddot{P} \end{Bmatrix} + \begin{bmatrix} B & 0 \\ 0 & R \end{bmatrix}\begin{Bmatrix} \dot{u} \\ \dot{P} \end{Bmatrix} + \begin{bmatrix} K & -A \\ 0 & S \end{bmatrix}\begin{Bmatrix} u \\ P \end{Bmatrix} = \begin{bmatrix} \Gamma_F \\ 0 \end{bmatrix}\{F_\mathrm{e}\} \tag{10.10}$$

Physically, the above matrix partitions play the following roles:

(a) [C] represents flexibility or compliance of the fluid medium.
(b) [S] represents "inverse mass" or susceptance of the fluid medium.
(c) [R] represents radiating acoustic wave losses *only* for an infinite fluid medium.
(d) [A] represents the area of the fluid-structure interface.
(e) [Γ_F] represents spatial allocation of applied external loads.

While the fluid compliance matrix, [C], is symmetric and positive-definite, the fluid susceptance matrix [S] is symmetric and positive-semi-definite, due to the fact that uniform pressure distribution (unless at least one pressure DOF is constrained) results in no fluid motions [4].

The Zienkeiwicz equations can be re-cast in standard symmetric form by substitution of the pressure-volumetric strain transformation (only for finite fluid media where $[R] = [0]$),

$$[C]\{P\} = \{v\} \tag{10.11}$$

which substituted into Eq. (10.8) yields,

$$[S]\{P\} = -\{\ddot{v}\} - \left[A^T\right]\{\ddot{u}\} \tag{10.12}$$

Note that the above equation clearly indicated that fluid pressures are directly related to accelerations; therefore pressure DOFs play a role corresponding to acceleration DOFs in experimental modal analysis.

Introduction of a small perturbation in the singular susceptance matrix, [S], permits its explicit inversion, which results in the symmetric hydroelastic system equations (for a finite fluid medium) by substitution into Eq. (10.10),

$$\begin{bmatrix} M + AS^{-1}A^T & AS^{-1} \\ S^{-1}A^T & S^{-1} \end{bmatrix} \begin{Bmatrix} \ddot{u} \\ \ddot{v} \end{Bmatrix} + \begin{bmatrix} B & 0 \\ 0 & 0 \end{bmatrix} \begin{Bmatrix} \ddot{u} \\ \ddot{v} \end{Bmatrix} + \begin{bmatrix} K & 0 \\ 0 & C^{-1} \end{bmatrix} \begin{Bmatrix} u \\ v \end{Bmatrix} = \begin{bmatrix} \Gamma_F \\ 0 \end{bmatrix} \{F_e\} \tag{10.13}$$

10.3.3 Experimental Modal Analysis (EMA) Considerations

Conventional laboratory modal testing typically results in estimated frequency response function (FRF) arrays associated with measured accelerations, $\left[\ddot{U}\,(f)\right]$, and (one or more) (unit) applied forces, $[F(f)]$. When strain measurements are made, additional FRF arrays, $[\varepsilon(f)]$, may be estimated. Moreover, when the test article either interacts with a liquid (hydroelasticity) or gas (vibroacoustics), dynamic pressure FRF arrays, $[P(f)]$, may be relevant. Since most EMA techniques focus on acceleration data, the following augmented FRF arrays appear to be of consistent character:

(a) Accelerations and strain "accelerations" by virtue of Eq. (10.2)

$$\begin{bmatrix} \ddot{U}(f) \\ \ddot{\varepsilon}(f) \end{bmatrix} \sim \begin{bmatrix} I \\ K_\varepsilon \end{bmatrix} \left[\ddot{U}(f)\right] \tag{10.14}$$

(b) Accelerations and pressures by virtue of Eq. (10.12)

$$\begin{bmatrix} \ddot{U}(f) \\ P(f) \end{bmatrix} \sim \begin{bmatrix} \mathrm{I} & 0 \\ -S^{-1}A^T & -S^{-1} \end{bmatrix} \begin{bmatrix} \ddot{U}(f) \\ \ddot{v}(f) \end{bmatrix} \tag{10.15}$$

(c) Accelerations, pressures, and strain "accelerations" by virtue of Eqs. (10.2) and (10.12)

$$\begin{bmatrix} \ddot{U}(f) \\ \ddot{\varepsilon}(f) \\ P(f) \end{bmatrix} \sim \begin{bmatrix} \mathrm{I} & 0 \\ K_\varepsilon & 0 \\ -S^{-1}A^T & -S^{-1} \end{bmatrix} \begin{bmatrix} \ddot{U}(f) \\ \ddot{v}(f) \end{bmatrix} \tag{10.16}$$

In the present paper, application of general cases (a) and (b) are explored with simple example analytically simulated test articles. Moreover, EMA calculations employ versions of the Simultaneous Frequency Domain Method (SFD) [5–7], for which an overview is provided in the Appendix of this paper.

10.4 Illustrative Example 1: In Vacuo Structure Accelerations and Strains

10.4.1 Simulated Measured Data

The first illustrative example system consists of a lumped parameter, five mass, rod type structure, which is depicted below in Fig. 10.1.

Matrix properties and theoretical (real and complex) modal solutions associated with this structure are summarized below in Table 10.1.

It should be noted that the rod's actual modes are complex due to the nonproportional viscous damping matrix, [B].

Simulated acceleration and strain FRFs (depicted below in terms of magnitude and phase versus frequency in Figs. 10.2 and 10.3, respectively) are formed by direct solution to frequency domain expressions of Eqs. (10.1) and (10.2); note that the strains are calculated as differences of successive displacements divided by the spacing ($L = 0.2$).

Note that the strain FRFs, illustrated in Fig. 10.3, have low-frequency magnitudes that are characteristic of displacement FRFs. This contrasts with the acceleration FRFs, illustrated in Fig. 10.2, which have asymptote to null magnitudes at low frequency. The strain acceleration FRFs (formed via multiplication of strain FRFs by $-(2\pi f)^2$), illustrated below in Fig. 10.4, however, possess low-frequency asymptotic behavior consistent with acceleration FRFs.

Five simulated measured cases are considered to investigate effectiveness of combined acceleration and strain FRF data for EMA, specifically:

Case 1: Five acceleration response FRFs representing a conventional EMA array typically employed for a process aimed at satisfying mass-weighted orthogonality criteria according to NASA STD-5002 [8] or SMC-S-004 [9].

Case 2: One acceleration response FRF and four strain "acceleration" FRFs representing situations in which some "mass points" are inaccessible (e.g., enclosed regions).

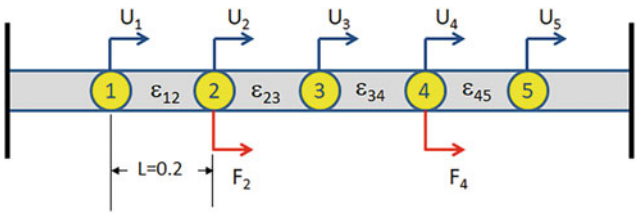

Fig. 10.1 Five mass rod structure

Table 10.1 Five mass rod structure matrices and theoretical modal solutions

K					*M*					*B*					Γ_F
200000	−100000	0	0	0	1	0	0	0	0	16.96	−2.70	−0.13	−0.01	0.00	0
−100000	110000	−10000	0	0	0	0.9	0	0	0	−2.70	5.73	−0.48	−0.02	−0.01	0.5
0	−10000	20000	−10000	0	0	0	1	0	0	−0.13	−0.48	2.73	−0.51	−0.12	0
0	0	−10000	110000	−100000	0	0	0	1.1	0	−0.01	−0.02	−0.51	6.28	−2.81	1
0	0	0	−100000	200000	0	0	0	0	1	0.00	−0.01	−0.12	−2.81	17.06	0

Real modal analysis results

Freq (Hz)	Zeta (%)	Phi				
19.55	1.11	0.13	−0.26	−0.67	0.01	1.00
33.39	1.54	0.24	−0.40	−1.00	0.00	−0.74
36.21	1.56	1.00	−0.25	0.40	−0.02	0.03
80.80	1.61	0.25	1.00	−0.28	0.58	−0.01
83.25	1.54	0.14	0.64	−0.19	−1.00	0.01

Complex modal analysis results

Freq (Hz)	**Zeta (%)**	**|Phi|**					**Phase of Phi (deg)**				
19.55	1.11	0.13	0.26	0.67	0.01	1.00	−0.7	178.3	−0.5	178.6	0.0
33.38	1.54	0.24	0.40	1.00	0.00	0.74	−0.4	178.7	0.0	−2.5	178.9
36.20	1.56	1.00	0.25	0.40	0.02	0.03	0.0	179.7	178.6	−1.9	−1.8
80.79	1.61	0.25	1.00	0.28	0.58	0.01	−0.4	0.0	−1.4	178.8	177.6
83.24	1.54	0.14	0.64	0.19	1.00	0.01	−0.7	−0.5	−1.9	0.0	−1.2

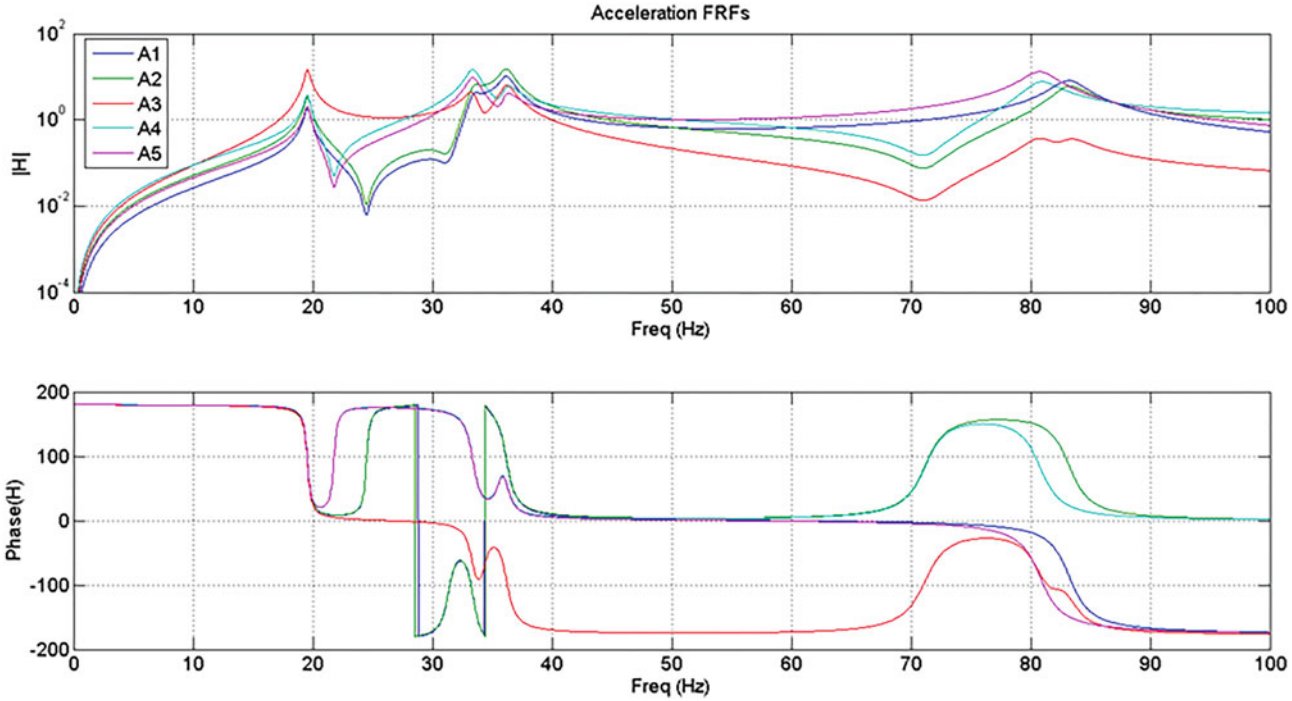

Fig. 10.2 Illustrative example 1 acceleration FRFs

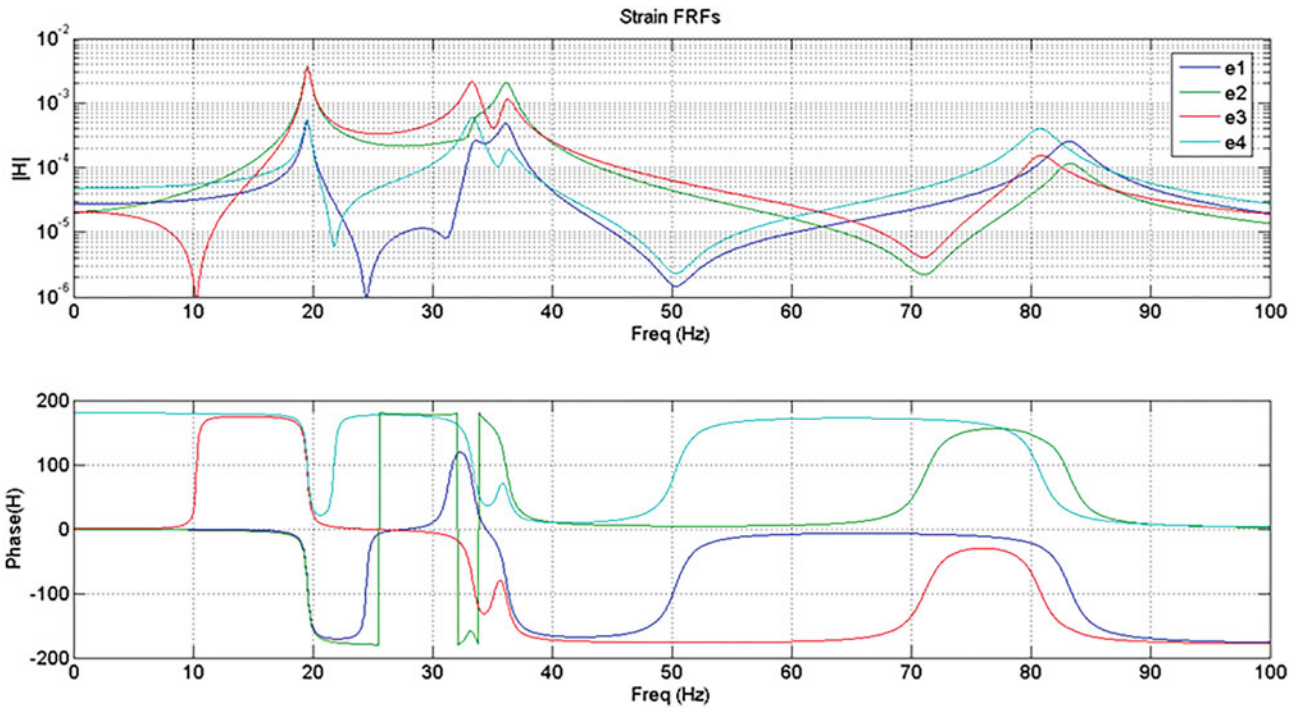

Fig. 10.3 Illustrative example 1 strain FRFs

Case 3: All five acceleration response FRFs and all four strain "acceleration" FRFs representing a thoroughly mapped test article.

Case 4: All five acceleration response FRFs and all four strain "displacement" FRFs representing a thoroughly mapped test article [to demonstrate issues associated with mixing of acceleration and displacement FRFs in EMA].

Case 5: Employment of strain "displacement" FRFs and acceleration FRFs to estimate load transformation matrices [for an augmented EMA process with strain playing a "surrogate" role].

10.4.2 Experimental Modal Analysis

EMA results, based on SFD-2018 computations, for Cases 1–4 (with modes unit normalized to the common response channel, A1) are presented below in Table 10.2.

EMA results for all four cases indicate consistent values for all modal frequencies, damping, and complex modes [eigenvectors]. This level of consistency occurs due to the fact that the simulated FRF data is noise-free, which is never the case with actual measured data.

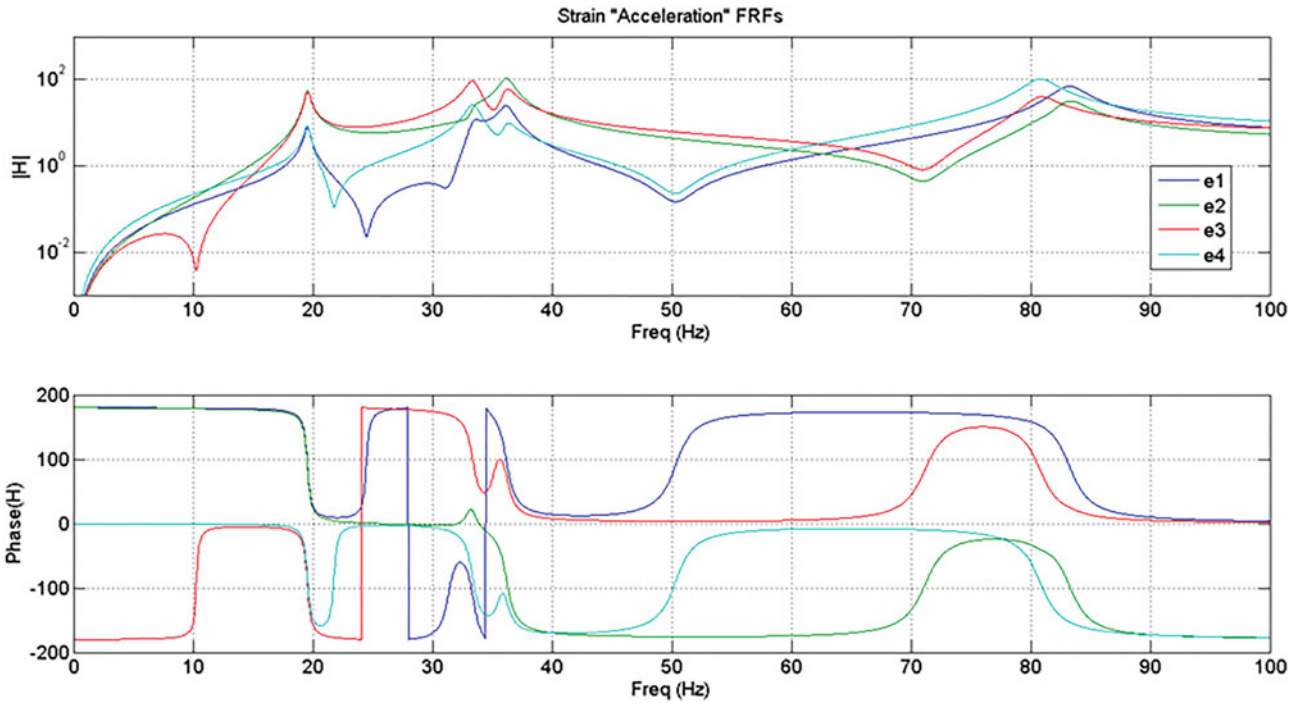

Fig. 10.4 Illustrative example 1 strain acceleration FRFs

Table 10.2 EMA (SFD-2018) results for cases 1–4

		Case 1					Case 2					Case 3					Case 4				
	Mode	1	2	3	4	5	1	2	3	4	5	1	2	3	4	5	1	2	3	4	5
	Freq (HZ)	19.55	33.38	36.20	80.79	83.24	19.55	33.38	36.20	80.79	83.24	19.55	33.38	36.20	80.79	83.24	19.55	33.38	36.20	80.79	83.24
	Zeta (%)	1.11	1.54	1.56	1.61	1.54	1.11	1.54	1.56	1.61	1.54	1.11	1.54	1.56	1.61	1.54	1.11	1.54	1.56	1.61	1.54
Mag	A1	1.00	1.00	1.00	1.00	1.00	1.00	1.00	1.00	1.00	1.00	1.00	1.00	1.00	1.00	1.00	1.00	1.00	1.00	1.00	1.00
Mag	A2	1.85	1.56	1.48	0.58	0.74						1.85	1.56	1.48	0.58	0.74	1.85	1.56	1.48	0.58	0.74
Mag	A3	7.83	0.98	0.60	2.95	0.03						7.83	0.98	0.60	2.95	0.03	7.83	0.98	0.60	2.95	0.03
Mag	A4	1.99	3.92	0.42	70.80	0.01						1.99	3.92	0.42	70.80	0.01	1.99	3.92	0.42	70.80	0.01
Mag	A5	1.08	2.51	0.28	122.57	0.01						1.08	2.51	0.28	122.57	0.01	1.08	2.51	0.28	122.57	0.01
Mag	e12A						4.25	2.80	2.41	7.89	8.68	4.25	2.80	2.41	7.89	8.68					
Mag	e23A						29.89	2.89	10.40	11.88	3.83	29.89	2.89	10.40	11.88	3.83					
Mag	e34A						29.18	24.49	5.07	368.75	0.17	29.18	24.49	5.07	368.75	0.17					
Mag	e45A						4.57	7.03	0.68	966.79	0.06	4.57	7.03	0.68	966.79	0.06					
Mag	e12U																2.42E-04	7.22E-05	4.37E-05	1.58E-05	3.16E-05
Mag	e23U																1.95E-03	5.34E-05	2.04E-04	8.07E-05	1.35E-05
Mag	e34U																1.96E-03	5.52E-04	9.40E-05	1.42E-03	7.44E-07
Mag	e45U																2.33E-04	1.44E-04	7.46E-06	3.74E-03	3.36E-07
Phase (deg)	A1	0.00	0.00	0.00	0.00	0.00	0.00	0.00	0.00	0.00	0.00	0.00	0.00	0.00	0.00	0.00	0.00	0.00	0.00	0.00	0.00
Phase (deg)	A2	0.31	0.48	0.52	178.87	178.87						0.31	0.48	0.52	178.87	178.87	0.31	0.48	0.52	178.87	178.87
Phase (deg)	A3	0.67	1.43	179.17	179.50	-1.82						0.67	1.43	179.17	179.50	-1.82	0.67	1.43	179.17	179.50	-1.82
Phase (deg)	A4	0.29	-178.26	-0.89	0.25	177.62						0.29	-178.26	-0.89	0.25	177.62	0.29	-178.26	-0.89	0.25	177.62
Phase (deg)	A5	-0.02	-178.75	-1.42	-178.60	-1.22						-0.02	-178.75	-1.42	-178.60	-1.22	-0.02	-178.75	-1.42	-178.60	-1.22
Phase (deg)	e12A						0.68	1.33	1.60	179.59	179.52	0.68	1.33	1.60	179.59	179.52					
Phase (deg)	e23A						0.79	178.86	-179.87	179.65	-1.16	0.79	178.86	-179.87	179.65	-1.16					
Phase (deg)	e34A						-179.20	-178.32	-0.85	0.22	178.10	-179.20	-178.32	-0.85	0.22	178.10					
Phase (deg)	e45A						-179.34	2.60	-179.80	-179.02	-1.71	-179.34	2.60	-179.80	-179.02	-1.71					
Phase (deg)	e12U																-179.43	-179.35	-179.07	-1.44	-1.01
Phase (deg)	e23U																-179.33	0.58	-0.34	28.50	176.69
Phase (deg)	e34U																0.68	1.35	178.09	177.88	26.53
Phase (deg)	e45U																0.54	-178.17	-0.65	0.45	0.38

It is of interest to note that all EMA modes (for Cases 1–4) computed by SFD-2018 [7] indicate clear modal isolation based on left-hand eigenvector orthogonality checks. Effectiveness of the mode isolation process is demonstrated below in Figs. 10.5 and 10.6, which, respectively, depict the (Case 3) physical FRF,$\ddot{U}_3(f)$, and generalized modal FRFs, $h_4(f)$ and $h_5(f)$, associated with modes 4 and 5.

Further insight into the quality of EMA results for the four cases is realized by reconstruction of (simulated) measured FRF data using estimated system eigenvalues and modal vectors. "Classic" SFD [5, 6] estimation of experimental modal vectors using linear least squares calculation is a feature of many EMA techniques [10]. Strain-displacement FRF reconstruction

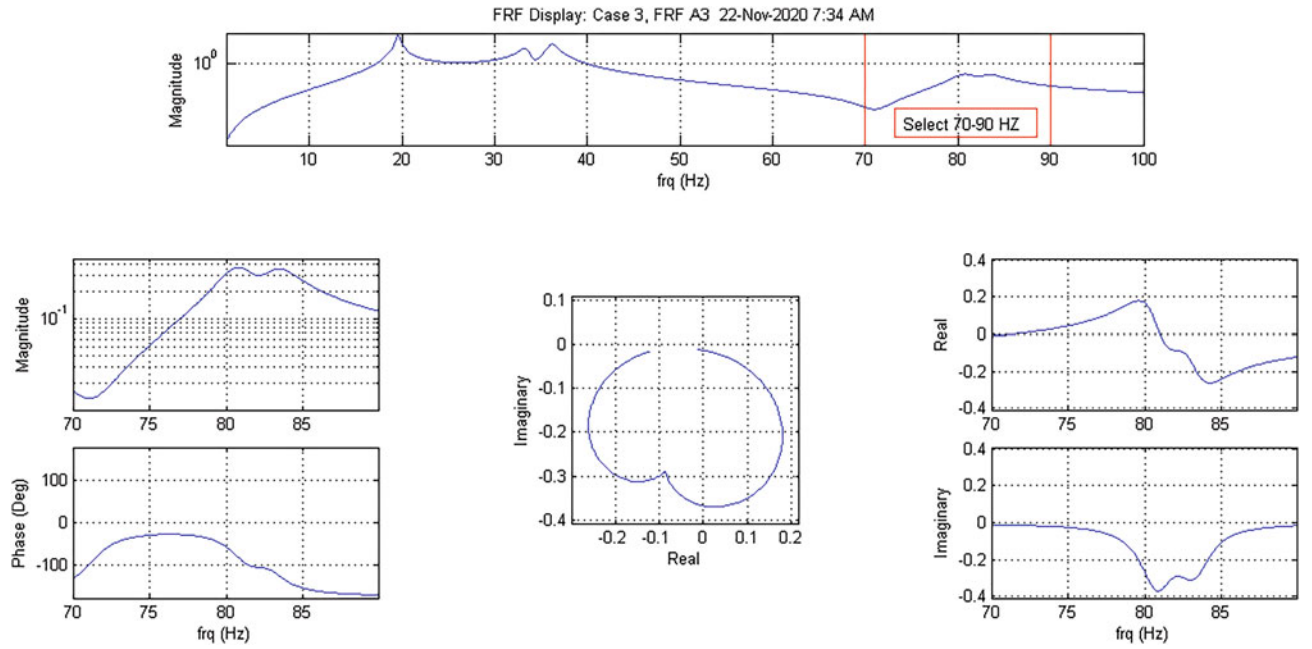

Fig. 10.5 Case 3 physical FRF $\ddot{U}_3(f)$in the 70–90 Hz frequency band

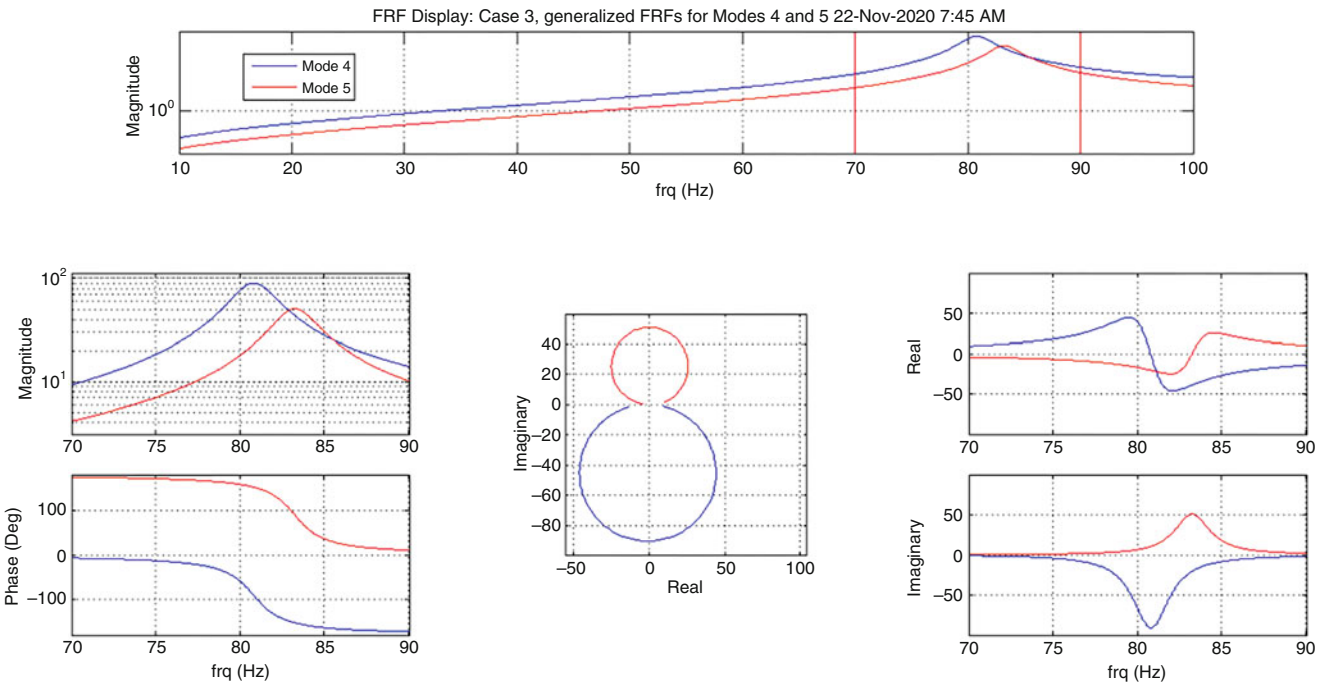

Fig. 10.6 Case 3 generalized modal FRFs, $h_4(f)$ and $h_5(f)$

for Case 4, provided below in Fig. 10.7, illustrates the failure to accurately reconstruct the function when low-frequency residuals are not included.

It is clearly illustrated in the above results that inclusion of FRF reconstruction deficiencies is eliminated when low-frequency residuals are included in the FRF reconstruction process. While the low-frequency residual is not required for acceleration FRFs, it is required for strain-displacement FRFs to compensate for the fact that modal displacement FRFs are "$-1/(2\pi f)^2$" times modal acceleration FRFs.

10.4.3 Strain Viewed as a Surrogate Variable

In addition to incorporation of strain FRFs in the EMA process (Cases 2–4), strain FRFs may be viewed as "surrogates" with respect to acceleration FRFs (Case 5) to be employed for direct estimation of LTMs (see Eq. (10.5)). Estimation of real-valued coefficient matrices is guaranteed when the least-squares process in cast as,

$$\left[\mathrm{LTM}_{\varepsilon,F}\ \ \mathrm{LTM}_{\varepsilon,\ddot{u}}\right] = \left(\begin{bmatrix} \varepsilon(f)_{\mathrm{Real}} & \varepsilon(f)_{\mathrm{Imag}} \end{bmatrix} \cdot \begin{bmatrix} \mathrm{F}(f)_{\mathrm{Real}} & \mathrm{F}(f)_{\mathrm{Imag}} \\ \ddot{\mathrm{U}}(f)_{\mathrm{Real}} & \ddot{\mathrm{U}}(f)_{\mathrm{Imag}} \end{bmatrix}^{\mathrm{T}}\right) \cdot \left(\begin{bmatrix} \mathrm{F}(f)_{\mathrm{Real}} & \mathrm{F}(f)_{\mathrm{Imag}} \\ \ddot{\mathrm{U}}(f)_{\mathrm{Real}} & \ddot{\mathrm{U}}(f)_{\mathrm{Imag}} \end{bmatrix} \cdot \begin{bmatrix} \mathrm{F}(f)_{\mathrm{Real}} & \mathrm{F}(f)_{\mathrm{Imag}} \\ \ddot{\mathrm{U}}(f)_{\mathrm{Real}} & \ddot{\mathrm{U}}(f)_{\mathrm{Imag}} \end{bmatrix}^{\mathrm{T}}\right)^{-1}. \tag{10.17}$$

The estimated load transformation matrices are illustrated below in Table 10.3.

In addition, recovery of measured strains employing the estimated load LTMs yields nearly perfect strain FRF functions, as indicated below for $\varepsilon_{45}(f)$, as illustrated below in Fig. 10.8.

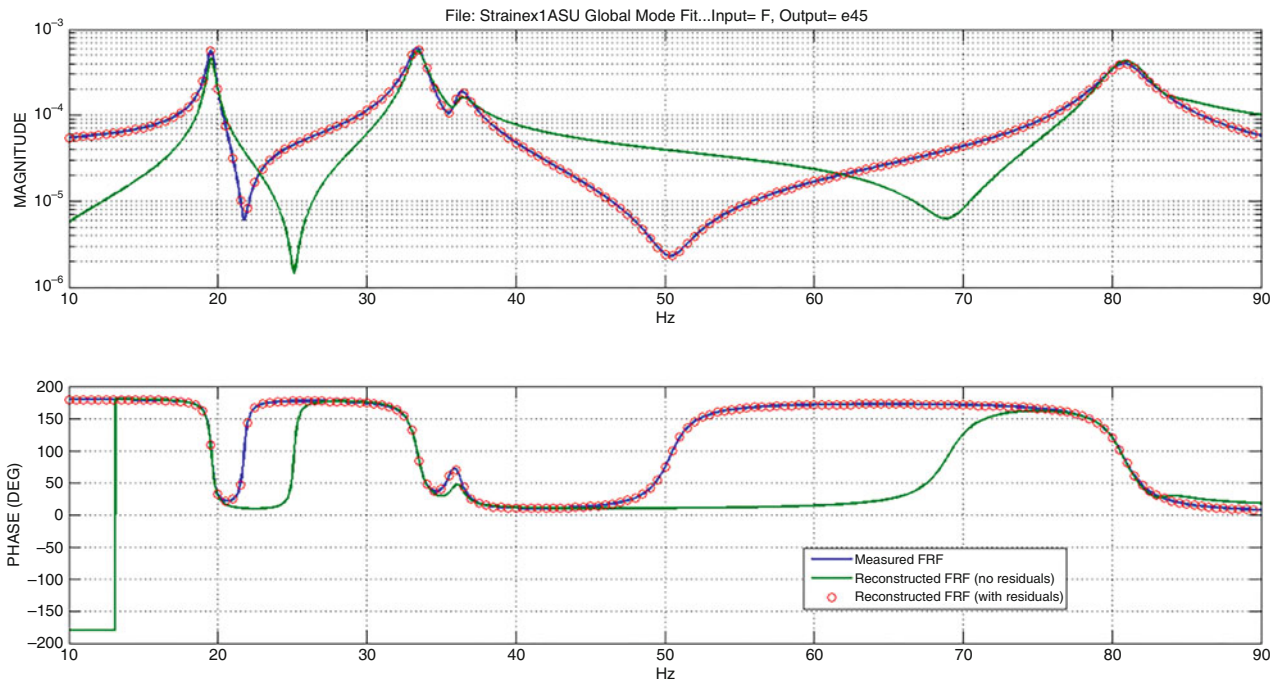

Fig. 10.7 Case 4 strain FRF reconstruction results

Table 10.3 Estimated load transformation matrices

$\mathrm{LTM}_{\varepsilon F} \times 10^5$		$\mathrm{LTM}_{\varepsilon A} \times 10^5$					
	F		A_1	A_2	A_3	A_4	A_5
ε_{12}	2.6828	ε_{12}	0.1949	−4.1138	−2.4963	−0.4841	−0.1967
ε_{23}	2.0399	ε_{23}	2.1052	3.7231	−25.0098	−4.4893	−2.0379
ε_{34}	2.0040	ε_{34}	2.1318	3.8198	24.9534	−4.6076	−2.0917
ε_{45}	−4.7243	ε_{45}	0.2466	0.3273	2.5098	5.0527	−0.2206

10.5 Illustrative Example 2: Hydroelastic System Accelerations and Fluid Pressures

10.5.1 Simulated Measured Data

The second illustrative example system consists of a lumped parameter, five mass and five fluid DOF, hydroelastic system, which is depicted below in Fig. 10.9.

Matrix properties associated with this hydroelastic system in terms of the unsymmetric Zienkeiwicz formulation (Eq. (10.10)) are summarized below in Table 10.4.

In addition, matrix properties associated with the corresponding symmetric hydroelastic formulation (Eq. (10.13)) are summarized below in Table 10.5.

Note that the system's actual modes are complex due to the nonproportional viscous damping matrix, [B].

The (unsymmetrical Zienkeiwicz) hydroelastic system complex modes in the frequency band below 20 Hz are summarized below in Table 10.6.

The zero eigenvalue mode of no consequence (impossible to excite) is associated with uniform fluid pressure distribution, which is consistent with "null" fluid motion [4]. It also should be noted that the structural and fluid modal kinetic energies are determined by product operations involving left- and right-hand complex eigenvectors [7].

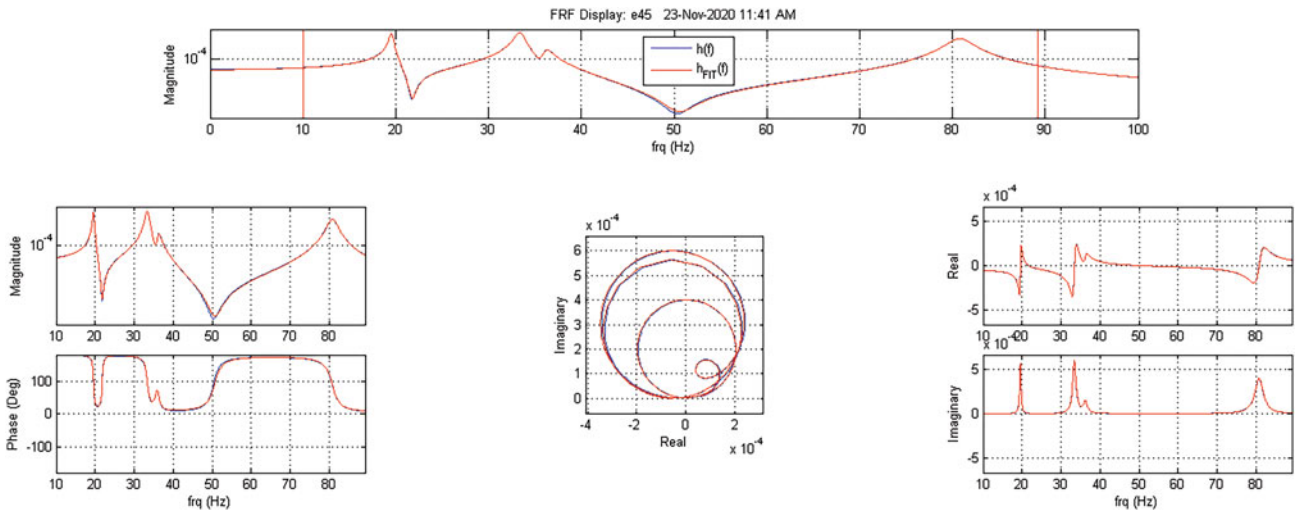

Fig. 10.8 Measured and Reconstructed Strain FRF, $\varepsilon_{45}(f)$

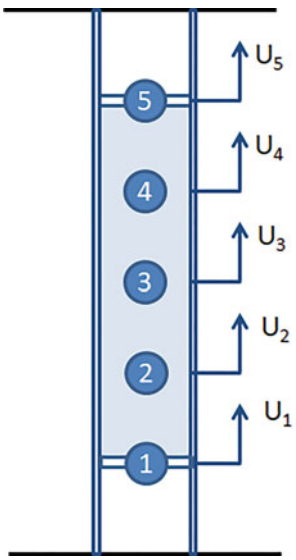

Fig. 10.9 Five mass and five fluid DOF hydroelastic system

Table 10.4 Hydroelastic system matrices (Zienkeiwicz formulation)

M (Zienkeiwicz)

0.813884										
	1.627768									
		1.627768								
			1.627768							
				813.8841						
-31415.9					633.2404					
					1266.481					
						1266.481				
							1266.481			
				31415.93					633.2404	

B (Zienkeiwicz)

155.8016	-50.435	-6.54896	-1.72255	-4.96768						
-50.435	204.1842	-65.2555	-10.004	-21.5734						
-6.54896	-65.2555	207.2781	-61.8535	-43.1292						
-1.72255	-10.004	-61.8535	217.1959	-126.366						
-4.96768	-21.5734	-43.1292	-126.366	4049.359						

K (Zienkeiwicz)

3141593	-1570796				31415.93					
-1570796	3141593	-1570796								
	-1570796	3141593	-1570796							
		-1570796	3141593	-1570796						
			-1570796	3141593					-31415.9	
					1678201	-1678201				
					-1678201	3356402	-1678201			
						-1678201	3356402	-1678201		
							-1678201	3356402	-1678201	
								-1678201	1678201	

Γ

1

Table 10.5 Hydroelastic system matrices (symmetric formulation)

M (Symmetrical)

5.88E+08				-5.9E+08	-18720	-18720	-18720	-18720	-18720	
	1.627768									
		1.627768								
			1.627768							
-5.9E+08				5.88E+08	18720	18720.02	18720.04	18720.06	18720.07	
-18720				18720	0.595876	0.595876	0.595876	0.595876	0.595876	
-18720				18720.02	0.595876	0.595877	0.595877	0.595877	0.595877	
-18720				18720.04	0.595876	0.595877	0.595877	0.595877	0.595877	
-18720				18720.06	0.595876	0.595877	0.595877	0.595878	0.595878	
-18720				18720.07	0.595876	0.595877	0.595877	0.595878	0.595878	

B (Symmetrical)

155.8016	-50.435	-6.54896	-1.72255	-4.96768						
-50.435	204.1842	-65.2555	-10.004	-21.5734						
-6.54896	-65.2555	207.2781	-61.8535	-43.1292						
-1.72255	-10.004	-61.8535	217.1959	-126.366						
-4.96768	-21.5734	-43.1292	-126.366	4049.359						

K (Symmetrical)

3141593	-1570796									
-1570796	3141593	-1570796								
	-1570796	3141593	-1570796							
	0	-1570796	3141593	-1570796						
	0		-1570796	3141593						
					0.001579					
						0.00079				
							0.00079			
								0.00079		
									0.001579	

Γ

1

Table 10.6 Hydroelastic system (Zienkeiwicz model) modes

Mode	No Consequence		1		2		3		4		5	
Freq (Hz)	0.0000		3.4889		6.6810		8.5186		10.8090		12.9411	
Zeta (%)	0.0000		0.7046		1.2533		0.9557		0.2655		1.3070	
Gain (rel)	0.0000		0.0517		0.1729		0.2211		0.1889		1.0000	
DOF	Mag	Phase (deg)	Mag	Phase (deg)	Mag	Phase (deg)	Mag	Phase (deg)	Mag	Phase (deg)	Mag	Phase (deg)
U1	0.0133	180.00	0.0210	179.24	0.0107	0.25	0.0157	177.24	0.0070	-0.68	0.0009	-179.44
U2	0.0067	-180.00	0.0219	178.61	0.0017	19.68	0.0167	177.61	0.0033	-1.71	0.0030	-177.56
U3	0.0000	90.00	0.0229	178.08	0.0075	171.18	0.0176	178.03	0.0004	-165.05	0.0050	-177.25
U4	0.0067	0.00	0.0238	177.61	0.0165	174.02	0.0185	178.46	0.0040	-178.97	0.0071	-177.12
U5	0.0133	0.00	0.0248	177.19	0.0255	174.84	0.0193	178.88	0.0077	-179.63	0.0090	-177.03
P1	1.0000	0.00	1.0000	0.00	0.9843	178.71	0.7348	-3.00	0.5331	179.87	0.0588	-174.42
P2	1.0000	0.00	0.6300	-0.25	0.0407	57.07	0.9020	179.22	1.0000	0.00	0.0264	161.52
P3	1.0000	0.00	0.0325	-13.64	1.0000	0.00	0.5920	172.85	0.9479	-178.81	0.1353	-6.78
P4	1.0000	0.00	0.5785	-179.01	0.6517	-5.95	1.0000	0.00	0.4057	6.62	0.3792	176.69
P5	1.0000	0.00	0.9786	-179.66	0.5716	-173.28	0.4409	-15.12	0.3564	-9.19	1.0000	0.00
KEU (%)	14.19	0.00	43.41	-1.99	39.66	-2.70	23.53	2.39	8.17	0.24	15.72	10.62
KEP (%)	85.81	0.00	56.64	1.52	60.41	1.77	76.50	-0.73	91.83	-0.02	84.60	-1.96
Total KE (%)	100.00	0.00	100.00	0.00	100.00	0.00	100.00	0.00	100.00	0.00	100.00	0.00

Simulated acceleration and pressure FRFs (depicted below in terms of magnitude and phase versus frequency in Figs. 10.10 and 10.11, respectively) are formed by direct frequency domain solution of Eq. (10.10); note that the pressure FRFs are scaled by an "inertance" factor, $L_e/(_{f1}A_{f1}) = 68.015$ resulting in acceleration unit pressure FRFs.

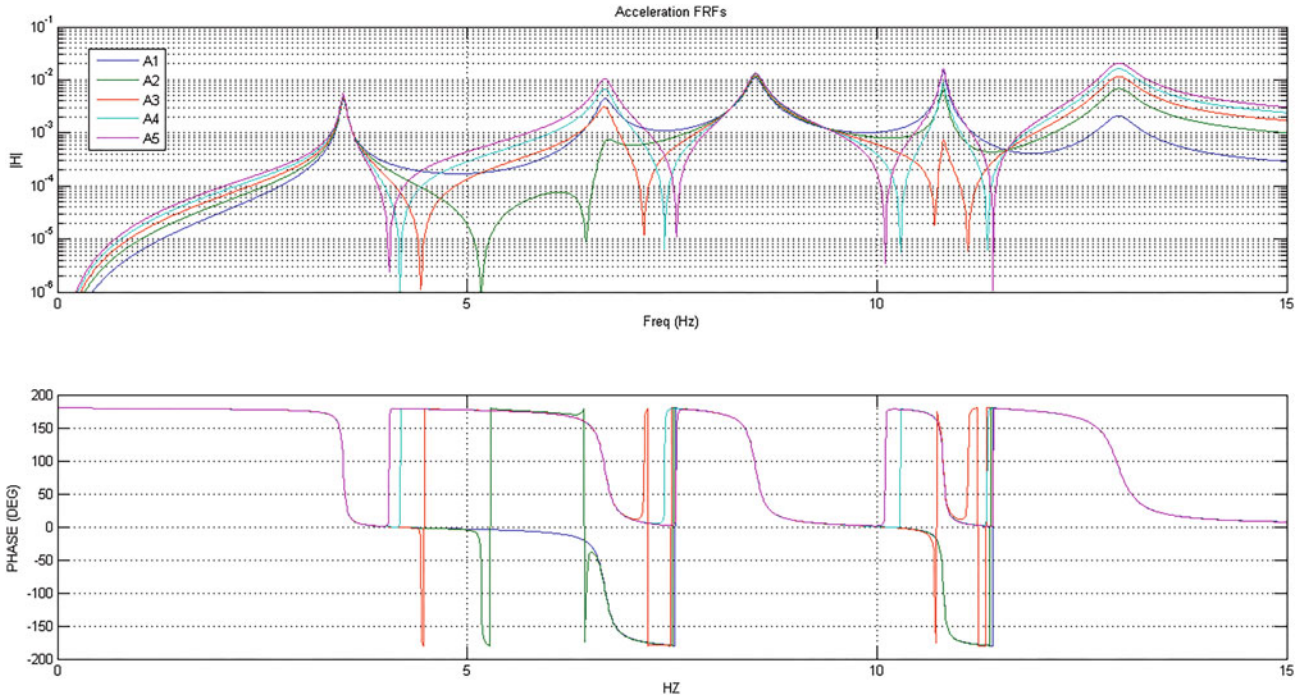

Fig. 10.10 Hydroelastic system acceleration FRFs

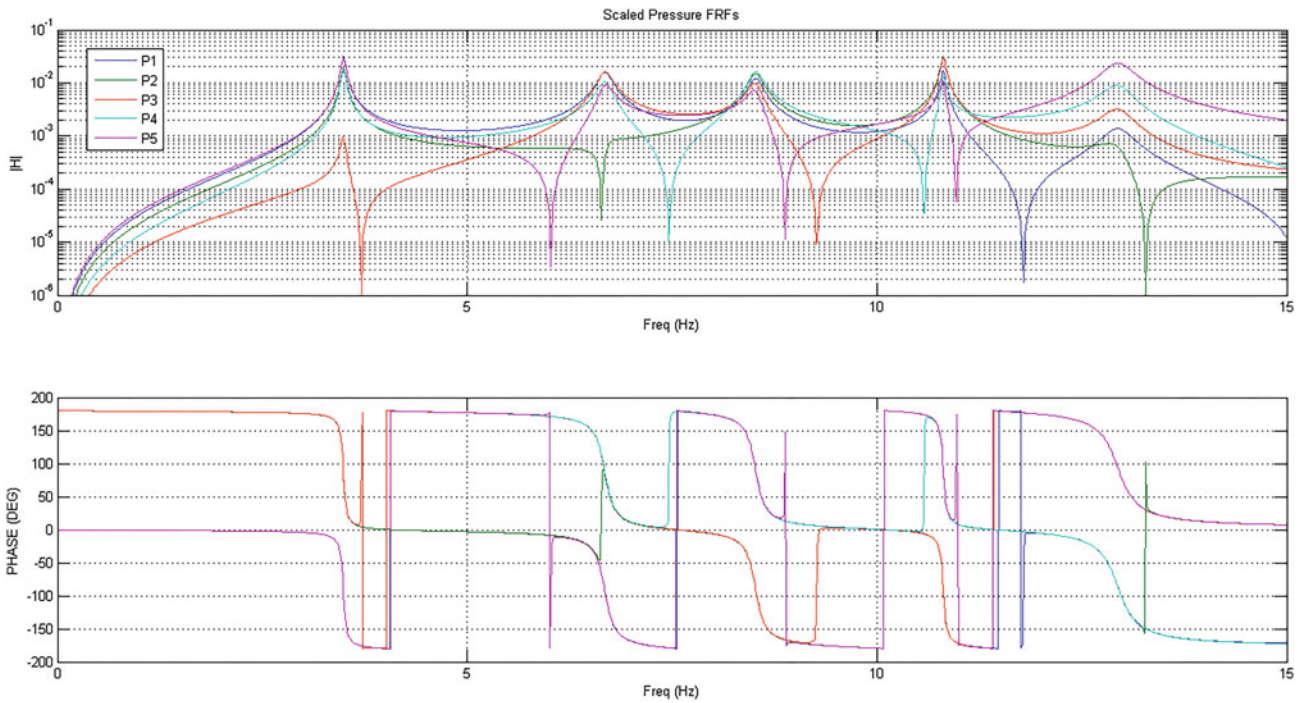

Fig. 10.11 Hydroelastic system scaled pressure FRFs

10.5.2 Experimental Modal Analysis

EMA was conducted on the simulated hydroelastic FRFs employing both SFD-2018 and "Classic" SFD methods. A comparison of theoretical and EMA estimated complex eigenvalues in the 0–15 Hz band, presented below in Table 10.7,

clearly integrity of the EMA process. It should be pointed out that the "Classic" SFD results suggest that other EMA techniques [10] should produce results of similar integrity.

Validation of SFD-2018 estimated modes is demonstrated by effectiveness of left-hand eigenvector orthogonality (mode isolation) checks, shown below in Fig. 10.12.

Validation of "Classic" SFD estimated modes is demonstrated below in Fig. 10.13 via reconstruction of (simulated) measured FRF data using estimated system eigenvalues and modal vectors.

Table 10.7 Comparison of theoretical and EMA complex eigenvalues

	Model		SFD-2018		Classic SFD	
Mode	Freq (Hz)	Zeta (%)	Freq (Hz)	Zeta (%)	Freq (Hz)	Zeta (%)
1	3.489	0.705	3.489	0.705	3.489	0.706
2	6.681	1.253	6.681	1.253	6.681	1.254
3	8.519	0.956	8.519	0.956	8.519	0.957
4	10.809	0.266	10.809	0.266	10.809	0.266
5	12.941	1.307	12.941	1.307	12.941	1.304

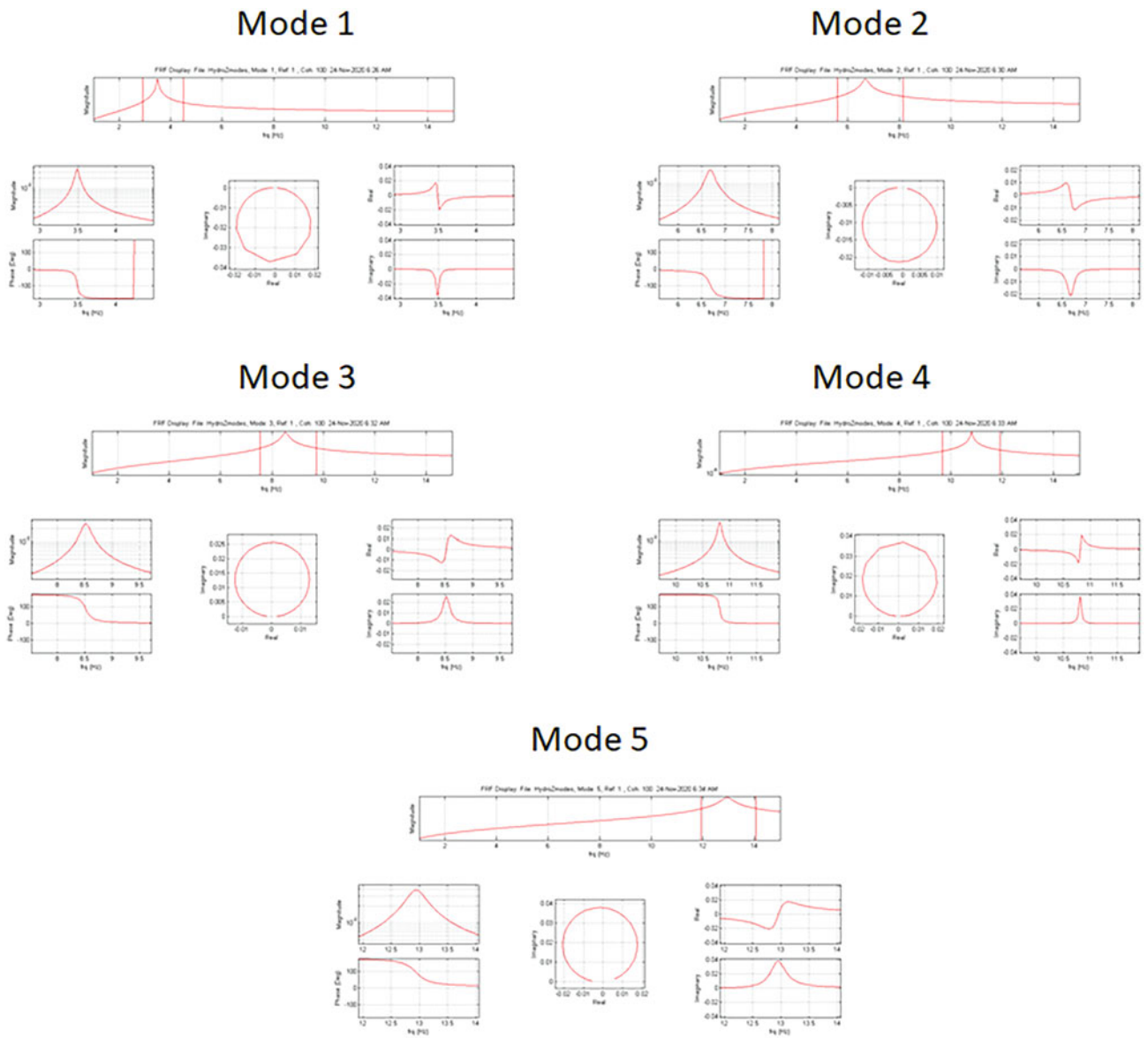

Fig. 10.12 SFD-2018 validation via complex mode isolation checks

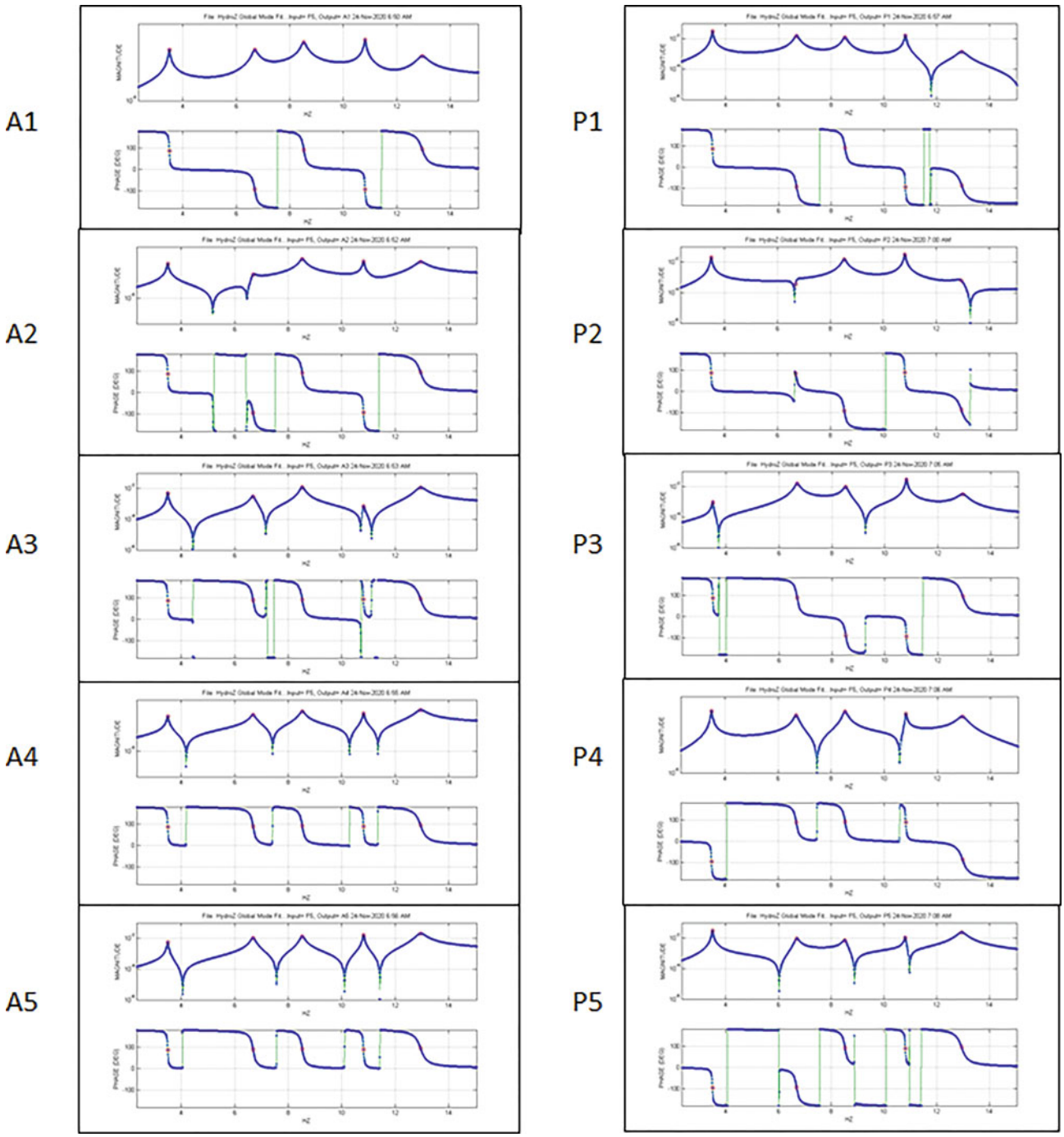

Fig. 10.13 "Classic" SFD validation via FRF reconstruction

Again it is pointed out that the "Classic" SFD results suggest that other EMA techniques [10] should produce results of similar integrity.

10.6 Conclusions

The overall goal of this paper was to introduce and demonstrate a basis for augmentation of measured *acceleration* response variables with measured *strain* and *fluid pressure* variables to enhance the modal test process for in vacuo structures and hydroelastic/vibroacoustic systems, respectively. Measured *strains* have been utilized by the technical community for understanding and quantification of redundant load paths. A rigorous theoretical analysis demonstrated that *strain-accelerations and fluid pressures* play roles that are consistent with accelerations.

Two simple illustrative examples clearly illustrate feasibility of measured *strains* and *fluid pressures* augmenting measured *accelerations* in experimental modal analysis. This finding goes a step beyond established past utilization of *strains* and *fluid pressures* in a surrogate role in experimental modal analysis. While *strain-accelerations* are definitely consistent with acceleration variables, employment of *strain-displacements* were found to be acceptable response variables through incorporation of quasi-static residuals in experimental modal analysis calculations (with some reservations on the part of this writer).

Augmentation of measured *acceleration* response variables with measured *strain* and *fluid pressure* variables produces mathematical experimental modal vectors that depart from application of established NASA and USAF criteria for experimental mode verification and validation and test-analysis correlation. That being said, the acceleration partition of the augmented experimental modal vectors may continue to be employed to satisfy the established U.S. government criteria. Enhanced experimental mode orthogonality, based on exploitation of SFD-2018 calculated left-hand eigenvectors, however, serves to extend the process of experimental mode verification and validation.

The subject matter and results presented in this paper represents an important first step towards utilization of measured *strain* and fluid *pressure* variables in experimental modal analysis (beyond their well-established roles as surrogate data). Much additional work is required in the experimental arena to secure broad peer community acceptance.

A.1 Appendix: The Simultaneous Frequency Domain Method (SFD)

A.1.1 Effective Dynamic Systems

The SFD method, introduced in 1981, has undergone substantial revision and refinement since that time. SFD describes physical FRFs associated with a series of "*N*" excitations in terms of the product of (1) a real reduction transformation matrix and (2) generalized FRFs,

$$\left[\ddot{U}_1(f)\ \ddot{U}_2(f)\ \ldots\ \ddot{U}_N(f)\right] = [V]\left[\ddot{\xi}_1(f)\ \ddot{\xi}_2(f)\ \ldots\ \ddot{\xi}_N(f)\right]. \tag{10.A1}$$

By performing singular value decomposition (SVD) analysis of the physical FRF collection, a dominant set of real generalized trial vectors, $[V]$, and complex generalized FRFs, $\left[\ddot{\xi}_1(f)\ \ddot{\xi}_2(f)\ \ldots\ \ddot{\xi}_N(f)\right]$, is obtained. Unit normalization of the SVD trial vectors is expressed as,

$$[V]^T\,[V] = [\mathrm{I}]\,. \tag{10.A2}$$

Theoretically, the generalized FRF array describes the following (real coefficient matrix) dynamic system equations,

$$\left[\ddot{\xi}(f)\right] + \left[\tilde{B}\right]\left[\dot{\xi}(f)\right] + \left[\tilde{K}\right][\xi(f)] = \left[\tilde{\Gamma}\right][F(f)]\,, \text{ where } \left[\tilde{B}\right] = \left[M^{-1}\right][B] \text{ and } \left[\tilde{K}\right] = \left[M^{-1}\right][K]\,. \tag{10.A3}$$

Estimation of experimental modal parameters is performed by complex eigenvalue analysis of the state variable form of the effective dynamic system,

$$\left\{\begin{matrix}\ddot{\xi}\\ \dot{\xi}\end{matrix}\right\} = \left[\begin{matrix}-\tilde{B} & -\tilde{K}\\ \mathrm{I} & 0\end{matrix}\right]\left\{\begin{matrix}\dot{\xi}\\ \xi\end{matrix}\right\} + \left[\begin{matrix}\tilde{\Gamma}\\ 0\end{matrix}\right]\{F\}\,, \tag{10.A4}$$

which is of the general type,

$$\{\dot{\eta}\} = \left[A_\eta\right]\{\eta\} + \left[\Gamma_\eta\right]\{F\}\,. \tag{10.A5}$$

Complex eigenvalue analysis of the effective dynamic system produces:

$$\begin{array}{ll} \text{(a)} & \{\eta\} = \left[\Phi_\eta\right]\{q\}\text{, where the "left-handed" eigenvectors are } \left[\Phi_{\eta L}\right] = \left[\Phi_\eta\right]^{-1} \\ \text{(b)} & \left[\Phi_{\eta L}\right]\cdot\left[\Phi_\eta\right] = [I]\,,\ \left[\Phi_{\eta L}\right]\cdot\left[A_\eta\right]\left[\Phi_\eta\right] = [\lambda] \quad \text{(complex eigenvalues)} \\ \text{(c)} & \left[\Phi_{\eta L}\right]\cdot\left[\Gamma_\eta\right] = [\gamma] \quad \text{(modal gains)} \\ \text{(d)} & \dot{q}_j - \lambda_j q_j = (\gamma)_j\,[F(f)] \quad \text{(frequency response of individual modes)}\,. \end{array} \tag{10.A6}$$

Recovery of experimental modes in terms of the physical DOFs involves back transformation employing the trial vector matrix, $[V]$, specifically,

$$[\Phi] = [V]\left[\Phi_\eta\right],\quad [\Phi_L] = \left[\Phi_{\eta L}\right]\left[V^T\right],\quad [\mathrm{OR}] = [\Phi_L][\Phi] \equiv [I]\,. \tag{10.A7}$$

A.1.2 "Classic" SFD

Estimation of the effective dynamic system with the SFD method (and more generally any method that performs similar system "plant" estimation operations) will pick up spurious "noise" degrees of freedom and associated spurious modes. Over the years since 1981, the writer has employed a heuristic practice in versions of SFD algorithms that select "authentic" modes from the complete set, which is estimated in selected frequency bands. The heuristic criteria include (1) elimination of modes having negative damping, (2) modes with very low modal gain, and (3) other modes that appear spurious from any number of physical/experience based considerations. Prior to 2018, the "Classic" SFD method (this writer's version) did not make use of the complex modes associated with the effective dynamic system (Eqs. (10.A4)–(10.A7)).

The theoretical relationship between FRFs and modal parameters (assuming that modal vectors are real) is

$$[H(f)] = [\Phi]\cdot[h(f)]\,, \tag{10.A8}$$

where $[\Phi]$ is the unknown real modal matrix and $[h(f)]$ is the SDOF acceleration FRF matrix. The terms of $[h(f)]$ are defined as,

$$h_n(f) = \frac{-(f/f_n)^2}{\left(1 + 2\mathrm{i}\zeta_n\,(f/f_n) - (f/f_n)^2\right)}, \tag{10.A9}$$

where f_n and ζ_n are the modal frequency and damping associated with the particular experimental mode. Since the modal SDOF acceleration matrix is completely known, the real modal matrix is obtained by linear least squares analysis. At the experimental modal analyst's discretion (highly recommended), low- and/or high-frequency residual modal frequencies may be added to the set of identified eigenvalues (the low-frequency residual FRF has a frequency close to "0" and a user-selected damping value, e.g., $\zeta_n = 0.01$, and the high-frequency residual has a frequency substantially higher than the highest experimental modal frequency and a user-selected damping value, e.g., $\zeta_n = 0.01$) to enhance accuracy of modal vector estimates.

The theoretical relationship between FRFs and modal parameters (assuming that modal vectors are complex) is,

$$[H(f)] = -(2\pi\cdot f)\cdot\sum_{n=1}^{N}\left(\frac{\Phi_n}{\lambda_n - \mathrm{i}\,(2\pi\cdot f)} + \frac{\Phi_n^*}{\lambda_n^* - i\,(2\pi\cdot f)}\right), \tag{10.A10}$$

where Φ_n is the unknown nth complex modal residue vector and λ_n is the nth (positive imaginary part) complex eigenvalue. The complex modal residue vectors are proportional to the complex system modes. Complex eigenvalues (when critical damping ratio is less than 1.0) are,

$$\lambda_n = -\zeta_n\omega_n + i\omega_n. \tag{10.A11}$$

Since the complex eigenvalues are completely known, the complex modal residue vectors (proportional to the complex modal vectors) are obtained by linear least squares analysis. As for the case of real modes, low- and/or high-frequency residual modal frequencies may be added to the set of identified eigenvalues to enhance accuracy of modal vector estimates.

Regardless of whether the user chooses to estimate real or complex modal vectors, reconstructed FRFs calculated from identified modal parameters serve as a means for a quality check on the overall "Classic" SFD process.

A.1.3 SFD 2018: A Fresh Look at Experimental Modal Analysis

The initial point of departure from "Classic" SFD practice is estimation of an effective dynamic system over the entire frequency band of interest (rather than selected sub-frequency bands). In order to achieve a satisfactory estimation for the effective dynamic system, the "tolerance" factor (Δ) employed in the SVD process is set to a sufficiently low value (10^{-5}); in previous sub-frequency band SFD calculations, the SVD "tolerance" factor was set to a value of 10^{-2}. Computation of effective dynamic system modal parameters, from the first-order system described in Eq. (10.A4), yields complex modes with eigenvalues having negative and positive imaginary parts. The first level of mode down-selection is to eliminate all modal eigenvalues and eigenvectors that are outside the positive frequency band of interest. A vital component of the mode down-selection process is selection of left-hand eigenvectors. $[\Phi_{\eta L}]$ that correspond to their $[\Phi_{\eta}]$ counterparts; this circumvents issues associated with more involved procedures for computation of a truncated left-hand eigenvector set.

Two computational procedures estimate uncoupled experimental modal FRFs (labeled with subscript "*A*"). The first method computes the exact modal solution from the estimated modal parameters of Eq. ((10.A6)-(d)). Specifically,

$$\left(h_j\right)_A = \left(\dot{q}_j\right)_A = \left(\frac{i2\pi f}{i2\pi f - \lambda_j}\right)\left(\gamma_j\right). \tag{10.A12}$$

The second method estimates uncoupled experimental modal FRFs (labeled with subscript "*E*") from linear combinations of the generalized FRFs (see Eqs. (10.A6)-(a) and (10.A6)-(b)) as follows:

$$\left(h_j\right)_E = \left(\dot{q}_j\right)_E = \left[\Phi_{\eta L}\right]_j \cdot (\dot{\eta}). \tag{10.A13}$$

Verification and validation of any candidate estimated experimental mode is now to be judged on the basis of (a) graphical displays of the modal FRFs, and (b) a new modal coherence metric, which is defined as,

$$COH_j = \frac{\left|\left[h_j(f)\right]_A^* \cdot \left[h_j(f)\right]_E\right|^2}{\left|\left[h_j(f)\right]_A^* \cdot \left[h_j(f)\right]_A\right| \cdot \left|\left[h_j(f)\right]_E^* \cdot \left[h_j(f)\right]_E\right|}. \tag{10.A14}$$

References

1. Williams, D.: Dynamic loads on aeroplanes under given impulsive load with particular reference to landing and gust loads on a large flying boat. Great Britain Royal Aircraft Establishment Reports SME 3309 and 3316 (1943)
2. Zienkiewicz, O.C., Taylor, R.L., Zhu, J.Z.: The Finite Element Method, Its Basis and Fundamentals, 6th edn. Elsevier (2005)
3. Toupin, R.A.: A variational principle for the mesh-type analysis of a mechanical system. J. Appl. Mech. **74** (1952)
4. Coppolino, R.N.: A numerically efficient finite element hydroelastic analysis, NASA CR-2662 (1976)
5. Coppolino, R.: A simultaneous frequency domain technique for estimation of modal parameters from measured data, SAE Paper 811046 (1981)
6. Coppolino, R., Stroud, R.: A global technique for estimation of modal parameters from measured data, SAE Paper 851926 (1985)
7. Coppolino, R.N.: Experimental mode verification (EMV) using left-hand eigenvectors, IMAC 37 Proceedings (2019)
8. Load analysis of spacecraft and payloads, NASA-STD-5002 (1996)
9. Independent structural loads analysis, USAF Space Command, SMC-S-004 (2008)
10. Piersol, A.G., Paez, T.L. (eds.): Harris' Shock and Vibration Handbook, 6th edn. McGraw-Hill (2010) (Chapter 21, Experimental modal analysis, allemang and brown)

Chapter 11
Dynamic Behavior of Post-Buckled Fixed-Fixed Composite Skin Panels

Andrew J. Ehler, Amanda J. Lial, Jason A. Cohrs, Matthew P. Snyder, and Matthew B. Obenchain

Abstract The purpose of this experiment was to observe the dynamic behavior of bi-stable composite plates with fixed-fixed boundary conditions. In particular, the team sought to observe the minimum energy required to induce snap-through of post-buckled carbon epoxy composites fixed inside an aluminum frame. Initially, students collected the time response of the plate using an impact hammer and laser vibrometer. From the frequency response, the natural frequencies of the plates were determined and compared to analytically predicted results based upon a model constructed using thin plate theory and classical laminate theory. Next, the dynamic responses of the plates were obtained by applying various loading conditions with the use of a shaker table. These tests yielded validating natural frequencies to impact testing and the resonant frequencies of post-buckled plates. The minimum loading conditions required to cause snap-through in a post-buckled plate were found and analyzed across various conditions. These results provide a basis for determining minimum energy requirements required to cause buckling behavior in composite plates for applications to the hypersonic environment.

Keywords Composites · Dynamic response · Snap-through · Natural frequency · Vibrations

11.1 Introduction

Composite skin panels are an increasingly attractive option for aerospace applications, and foundational research is advancing to develop the understanding of the scientific community with respect to their response under dynamic loading conditions. Much of the previous research that has occurred on this topic has been with free boundary conditions. For example, Ranaparkhi and Sarnobat compared experimental results while supporting composite plates with strings to create a free boundary condition and then found their experimental results to be congruent with finite element analysis results [1]. Pingulkar analyzed the vibration of composite plates in a cantilever configuration, and these experimental results were also found to closely agree with an associated finite element model [2].

In a hypersonic environment, thermal forces and aerodynamic forces can combine to force buckling and post-buckled behavior in flight. The specific phenomenon this study addresses is bi-stable snap-through of a representative composite panel through frequency response analysis. Different anisotropic panels were manufactured in both uniaxial and cross-ply configurations with carbon-epoxy laminates. This study adds to the research done by McLean et al. [3] by reassessing their predictive modeling code and its ability to predict natural frequencies of composite plates as well as further analyzing the minimum energy requirements to produce snap-through across various plate layering configurations.

A. J. Ehler · A. J. Lial · J. A. Cohrs · M. P. Snyder (✉) · M. B. Obenchain
Department of Mechanical Engineering, United States Air Force Academy, USAF Academy, CO, USA
e-mail: c21andrew.ehler@afacademy.af.edu; c21amanda.lial@afacademy.af.edu; c21jason.cohrs@afacademy.af.edu; matthew.snyder@usafa.edu; matthew.obenchain@afacademy.af.edu

B. J. Dilworth, M. Mains (eds.), *Topics in Modal Analysis & Testing, Volume 8*, Conference Proceedings of the Society for Experimental Mechanics Series, https://doi.org/10.1007/978-3-030-75996-4_11

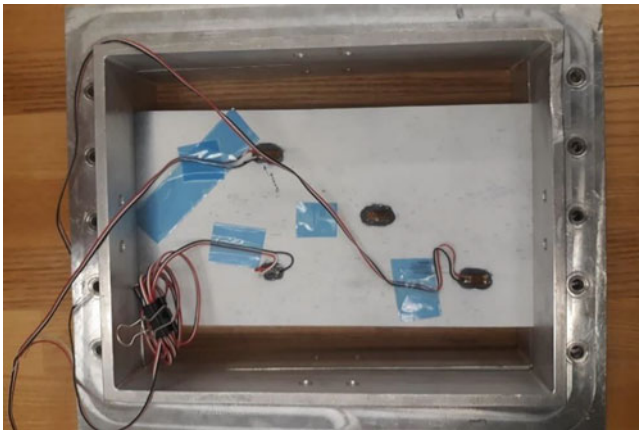

Fig. 11.1 Strain gage positioning on the composite plate

11.2 Experimental Methods

11.2.1 Testing Setup

Carbon-epoxy laminates were previously manufactured in-house using standard layup techniques [3]. The two specimens used in this study were plates with laminate configurations of $[0]_4$ and $[0/90]_s$ which were 5 × 12 in. These specimens were then uniformly marked with 15 grid points. For this study, the plates were affixed in an aluminum test fixture in order to maintain fixed boundary conditions on each end. When affixing the carbon epoxy composite specimen in the aluminum test fixture, the goal was to have zero strain on the composite plate after tightening the bolts of the metal frame. This ensured that no buckling was present in the system prior to experimentation. In order to do this, the bolts were tightened in an alternating pattern similar to that of torqueing down a tire. The strain on the plate was recorded using strain gauges shown in the setup above in Fig. 11.1. While it proved impossible to reduce the strain throughout the plate to zero and maintain suitable fixed-fixed boundary conditions, strain could be minimized using this method incrementally. The six surrounding bolts were first torqued to 5.42 Nm and then to 9.49 Nm. A possible source of error addressed by the team in this process was slight warping on a corner of the frame. In future testing, the team recommends examining better means to create a zero-strain environment either by using a medium inside the frame or creating a new testing frame.

11.2.2 Impact Testing

Once the composite plate was properly affixed inside the test fixture, the frame was inserted into a foam block to prevent vibration interference from outside noise as show in Fig. 11.2. A tripod holding the Polytec CLV 3D laser vibrometer was placed above the specimen. The laser from the vibrometer was oriented over a specific point. This point was not hit with the hammer; however, the remaining 14 points were. An impact hammer was used to deliver a firm, quick "tap" on the specimen's points. The data produced from the impact was recorded using VibSoft and exported to MATLAB. The vibrometer was set at six different locations on the plate as denoted by graphite squares to determine if results were consistent. The data from VibSoft was imported into MATLAB to plot the results.

11.2.3 Shaker Table Testing

Following completion of the impact testing, shaker table testing was conducted. The test fixture was mounted onto the table and two accelerometers placed on the plate according to Fig. 11.3 below. The same set of data collection was performed on each specimen.

Fig. 11.2 Impact testing setup showing vibrometer and foam holder with test fixture

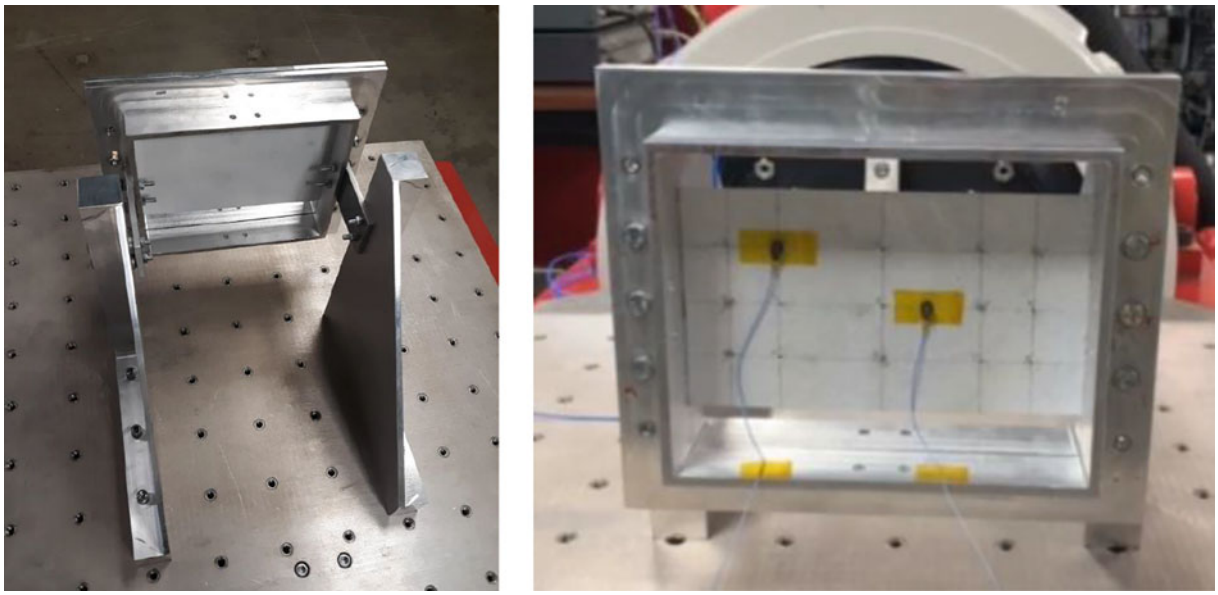

Fig. 11.3 Composite plate and metal frame system set transverse to the shaker table

Testing began with a low amplitude-frequency sweep at 0.25 g on the plates. Then, buckling was induced by putting pressure on the center of the plate evenly using a ruler to create a deformation of 1.5 mm, and the frequency sweep was again repeated at 0.25 g and the response data was recorded. Then, starting at 0.5 g, the amplitude of the loading was increased by 0.5 g increments up to 3 g in order to observe the frequency response to induced vibration. Finally, after determining the frequency at which the minimum energy necessary to induce a chaotic snap-through region, two tests were run. First, the plates were tested at a high amplitude of g loading which was decreased until the chaotic snap-through region ceased. Then, the opposite procedure was executed starting from a low g amplitude and moving up until the chaotic snap-through region was reached.

11.3 Results and Discussion

11.3.1 Determination of Natural Frequencies

Data collected from the impact testing experiments were analyzed in order to determine the frequency response of the plates. Magnitude responses from the six vibrometer-measurement locations were plotted against the corresponding frequencies. Peaks in these frequencies indicate the natural frequencies of the composite plates. Figures 11.4 and 11.5 show the results of this analysis for the $[0]_4$ and $[0/90]_s$ plates. Notable in these figures are the large spikes present around the 25 Hz location. The team believes that these peaks are most attributable to environmental factors in the testing location. This would explain the large magnitude of the peaks compared to the resonance peaks. The consistency in these spikes across tests conducted on multiple plate configurations and the lack of analytical evidence supporting a natural frequency at this frequency indicate these are from outside factors.

The results in Fig. 11.4 for the $[0]_4$ plate indicate the first three natural frequencies occurring at 118.3, 132, and 208.6 Hz. Analytical predictions for these frequencies were determined using the methodology described in [3]. This analysis considered the layup configuration of the plate and the fixed-fixed boundary conditions, and indicated the natural frequencies

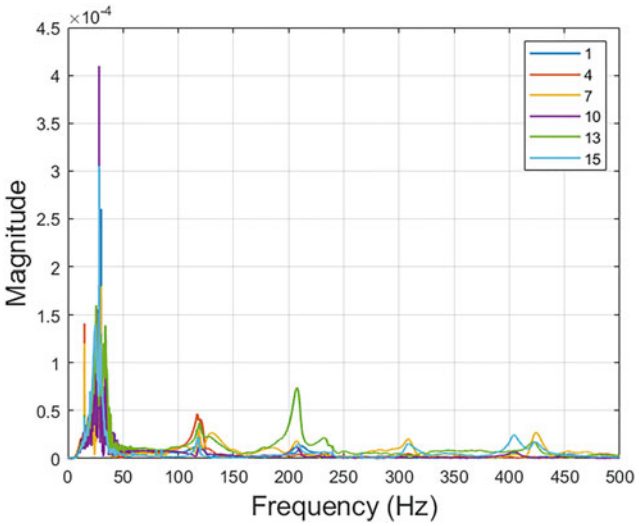

Fig. 11.4 FRF magnitude response for $[0]_4$ plate

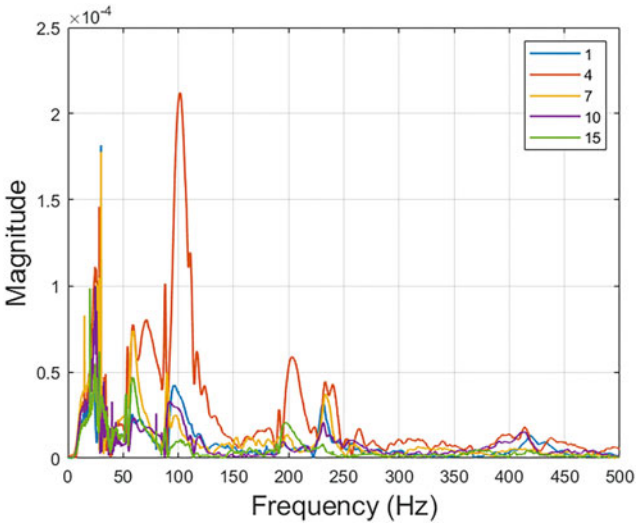

Fig. 11.5 FRF magnitude response for $[0/90]_s$ plate

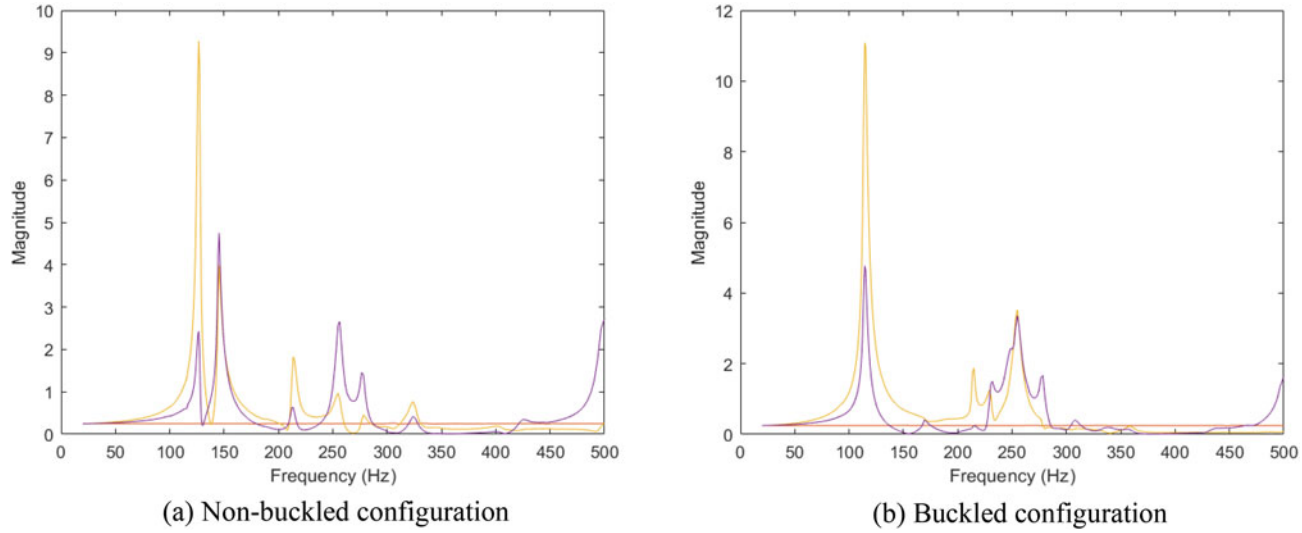

Fig. 11.6 Sine sweep magnitude responses of $[0]_4$ plate for non-buckled and buckled configurations

to be 103.5, 153.1, and 259.9 Hz. These results matched overall behavior, but they were not accurate in predicting specific values. Part of this may be due to inconsistencies in the boundary conditions from being truly fixed-fixed in the experimental testing. Additionally, inconsistencies in the material may further contribute to differing values.

Due to surface irregularities on the $[0/90]_s$ plate, noisier vibrometer data were collected at several of the testing points than the data found for the $[0]_4$ plate. This caused some difficulty differentiating between the peaks indicating the natural frequencies. Namely, referring to Fig. 11.5, there appears to be a resonance peak around 60 Hz. However, analysis on other plates with similar conditions showed that this peak is likely an artifact of the plate surface rather than the fundamental frequency. From this, the group concluded that the first three natural frequencies occurred at 101.3, 196.7, and 232.0 Hz. Analytical predictions based upon the geometry and material of the plate yielded natural frequencies of 97.1, 188.8, and 267.72 Hz. Similar to the $[0]_4$ plate, the analytical predictions vary from the experimentally obtained results. However, especially notable in these results is that the first two resonance frequencies closely match the predicted results compared to the third frequency. This suggests the analytical model may be more accurate in predicting natural frequencies associated with the lower modes than it is with the higher modes.

11.3.2 Changes in Natural Frequency of Post-Buckled Configuration

Following completion and analysis of the impact testing using a laser vibrometer, the plates were tested on a shaker table. The sine sweep using a flat, pre-buckled configuration for the $[0]_4$ plate yielded resonance peaks at 126.0, 145.5, and 206.6 Hz as shown in Fig. 11.6a. In this figure, the two data sets represent the two accelerometers attached to the plate. The observed natural frequencies closely match the predicted natural frequencies and those determined during the impact testing, thus confirming the team's conclusions concerning the experimentally used plates' natural frequencies. Following the reconfiguration of the plate to a post-buckled state, the sine sweep was re-run and the magnitude was again plotted against the frequency as shown in Fig. 11.6b. The resonance peaks for the buckled configuration were much less defined, apart from the fundamental frequency at 115.2 Hz. The results showed lesser defined peaks at 213.6 and 239.1 Hz. The slight shift left on the first natural frequency was expected, as buckling reduces the effective stiffness of the plate, thus lowering the expected fundamental frequency. Analysis focused on higher frequencies was not considered.

The same analysis was conducted on sine sweeps conducted on the $[0/90]_S$ plate. The non-buckled configuration shown in Fig. 11.7a had resonance peaks at 91.3, 173.5, and 215.0 Hz. In Fig. 11.7b, the buckled configuration had peaks 68.7, 159.9, and 213.6 Hz. These results correspond with the findings of the $[0]_4$ plate analysis. The fundamental frequency shifted left from the non-buckled configuration as expected. While the higher frequencies still saw some shift from the non-buckled configuration, the differences were not as drastic as the $[0]_4$ plate.

The summary of the results for the natural frequency behaviors of the two composite plates tested are shown in Table 11.1 below. These results indicate that there was consistency among the three test and analytical procedures in determining

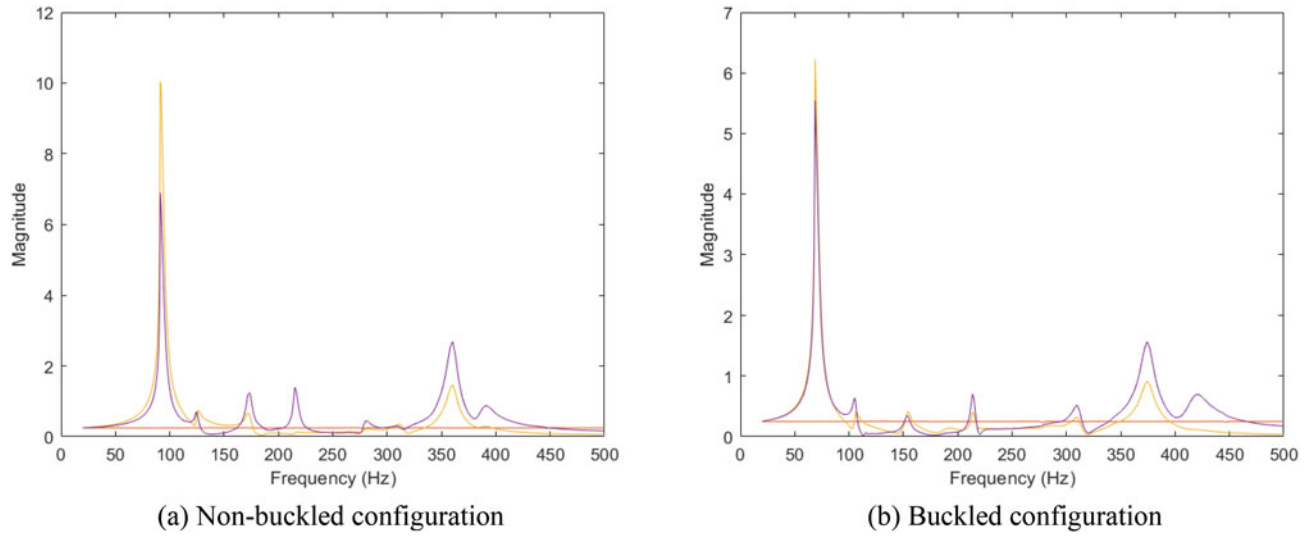

Fig. 11.7 Sine sweep magnitude responses of $[0/90]_S$ plate for non-buckled and buckled configurations

Table 11.1 Fundamental frequency for non-buckled plates across tests

	$[0]_4$ Plate (Hz)	$[0/90]_S$ Plate (Hz)
Predicted frequency	103.5	97.1
Impact test frequency	118.3	101.3
Shaker table frequency	126.0	91.3

the natural frequency of the composite plates. Of note is the relative inconsistency between the placements of the results. The predicted frequency based upon the analytically model was not always the lowest nor was the shaker table always the highest as indicated by the $[0]_4$ plate. Instead, the relative values of the natural frequencies varied across the tests. The researchers conclude that these differences were therefore most attributable to the testing conditions and inconsistencies within the testing frame and setups. Further experimentation is needed to find if these inconsistencies can be reduced.

11.3.3 Determination of Minimum g-Loading

After determining the fundamental frequencies of the buckled plates, the minimum energy required to produce the chaotic snap-through effects was determined. Sine sweeps of the buckled plate configurations were once again analyzed to determine the g-loading at which snap-through occurs. Below in Fig. 11.8 is a demonstration of this phenomenon as seen in the magnitude response.

In the 2.0 g loading in Fig. 11.8a, there was a slight perturbation in the curve rising to the peak about the 101.5 Hz point. This represents the point at which snap-through was about to occur and caused non-uniform deflections detected by the accelerometers. Figure 11.8b fully shows this snap-through. At 2.5 g, there was significant disturbance from 98.4 Hz until 112.0 Hz. These disturbances reflect snap-through in the plate. The abnormal magnitude response detected by accelerometers corresponds to the abnormal plate motion. From this, one can conclude that the minimum g-loading required to obtain snap-through was within this range of frequencies and between 2.0 and 2.5 g.

Frequencies were set in increments in this range and the minimum g-loading determined. Referring to Fig. 11.9, this minimum g-loading occurred at around a frequency of 99 Hz. The team also found that the minimum g-loading required for snap-through depended on whether snap-through had already occurred or not. When higher g-loads were applied to generate snap-through and then reduced until snap-through ceased, the required loading was lower, as indicated by the blue line. However, when g-loading was gradually applied until snap-through occurred, the g-loading was higher, as indicated by the red line. The researchers postulate that such behavior is seen because there is a certain potential energy required to overcome inertia in order to initiate snap-through. This allows the minimum g-loading to maintain snap-through to be smaller than that required to cause snap-through. The minimums for the increasing and decreasing loads were 2.19 and 1.95 g respectively.

The g-loading test analysis was repeated with the $[0/90]_s$ plate to further analyze and confirm the results of the $[0]_4$ plate. Below in Fig. 11.10 are the sine sweep results of three different loading conditions showing the snap-through phenomenon.

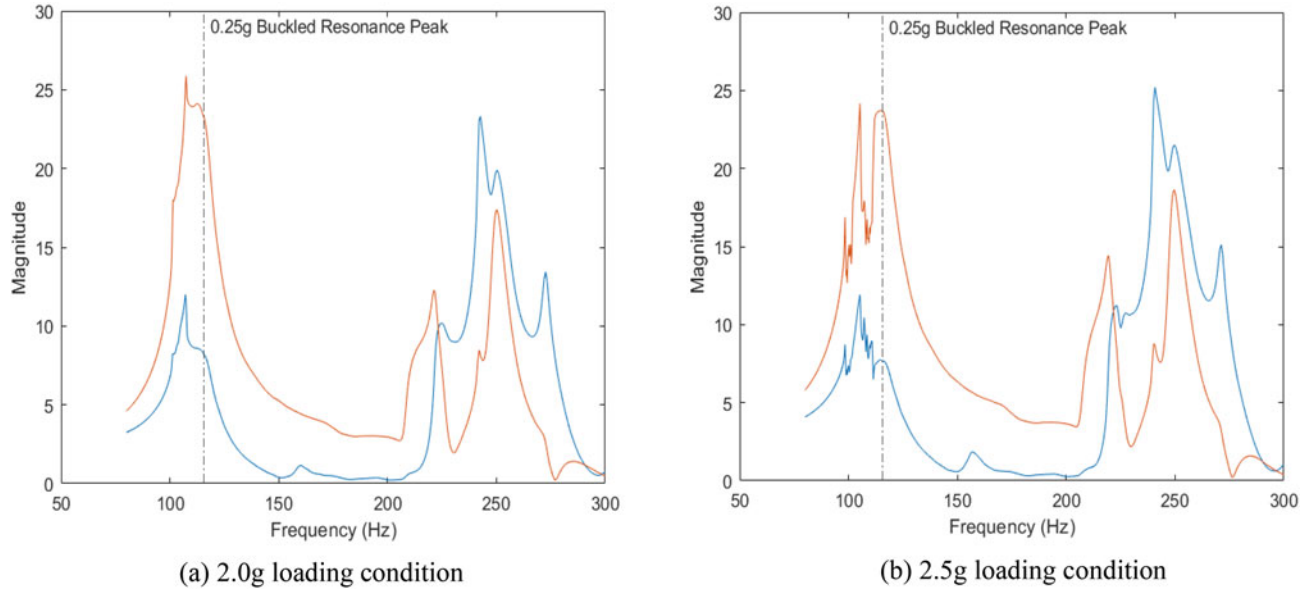

Fig. 11.8 Sine sweep magnitude responses of $[0]_4$ plate at varying g-loads demonstrating snap-through phenomenon

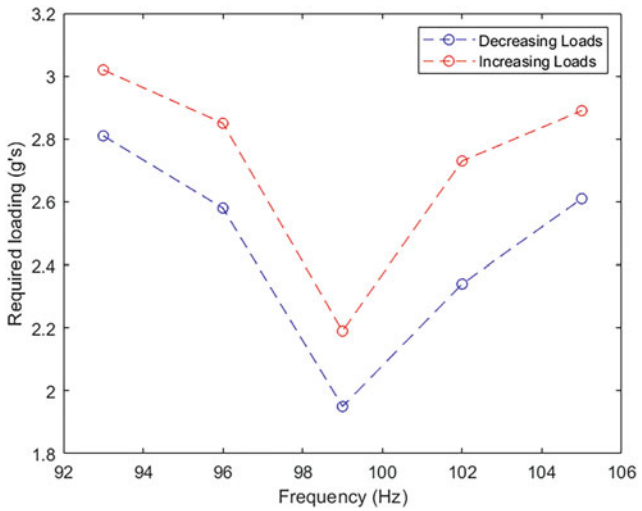

Fig. 11.9 Minimum g-loading required to incite snap-through behavior for $[0]_4$ plate

In (a), there is a slight disturbance indicating potential snap-through at 73.4 Hz. In (b) at 2.5 g, snap-through is evident from 71.5 to 78.9 Hz. This region expands in (c) at 3.0 g, ranging from 69.7 to 82.4 Hz. This region illustrates a chaotic snap-through region where the plate moved rapidly back and forth between the two stable equilibria. The expansion of the snap-through across a larger range of frequencies was expected, as the greater energy present in higher loading conditions allows snap-through to occur further from the resonance peak. As with the $[0]_4$ plate, the minimum g-loading to cause snap-through was examined. At a frequency of 70 Hz, snap-through could be maintained with a g-loading of 2.19 g. This corresponded to the same g-loading for the $[0]_4$ plate.

11.4 Conclusions

The results of these experiments demonstrated the usefulness of examining the dynamic response of bi-stable composite plates. The analytical model was capable of predicting generalized behavior of the natural frequencies of the composite plates. However, more analysis should be done to assess whether the differences were attributable to improper testing

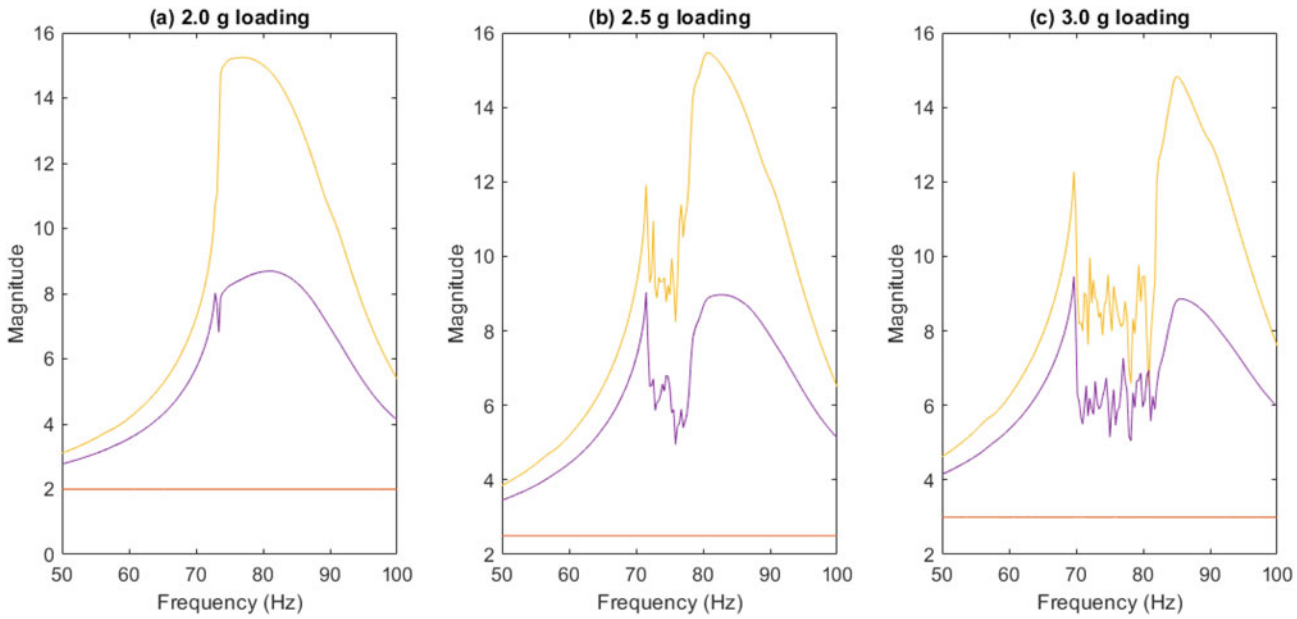

Fig. 11.10 Sine sweep magnitude responses of $[0/90]_S$ plate at varying g-loading conditions

environment procedures or whether the model must be refined. Moreover, the model does not yet predict the buckled behavior of the plates, which is necessary to predict the minimum g-loading.

The dynamic testing results showed that natural frequencies found for flat-plate, non-buckled configurations closely matched those obtained with the laser vibrometer. When moved to the post-buckled configuration, the resonant frequencies of the plates shifted downwards. As increased g-loading was applied, the snap-through behavior was observed. By incrementally increasing the loading about the fundamental frequency, the region of frequencies in which the snap-through behavior occurred also increased. Determining the minimum energy required for snap-through yielded two results. There was a minimum g-loading associated with maintaining snap-through behavior and a higher g-loading associated with causing snap-through behavior. Future analysis should focus more on the greater loads needed to initiate snap-through, as this is the primary concern for hypersonic applications. In our case analysis, both of the minimum loading conditions associated with causing snap-through behavior occurred at 2.19 g.

References

1. Ratnaparkhi, S.U., Sarnobat, S.S.: Vibration analysis of composite plate. Int. J. Mod. Eng. Res. **3**(1), 377–380 (2013)
2. Pingulkar, P., Suresha, B.: Free vibration analysis of laminated composite plates using finite element method. Polym. Polym. Compos. **24**(7), 529–538 (2016)
3. McLean, C.M., Ferguson, J.I., Phillips, S.C., Cabri, A.R., Snyder, M.P., Obenchain, M.B., Spottswood, S.M.: Dynamic behavior of bi-stable fixed-fixed composite plates, AIAA SciTech 2019 Forum (January 2019).